Tampereen teknillinen yliopisto. Julkaisu 695
Tampere University of Technology. Publication 695

Markku Leino

Finite-Temperature Quantum Statistics of a Few Confined Electrons and Atoms – Path-Integral Approach

Thesis for the degree of Doctor of Technology to be presented with due permission for public examination and criticism in Sähkötalo Building, Auditorium S4, at Tampere University of Technology, on the 16th of November 2007, at 12 noon.

Tampereen teknillinen yliopisto - Tampere University of Technology
Tampere 2007

ISBN 978-952-15-1875-1
ISSN 1459-2045

ABSTRACT

The characteristics of Nature can be surveyed in surprisingly wide scope by applying path-integrals. For example, studies of the behavior of condensed helium at temperatures of milli-Kelvins to the investigations of properties of light elements in the interior of giant planets are conducted using path-integrals—does Jupiter have a rocky core or what is the cause of supra liquids? Particularly, finite temperature is naturally taken into account readily, which is a rather difficult task with other quantum methods. Furthermore, the path-integrals allow us to study the phenomena beyond the Nature—that is the vague district between the classical Nature and quantum Nature.

The work presented in this thesis is based on the the path-integral formalism which is used to describe few-particle quantum systems, concentrating on many-body correlations and temperature effects. The path-integrals are evaluated with Monte Carlo methods, and therefore the foundations of Monte Carlo is briefly introduced. Furthermore, the estimators of potential and kinetic energies and distribution functions are given and their efficiency is studied. These are applied to nanophysics, surface science and molecular physics.

First, we study objects of modern nanophysics, called quantum dots. Properties of charge carriers that are restricted to a small confinement are essential in understanding and development of novel semiconductor technologies. We evaluate the one-electron distributions and two-electron correlation functions, and study the finite temperature effects on both in a two coupled disc-like quantum dots with one or two electrons. It is found that an increase of temperature broadens the distributions as expected, the effect being smaller for correlated electrons than for the single ones. Also, the two-electron pure state energetics of a parabolic quantum dot is resolved from the finite-temperature mixed state energies, and the correlation induced shifts of the first and second excited states are evaluated.

Second, finite temperature many-body quantum behavior of hydrogen adsorbates on Ni(001) surface is simulated. The adsorbate–surface and adsorbate–adsorbate interactions are described by the many-body alloy potential form, fitted to the adsorption parameters from density functional theory calculations. This allows consideration of substrate atom dynamics, too. Temperatures 100 K and 300 K and coverages from $1/8$ to $7/8$ are considered. Also quantum and classical adsorbate behavior are compared.

At low temperatures, the quantum delocalization of the adsorbates is consider-

able with all studied coverages, and therefore, the temperature dependence of the distributions is weak. At higher temperatures, however, the thermal dynamics of the substrate dominates all studied phenomena and a classical description seems to be sufficient. At $T = 300$ K, however, the H–H interaction energy has a considerable effect on distributions and energetics. Both temperature and coverage dependencies become strong at studied temperatures.

Third, the coupled quantum dynamics of the electron and the nuclei in the hydrogen molecule ion, a three body system, is studied. The coupling effects are demonstrated by comparing differences in adiabatic Born–Oppenheimer and non-adiabatic simulations, and inspecting projections of the full three-body statistics onto adiabatic Born–Oppenheimer approximation. The nuclear pair correlation function is found to broaden and the average bond length is larger. Also, a non-adiabatic correction to the binding energy is found.

Computating capacity is found to become the limiting factor in all simulations with increasing accuracy or increasing number of particles. Besides that, it should be noted that adopting efficient algorithms is very crucial.

FOREWORD

Path-integrals are an alternative—but equivalent to the conventational wavefunction—description of quantum mechanics. It has the origin in the PhD work of Richard Feynman at Princeton (Brown, 2005). Feynman emphasizes the experimental nature of physics, mastering the mathematical tools, too. The *gedanken* experiments of Feynman are simple and pedacogical, and thus, are not easy to conduct in the real world—while revealing the *character of physical law* very clearly.

Though the concept of path-integrals have arisen from quantum mechanics, these are a powerful tool in many other branches of science and mathematics, e.g. financial mathematics, too. However, there is some theoretical work still to be done: the time-dependent path-integrals are not on a perfectly solid ground, yet, and solutions to fermion sign as well as Coulomb singularity problems need more development. Despite that, it should be noted, that essentially we are able to solve all path-integrals in quantum mechanics which correspond to problems for which the Schrödinger equation have exact analytical solutions, see Grosche and Steiner (1995) for an extensive listing.

Quantum Mechanics and Path Integrals, Feynman and Hibbs (1965), is an excellent book to start studying time-dependent quantum mechanics and path-integrals. The stationary systems are studied in Feynman (1948) and Feynman (1972), which is a collection of lectures on statistical mechanics. Kleinert has conducted research in collaboration with Feynman, and his brick (2004) deals mainly with time-dependent problems. The book of Schulman (1981) has more physical point of view, and is more readable still being quite rigorous. Müller-Kirsten (2006) deals with general quantum mechanics and also with path-integrals, Ballentine (1999) and Binder and Heermann (2001) have also written some chapters about path-integrals.

Furthermore, there exist many lecture notes on the subject, nowadays freely available on the internet. Some of those are Ali and Inomata, Wetterich (2006), Ingold or Simmons. Also, one should take a look at the large quantity of works of Ceperley and Tuckerman, both concentrating on numerical evaluation of path-integrals.

This thesis collects and completes the results of a study which I have conducted under supervision of Professor Tapio T. Rantala at the Institute of Physics, Tampere University of Technology. The thesis is partitioned in three chapters. The first part describes the foundations of quantum mechanics and path-integrals,

the second part guides to the Monte Carlo simulations and to the estimation of properties, and the third part is a summary to our applications of path-integrals to nanophysics, surface science and molecular physics.

The two questions, about *fermion sign problem* and *Coulomb singularity* are not considered in this thesis in detail. These problems plague the path-integral many-body calculations, and must be solved—or somehow circumvented—in *ab initio* material design. In literature, many different approaches are invented to overcome the problems.

In this work, all mathematical terminology—where possible—refers to free resources, such as Wolfram MathWorld (`www.mathworld.com`) or Wikipedia, the free encyclopedia (`www.wikipedia.org`). Furthermore, every algebraic step is clearly visible, while most of the arithmetical steps are left out to shorten the notation, allowing a more readable introduction to quantum mechanics within the path-integral formalism.

First and foremost, I would like to thank my supervisor, professor Tapio T. Rantala for his guidance and support during these years needed to finish this thesis. I would also like to thank the crew of TCOMP and Institute of Physics, particularly docents Jouko Nieminen and Matti Lindroos. The younger generation of TCOMP need commendations, with special respects to Mr. Jussi Ojanen and Mr. Ilkka Kylänpää. This thesis was reviewed and critized by two distinguished experts, Anders Sandvik and Göran Wahnström, to whom I express my gratitude. I would like to thank the Finnish Cultural Foundation (Pirkanmaan Maakuntarahasto) and the Graduate School of Tampere University of Technology for financial support. Last but not least, I want to thank my family, my relatives and all my friends. *Onko helmenkalastajilla arkea?*

List of Publications

The thesis includes the following publications

- Paper I: M. Leino and T. T. Rantala, *Finite-temperature effects on correlation of electrons in quantum dots*, Physica Scripta, T114, 44–48, 2004, Leino and Rantala (2004),
- Paper II: M. Leino and T. T. Rantala, *Temperature effects on electron correlations in two coupled quantum dots*, Few Body Systems, 40(3–4), 237–252, June 2007, Leino and Rantala (2007),
- Paper III: M. Leino, J. Nieminen, and T. T. Rantala, *Finite temperature quantum distribution of hydrogen adsorbate on nickel (001) surface*, Surface Science, 600, 1860–1869, March 2006, Leino et al. (2006),
- Paper IV: M. Leino, I. Kylänpää, and T. T. Rantala, *Coverage dependence of finite temperature quantum distribution of hydrogen on nickel (001) surface*, Surface Science, 601, 1246–1254, March 2007 Leino et al. (2007), and
- Paper V: I. Kylänpää, M. Leino, and T. T. Rantala, *Hydrogen molecule ion: Path integral Monte Carlo approach*, Accepted to Physical Review A, 2007, Kylänpää et al. (2007).

The author has carried out the calculations and analysis of results including writing of manuscripts for Papers I–IV, except for the MBA-fitting in Paper III. Paper V is based on the Fortran program that author initially coded for calculations related to papers I-IV, and also, the present author has partly written and analyzed the results.

CONTENTS

INTRODUCTION TO PATH-INTEGRALS

Mä metsän polkuja kuljen
Mä metsän polkuja kuljen
kesä-illalla aatteissain
ja riemusta rintani paisuu
ja ma laulelen, laulelen vain.
...

Microscopic properties of Nature are described astonishing well by a mathematical structure called *quantum mechanics*. It is postulated in section 1.1, where the ideas of state, observable and measurement are given. Some of the tools of functional analysis and measure theory, which are given in this section, however, are not essential in the following sections. These are given to link the quantum mechanics with rigorous mathematical theory. Section 1.2 extends basic ideas to density matrices, and thereafter, the path-integrals are introduced.

First, section 1.3 deals with the concept of path-integrals by using the free particle and related systems. Then, in section 1.4, path-integrals of quantum particles in general potentials are considered. Also, the dynamical, or time-dependent path-integral is introduced. The results needed in computations are shown again in a compact form in section 1.5. The special example of the harmonic oscillator is worked out in detail in section 1.6.

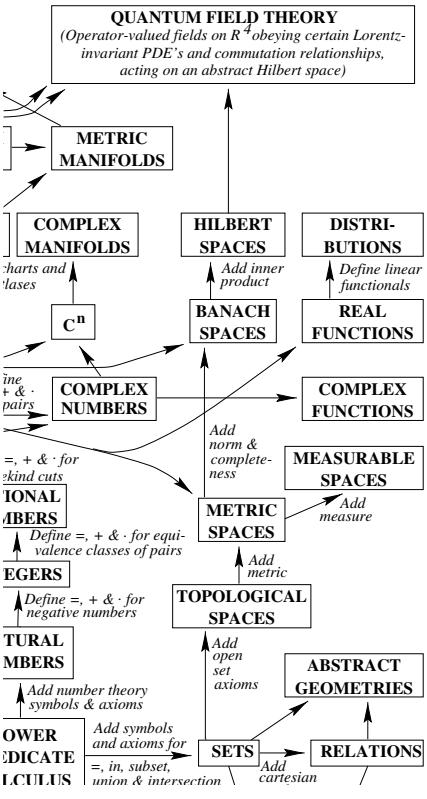

Some mathematical structures and their relations according to Tegmark (1998).

1.1 POSTULATES OF QUANTUM MECHANICS

The mathematical formalism of quantum mechanics is well developed and can be abstracted from any of several textbooks. The postulates and formalism that are presented here are extracted mainly from the books of Atkins and Friedman (1970), Ballentine (1970, 1999), Cronström and Montonen (1991), Lahti (2005),

Nielsen and Chuang (2002). Furthermore, some more mathematically oriented textbooks are used, especially von Neumann (1955, p. 36–46) and textbooks of standard functional analysis (Gariepy and Ziemer, 1995, Pedersen, 2000).

The primitive concepts are those of *state* and *observable*, and the practise needs the definition for the process of *measurement* and *composite systems*, too.

1.1.1 STATE

The basis for separable Hilbert space is at most countable.

Hermiatian, aka self-adjoint, aka conjugate symmetric.

The description of a physical system $\mathcal{S}$ is based on a complex, separable (usually infinite dimensional) Hilbert[1] space $\mathcal{H}$ known also as the *state space*. The Hilbert space is linear and complete, and there is a Hermitian[2] inner product. Especially in texts about physics, the inner product is usually postulated to be linear subject to the second argument and antilinear to the first argument, and that is denoted by $\langle\cdot|\cdot\rangle$, opposed to mathematics notation $(\cdot|\cdot)$ or $(\cdot,\cdot)$ (Kahanpää, 2005, Footnote in p. 49). A Hilbert space is equipped with an orthonormal basis, and all elements of the Hilbert space can be written in a unique way as a linear expansion, or sum of multiples, of these basis elements. In some physical cases the Hilbert space must be extended to the sc. *Rigged Hilbert space* (Ballentine, 1999).

aka. Gelfand triple, nested Hilbert space, equipped Hilbert space. With that one can handle some pathological problems, e.g. normalization of $\exp(\imath px)$.

Postulate 1. *Each state $\widehat{\rho}$ of the system $\mathcal{S}$ is represented by some self-adjoint, nonnegative, and of unit trace operator in the Hilbert space $\mathcal{H}$*

$$\widehat{\rho} : \mathcal{H} \to \mathcal{H}.$$

The term *density function* is not widely used in literature.

The state is also called a statistical operator, density operator, or density matrix, although the latter term should be restricted to its matrix form (in coordinate representation). The set of all states is convex: if $\widehat{\rho}_1$ and $\widehat{\rho}_2$ are states, then $t\widehat{\rho}_1 + (1-t)\widehat{\rho}_2$ is also a state when $t \in [0,1]$. The state $\widehat{\rho} = \widehat{\rho}^2$ is called a *pure state* if it belongs to the extreme point of the convex set. Otherwise, it is called a *mixed state*.

Canonical is an adjective derived from *canon* which comes from the Greek *kanon* (rule). Mathematicians use the word *canonical* to refer to concepts that have a kind of uniqueness or naturalness. A *canonical form* of an object is a standard presentation.

Because the set $\{\lambda \in \sigma(\widehat{\rho}) |\ |\lambda| > \epsilon > 0\}$ is finite for discrete spectrum, the zero-excluding spectrum $\sigma(\widehat{\rho}) \setminus \{0\}$ can be arranged to a sequence (λ_i), and the measure $\mathrm{d}E(\lambda)$ in spectral theorem $\widehat{\rho} = \int_{\sigma(\widehat{\rho})} \lambda \mathrm{d}E(\lambda)$ reduces to a projection $P_n = \mathrm{d}E(\{\lambda_n\}) = |\phi_n\rangle\langle\phi_n|$.

All states $\widehat{\rho}$ can be diagonalized in terms of its eigenvalues and eigenvectors, resulting in sc. *canonical expansion*

$$\widehat{\rho} = \sum_{i=0}^{\infty} \rho_i \widehat{P}_i, \tag{1.1}$$

where $\rho_i \in [0,1]$, $\sum \rho_i = 1$, and $\widehat{P}_i$ is an orthogonal projection operator to eigenspace $\widehat{P}_i(\mathcal{H}) = \ker(\widehat{\rho} - \rho_i \widehat{I})$, related to the orthonormal set of eigenvectors $\{|\phi_i\rangle\}$ of $\widehat{\rho}$ for the discrete (point) spectrum by

$$\widehat{P}_i = \sum_{j=0}^{d_i} |\phi_{i_j}\rangle\langle\phi_{i_j}|. \tag{1.2}$$

[1] David Hilbert, 23 Jan 1862–14 Feb 1943 (Königsberg, Prussia, now Kaliningrad–Göttingen, Germany).

[2] Charles Hermite, 24 Dec 1822–14 Jan 1901 (Dieuze, Lorraine, France–Paris, France)

If the state is pure, only one eigenvalue (or probability, or weight) ρ_i differs from zero, in Eq. (1.1). The $|\phi_i\rangle \in \mathcal{H}$ is called a *ket* vector and $\langle\phi_i| \in \mathcal{H}^\dagger$ (dual space) is called a *bra* vector, and the parameter j labels the degenerate eigenvectors which belong to the same eigenvalue ρ_i of $\widehat{\rho}$. Furthermore, the projection operator satisfies the identity property,

Note that $\widehat{\rho} = \widehat{I}\widehat{\rho}\widehat{I} = \sum_{ij} |\phi_i\rangle\langle\phi_i|\widehat{\rho}|\psi_j\rangle\langle\psi_j| \equiv \sum_{ij} |\phi_i\rangle\rho_{ij}\langle\psi_j|$ can be diagonalized.

$$\widehat{I} = \sum_{i=0}^{\infty} \widehat{P}(|\phi_i\rangle) = \sum_{i=0}^{\infty} |\phi_i\rangle\langle\phi_i|. \tag{1.3}$$

The sums in Eq. (1.2) and Eq. (1.3) become integrals in the case of continuous spectra. The eigenvectors and eigenvalues of a density operator indicate one of many possible ensembles that may give rise to a specific density operator, and the generalized projection operator $|\phi\rangle\langle\psi|$ denotes an operator $|\chi\rangle \to \langle\psi|\chi\rangle|\phi\rangle$.

The numbers $\langle\psi_i|\chi\rangle$ are called the coordinates (abstract Fourier coefficients) of vector $|\chi\rangle$ related to orthonormal sequence $\{|\psi_i\rangle\}_0^\infty$. Also, those are called as the scalar projections of $|\chi\rangle$ in direction $|\psi_i\rangle$.

The *Frechet*[3] *–Riesz*[4] *representation theorem* states that a Hilbert space identifies with its dual: Let $\phi \in \mathcal{H}$ be a continuous linear functional. Then there is a unique $z \in \mathcal{H}$ such that $\phi(x) = \langle x|z\rangle$ for all $x \in \mathcal{H}$. So the segregation of bra and ket vectors is not necessary in the case of Hilbert space.

According to the Frechet'–Riesz' representation theorem, there exists a function $\mathcal{H} \times \mathcal{H} \to \mathcal{H} : \rho(X, Y) \equiv \langle X|\widehat{\rho}|Y\rangle$, which in coordinate basis, $X, Y \in \mathbb{R}^n \subset \mathcal{H}$, is called the density matrix.

1.1.2 PHYSICAL QUANTITY

If a physical quantity has only a discrete spectrum, $\sigma_p(\widehat{A}) = \{a_1, a_2, \dots\}$, then $\widehat{A}$, with finite trace, can be expressed as a spectral representation

$$\widehat{A} = \sum_{i=1} a_i \widehat{P}_i, \tag{1.4}$$

where the numbers $a_i \in \sigma_p(\widehat{A})$ are the eigenvalues of $\widehat{A}$ and the $\widehat{P}_i$ are the projection operators described in Eq. (1.2). The proof is omitted here, see Nielsen and Chuang (2002, p. 72) or Lahti and Ylinen (1989). Generalization to the continuous spectrum is straightforward. Eq. (1.4) is equivalent to the statement that an observable must posses a complete orthogonal set of eigenvectors (Ballentine, 1970), thus, the eigenvectors of $\widehat{A}$ generate an orthonormal basis $(|\phi_{i_j}\rangle)$ to the Hilbert space $\mathcal{H}$. Therefore any vector state $|\psi\rangle$ of $\mathcal{H}$ can be expressed as a superposition

If $\widehat{A} \in \mathcal{H}$ is a self-adjoint operator, then there exists an unique spectral measure E satisfying

$$\widehat{A} = \int_{\mathbb{R}} \lambda \mathrm{d}E.$$

There is the least subset $\sigma(\widehat{A}) \subseteq \mathbb{R}$ such that integration over $\sigma(\widehat{A})$ yields the same result. The eigenequation: $\widehat{A}|\phi_{i_j}\rangle = a_i|\phi_{i_j}\rangle$.

$$|\psi\rangle = \sum_i \sum_{j=1}^{d_i} \langle\phi_{i_j}|\psi\rangle|\phi_{i_j}\rangle, \tag{1.5}$$

where i labels the eigenspaces, and for any i, j labels the basis for current eigenspace, which is also called a *degeneracy*. When an eigenspace is more than one dimensional, we say that it is degenerate.

Let X be a set. Then a Borel σ-algebra F is a nonempty collection of open subsets of such that: (1) $X \in F$, (2) If $A \in F$, then $A^c \in F$, and (3) If $A_n \in F$ for $n \in \mathbb{N}$, then $\cup_{n=1}^{\infty} A_n \in F$.

The justification to present a physical quantity, or observable, as a self-adjoint operator is based on the spectral theorem; according to that every self-adjoint operator $\widehat{A} : \mathcal{D}(\widehat{A}) \to \mathcal{H}$ and *real spectral measure*s from Borel[5] algebra of $\mathbb{R}$ to

A mapping $\mu : \sigma\text{-algebra} \to [0, \infty]$ is a measure, if $\mu(\emptyset) = 0$ and $\mu(\cup_{i=1}^{\infty} E_i) = \sum_{i=1}^{\infty} \mu(E_i)$.

[3] Maurice René Fréchet, 2 Sep 1878–4 June 1973 (Maligny, Yonne, Bourgogne, France–Paris)

[4] Frigyes Riesz, 22 Jan 1880–28 Feb 1956 (Györ, Austria-Hungary–Budapest,Hungary)

[5] Armand Borel, 21 May 1923–11 Aug 2003 (La Chaux-de-Fonds, Switzerland–Princeton, New Jersey)

a set of all bounded linear operators in $\mathcal{H}$, $E^A : \mathcal{B}(\mathbb{R}) \to L(\mathcal{H})$ are in one-to-one correspondence to each other (Lahti, 2005, p. 13). Spectral measure E^A associated to operator $\widehat{A}$ is related to the spectral representation of $\widehat{A}$, Eq. (1.4), by

$$E^A(\{a_i\}) = \sum_{j=1}^{d_i} \widehat{P}_i = \sum_{j=1}^{d_i} |\phi_{i_j}\rangle\langle\phi_{i_j}|.$$

$E^A_\rho : \mathcal{B}(\mathbb{R}) \to (0,1)$, sometimes referred as $p^A_\rho = \int_{\mathbb{R}} \mathrm{d}E^A_\rho$.

Some usually met observables in quantum mechanics are the energy (free energy, total energy, kinetic energy, interaction energy, correlation energy, exchange energy), the position or momentum of particles, pair correlations between particles, pressure, or entropy.

$S = -k_{\mathrm{B}}\langle \ln \widehat{\rho}\rangle$.

1.1.3 MEASUREMENT

Any pair of state $\widehat{\rho}$ and quantity $\widehat{A}$ of the system $\mathcal{S}$ defines a probability measure p^A_ρ, and the quantity $\widehat{A}$ can be identified with the mapping $\widehat{\rho} \to p^A_\rho$. The trace operator Tr is used in mapping.

$p^A_\rho = \int_{\mathbb{R}} \mathrm{d}E^A_\rho$.

Postulate 2. *The expectation value of an observable $\widehat{A}$ in a state $\widehat{\rho}$ is given by*

$$\langle \widehat{A} \rangle = \mathrm{Tr}(\widehat{\rho}\widehat{A}), \tag{1.6}$$

where Tr $(\cdot)$ is the trace of the operator in the parentheses.

$\mathrm{Tr}\,(\widehat{A}\widehat{B}) = \sum_\phi \langle\phi|\widehat{A}\widehat{B}|\phi\rangle = \sum_\phi \sum_\xi \langle\phi|\widehat{A}|\xi\rangle\langle\xi|\widehat{B}|\phi\rangle = \sum_\phi \sum_\xi \langle\xi|\widehat{B}|\phi\rangle\langle\phi|\widehat{A}|\xi\rangle = \mathrm{Tr}\,(\widehat{B}\widehat{A})$.

The trace is cyclic, $\mathrm{Tr}\,(\widehat{A}\widehat{B}) = \mathrm{Tr}\,(\widehat{B}\widehat{A})$, and linear, $\mathrm{Tr}\,(a\widehat{A} + b\widehat{B}) = a\mathrm{Tr}\,(\widehat{A}) + b\mathrm{Tr}\,(\widehat{B})$. Furthermore, from the cyclic property it follows that trace is invariant under unitary transfomations. The expectation value converges for all trace class operators. Because the series expansion of the state $\widehat{\rho}$ is not unique, then for every quantity $\widehat{A}$ it holds

$$\langle \widehat{A} \rangle = \sum t_i \langle\phi_i|\widehat{A}|\phi_i\rangle = \sum s_i \langle\psi_i|\widehat{A}|\psi_i\rangle,$$

if $\{(|\phi_i\rangle, t_i)\}$ and $\{(|\psi_i\rangle, s_i)\}$ are the weighted vector state sequencies of $\widehat{\rho}$. Thus, the two sets are indistinguishable. For a discrete spectrum $\sigma_p(\widehat{A})$ and specially, for a vector state $|\psi\rangle\langle\psi|$, we get

For the state $|\psi\rangle$, the measure is $\langle \widehat{A} \rangle = \int_{\mathbb{R}} \mathrm{d}E^A_{|\psi\rangle} = \langle\psi|\widehat{A}|\psi\rangle$.

$$\langle \widehat{A} \rangle = \mathrm{Tr}\,(|\psi\rangle\langle\psi|\widehat{A})) = \langle\psi|\widehat{A}|\psi\rangle$$

and, furthermore, by using the eigenspace expansion of operator $\widehat{A}$, Eq. (1.4), this can be written as

The variance $\sigma^2_A \equiv \langle \widehat{A}^2 \rangle - \langle \widehat{A} \rangle^2$ can also be calculated, and for the vector state $|\psi\rangle$ the variance vanishes, $\sigma^2_A = 0$.

$$\langle\psi|\widehat{A}|\psi\rangle = \sum_i a_i \langle\psi|P_i|\psi\rangle = \sum_i a_i \sum_{j=1}^{d_i} |\langle\phi_{i_j}|\psi\rangle|^2,$$

The orthonormal basis of eigenspace $E^A(\{a_i\})(\mathcal{H}) = \ker(\widehat{A} - a_k\widehat{I})$.

where $\{\phi_{i_1}, \ldots, \phi_{i_{d_i}}\}$ is the set of degenerate eigenvectors corresponding to the eigenvalue a_i.

In the position representation of density matrices the trace is written as an integral, and thus we get, after substituting an identity operator $\int |x'\rangle\langle x'|\mathrm{d}x'$ between $\widehat{\rho}$ and $\widehat{A}$

$$\langle\widehat{A}\rangle = \int \langle x|\widehat{\rho}|x'\rangle\langle x'|\widehat{A}|x\rangle \mathrm{d}x\mathrm{d}x' \equiv \int \rho(x,x')A(x',x)\mathrm{d}x\mathrm{d}x'.$$

Usually, only diagonal operators are used, thus

$$\langle x'|\widehat{A}|x\rangle = \langle x|A(x')|x'\rangle = A(x',x')\langle x|x'\rangle \equiv A(x')\langle x|x'\rangle \tag{1.7}$$

giving $\langle\widehat{A}\rangle = \int \rho(x,x)A(x)\mathrm{d}x$ for normalized density matrix $\rho(x,x')$.

E.g. for position, $\widehat{A}(\vec{x}) = \vec{x}$, and $\langle\vec{x}\rangle = \int \vec{x}\rho(\vec{x},\vec{x};\beta)\mathrm{d}\vec{x}$, and for momentum $\widehat{A}(\vec{x}) = \widehat{p} = -\imath\hbar\partial_{\vec{x}}$ we get after integrating by parts $\langle\widehat{p}\rangle = \imath\hbar\int(\partial_{\vec{x}}\rho(\vec{x},\vec{x}'))_{\vec{x}'=\vec{x}}\mathrm{d}\vec{x}$.

1.1.4 COMPOSITE SYSTEMS

Suppose the system we are interested in is made up of two or more distinct physical systems, $\mathcal{S}_1$ and $\mathcal{S}_2$ with Hilbert spaces $\mathcal{H}_1$ and $\mathcal{H}_2$, respectively. The Hilbert space of the composite system, $\mathcal{S} = \mathcal{S}_1 + \mathcal{S}_2$, is the tensor product $\mathcal{H} = \mathcal{H}_1 \otimes \mathcal{H}_2$, and there exists a bilinear mapping $f : \mathcal{H}_1 \times \mathcal{H}_2 \to \mathcal{H}$ such that

Tensor product is also called an *outer product*. *Kronecker product* is a special case of tensor product on matrices and *dyadic product* on vectors.

$$\langle f(\phi_1,\psi_1)|f(\phi_2,\psi_2)\rangle_{\mathcal{H}} = \langle\phi_1|\phi_2\rangle_{\mathcal{H}_1}\langle\psi_1|\psi_2\rangle_{\mathcal{H}_2}$$

for all $\phi_1, \phi_2 \in \mathcal{H}_1$ and $\psi_1, \psi_2 \in \mathcal{H}_2$. Furthermore, the set $\{f(\phi,\psi)|\phi \in \mathcal{H}_1, \psi \in \mathcal{H}_2\}$ spans a dense subspace in $\mathcal{H}$. The function f is written as $f(\phi,\psi) \equiv |\phi\rangle \otimes |\psi\rangle$.

Postulate 3. *The state space of a composite physical system is the tensor product of the states of the component physical systems. If the component systems are numbered from* 1 *to* N*, and the system number* i *is prepared in the state* $|\psi_i\rangle$*, then the joint composed system is at state*

$$|\psi_1,\psi_2,\cdots,\psi_N\rangle \equiv |\psi_1\rangle \otimes |\psi_2\rangle \otimes \cdots \otimes |\psi_N\rangle. \tag{1.8}$$

Often the tensor product mark, $\otimes$, is not explicitly written, thus we write for the N-particle ket $|\psi_1,\psi_2,\cdots,\psi_N\rangle = |\psi_1\rangle|\psi_2\rangle\cdots|\psi_N\rangle$. Because the subspace spanned by $f(\phi,\psi)$ is dense, the orthonormal basis $\{|\phi_i\rangle\} \subset \mathcal{H}_1$ and $\{|\psi_i\rangle\} \subset \mathcal{H}_2$ generate an orthonormal basis to $\mathcal{H}$ with the help of tensor product; $\{|\phi_i\rangle \otimes |\psi_j\rangle\} \subset \mathcal{H}$ is an orthonormal basis of the composed system $\mathcal{S}$. All states $|\xi\rangle \in \mathcal{H}$ can be written with the help of basis, such as $|\xi\rangle = \sum_{ij}\langle\phi_i \otimes \psi_j|\xi\rangle\phi_i \otimes \psi_j$

The special characteristic in quantum mechanics is that identical particles are undistinguishable. This poses new complications, such that, actually, Eq. (1.8) is not valid, but the state must have a well defined symmetry. The systems we are considering in this thesis, however, essentially does not need the use of Bose[6] or Fermi[7] symmetries. Thus, the definition given in Eq. (1.8) is assumed to be valid here.

Symmetric sum

$$|\psi_1,\psi_2,\cdots,\psi_N\rangle = \sum_{i=1}^{N}(\pm 1)^N|\psi_1\psi_2\cdots\psi_N\rangle,$$

where $+$ sign is for bosons and $-$ sign for fermions.

For example, the quantum mechanics of spin-$\frac{1}{2}$ hydrogen atom is based on Hilbert

Hilbert space $L^2(\mathbb{R}^3_p,\mathbb{C}^2) \triangleq L^2(\mathbb{R}^3_p) \otimes \mathbb{C}^2$ is the outer product space of square-integrable function (L^2) and spin space ($\mathbb{C}^2$).

[6] Satyendranath Bose, 1 Jan 1894–4 Feb 1974 (Calcutta, India–Calcutta)
[7] Enrico Fermi, 29 Sep 1901–28 Nov 1954 (Rome, Italy–Chicago)

spaces $\mathcal{H}_p \triangleq L^2(\mathbb{R}^3_p, \mathbb{C}^2)$ and $\mathcal{H}_e \triangleq L^2(\mathbb{R}^3_e, \mathbb{C}^2)$ where the subscripts p and e refer to proton and electron, respectively. Thus, a hydrogen atom can be regarded as (Lahti, 2005, p. 26)

$$\begin{aligned}\mathcal{H}_p \otimes \mathcal{H}_e &\triangleq L^2(\mathbb{R}^3_p, \mathbb{C}^2) \otimes L^2(\mathbb{R}^3_e, \mathbb{C}^2) \\ &\triangleq L^2(\mathbb{R}^6, \mathbb{C}^4) \\ &\triangleq L^2(\mathbb{R}^3_{\text{cm}}) \otimes L^2(\mathbb{R}^3_{\text{rel}}) \otimes \mathbb{C}^2 \otimes \mathbb{C}^2,\end{aligned}$$

where the subscripts cm and rel are center of mass motion and relative motion. Usually, when speaking about the hydrogen atom, the space $L^2(\mathbb{R}^3_{\text{rel}})$ is considered; the quantum nucleus is taken into account only in a few studies so far.

Most of the definitions and results in this thesis are given for one particle in one-dimensional space, but the many of the results are easy to generalize following the idea given in Postulate 4.

1.2 DENSITY MATRICES

For a given density operator $\widehat{\rho} = \sum_i \rho_i |\phi_i\rangle\langle\phi_i|$, neither the states $|\phi_i\rangle$ nor the weights ρ_i are necessarily unique, as was earlier pointed out. The quantum mechanical system can be prepared many by means in a given mixed state, $\widehat{\rho}$, e.g. by measuring the system properly. One way to set up the system is the use of equilibrium distributions.

Other canonical ensembles are micro canonical (N, V, E) and (Gibbs's) grand canonical (μ, V, T). In the former, we need sc. Fock space.

The probability distribution that maximizes the entropy, $S = -\widehat{\rho}\ln\widehat{\rho}$, requiring that the number of particles is fixed and the mean value of energy $\langle\widehat{H}\rangle = E$ is constant (N, V, T distribution), is called the *canonical ensemble*. Here, for simplicity the number of particles is assumed to be $N = 1$. Next, the *density operator* $\widehat{\rho}$ for the canonical ensemble is defined by using the method of Lagrange[8] undeterminant coefficients, and a little algebra shows that

$\delta \ln\widehat{\rho} = \widehat{\rho}^{-1}\delta\rho - \frac{1}{2}\widehat{\rho}^{-2}\delta^2 + \cdots$

$$\begin{aligned}&\delta(\langle S\rangle - \lambda_1\langle\widehat{H}\rangle - \lambda_2\langle\widehat{I}\rangle) = 0 \\ &= \text{Tr}\,\delta\rho(-\ln\widehat{\rho} - \widehat{I} - \lambda_1\widehat{H} - \lambda_2\widehat{I}),\end{aligned}$$

where λ_1 and λ_2 are the undetermined multipliers. Requiring that the variation of the expression must vanish, we get

$$\widehat{\rho}(\beta) = \frac{1}{Q}\mathrm{e}^{-\beta\widehat{H}}, \tag{1.9}$$

where the coefficients are named differently. The probability distribution given in Eq. (1.9) is called the *canonical* or *Boltzmann*[9] distribution. The constant Q is called the *partition function*, and is given by

$$Q = \text{Tr}\,\mathrm{e}^{-\beta\widehat{H}}.$$

E.g. total energy: $E = -\partial\ln Q/\partial\beta$, entropy: $S = \partial(T\ln Q)/\partial T$, free energy: $F = -k_{\text{B}}T\ln Q$.

All thermal properties of an equilibrium distribution can be calculated from the

[8] Joseph-Louis Lagrange, 25 Jan 1736–10 Apr 1813, (Turin, Sardinia–Paris)

[9] Ludwig Boltzmann, 20 Feb 1844–5 Oct 1906 (Vienna, Austria–Duino, near Trieste, Austria (now Italy))

partition function (Arponen, 1994, p. 102). The parameter β defines the temperature T of the system; $\beta = 1/(k_{\mathrm{B}}T)$, where k_{B} is called the *Boltzmann* constant. Furthermore, β is also the inverse temperature of the surrounding system, which is in thermal contact only with the system, thus in a *heat bath*.

Temperature is defined as $k_{\mathrm{B}}T = (\delta E/\delta S)_{V,N}$. Because $\langle S\rangle = -\langle \ln \widehat{\rho}\rangle = \beta E + \ln Q$, $\delta S = (E\delta\beta + \beta\delta E + \delta Q/Q)$, and $\delta Q = -\delta\beta E Q$, we get that $\delta S = \beta\delta E$ and $\delta E/\delta S = 1/\beta$.

By differentiating Eq. (1.9)—assuming $Q \equiv 1$, because $\widehat{\rho}$ can always be normalized afterwards—we get a differential equation for β-independent Hamiltonian[10] $\widehat{H}$

$$\frac{\partial \widehat{\rho}}{\partial \beta} = -\widehat{H}\widehat{\rho} \tag{1.10a}$$

When $\widehat{H} \equiv -\frac{1}{2}\nabla^2 + \widehat{V}$, equation (1.10a) is also called *diffusion* equation (β corresponds time) or heat equation or *Kolmogorov's backward* equation or Smoluchowski equation or Fokker–Planck equation.

with the initial condition

$$\lim_{\beta\to 0} \widehat{\rho}(\beta) = \widehat{1}. \tag{1.10b}$$

This is called *Bloch*[11] *equation*. It describes the evolution of the density operator with respect to the parameter β, or inverse temperature. Thus, it is an alternative, and sometimes very convenient method of obtaining the density operator $\widehat{\rho}$. The physically correct initial condition $\widehat{\rho}(0)$ (Bloch equation with Q included) of the solution $\widehat{\rho}(\beta) = \widehat{\rho}(0)\exp(-\beta\widehat{H})$ is chosen such that the density matrix is normalized to one, Tr $\widehat{\rho}(\beta) = 1$.

Furthermore, remember that the density operator can be written in terms of an orthonormal sequence of Hilbert space $\widehat{\rho}(\beta) = \widehat{\rho}(0)\sum_{i=1}^{\infty}\exp(-\beta\widehat{H})\widehat{P}_i$ as described earlier, see Eq. (1.1).

The eigenvalue equation $\widehat{\rho}|\phi_n\rangle = p_n|\phi_n\rangle$ gives the probabilities of the system being in energy eigenstate $|\phi_n\rangle$

The energy eigenstates is a complete orthonormal set of vectors in $\mathcal{H}$.

$$p_n = \frac{1}{Q}\mathrm{e}^{-\beta E_n},$$

with normalization condition $\sum_n p_n = 1$ and $p_n \geq 0$ for all n. The canonical distribution of one-particle system, with one-particle energy ϵ_n, is also called Boltzmann distribution (Arponen, 1994, p. 100). The probability of the nth state is $p_n = \exp(-\beta\epsilon_n)/Q$, and $\exp(-\beta\epsilon_n)$ is called the Boltzmann factor

The density matrices in this thesis are of this type, and most of them are discussed in coordinate basis, i.e.

$$\rho(x, y; \beta) = \langle x|\widehat{\rho}(\beta)|y\rangle,$$

which is the unique solution for the Bloch equation, Eq. (1.10a), (Barker, 1978). It is called also the Green's function $G(x, y; \beta)$, the fundamental solution, or propagator, because it describes how the particle travels or propagates from y to x in imaginary time β (Keller and McLaughlin, 1975).

1.2.1 FREE PARTICLE

For a one-dimensional free particle, the Hamiltonian takes the form $\widehat{H} \equiv \widehat{T} \equiv -\frac{\hbar^2}{2m}\nabla^2$, and the Bloch differential equation, Eq. (1.10a), in coordinate basis with

[10] Sir William Rowan Hamilton, 4 Aug 1805–2 Sept 1865 (Dublin, Ireland–Dublin)

[11] Felix Bloch, 23 Oct 1905–10 Sep 1983 (Zurich, Switzerland–Zurich)

cartesian[12] coordinates becomes

$$\frac{\partial \rho_0(x,y;\beta)}{\partial \beta} = \frac{\hbar^2}{2m}\frac{\partial^2}{\partial x^2}\rho_0(x,y;\beta).$$

This is a standard text-book diffusion-type equation, and the solution to this equation is easily seen to be, see Feynman (1972, p. 49), Strauss (1992, p. 48) or Tervo (2000, p. 167) (or any other book about partial differential equations)

$$\rho_0(x,y;\beta) = \sqrt{\frac{m}{2\pi\hbar^2\beta}}\exp\left[-\frac{m}{2\hbar^2\beta}(x-y)^2\right], \tag{1.11}$$

Ex. Show by integrating that $\rho_0(x,y;\beta) = \int \rho_0(x,z;\beta)\rho_0(z,y;\beta)\mathrm{d}z$.

where the constant is chosen such that the boundary condition, Eq. (1.10b) is satisfied

$$\lim_{\beta\to 0}\rho_0(x,y;\beta) = \delta(x-y).$$

Remember that $\delta(x) = \lim_{\beta\to 0}\frac{1}{2\sqrt{\pi\beta}}\mathrm{e}^{-x^2/4\beta}$ and $\delta(ax) = (1/|a|)\delta(x)$. Note that there is no such a function $\delta(x)$ which is supposed to be zero for $x \neq 0$ and to be infinite at $x = 0$. Thus δ must be defined as a generalized function, as a distribution, or as a linear functional characterized by the above identity(Keller75).

Instead of solving the differential equation for the free particle, use can be made of the existence of a basis in Hilbert space. Write

$$\rho_0(x,y;\beta) = \mathrm{e}^{-\beta\widehat{H}}\sum_i \langle x|\psi_i\rangle\langle\psi_i|y\rangle = \sum_i \mathrm{e}^{-\beta E_i}\psi_i(x)\psi_i^*(y). \tag{1.12}$$

If the particle is in a large box of volume V, take the wave function to be as the momentum eigenfunction in coordinate basis $\psi_p(x)$ and since the p's are distributed over a continuum, the sum over the "indices" p is really equivalent to an integral over the values of p (Feynman and Hibbs, 1965, p. 88), (Ceperley, 1995, p. 284), namely

$$\sum_i \to \int \frac{V\mathrm{d}p}{2\pi\hbar} \qquad \text{and} \qquad \psi_i(x) \to \psi_p(x) = \frac{1}{\sqrt{V}}\mathrm{e}^{\imath px/\hbar}$$

with total energy $E_p = p^2/2m$, thus getting

For $a > 0$ we have $\int_{-\infty}^{\infty}\exp\left(-ax^2+bx\right)\mathrm{d}x = \sqrt{\frac{\pi}{a}}\exp\left(\frac{b^2}{4a}\right)$.

$$\begin{aligned}
\rho_0(x,y;\beta) &= \langle x|\mathrm{e}^{-\beta\widehat{T}}|y\rangle \\
&= \int \langle x|\mathrm{e}^{-\beta\widehat{p}^2/2m}|p\rangle\langle p|y\rangle\mathrm{d}p \\
&= \int \langle x|p\rangle\langle p|y\rangle\mathrm{e}^{-\beta p^2/2m}\mathrm{d}p \\
&= \left(\frac{1}{2\pi\hbar}\right)\int \mathrm{e}^{\imath p(x-y)/\hbar}\mathrm{e}^{-\beta p^2/2m}\mathrm{d}p \\
&= \left(\frac{m}{2\pi\hbar^2\beta}\right)^{1/2}\exp\left[-\frac{m}{2\hbar^2\beta}(x-y)^2\right]
\end{aligned} \tag{1.13}$$

but the change of variables needed here is not really legitimate because $\imath p$ is complex, but can be justified as a "shift of contours," as is done in any respectable complex analysis course, see Strauss (1992, p. 326).

[12] René Descartes, 31 Mar 1596–11 Feb 1650 (La Haye (now Descartes), France–Stockholm, Sweden)

1.2.2 HARMONIC OSCILLATOR

The harmonic oscillator is a particle confined in a potential $V(x) = \frac{1}{2}m\omega x^2$, where $\omega = \sqrt{k/m}$ is called the frequency of oscillatory motion with k being the force constant. Evaluation of the partial density matrix for harmonic oscillator is straightforward but tedious. Therefore, by quoting Feynman (1972, p. 51), the result is

$$\rho_{\text{ho}}(x,y;\beta) = \sqrt{\frac{m\omega}{2\pi\hbar\sinh\hbar\omega\beta}} \times \exp\left[\frac{-m\omega}{2\hbar\sinh\hbar\omega\beta}\left[(x^2+y^2)\cosh\hbar\omega\beta - 2xy\right]\right]. \tag{1.14}$$

The diagonal density matrix is

$$\rho_{\text{ho}}(x,x;\beta) = \sqrt{\frac{m\omega}{2\pi\hbar\sinh\hbar\omega\beta}} \times \exp\left(\frac{-m\omega}{\hbar}x^2\tanh\hbar\omega\beta\right)$$

because

$$\frac{\cosh 2x - 1}{\sinh 2x} = \tanh x.$$

Ex. Show by integrating that

$$\rho_{\text{ho}}(x,y;\beta) = \int \rho_{\text{ho}}(x,y';\tfrac{\beta}{2})\rho_{\text{ho}}(y',y;\tfrac{\beta}{2})\mathrm{d}y'.$$

By defining new position variables $\chi = \sqrt{m\omega/\hbar}x$ and $\xi = \sqrt{m\omega/\hbar}y$ and new coefficient $w = \exp(-\beta\hbar\omega)$, we can write (Barone et al., 2003)

$$\sinh\hbar\omega\beta = \frac{1-w^2}{2w}$$
$$\cosh\hbar\omega\beta = \frac{1+w^2}{2w}$$

and, thus, the density matrix can be written as

$$\rho_{\text{ho}}(x,y;\beta) = \sqrt{\frac{wm\omega}{\pi\hbar}}\exp\left[-\tfrac{1}{2}(\chi^2+\xi^2)\right](1-w^2)^{-1/2}\exp\left[-\frac{w^2(\chi^2+\xi^2)+2w\chi\xi}{1-w^2}\right]$$

and, by applying *Mehler's Hermite polynomial formula*, we get the spectral representation

$$\rho_{\text{ho}}(x,y;\beta) = \sqrt{\frac{m\omega}{\pi\hbar}}\exp\left[-\frac{m\omega}{2\hbar}(x^2+y^2)\right]\times \sum_{n=0}^{\infty}\frac{1}{2^n n!}H_n(\sqrt{m\omega/\hbar}x)H_n(\sqrt{m\omega/\hbar}y)e^{-\beta\hbar\omega(n+1/2)}$$

Mehler's Hermite polynomial formula states that

$$\sum_{n=0}^{\infty}\frac{w^n}{2^n n!}H_n(x)H_n(y) = (1-w^2)^{-1/2}\exp\left(\frac{2xyw-(x^2+y^2)w^2}{1-w^2}\right)$$

where $H_n(x)$ is the Hermite polynomial, and $|w|<1$.
Hermite polynomials are

$$H_n(x) = (-1)^n \mathrm{e}^{x^2}\frac{\mathrm{d}^n}{\mathrm{d}x^n}\mathrm{e}^{-x^2}.$$

for the harmonic oscillator. From this proposition, the energetics, the wave functions and the normalization coefficients can be extracted. Instead of using the Mehler's formula, just by expanding the density matrix of harmonic oscillator, Eq. (1.14), in successive powers of $\exp(-\beta\hbar\omega)$, the wave functions can be achieved, see Feynman and Hibbs (1965, p. 200).

Now, if the temperature is high, $\beta \to 0$, or confining potential is small $\omega \to 0$, Eq. (1.14), reduces to that of free particle, Eq. (1.11), as can be seen easily by expanding the hyperbolic functions in Taylor series.

$\sinh 2x = 2x + \frac{4}{3}x^3 + \cdots$
$\cosh 2x = 1 + 2x^2 + \cdots$

1.3 PATH-INTEGRALS

Now we have developed the theory for one quantum particle in density matrix formalism. The results presented here can be straigthforwardly generalized to N noninteracting particles with definite symmetry, but the existence of mutual

interaction between particles makes things more complicated. Thus, we follow here the path with one particle, only. The next task is to make the density matrix look like a path, and we note that it implies some integrations. Therefore, we get the path-integrals, and, furthermore, find the continuous and discrete versions of it.

The path-integrals arise from the fact that (Schulman, 1981) for any operator $\exp(\widehat{A}) = \exp(\widehat{A}/M)^M$ for all $M \in \mathbb{R} \setminus \{0\}$. Thus, the density operator $\widehat{\rho}(\beta)$ in Eq. (1.9) can be developed incrementally (Feynman, 1972, p. 72) with M steps

$$\widehat{\rho}(\beta) = \mathrm{e}^{-\tau\widehat{H}}\mathrm{e}^{-\tau\widehat{H}}\cdots\mathrm{e}^{-\tau\widehat{H}},$$

where $M\tau = \beta$. In the coordinate basis, the density matrix becomes, by inserting totally $M-1$ identity operators in between adjacent short *time slice* propagators

Note that in the discrete representation the end-points x and y are replaced by x_0 and x_M, respectively, to explicitly show the dependence on M.

$$\rho(x_0, x_M; \beta) = \int \rho(x_0, x_1; \tau)\rho(x_1, x_2; \tau)\cdots\rho(x_{M-1}, x_M; \tau)\mathrm{d}x_1\cdots\mathrm{d}x_{M-1}. \quad (1.15)$$

Thus, the particle propagates from $x = x_0$ to $y = x_M$ via route $x_1, x_2, \ldots, x_{M-1}$, which defines a path (Feynman, 1972, p. 72). The total propagator $\rho(x, y; \beta)$ is given by a sum (or an integral) over all possible—though they are prohibited in a classical sense—paths.

Fixed point ($f(x) = x$) theorem; contraction (A mapping f from a metric space (M, d) into itself is called a contraction if $\exists\alpha \in (0, 1)$ such that $d(f(x), f(y)) \leq \alpha d(x, y)\forall x, y \in M$).

First, in forthcoming sections, we deal with the free particle and some problems related to that, and then find the general statement and see how it is related to Schrödinger[13] formulation, and lastly we consider the special case of harmonic potential.

1.3.1 FREE PARTICLE

For the free particle, with Hamiltonian including only kinetic energy term, $\widehat{H} = \widehat{T} = \frac{\widehat{p}^2}{2m}$ as in section 1.2.1, the path-integral result is achieved trivially. Clearly, by writing the discrete path on $\rho_0(x_0, x_M; \beta) = (\frac{m}{2\pi\hbar^2\beta})^{1/2}\exp[-\frac{m}{2\hbar^2\beta}(x_0 - x_M)^2]$, see Eq. (1.11), and by using $M-1$ intermediate steps $(x_i)_{i=1}^{M-1}$, we get

$$\exp(\alpha\widehat{A})\exp(\alpha\widehat{A}) = \sum_{n=0}^{\infty}\frac{(\alpha\widehat{A})^n}{n!}\sum_{m=0}^{\infty}\frac{(\alpha\widehat{A})^m}{m!} = \sum_{n=0}^{\infty}\frac{(2\alpha\widehat{A})^n}{n!} = \exp(2\alpha\widehat{A}).$$

$$\rho_0(x, y; \beta) = \lim_{\substack{M\to\infty \\ M\tau=\beta}}\int \rho_0(x_0, x_1; \tau)\rho_0(x_1, x_2; \tau)\cdots\rho_0(x_{M-1}, x_M; \tau)\mathrm{d}x_1\cdots\mathrm{d}x_{M-1} \quad (1.16)$$

$$= \lim_{\substack{M\to\infty \\ M\tau=\beta}}\left(\frac{m}{2\pi\hbar^2\tau}\right)^{M/2}\int\exp\left[\frac{-m}{2\hbar^2\tau}\sum_{i=1}^{M}(x_{i-1} - x_i)^2\right]\mathrm{d}x_1\cdots\mathrm{d}x_{M-1}$$

because the Hamiltonian commutes with itself. Here, the two undefined variables must be defined, so let $x_0 = x$ and $x_M = y$. To find the path-integral representation of free-particle density matrix, first take the limit and buck against

[13] Erwin Rudolf Josef Alexander Schrödinger, 12 Aug 1887–4 Jan 1961 (Erdberg, Vienna, Austria–Vienna)

theoretical problems. Here, we try the continuous case to taste the formalism of path-integrals, and postpone most of the problems to the next section.

The limiting function $(x_i)_i^{M-1} \xrightarrow{M\to\infty} x(u)$ is *assumed* to be continuous. The easy way to make the function continuous is by piecewise linear interpolation between adjacent points x_{i-1} and x_i, but that is not the only method, e.g. the knowledge of the classical orbits could be taken advantage of (Feynman and Hibbs, 1965). By dividing the finite differences $x_{i-1} - x_i = x(i\tau - \tau) - x(i\tau)$ in the sum with τ, the result will approach to $-\mathrm{d}x(u)/\mathrm{d}u|_{u=i\tau}$, a negative derivative of $x(u)$ with respect to the parameter u. Summation in the exponential can be written as an integral with the help of Riemann sum. Furthermore, the integral measure $(\mathrm{d}x_i)_{i=1}^{M-1}$ will be written as

$$\lim_{\substack{M\to\infty \\ M\tau=\beta}} \int \frac{\mathrm{d}x_1}{\sqrt{2\pi\hbar^2\tau/m}} \cdots \frac{\mathrm{d}x_{M-1}}{\sqrt{2\pi\hbar^2\tau/m}} = \iint \mathcal{D}x(u),$$

which indicates the integration over all possible paths. There are many ways to define a subset of all the paths between x and y, as Feynman and Hibbs (1965) argued. Thus, we find that the path-integral for the free particle will be

$$\rho_0(x, y; \beta) = \iint \exp\left[\int_0^\beta \frac{m}{2\hbar^2}\dot{x}^2(u)\mathrm{d}u\right] \mathcal{D}x(u) \tag{1.17}$$

with constraints $x(0) = x$ and $x(\beta) = y$. The integral term in the exponential is usually called an *Euclidian*[14] *action*.

The density matrix in the path-integral formalism can be calculated for some systems by using the method of variations in classical path, $x_{\mathrm{cl}}(u)$ (Feynman, 1972, p. 79). Thus, let the total quantum path be $x(u) = x_{\mathrm{cl}}(u) + \delta x(u)$ with boundary conditions for the deviation from the classical path $x_{\mathrm{cl}}(u)$ be $\delta x(0) = 0$ and $\delta x(\beta) = 0$. In the case of free particle, the classical path x_{cl} is straight line, with differential respect to β being constant, which is called velocity $v = (y - x)/\beta$. Then, the Euclidian action without the constant $m/2\hbar^2$ will be

$$\int_0^\beta (v + \tfrac{\mathrm{d}}{\mathrm{d}u}\delta x(u))^2 \mathrm{d}u = \beta v^2 + \int_0^\beta (\tfrac{\mathrm{d}}{\mathrm{d}u}\delta x(u))^2 \mathrm{d}u$$

because of the boundary conditions on variation, $\delta x(u)$ eliminates the crossterm. So, the density matrix (1.17) can be written with the help of a classical "straight-line" density and the quantum part, as

$$\rho_0(x, y; \beta) = \exp\left[\frac{-m(x-y)^2}{2\hbar^2\beta}\right] F(\beta)$$

with path-integral $F(\beta)$ which is the quantum part, and depends β only, not the end points any more,

$$F(\beta) = \iint \exp\left[\frac{-m}{2\hbar^2}\int_0^\beta \tfrac{\mathrm{d}}{\mathrm{d}u}\delta x^2(u)\mathrm{d}u\right] \mathcal{D}y(u).$$

[14] Euclid of Alexandria, (about) 325 BC–265 BC (Alexandria, Egypt)

Function f is continuous if the preimage of any open set is open. Actually, almost all paths are continuous but nowhere differentiable, see section 1.4.3.

$$f'(x) = \lim_{h\to 0} \frac{f(x+h) - f(x)}{h}.$$

The limit

$$\lim_{\max \Delta x_k \to 0} \sum_{k=1}^{n} f(x_k^*) \equiv \int_a^b f(x)\mathrm{d}x\Delta x_k$$

where $x_k^* \in \Delta x_k$ defines the Riemann integral.

The equation of motion $x(u)$ for a free particle is according to Euler–Lagrange formalism is

$$x(u) = x(0) + \frac{x(\beta) - x(0)}{\beta}u.$$

For continuous f, g, $\lim_{x\to x_0} f(x) = f(\lim_{x\to x_0} x)$ and $\lim_{x\to x_0} f(x)g(x) = f(\lim_{x\to x_0} x)g(\lim_{x\to x_0} x)$. Function f is continuous if the preimage of any open set is open.

We still need to solve $F(\beta)$. According to the convolution theorem of density matrices, we have $\rho_0(x,y;\beta_1+\beta_2) = \int \rho(x,x';\beta_1)\rho(x',y;\beta_2)\mathrm{d}x'$, thus giving

$$F(\beta_1+\beta_2) = \sqrt{\frac{2\pi\hbar^2\beta_1\beta_2}{m(\beta_1+\beta_2)}}F(\beta_1)F(\beta_2),$$

from which we get the continuous solution for $F(\beta)$,

$$F(\beta) = \left[\frac{m}{2\pi\hbar^2\beta}\right]^{1/2} \mathrm{e}^{\alpha\beta}$$

with $\alpha \in \mathbb{R}$. Furthermore, because our density matrix ρ_0 is unnormalized, it must be normalized with Tr $\widehat{\rho}$ when calculating the expectation values of observables, see Eq. (1.6), and immediately we note that the $F(\beta)$ cancels out. On the other hand, below we will find, that $\alpha = 0$. The method of variations in the classical path can be widely used in evaluating path-integrals, but in this thesis we will work in a different direction, from the discrete versions to continuous case.

To evaluate the discrete path-integral, one must return to the definition, Eq. (1.16), and first, integrate and then take the limit. The integrand consists of a set of Gaussian[15] integrals, only. These can be integrated recursively (Feynman and Hibbs, 1965, p. 42), by noting that

$$\begin{aligned}\left(\frac{m}{2\pi\hbar^2\tau}\right)^{2/2} \int_{-\infty}^{\infty} \exp\left[\frac{-m}{2\hbar^2\tau}\left((x_0-x_1)^2+(x_1-x_2)^2\right)\right]\mathrm{d}x_1 \\ = \left(\frac{m}{2\pi\hbar^2 2\tau}\right)^{1/2} \exp\left[\frac{-m}{2\hbar^2 2\tau}\left(x_0-x_2\right)^2\right].\end{aligned}$$

Next we multiply this result by the next term in the product (or sum), $\rho_0(x_2,x_3;\tau)$, and integrate again, this time over x_2. The result is similar to the previous, expect that $(x_0-x_2)^2$ becomes $(x_0-x_3)^2$ and factor 2τ is replaced by 3τ in the coefficient and variance. In this way a recursion process is established, which, after M steps, gives

$$\rho_0(x_0,x_M;\beta) = \left(\frac{m}{2\pi\hbar^2\beta}\right)^{1/2} \exp\left[\frac{-m}{2\hbar^2\beta}\left(x_0-x_M\right)^2\right], \tag{1.18}$$

since $M\tau = \beta$.

Other, perhaps numerically more favoured method is the sc. *staging method*, see Sprik et al. (1985b) for an introduction, more can be found e.g. in i Barberà (2002), Martyna et al. (1999), Pollock and Ceperley (1984), Sprik et al. (1985a,b), Tuckerman et al. (1993, 1996), where the coupled springs $(x_{i-1}-x_i)^2$ can be decoupled by defining new variables u_i. The staging method has more advantages in computational procedures.

[15] Johann Carl Friedrich Gauss, 30 Apr 1777–23 Feb 1855 (Brunswick, Duchy of Brunswick (now Germany)–Göttingen, Hanover (now Germany))

Starting as earlier, that is, writing the density matrix as a product of M high temperature density matrices, and integrating, we arrive at

$$\begin{aligned}\rho_0(x_0,x_M;\beta) &= \int \rho_0(x_0,x_1;\tau)\rho_0(x_1,x_2;\tau)\cdots\rho_0(x_{M-1},x_M;\tau)\mathrm{d}x_1\mathrm{d}x_2\cdots\mathrm{d}x_{M-1}\\ &= \int \rho_0(x_0,x_M;\beta)\left[\frac{\rho_0(x_0,x_1;\tau)\rho_0(x_1,x_M;(M-1)\tau)}{\rho_0(x_0,x_M;\beta)}\right]\times\\ &\quad\times\left[\frac{\rho_0(x_1,x_2;\tau)\rho_0(x_2,x_M;(M-2)\tau)}{\rho_0(x_1,x_M;(M-1)\tau)}\right]\times\cdots\\ &\quad\times\left[\frac{\rho_0(x_{M-2},x_{M-1};\tau)\rho_0(x_{M-1},x_M;\tau)}{\rho_0(x_{M-2},x_M;2\tau)}\right]\mathrm{d}x_1\mathrm{d}x_2\cdots\mathrm{d}x_{M-1},\end{aligned}$$

where there are totally $M-1$ different conditional probabilities for picking up the next point, or *bead*, x_{i+1} based on the present bead x_i and the final bead x_M, in square brackets. The intermediate beads are referred as to the staging beads, the other beads as end point beads. Each of the square brackets must be evaluated. By simple arithmetics the ith bracket can be written as

$$\begin{aligned}&\frac{\rho_0(x_i,x_{i+1};\tau)\rho_0(x_{i+1},x_M;(M-1-i)\tau)}{\rho_0(x_i,x_M;(M-i)\tau)}\\ &=\left[\frac{m_{i+1}}{2\pi\hbar^2\tau}\right]^{1/2}\exp\left[-\frac{m_{i+1}}{2\hbar^2\tau}(x_{i+1}-\tilde{x}_{i+1})^2\right],\end{aligned}$$

where we have defined

$$\begin{aligned}m_{i+1} &= \frac{M-i}{M-1-i}m\\ \tilde{x}_{i+1} &= \frac{x_M+x_i(M-1-i)}{M-i}\end{aligned}$$

and $i=1,\ldots,M-2$. Now, make the change of variables

$$\begin{aligned}u_1 &= x_1\\ u_i &= x_i-\tilde{x}_i,\quad i=1,\ldots,M-1.\end{aligned}$$

The inverse transformation is

$$x_i = u_i + \frac{x_M+(M-i)x_{i-1}}{M-i-1}.$$

Thus we arrive at

$$\begin{aligned}\rho_0(x_0,x_M;\beta) &= \rho_0(x_0,x_M;\beta)\prod_{i=1}^{M-1}\int\left(\frac{m_i}{2\pi\hbar^2\tau}\right)^{1/2}\exp\left[\frac{-m_i}{2\hbar^2\tau}u_i^2\right]\mathrm{d}u_i\\ &= \rho_0(x_0,x_M;\beta)\end{aligned}$$

The terms in Jacobian of transformation are

$$\frac{\partial u_i}{\partial x_i}=1 \text{ and } \frac{\partial u_i}{\partial x_{i-1}} = -\frac{M-i-1}{M-i}$$

and the determinant of the Jacobian becomes according to the expansion by Minors

$$\frac{\partial(u)}{\partial(x)} = \prod_{i=1}^{M-1}\frac{\partial u_i}{\partial x_i} = 1.$$

because the Gaussian integrations are not coupled anymore, these can be integrated straightforwardly. Thus we arrive at the same result as earlier, as is expected.

Remember that

$$\int_{-\infty}^{\infty}\exp(-ax^2)\mathrm{d}x = \sqrt{\pi/a}.$$

Of course, there is plenty of different methods to integrate the Gaussian functions, see e.g. Feynman and Hibbs (1965, p. 43) for one more.

Now, after the integrations are completed and we have the discrete path-integral density matrix for the free particle, the limit to continuous path-integral may be taken. The limiting process is trivial, and the classical case, the discrete path-integral representation and continuous path-integral scheme all yields the same result as the density matrix formalism, Eqs. (1.11) and (1.18). By equating equations (1.17) and (1.18) we find that

$$\iint\exp\left[\frac{-m}{2\hbar^2}\int_0^\beta\left(\frac{\mathrm{d}x(u)}{\mathrm{d}u}\right)^2\mathrm{d}u\right]\mathcal{D}x(u) = \left(\frac{m}{2\pi\hbar^2\beta}\right)^{1/2}\exp\left[\frac{-m}{2\hbar^2\beta}(x-y)^2\right],$$

and thus, for the free-particle only the classical paths are required to get a correct description of its dynamics (statistics), or differently stated, the result is independent of the path. Furthermore, the classical paths are dependent only on the boundary conditions, $x(0) = x$ and $x(\beta) = y$.

Note that

$$\frac{-m}{2\hbar^2}\int_0^\beta \left(\frac{\mathrm{d}x(u)}{\mathrm{d}u}\right)^2 \mathrm{d}u = \frac{-m}{2\hbar}\int_0^{\hbar\beta} \left(\frac{\mathrm{d}x(\tau)}{\mathrm{d}\tau}\right)^2 \mathrm{d}\tau.$$

The coefficient for the exponential term, also the variance divided by $\sqrt{2\pi}$, in Eq. (1.18) shows the spatial width of a free particle at finite temperature. It is the inverse of "thermal de Broglie[16] wavelength", and thus given the name Λ_β, or more formally stated,

The thermal de Broglie wavelength is originally defined for a free ideal gas of massive particles in equilibrium.

$$\Lambda_\beta = \left(\frac{2\pi\hbar^2\beta}{m}\right)^{1/2}. \tag{1.19}$$

For free ideal gas, when the $\Lambda_\beta \ll d$, the interparticle distance, the gas can be considered to be a classical or Maxwell-Boltzmann gas. If $\Lambda_\beta \gg d$ quantum effects will dominate and the gas must be treated as a Fermi gas or a Bose gas, see Sec. 1.1.4.

1.3.2 INFINITE BARRIER

The easiest quantum mechanical problem of a particle confined in some region are the problems of reflecting wall and infinite square well. We consider these examples using the finite-temperature path-integral formalism. The material used here is extracted from the book of Schulman, (Schulman, 1981, p. 40 and p. 61–63 and 156), and articles of Barker (1978), Fulling and Güntürk (2003), Goodman (1981), Grosche (1993), Keller and McLaughlin (1975), Nevels et al. (1993). The potential function for infinite barrier (or hard wall) is

Note that, in rigorous qm there might be problems, because the potential is not differentiable everywhere, see Prugovecki (1971).

$$V(x) = \begin{cases} 0 & \text{for } x > 0 \\ \infty & \text{for } x \leq 0. \end{cases}$$

The Schrödinger solution for momentum eigenstates is

$$\langle x|p\rangle = \begin{cases} \frac{1}{\sqrt{\pi\hbar}}\sin(px/\hbar) & \text{for } x > 0 \\ 0 & \text{for } x \leq 0, \end{cases}$$

The potential can also be thought of as a restriction on the domain of position, now we have $\rho : \mathbb{R}_+ \times \mathbb{R}_+ \to \mathbb{R}_+$ instead of the domain in $\mathbb{R}$ earlier. Even the quantum mechanical tunneling to negative x-axis is forbidden. Nonetheless, it is easy to expect that the solution is of the form of the free particle ρ_0, but there might be refinements arising from the boundary.

The solution can be written as

$$\begin{aligned} \rho_\mathrm{b}(x,y;\beta) &= \rho_0(x,y;\beta) - \rho_0(x,-y;\beta) \\ &= \sqrt{\frac{m}{2\pi\hbar^2\beta}}\left[\exp\left(\frac{-m}{2\hbar^2\beta}(x-y)^2\right) - \exp\left(\frac{-m}{2\hbar^2\beta}(x+y)^2\right)\right] \\ &= \rho_0(x,y;\beta) - \rho_0(-x,y;\beta). \end{aligned} \tag{1.20}$$

$\lim_{\beta\to 0}\rho_\mathrm{b}(x,y;\beta) = \delta(x-y) - \delta(x+y)$

but the former delta function is zero everywhere in the domain.

The density matrix ρ_b satisfies the Bloch equation, Eq. (1.10a), because both terms in the summation satisfy it. Also, the correct initial condition in the domain is

[16] Louis Victor Pierre Raymond duc de Broglie 15 Aug 1892–19 Mar 1987 (Dieppe, France–Paris)

achieved, see Eq. (1.10b). Thus, because of uniqueness property of partial differential equations, the Eq. (1.20) must be the correct density matrix for the potential barrier. Instead of just the mathematical jargon, there are two more path-integral, or physical, justifications for the result.

The first method is called the *method of images*, and is based on *physical intuition*. Because the particle is free on its domain, its density matrix would be closely related to that of free particle. As we saw in Eq. (1.18), the free particle density matrix depends only on the straight paths between the end points. Here, there are two such classical paths: one of a free particle and the other of a particle that bounces off the wall on its way; thus its a path where the y is reflected about the line $y = 0$ to $-y$ and then constructed the new free particle path from x to $-y$, giving $\rho_0(x, -y; \beta)$. By applying the Feynman[17] summation over the classical paths, the result is almost that given in Eq. (1.20), the only difference being the phase factor in reflected path, here its by the boundary condition $-1 = \exp(\imath\pi)$. Schulman (1981, p. 40) argued, that the phase factor might be $\exp(\imath\pi/2)$ because of a turning point, but there is no way for a phase of π to occur in one dimension!

Straight in Euclidean sense.

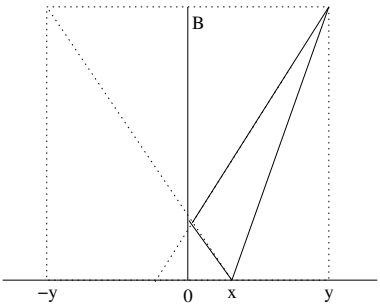

Bounced path according to Goodman (1981).

Goodman (1981) argues that every path must be counted, and that there is no *a priori* reason for preferring the classical paths. Furthermore, the reflected path is not even physically allowed, since it intersects at one point the forbidden region $x \leq 0$.

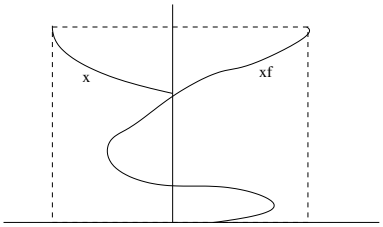

Forbidden and allowed path according to Goodman (1981).

The second method, introduced by Goodman (Goodman, 1981), concentrates on all these forbidden paths, where the trajectory $x_f(\tau) < 0$ for some τ. Consider an arbitrary forbidden path $x_f(\tau)$ from $x(0) = x$ to $x(\tau) = y$ and let $\tau_{\max}$ be the maximum time slice for which $x(\tau) < 0$. Clearly $\tau_{\max}$ exists because $x(\tau)$ is continuous. Now, define a permitted path $x(\tau)$ in $\mathbb{R}$ from x to $-y$ such that

$$x(\tau) = \begin{cases} x_f(\tau) & \text{for } \tau \leq \tau_{\max} \\ -x_f(\tau) & \text{for } \tau > \tau_{\max}. \end{cases}$$

For the continuity of paths, see sec. 1.4.3.

Note that

$$\int_0^\beta \dot{x}_f^2(\tau)\mathrm{d}\tau = \int_0^\beta \dot{x}^2(\tau)\mathrm{d}\tau.$$

Thus, the mapping between forbidden and permitted paths is bijective, and we see, while keeping the continuous free particle density matrix, Eq. (1.17), in mind, that

A function $f : A \to B$ is *bijective* if it is both, *surjective* (*onto*) and *injective* (*one-to-one*). f is *onto*, if $f(A) = B$. f is *injective*, if $f(x) = f(y) \Rightarrow x = y$.

$$\iint_x^y \exp\left[-\frac{1}{\hbar^2}\int_0^\beta \frac{m}{2}\dot{x}_f^2(\tau)\mathrm{d}\tau\right]\mathcal{D}(x_f) = \iint_x^{-y} \exp\left[-\frac{1}{\hbar^2}\int_0^\beta \frac{m}{2}\dot{x}^2(\tau)\mathrm{d}\tau\right]\mathcal{D}(x)$$

and we may conclude that, the second term in Eq. (1.20) cancels exactly the contribution from the forbidden paths in the first term. This method is called the *forbidden path method*.

Furthermore, there is a third method for obtaining the same result. It is based eigenfunction expansion, which is based on presenting the propagator in form of Dirac-delta functions, see Grosche (1993).

[17] Richard Phillips Feynman, 11 May 1918–15 Feb 1988 (Far Rockaway, New York–Los Angeles, California

1.3.3 PARTICLE IN A BOX

The problem of infinite square-well potential can be solved using the same methods described earlier. Thus, the image, forbidden paths and eigenfunction-expansion methods are available here, too. The potential is of the form

$$V(x) = \begin{cases} \infty & \text{for } x < 0 \\ 0 & \text{for } 0 < x < L \\ \infty & \text{for } x > L, \end{cases}$$

The Schrödinger solution reads

$$\langle x|n\rangle = \sqrt{\frac{2}{L}} \sin\left(\frac{n}{L}\pi x\right)$$
$$E_n = \frac{\pi^2\hbar^2 n^2}{2mL^2} \equiv E_1 n^2.$$

but the system can also be thought as being in a manifold, or a restriction of space, with $x \in [0, L]$.

A manifold is a topological space that is locally Euclidean. One of the goals of topology is to find ways of distinguishing manifolds.

The particle confined in a box can bounce from the walls infinitely many times, and thus, the method of images must be used repeatedly. We get,

$$\rho_{\mathrm{w}}(x, y; \beta) = \sum_{r=-\infty}^{\infty} (-1)^r \rho_0(x, x_r; \beta), \tag{1.21}$$

Because we are doing nonrelativistic qm, we are not supposed to worry about the fact that the speed of these paths becomes arbitrary large as $|r|$ increases.

where

$$x_r = \begin{cases} rL + y & \text{for } r \text{ even} \\ (r+1)L - y & \text{for } r \text{ odd} \end{cases}$$

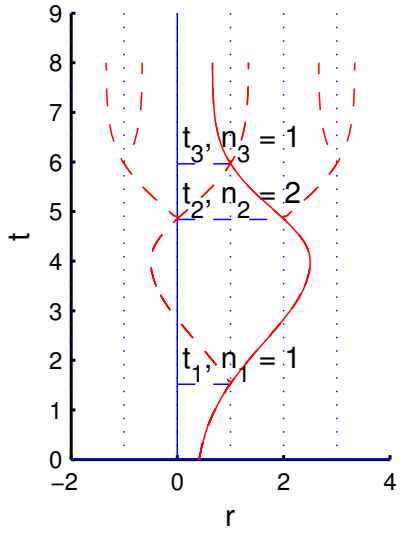

The cancelling paths. There are eight (2^3) different paths, (Goodman, 1981).

and $\rho_0(x, x_r; \beta)$ is the density matrix for a free particle, Eq. (1.18). The density matrix $\rho_{\mathrm{w}}(x, y; \beta)$ is a sum over all paths by which a particle could travel from the source point x to the point y, obeying classical mechanics. We may interpret $x - x_r$ as the separation between x and the *original* source point y along a path that winds around the original circular space several times. The integer r can be though as a *winding* number.

The density matrix (1.21) is periodic in x with period L and hence satisfies the boundary conditions. Furthermore, it satisfies the correct differential equation, and for x and y both between 0 and L it has the right initial conditions, because the term for $n = 0$ reproduces the needed delta function while the other terms vanish. Therefore, it must be the correct propagator, as described in Fulling and Güntürk (2003).

As in the case of infinite barrier, the result, Eq. (1.21), can be justified with the path cancellation (Goodman, 1981). Let $x_f(\tau) : [0, \beta] \to \mathbb{R}$ be a forbidden path, with $x_f(0) = x$ and $x_f(\tau) = y$. This path intersects some of the lines $x = rL$, where $r \in \mathbb{Z}$ is an integer. Define τ_{n_i} to be the largest time slice, when $x_f(\tau) = n_i L$ before $x_f(\tau)$ terminates *or* intersects any other these lines. Let n_k be the last vertical line that the path intersects—at time slice τ_{n_k}. Now, the original path can be reflected to give 2^k (if k is finite) new paths with the end-points $x(\tau)$ at image points, by

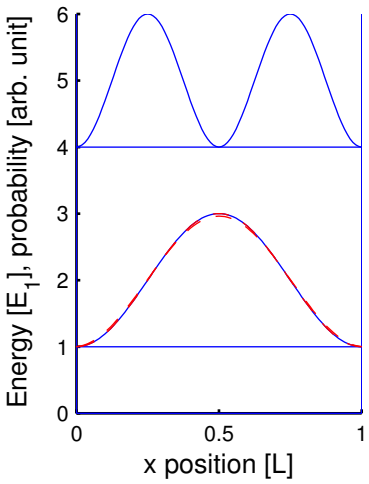

Figure 1.1: Particle in a potential well. In the figure, the square of two lowest energy states are drawn (solid). Also, path-integral diagonal density matrix, Eq. (1.21) is shown (dashed). The lower path-integral density is for $r = 0$ only. The other, that matches exactly with the Schrödinger result, is for $r = \{-1, 0, 1\}$. Note that, the Boltzmann factor for the second and higher states is zero at "normal" temperatures. The structure parameters are $m = 1, L = 1$.

using e.g. following relation

$$
\begin{aligned}
x_1(\tau) &= x_f(\tau) \\
&\vdots \\
x_{2^i+j}(\tau) &= \begin{cases} 2n_{k-i}L - x_j(\tau) & \text{for } \tau \geq \tau_{k-i} \\ x_j(\tau) & \text{for } \tau < \tau_{k-i}. \end{cases}
\end{aligned}
$$

These 2^k paths belong to the same equivalence class because they can be transformed into each other by reflection. All these distinct 2^k paths have the same free-particle action, because the square of the velocity is unchanged except at a finite number of points, which is a set of measure zero. Furthermore, an equal number of the reflected paths terminate at even-numbered as odd-numbered image points, as can be seen in the definition of the reflection process, resulting in a zero net effect. Thus, the path-integration over the forbidden paths yields zero, or differently stated

An equivalence class is defined as a subset of the form $\{x \in X | xRa\}$, where is a an element of X and the notation "xRa" is used to mean that there is an equivalence relation between x and a.

$$
\sum_{r=-\infty}^{\infty} \iint_x^y \exp\left[\frac{m}{2\hbar}\int_0^\beta \dot{x}_f^2(\tau)\mathrm{d}\tau\right] \mathcal{D}x_f(\tau) = 0.
$$

The only approximation is that the path is somehow well behaved, a sufficient condition being that it is piecewise continuously differentiable (Goodman, 1981). In general, they are not. However, if the path-integral is the limit of integrals over piecewise linear paths, the above arguments are valid, and Goodman argued,

that if they are valid at each step in the limiting process, then they are valid in the limit.

We conclude that the image points cancel the contribution of the free particle propagator $\rho_0(x,y;\beta)$ from paths that enter the forbidden regions $x \leq 0$ and $x \geq L$.

Furthermore, by using the intermediate result in deriving the free-particle density matrix, Eq. (1.13), the path-integral density-matrix for the particle in a box can be calculated (Goodman, 1981) to give

$$\begin{aligned}\rho_{\mathrm{w}}(x,y;\beta) =& \frac{1}{2\pi\hbar}\sum_{r=-\infty}^{\infty}\int_{-\infty}^{\infty}\Big[\exp\left(-\frac{\beta p^2}{2m}-\frac{\imath p}{\hbar}(x-2rL-y)\right)\\ &-\exp\left(-\frac{\beta p^2}{2m}-\frac{\imath p}{\hbar}(x-2rL+y)\right)\Big]\mathrm{d}p\\ =&\frac{1}{2\pi\hbar}\int_{-\infty}^{\infty}\exp\left(-\frac{\beta p^2}{2m}\right)\exp\left(-\frac{\imath p x}{\hbar}\right)\Big[2\imath\sin\frac{py}{\hbar}\Big]\sum_{r=-\infty}^{\infty}\exp\left(\frac{2\imath rLp}{\hbar}\right)\mathrm{d}p.\end{aligned}$$

The summation in $D_N(u)=\sum_{n=-N}^{N}\mathrm{e}^{\imath nu}$ is a finite geometric series, and the sum equals $D_N=\sin((N+\frac{1}{2})u)/\sin(u/2)$. $D_N(u)$ is called the Dirichlet kernel. It has period 2π, and $\int_{-\pi}^{\pi}D_N(u)\mathrm{d}u=2\pi$. Furthermore, $\lim_{N\to\infty}D_N(u)=2\pi\delta(u)$. By extending the integration limits ad infinum, we get the Poisson[18] sum formula

$$\sum_{n=-\infty}^{\infty}\mathrm{e}^{\imath bnu}=\frac{2\pi}{b}\sum_{m=-\infty}^{\infty}\delta\left(u-m\frac{2\pi}{b}\right).$$

The sum over r is easily evaluated by the Poisson sum rule,

$$\sum_{r=-\infty}^{\infty}\exp\left[\imath\frac{2L}{\hbar}pr\right]=\frac{\hbar\pi}{L}\sum_{n=-\infty}^{\infty}\delta(p-\frac{\hbar\pi}{L}n),$$

where the Dirac delta function is in a distribution sense, thus it picks out the values $p=\hbar\pi n/L$ of the integral over momentum, p. Thus, we are left with

$$\rho_{\mathrm{b}}(x,y;\beta)=\frac{\imath}{L}\sum_{n=-\infty}^{\infty}\exp\left(-\beta E_n\right)\exp(-\imath k_n x)\sin(k_n y),$$

where $E_n=(1/2m)(\pi n\hbar/L)^2$ and $k_n=\pi n/L$. Now, because $\sin 0=0$, the term with $n=0$ vanishes, and the positive and negative terms in summation index can be combined

$$\rho_{\mathrm{b}}(x,y;\beta)=\frac{2}{L}\sum_{n=1}^{\infty}\exp\left(-\beta E_n\right)\sin(k_n y)\sin(k_n x),$$

which is the familiar result from the Schrödinger formulation of the very same problem.

1.3.4 PERIODIC BOUNDARY CONDITIONS

The three most important boundary conditions are (1) *Dirichlet*: ρ; (2) *Neumann* $\partial\rho/\partial n$; (3) *Robin* $\partial\rho/\partial n+\alpha\rho$ is specified on the boundary.

In the previous problem, the domain of the free particle was restricted to an area $[0,L]$ with zero boundary conditions. Here, on the other hand, the actual problem is the same, but the conditions laid on density matrix are different. The characteristic is that the points x and $x+L$ of density matrix are identified. Usually, in solid state physics, these *boundary conditions* are called Born[20]–von Kármán[21]

[20] Max Born, 11 Dec 1882–5 Jan 1970 (Breslau (now Wroclaw), Prussian–Göttingen, Germany)

[21] Theodore von Kármán, 11 May 1881–6 May 1963 (Budapest, Austria-Hungary–Aachen, Germany)

condition when applied on wave function. This can be thought also as the particle is constrained to a circle.

This space is the group manifold of the group $SO(2)$, and with this metric, it is flat (Schulman, 1981).

For the travelling wave $\psi(x) = L^{-1/2}\exp(\pm\imath kx)$ the periodicity of density implies that $|\psi(x)|^2 = |\psi(x+L)|^2$. Thus, it immediately follows that $\psi(x) = C\psi(x+L)$ for any C such that $|C|^2 = 1$. We find that

$$\psi(x) = CL^{-1/2}\psi(x+L) \Rightarrow 1 = C\mathrm{e}^{\pm\imath kL}.$$

We therefore have a solution to k, actually $k = 2\pi n/L$ where $n \in \mathbb{Z}$. Thus, the travelling wave with periodic conditions is $\psi_n(x) = L^{-1/2}\exp(\pm 2\pi\imath nx/L)$. The eigenvalue (-energy) of this eigenfunction of the Laplacian with periodic boundary condition is readily calculated, and we find that

$$\frac{-\hbar^2}{2m}\nabla^2\psi_n(x) = \frac{2\hbar^2\pi^2n^2}{mL^2}\psi_n(x),$$

which gives that $E_n = 2\hbar^2\pi^2n^2/(mL^2)$. Armed with this representation of wave functions, we can employ the Boltzmann summation, Eq. (1.12) or Eq. (1.1), to get the density matrix,

For time-dependent density the path-integral solution can be found straightforwardly, see Schulman (1981, p. 193–195).

$$\rho_{\mathrm{pbc}}(x,x') = \frac{1}{L}\sum_{n=-\infty}^{\infty}\left[\exp\left(-\frac{2\hbar^2\pi^2}{mL^2}\beta\right)\right]^{n^2}\exp\left(\frac{2\pi\imath n}{L}(x'-x)\right) \tag{1.22a}$$

$$= \frac{1}{L}\vartheta_3\left(z,q\right). \tag{1.22b}$$

In the last line the definition of Jacobi[22] theta function, ϑ_3, is used to simplify the notation. The abbreviations z and q denote

The Jacobi theta functions are the elliptic analogs of the exponential function, and may be used to express the Jacobi elliptic functions. These are quasi-doubly periodic.

$$z = \frac{\pi}{L}(x'-x)$$
$$q = \exp\left(-\frac{2\hbar^2\pi^2}{mL^2}\beta\right).$$

However, if the Gaussian is sharply peaked, or $\beta\hbar^2/m \ll L^2$, the summation in Eq. (1.22a) can be changed to integral which can be done exactly, giving

$$\rho_{\mathrm{pbc}}(x,x') = \sqrt{\frac{m}{2\pi\hbar^2\tau}}\exp\left(-\frac{m}{2\hbar^2\tau}(x-x')^2\right)$$

for the high-temperature τ. This is the free particle density matrix, given already in Eq. (1.11).

1.4 GENERAL PATH-INTEGRALS

So far we have been concentrating on the trivial example of free-particle and some modifications of that. Thus, the introduction part to the path-integrals is clear, and we can proceed deeper to the realms of path-integrals. There are many

[22] Carl Gustav Jacob Jacobi, 10 Dec 1804–18 Feb 1851 (Potsdam, Prussia (now Germany)–Berlin, Germany)

different routes to the general path-integral formalism; here we first propose the perturbation theory, and second the Trotter expansion. In the last subsection here, we show the mathematical problems and definitions and also the time-dependent path-integral.

1.4.1 PERTURBATION EXPANSION

Let the Hamiltonian operator be $\widehat{H} = \widehat{T} + \widehat{V}$ where $\widehat{T}$ the is part of the Hamiltonian which can be solved analytically. In the following $\widehat{T}$ is supposed to be kinetic energy Hamiltonian, but there is no restriction to that only. The Bloch equation, Eq. (1.10a), describes the quantum evoluation of both $\widehat{\rho}_0 = \exp(-\beta\widehat{T})$ and $\widehat{\rho} = \exp(-\beta\widehat{H})$, with the corresponding Hamiltonian operators. We assume (Feynman, 1972) that $\widehat{\rho}(\beta)$ is close to $\rho_0(\beta)$. Let us calculate the differential

$$\frac{\partial}{\partial\beta}(\mathrm{e}^{\beta\widehat{T}}\widehat{\rho}) = \mathrm{e}^{\beta\widehat{T}}\widehat{V}\widehat{\rho}(\beta).$$

Thus, by integrating both sides of the previous equation from $\beta' = 0$ to β, and multiplying it from left with $\mathrm{e}^{-\beta\widehat{T}} = \widehat{\rho}_0(\beta)$ we get the density operator $\widehat{\rho}(\beta)$ that is subject to a small perturbation $\widehat{V}$

Contraction: Let (M, d) be a metric space. A mapping $f : (M, d) \to (M, d)$ is a contraction, if $\exists\ \alpha \in (0, 1)$ such that $d(f(x), f(y)) \leq \alpha d(x, y)\ \forall x, y \in M$. Let f be a contraction. Then by Banach fixed point theorem f has exactly one fixed point.

$$\widehat{\rho}(\beta) = \widehat{\rho}_0(\beta) - \int_0^\beta \widehat{\rho}_0(\beta - \beta')\widehat{V}\widehat{\rho}(\beta')\mathrm{d}\beta'. \tag{1.23}$$

This should be compared to Dyson's[23] equation, $G = G_0 + GVG_0$. Again, multiplying Eq. (1.23) from left with bra $\langle x|$ and right with ket $|y\rangle$ and inserting an identity operator $\widehat{I} = \int |y'\rangle\langle y'|\mathrm{d}y'$ between $\widehat{\rho}_0$ and $\widehat{V}$ in the integral, it gives the coordinate representation (or density matrix) of the perturbation expansion

$$\rho(x, y; \beta) = \rho_0(x, y; \beta) - \int_{-\infty}^{\infty}\int_0^\beta \rho_0(x, y'; \beta - \beta')V(y')\rho(y', y; \beta')\mathrm{d}\beta'\mathrm{d}y'$$

because $\langle y'|\widehat{V} = V(y')\langle y'|$ for any diagonal potential operator $\widehat{V} : \mathcal{H} \to \mathbb{R}$. Actually, by iterating this procedure (by inserting the $\rho(\beta)$ in Eq. (1.23) to the integral in Eq. (1.23)), we get the Feynman diagrams used widely in the fields of many-body and high-energy physics. For small $\beta = \tau$, we can approximate $\rho(\tau)$ with $\rho_0(\tau)$ in the convolution term rather accurately,

$$\rho(x, y; \tau) \approx \rho_0(x, y; \tau) - \int_{-\infty}^{\infty}\int_0^\tau \rho_0(x, y'; \tau - \tau')V(y')\rho_0(y', y; \tau')\mathrm{d}\tau'\mathrm{d}y'.$$

The Gaussians are very localized at small τ, thus most of the contribution to the integral over y' occurs near $y' = x_0$, where

The extremum is found when the argument in exponential of $\rho_0(x, y'; \tau - \tau')\times \rho_0(y', y; \tau')$ is zero. By differentiating the argument respect to y', and solving for y' we get the desired result, x_0.

$$x_0 = \frac{\tau' x + (\tau - \tau')y}{\tau}.$$

[23] Freeman John Dyson, 15 Dec 1923– (Crowthorne, Berkshire, England)

The convolution becomes simple, because

$$\begin{aligned}\rho(x,y;\tau) &\approx \rho_0(x,y;\tau) - \int_0^\tau V(x_0)\int_{-\infty}^{\infty}\rho_0(x,y';\tau-\tau')\rho_0(y',y;\tau')\mathrm{d}\tau'\mathrm{d}y' \\ &= \rho_0(x,y;\tau) - \int_0^\tau V(x_0)\mathrm{d}\tau'\rho_0(x,y;\tau) \\ &\approx \rho_0(x,y;\tau) - \tau V(x)\rho_0(x,y;\tau)\end{aligned}$$

if $x \approx y$ and consequently x_0 is close to x and $V(x_0)$ is constant over the range of integration. This is acquired by the assumption that $|x-y|$ and τ are small. Thus, we arrive at the solution (Feynman, 1972, p. 75), that

$$\rho(x,y;\tau) \approx \rho_0(x,y;\tau)\left[1-\tau V(x)\right] \approx \rho_0(x,y;\tau)\mathrm{e}^{-\tau V(x)}.$$

Feynman gives some more approximations for the integral, e.g. $(\tau/2)(V(x)+V(y))$ or $\tau V((x+y)/2)$ but says that the original is accurate enough. The former approximation satisfies the hermitian property, and gives the same result for the discrete path-integral.

So, the discrete path-integral representation for the particle in a potential $V(x)$ is given by

$$\rho(x_0,x_M;\beta) \approx \left[\frac{mM}{2\pi\hbar^2\beta}\right]^{M/2}\int\exp\left[-\beta\sum_{n=1}^{M}\left(\frac{mM}{2\hbar^2\beta^2}(x_{n-1}-x_n)^2 + V(x_n)/M\right)\right]$$

which is, as shown, only an approximate solution, and requires that $^{(1)}$ the potential $V(x)$ is constant between two adjacent points, x_{n-1} and x_n. By increasing M, the distance between adjacent points x_i and x_{i-1} becomes smaller, because of the harmonic potential term in the exponential.

1.4.2 TROTTER EXPANSION

In the previous section, the discrete path-integral representation was achieved by using the perturbation expansion for the density matrices. Here, on the contrary, we stay in the path-integral formalism, and find out, in which conditions $\exp(\widehat{X}+\widehat{Y})$ can be written as a product $\exp(\widehat{X})\exp(\widehat{Y})$. This is preferable, because usually $\widehat{X}$ and $\widehat{Y}$ are trivially diagonalizable, as is already seen for $\widehat{T}$ and $\widehat{V}$. The problems arise, however, because the operators do not generally commute.

If the (C_0) class operators, or semigroups, T_t and T'_h, commutes we find that the semigroup condition $T_{t+s} = T_tT_s$ is satisfied for semigroup $U_{a,t} = T'_tT'_{at}$ because

$$U_{a,t+s} = T_tT'_{a(t+s)} = T_tT_sT'_{at}T'_{as} = T_tT'_{at}T_sT'_{as} = U_{at}U_{as}.$$

A contraction *semigroup* on Banach space X is a family of bounded everywhere defined linear operators P_t, $0 \le t < \infty$ mapping $X \to X$ such that $^{(a)}$ $P_0 = 1$, $^{(b)}$ $P_tP_s = P_{t+s}$ and $\|P_t\| \le q$, $0 \le t < \infty$ and $^{(c)}$ $\lim_{t\to 0} P_tf = f$. The term contraction comes from the fact that $\|P_t\| \le 1$.

(The rigorous proof is given in Trotter (1959)). This suggests that a "product semigroup"

$$S_{a,t} = \lim_{h\to 0}(T_hT'_{ah})^{t/h}$$

is also a semigroup for noncommutative semigroups. Here, we restrict the case to semigroups of type $\exp(-\tau\widehat{X})$ and wish to show that if $\widehat{T}$ and $\widehat{V}$ are linear operators on a Banach space X then

$$\mathrm{e}^{-\beta(\widehat{T}+\widehat{V})} = \lim_{M\to\infty}(\mathrm{e}^{-\beta\widehat{T}/M}\mathrm{e}^{-\beta\widehat{V}/M})^M. \tag{1.24}$$

The operators $\widehat{T}$, $\widehat{V}$ and $\widehat{H} \equiv \widehat{T} + \widehat{V}$ are infinitesimal generators of the contraction semigroups $\exp(-\tau\widehat{T})$, $\exp(-\tau\widehat{V})$ and $\exp(-\tau\widehat{H}) = \exp(-\tau(\widehat{T}+\widehat{V}))$, respectively. Unfortunately, the proof is too technical to show here, but it is described well in Trotter (1959) and Schulman (1981).

The generator $\widehat{A}$ of P_t is the operator defined by $\widehat{A}f = \lim_{t\to 0} t^{-1}(P_t - 1)f$ on the domain $D(\widehat{A})$ of all $f \in X$ for which the limit exists.
The norm used above is defined as follows $\|Q\| = \inf_{\beta\in B}\beta$ where $B = \{\beta | \|Qx\| \leq \beta\|x\| \; \forall \; x \in X\}$ and $\|x\|$ is the norm in X.

In the noncommutative case, Trotter found it necessary to impose a condition on the norms of $\exp(-\tau\widehat{T})$ and $\exp(-\tau\widehat{V})$, that is $||\mathrm{e}^{-\tau\widehat{V}}|| \leq M\mathrm{e}^{\omega\tau}$ for all $\tau > 0$. Applying this to potential operator $\widehat{V}$, we get

$$||\mathrm{e}^{-\tau\widehat{V}}\psi|| = \int \mathrm{e}^{-\tau V(x)}\psi^*(x)\mathrm{e}^{-\tau V(x)}\psi(x)\mathrm{d}x \leq \int \mathrm{e}^{-2\tau V(x)}\mathrm{d}x.$$

There are potentials, e.g. Coulomb potential, which are not bounded from below, and thus do not satisfy the criteria needed by the Trotter formula.

Error term, or a Landau symbol, was introduced by Paul Bachmann in 1894, in the 2nd vol. of *Analytische Zahlentheorie*. It was popularized by Edmund Landau. The big-O (*order of*), was originally a capital omicron.

The Trotter formula holds only in the limit, thus at some finite M we introduce an error term. For $\tau = \beta/M$ we find

$$\mathrm{e}^{-\tau(\widehat{T}+\widehat{V})} = \mathrm{e}^{-\tau\widehat{T}/M}\mathrm{e}^{-\tau\widehat{V}/M} + o(\tau)$$

with error term $o(\tau)$. In path-integral scheme, we need to multiply these sums M times, and thus there will be an error term $\sum_{i=1}^{M} o(\tau^M)$. However, the Trotter formula, Eq. (1.24), ensures that though $M \to \infty$ the overall error term stays small and reduces to finally zero.

Note that $\exp(\widehat{X}) = \sum_{n=0}^{\infty}\widehat{X}^n/n!$.

According to the Trotter formula, the short-time, or high-temperature density matrices $\rho(x_i, x_{i+1}; \tau)$ in expansion Eq. (1.15) can be written as a

$$\rho(x_i, x_{i+1}; \tau) \equiv \rho_0(x_i, x_{i+1}; \tau)\rho_1(x_{i+1}; \tau) + \langle x_i|o(\tau)|x_{i+1}\rangle$$

Note that $e^x = \lim_{n\to\infty}\left(1 + \frac{x+y_n}{n}\right)^n$.

for diagonal operators $\widehat{V}$, see Eq. (1.7). The one-particle density matrix for the potential term is $\rho_1(x_{i+1}; \tau) = \exp(-\tau V(x_{i+1}))$, and it includes the external potential and interactions between particles. Assuming that the error term $o(\tau)$ is negligible, we find that the discrete path-integral representation for the particle in a potential $V(x)$ at temperature β is

$$\rho(x_0, x_M; \beta) \approx \left[\frac{mM}{2\pi\hbar^2\beta}\right]^{M/2}\int \exp\left[-\beta\sum_{n=1}^{M}\left(\frac{mM}{2\hbar^2\beta^2}(x_{n-1} - x_n)^2 + V(x_n)/M\right)\right]$$

which is, as shown, only an approximate solution, and requires that (2) the potential $V(x)$ is bounded from below and that (3) the error term $o(\tau) = o(\beta/M)$ is negligible.

HIGHER ORDER EXPANSIONS

The Trotter formula uses only the first term in the series $\ln(\exp\widehat{X}\exp\widehat{Y})$. It ensures that by using the first-order approximation, the discrete path-integral density matrix will converge to the correct density matrix as the Trotter number M

approaches some higher integer, preferably infinity. However, by introducing higher order approximations in the exponential product, the convergence may be more certified and, furthermore, more rapid allowing the study of more complicated systems with reasonable CPU time in computations.

By writing out the formal power series for $\ln(\exp\widehat{X}\exp\widehat{Y})$, we get the sc. Hausdorff[24] series

$$\begin{aligned}\widehat{H} &= \widehat{X}+\widehat{Y}+\tfrac{1}{2}[\widehat{X},\widehat{Y}]+\tfrac{1}{12}([\widehat{X},[\widehat{X},\widehat{Y}]]-[\widehat{Y},[\widehat{X},\widehat{Y}]])-\tfrac{1}{24}[\widehat{X},[\widehat{Y},[\widehat{X},\widehat{Y}]]]+\cdots\\ &= \widehat{X}+\widehat{Y}+\tfrac{1}{2}[\widehat{X}\widehat{Y}]+\tfrac{1}{12}([\widehat{X}^2\widehat{Y}]-[\widehat{Y}\widehat{X}\widehat{Y}])-\tfrac{1}{24}[\widehat{X}\widehat{Y}\widehat{X}\widehat{Y}]+\cdots\end{aligned}$$

$$\mathrm{e}^{\widehat{X}}=\sum_{n=0}^{\infty}\frac{\widehat{X}^n}{n!}$$
$$\ln(1+\widehat{X})=\sum_{n=1}^{\infty}\frac{(-1)^{n-1}}{n}\widehat{X}^n.$$

with higher order terms, which are dependent on commutator of $\widehat{X}$ and $\widehat{Y}$. The *long commutator* $[\widehat{A}_1\widehat{A}_2\cdots\widehat{A}_n]=[A_1,[A_2,[\cdots[A_{n-1},A_n]]]]$ is a usual shorthand notation for commutators. The formal calculation is not very convenient, and within the framework of Lie[25] algebra more can be done. Originally the series $\ln(\exp\widehat{X}\exp\widehat{Y})$ was used to define a multiplication law in Lie groups associated to a given Lie algebra (Kurlin, 2006). The series contains commutators of all order and E. Dynkin[26] found a closed formula for the series, and nowadays, it is called *Baker*[27] *–Campbell*[28] *–Hausdorff* formula

Lie Algebra is a nonassociative algebra obeyed by objects such as the Lie bracket and Poisson bracket.

$$\ln(\mathrm{e}^{\widehat{X}}\mathrm{e}^{\widehat{Y}})=\sum_{n=1}^{\infty}\frac{(-1)^{n-1}}{n}\sum_{\substack{p_i,q_i\geq 0\\ p_i+q_i>0}}\frac{[\widehat{X}^{p_1}\widehat{Y}^{q_1}\widehat{X}^{p_2}\widehat{Y}^{q_2}\cdots\widehat{X}^{p_n}\widehat{Y}^{q_n}]}{p_1!q_1!\cdots p_n!q_n!\sum_{i=1}^{n}(p_i+q_i)},$$

and it provides us with the higher order correction terms. The proof is not presented here, see Kleinert (2004, p. 179), Kurlin (2006) or any standard Lie algebra text book. Both expansions shown here indicate that if the variables $\widehat{X}$ and $\widehat{Y}$ commute then $\ln(\exp\widehat{X}\exp\widehat{Y})=\widehat{X}+\widehat{Y}$. The Hausdorf series is not useful as is, but when then changing the infinity in the summation to some smaller integer, e.g. to 1 or 2 we get useful approximations.

The higher order terms can be used to obtain better discrete approximations to path-integrals, or even in generating better symplectic integrator to the solving of time-dependent Schrödinger equation (Chin and Chen, 2001). De Raedt and De Raedt (1983) introduced the Hermitian approximation

Symplectic integrator is a numerical integration scheme.

Hermitian property is important when calculating expectation values for operators which are not diagonal in the position representation.

$$\begin{aligned}\mathrm{e}^{-\tau(\widehat{X}+\widehat{Y})} &= g_4(\widehat{X},\widehat{Y})+O(\tau^5)\\ &= \mathrm{e}^{-\tau\widehat{X}/2}\mathrm{e}^{-\tau\widehat{Y}/2}\mathrm{e}^{-\tau^3\widehat{C}_3/2}\mathrm{e}^{-\tau\widehat{Y}/2}\mathrm{e}^{-\tau\widehat{X}/2}+O(\tau^5)\end{aligned}$$

with $C_3=[[\widehat{Y},\widehat{X}],\widehat{X}+2\widehat{Y}]$. They applied this to the harmonic oscillator and double well potential, and found that they converge much faster than the original

$[[y,x],x+2y]=$
$4yxy-2xyx+yx^2-2xy^2+x^2y-2y^2x.$

[24] Felix Hausdorff, 8 Nov 1868–26 Jan 1942 (Breslau, Germany (now Wroclaw, Poland–Bonn, Germany)

[25] Marius Sophus Lie, 17 Dec 1842–18 Feb 1899 (Nordfjordeide, Norway–Kristiania (now Oslo))

[26] Eugene Borisovich Dynkin, 11 May 1924– (St Petersburg)

[27] Henry Frederick Baker, 3 Jul 1866–17 Mar 1956 (Cambridge, England–Cambridge, Cambridgeshire)

[28] John Edward Campbell, 27 May 1862–1 Oct 1924 (Lisburn, Co Antrim, Ireland–Oxford, Oxfordshire,England)

Trotter expansion. Li and Broughton (1987) followed the work of De Raedts and found two more equally good approximants to g_4 by using the cyclic property of the trace, and found that a new averaged approximant would be

$$\begin{aligned} g_4^{(4)} &= \tfrac{2}{3} g_4(\widehat{X},\widehat{Y}) + \tfrac{1}{3} g_4(\widehat{Y},\widehat{X}) \\ &= \mathrm{e}^{-\tau\widehat{X}/2}\mathrm{e}^{-\tau\widehat{Y}/2}\mathrm{e}^{-\tau^3\widehat{C}_3'/24}\mathrm{e}^{-\tau\widehat{Y}/2}\mathrm{e}^{-\tau\widehat{X}/2}, \end{aligned}$$

where $C' = [[\widehat{Y},\widehat{X}],\widehat{Y}] = \frac{\hbar^2}{2m}(\nabla V)^2$when the definitions of $\widehat{X} = \widehat{T} = \frac{\hbar^2}{2m}\nabla^2$ and $\widehat{Y} = V$ are introduced. Thus, C' is only a function of coordinate and not of momentum. This approximant is applied to harmonic oscillator and double-well potentials, but also to the e–Li$^+$ system and the hydrogen atom, see Li and Broughton (1987) and Burghard et al. (1998). Barberá demonstrated the use of these higher-order approximants in his PhD Thesis (i Barberà, 2002), also. For the harmonic oscillator $V = \frac{1}{2}m\omega^2x^2$ we find that applying the correction C', results in an effective frequency $\omega_{\text{eff}} = (1 + \tau^2\omega^2/12)\omega$.

e–Li$^+$ interaction is modelled with a pseudopotential.

1.4.3 FEYNMAN–KAC FORMULA

The continuous path-integral is obtained by allowing τ to approach zero with the constraint that $M\tau = \beta$, thus

$$\begin{aligned} \rho(x,y;\beta) &= \lim_{\substack{M\to\infty \\ M\tau=\beta}} \int \rho(x,x_1;\tau)\cdots\rho(x_{M-1},y;\tau)\mathrm{d}x_1\cdots\mathrm{d}x_{M-1} \\ &= \lim_{\substack{M\to\infty \\ M\tau=\beta}} \left(\frac{m}{2\pi\hbar^2\tau}\right)^{1/2} \int \exp\left[-\sum_{i=1}^{M}\left(\frac{m}{2\hbar^2\tau}(x_{i-1}-x_i)^2 + \tau V(x_i)\right)\right] \\ &\quad \times \frac{\mathrm{d}x_1}{\sqrt{2\pi\hbar^2\tau/m}}\cdots\frac{\mathrm{d}x_{M-1}}{\sqrt{2\pi\hbar^2\tau/m}}. \end{aligned} \tag{1.25}$$

The *Wiener measure* and *Wiener integral* can be defined in a similar way.

The Eq. (1.25) can be thought as a "continuous" path (trajectory) of a particle moving from a point x to x_1, then from x_1 to x_2 and so on until it reaches the end-point y. Here, the path is constructed by connecting all the adjacent points x_i and x_{i+1} with a straight line, but instead of that, some other interpolation scheme, e.g. sections of the classical orbit (Andersson and Driver, 1999, Feynman and Hibbs, 1965), could be used. By integrating over the intermediate points, we include all the paths from x to y, and the limiting procedure allows us to make a more representative sample of all the paths in between x and y. As the time slice interval $\tau \to 0$ together with $M \to \infty$, the resulting integral could be interpreted as a single integral over the space of functions $f : [0,\beta] \to \mathbb{R}$ rather than multiple integrals over the underlying configuration space (Valtakoski, 2000).

It should be shown that the result is independent of interpolation scheme, to get the Riemann/ Lebesgue integral.

Although, Eq.(1.26) is an integral over paths, the definition, Eq. (1.25), does not involve paths; the variables x_i are independent variables of integration.

After a similar limiting process as the one shown in Section 1.3.1, we get the *Feynman*[29] *–Kac*[30] *formula* for the density matrix $\rho(x,y;\beta)$ in Eq. (1.25). It can be written formally as

The definition for the path-integral, Eq. (1.26), is given in Eq. (1.25). Note that the derivative $\dot{y}$ is to be calculated to nondifferentiable paths, see below.

[29] Richard Phillips Feynman, 11 May 1918–15 Feb 1988 (Far Rockaway, New York–Los Angeles, California)

[30] Mark Kac, 3 Aug 1914–26 Oct 1984 (Krzemieniec, Poland, Russian Empire–California, USA)

$$\rho(x,y;\beta)=\iint\exp\left[-\int_0^\beta\left(\tfrac{1}{2}m\dot{y}^2+V(y)\mathrm{d}\tau\right)\right]\mathcal{D}y(\tau) \tag{1.26}$$

with boundary conditions $y(0)=x$ and $y(\beta)=y$, for continuous V or having at most finite number of discontinuities. It should be noted that in the exponent of Eq. (1.26) is the integral of the Euclidian Lagrangian[31] function with *negative* potential, also called an Euclidian or imaginary time action or an action integral.

Actually, the Kolmogorov continuity theorem assures the continuity.

Lagrangian $\widehat{L}=\widehat{T}-\widehat{V}$ with inverse potential: $\widehat{V}\to-\widehat{V}$ gives Euclidian Lagrangian $\widehat{L}=\widehat{T}+\widehat{V}=\widehat{H}$, a Hamiltonian.

The "measure" $\mathcal{D}y(\tau)$ appearing in Feynman–Kac formula is problematic. In this case it is thought (*or defined*) as an infinite product of Lebesgue[32] measures

$$\mathcal{D}y(\tau)=\lim_{M\to\infty}\frac{\mathrm{d}y_1}{\sqrt{2\pi\hbar^2\tau/m}}\cdots\frac{\mathrm{d}y_{M-1}}{\sqrt{2\pi\hbar^2\tau/m}},$$

but neither it, nor the normalization constant $(m/2\pi\hbar^2\tau)^{1/2}$, has the limit of their own. Strictly speaking, the expression above is meaningless because there is no translational invariant (Lebesgue) measure in infinite dimensions, see Andersson and Driver (1999), Bodmann et al. (1997), and thus the heurestic interpretation of the "measure" $\mathcal{D}y$ is somewhat ambiguous in the literature, see Andersson and Driver (1999) for discussion.

The solution is to introduce Wiener's[33] measure. It was originally constructed as a mathematical model for the phenomenon of Brownian[34] motion. Mark Kac identified it as the key to a probabilistic representation of Schrödinger semigroups (Bodmann et al., 1997) and found that a similar representation could be given for solutions of the heat equation with external cooling terms.

The expectation occurring in this representation is of the same type that occurs in derivative security pricing.

The Wiener space $W([0,T];\mathbb{R}),T>0$ is the space of continuous paths from positive interval $[0,T]$ into Euclidian space $\mathbb{R}$ which start at the origin, $y(0)=0$, or differently stated (Andersson and Driver, 1999, Bodmann et al., 1997)

$$W([0,T];\mathbb{R})=\{y:[0,T]\to\mathbb{R}:y(0)=0\text{ and }y\text{ is continuous}\}.$$

The *Kolmogorov*[35] *extension theorem* states that there exists a unique measure on the space of paths in $\mathbb{R}$, the and Wiener measure $\mathcal{D}_{\mathrm{w}}y$ associated the Wiener space is the unique probability measure on $W([0,T];\mathbb{R})$. It is a Gaussian probability distribution (or measure) on the space of continuous paths y. Furthermore, the measure $\mathcal{D}_{\mathrm{w}}y$ is concentrated on continuous but nondifferentiable paths for almost all τ, these are the Brownian paths, which renders the exponent in Eq. (1.26) meaningless. The brownian paths are of fractal nature, having Hausdorff dimension larger than 1. It is easy to see, e.g. Abbot and Wise (1981), that the Hausdorff dimension of a one-dimensional quantum path is 2.

Stochastic process x is differentiable at t, if $\exists y_t$ with finite variance such that

$$\lim_{h\to0}\frac{x_{t+h}-x_t}{h}=y_t\equiv x'.$$

It can be shown that only (almost everywhere) nondifferentiable Brownian paths have a nonzero Wiener measure.

Since $\mathcal{D}y$ is a positive, countably additive and has a normalized measure, the powerful machinery of general integration and probability theory is at hand for

[31] Joseph-Louis Lagrange, 25 Jan 1736–10 Apr 1813 (Turin, Sardinia-Piedmont (now Italy)–Paris)
[32] Henri Léon Lebesgue, 28 June 1875–26 July 1941 (Beauvais, Oise, Picardie, France–Paris)
[33] Norbert Wiener, 26 Nov 1894–18 Mar 1964 (Columbia, Missouri, USA–Stockholm, Sweden)
[34] Robert Brown, 21 Dec 1773– 10 Jun 1858 (Montrose, Scotland–London))
[35] Andrey Nikolaevich Kolmogorov, 25 Apr 1903–20 Oct 1987 (Tambov, Tambov province, Russia–Moscow, Russia)

the computational estimation of Wiener integrals $\iint f(y)\mathcal{D}y$, where f is a function of the paths (Bodmann et al., 1997). Thus, the concept of stochastic integrals allows to give precise meaning in a suitable probabilistic sense to (line) integrals of the form given in Eq. (1.26).

Some cautions, or remarks, should be noted when dealing with the Feynman–Kac formula. First, transformations of coordinates in Eq. (1.26) seem to be easy. However, problems arise, because the paths that contribute to the value of the integral are nondifferentiable. Thus instead of the normal limiting process, more attention to the process should be paid. Second, the discretization from continuous x to some discrete x_i should be made with care. Actually, one can use infinitely many discretizations, $x_i + \lambda(x_{i-1} - x_i)$, where $\lambda \in [0, 1]$, but it can shown, see Valtakoski (2000, p. 23), that all these discretizations yield different results. Schulman points out this by noting that it is not clear where the vector potential $A(x)$ should be evaluated (Schulman, 1981, p. 23). In case of magnetic fields, the midpoint rule is the correct one. In quantum mechanics, fortunately, we always have the Schrödinger equation to check the correct discretization.

1.4.4 TIME-DEPENDENT PATH-INTEGRAL

The change of variables, $\beta \to \imath t$, is also called Wick rotation, or analytic continuation of β to the complex plane.

By a strict inspection of the Bloch equation, which is shown in the beginning of the thesis, Eq.(1.10a), we note that by a change of variable $\beta \to \imath t$ it transforms into time-dependent Schrödinger equation. By making a similar change of variables in the evolution of Eq. (1.26), we get the time-dependent quantum mechanical density matrix,

$$\rho(x, y; t) = \iint \exp\left[\imath \int_{t_0}^{t} \left(\tfrac{1}{2} m\dot{y}^2(t') - V(y(t'))\mathrm{d}t'\right)\right] \mathcal{D}y(t')$$

instead of quantum statistical. Now, there is the Lagrangian in the exponential instead of total energy Hamiltonian, resulting in an "imaginary variance" in Gaussian functions. Furthermore, the imaginary unit $\imath$ is plaguing the density matrix.

A mapping μ is a measure if $^{(1)}\ \mu(\emptyset) = 0$ and $^{(2)}\ \mu(\cup_{i=1}^{\infty} E_i) = \sum_{i=1}^{\infty} E_i$ for disjoint sets E_i.

A lot of work have been laid out to put the time-dependent problem on solid ground, because there is the problem that there cannot be such a measure to satisfy the time-dependent density matrix. The theory of measure can be generalized to complex measures, but this is not even a complex measure. No such countably additive measure exists due to the imaginary factor $\imath$ that makes the exponential oscillating. There is no measure-theoretic definition of the Feynman integral, it is only a linear functional, instead of a functional integral (Valtakoski, 2000, p. 30). There are, however, several definitions which do not use a measure at all (Keller and McLaughlin, 1975). For example, see the work of Cécile Morette DeWitt Cartier and DeWitt-Morette (1995), DeWitt (1972), Laidlaw and DeWitt (1971), Keller and McLaughlin (1975) or Valtakoski (2000) for references.

Furthermore, it can be shown, that the time-dependent path-integral density ma-

trix satisfies the Schrödinger equation, and thus is correct from the physical point of view. Furthermore, almost all quantum mechanical problems that can be solved from the Schrödinger formalism can be solved also by means of path integration (Grosche and Steiner, 1995).

The Schrödinger equation is a differential equation for ψ which is of first order in t and of second order in x, so it is like the heat equation, but differs by having a factor $\imath$. Because its solutions are wave-like, ψ is also called the wave function of the particle (Keller and McLaughlin, 1975).

1.5 DISCRETE PATH-INTEGRALS

Now the idea and concept of of path-integrals should be clear, but the useful results are hidden in the numerous previous pages. Thus, a brief summary is given here.

The evolution of density matrix at finite temperature T is governed by the Bloch equation, Eq. (1.10a), $\dot{\rho}(x,y;\beta) = -\widehat{H}\rho(x,y;\beta)$. The density matrix can be written with the help of wave functions $\phi_i(x)$, the solutions to the Schrödinger formalism, as is shown in Eq. (1.1), or

$$\rho(x,y;\beta) = \sum_i \mathrm{e}^{-\beta E_i}\phi_i(x)\phi_i^\dagger(y), \tag{1.27}$$

where E_i is the ith eigenenergy, $\widehat{H}|\phi_i\rangle = E_i|\phi_i\rangle$ and β is the inverse temperature, $\beta = 1/(k_\mathrm{B}T)$. The discrete path-integral formalism is obtained by writing density matrix $\rho(x_0, x_M;\beta)$ as an integral

$$\rho(x_0,x_M;\beta) = \int \rho(x_0,x_1;\tau)\rho(x_1,x_2;\tau)\cdots\rho(x_{M-1},x_M;\tau)\mathrm{d}x_1\cdots\mathrm{d}x_{M-1}$$

with $\tau = \beta/M$, $x_0 = x$ and $x_M = y$ inserting $M-1$ identity operators between short time propagators. This generates a trajectory, or a "path", going through the points x_0, x_1,..., x_M at imaginary times 0, β/M, $\ldots,\beta$. Here, the position eigenvector $|x\rangle$ shown in this section is readily generalized to N-body position, $|x\rangle \equiv |x^1, x^2, \ldots, x^N\rangle$. By using the Trotter formula, or higher order approximations, the product of density matrices in the integration can be approximated, and thus the density matrix becomes as shown in Eq. (1.25) where the continuous case for one particle is shown. The many-body density matrix in path-integral formalism is similar,

$$\rho(x_0,x_M;\beta) = \left[\frac{mM}{2\pi\hbar^2\beta}\right]^{MNd/2}\int \exp\left[-\beta\sum_{n=1}^{M}(T_i + V_p(x_{i-1},x_i))\right]\mathrm{d}x_1\cdots\mathrm{d}x_{M-1} \tag{1.28}$$

where

$$T_i \equiv T(x_{i-1}-x_i) = \sum_{j=1}^{N}\frac{m_j M}{2\hbar^2\beta^2}(x_{i-1}^j - x_i^j)^2$$

is the internal energy, and V_p includes the interaction between different particles

For example, for a two-particle system at high temperature or low τ the total density operator $\widehat{\rho}$ is a product of three terms, $\widehat{\rho} \approx \widehat{\rho}_0\widehat{\rho}_1\widehat{\rho}_2$, where we have the free-particle density operator, $\widehat{\rho}_0$, the density operator for the external potential, $\widehat{\rho}_1$, and the density operator for the interaction between particles, $\widehat{\rho}_2$. Thus, the density matrix is

$$\begin{aligned}
&\langle x_{i-1}^1 x_{i-1}^2|\widehat{\rho}(\tau)|x_i^1 x_i^2\rangle \\
\approx&\langle x_{i-1}^1 x_{i-1}^2|\widehat{\rho}_0\widehat{\rho}_1\widehat{\rho}_2|x_i^1 x_i^2\rangle \\
=&\int\langle x_{i-1}^1 x_{i-1}^2|\widehat{\rho}_0|y^1y^2\rangle \\
&\quad\times\langle y^1y^2|\widehat{\rho}_1|z^1z^2\rangle \\
&\quad\times\langle z^1z^2|\widehat{\rho}_2|x_i^1x_i^2\rangle\mathrm{d}y^{1,2}\mathrm{d}z^{1,2} \\
=&\int\langle x_{i-1}^1|\widehat{\rho}_0|y^1\rangle\langle x_{i-1}^2|\widehat{\rho}_0|y^2\rangle \\
&\quad\times\langle y^1|\widehat{\rho}_1|z^1\rangle\langle y^2|\widehat{\rho}_1|z^2\rangle \\
&\quad\times\langle z^1z^2|\widehat{\rho}_2|x_i^1x_i^2\rangle\mathrm{d}y^{1,2}\mathrm{d}z^{1,2} \\
=&\int\langle x_{i-1}^1|\widehat{\rho}_0|y^1\rangle\langle x_{i-1}^2|\widehat{\rho}_0|y^2\rangle \\
&\quad\times\langle y^1|\rho_1(z^1)|z^1\rangle\langle y^2|\rho_1(z^2)|z^2\rangle \\
&\quad\times\langle z^1z^2|\rho_2(x_i^1,x_i^2)|x_i^1x_i^2\rangle\mathrm{d}y^{1,2}\mathrm{d}z^{1,2} \\
=&\int\rho_0(x_{i-1}^1,y^1)\rho_0(x_{i-1}^2,y^2) \\
&\quad\times\rho_1(z^1)\langle y^1|z^1\rangle\rho_1(z^2)\langle y^2|z^2\rangle \\
&\quad\times\rho_2(x_i^1,x_i^2)\langle z^1z^2|x_i^1x_i^2\rangle\mathrm{d}y^{1,2}\mathrm{d}z^{1,2} \\
=&\rho_0(x_{i-1}^1,x_i^1)\rho_0(x_{i-1}^2,x_i^2) \\
&\quad\times\rho_1(x_i^1)\rho_1(x_i^2)\rho_2(x_i^1,x_i^2).
\end{aligned}$$

Usually ρ_1 is made hermitian.

and the effect of external potential. In the primitive and Hermitian approximation, suggested by the Trotter expansion, it is written as

$$V_p = \frac{1}{2M}\sum_{j=1}^{N}\Big[V(x_{i-1}^j) + V(x_i^j)\Big] + \frac{1}{M}\sum_{j=1}^{N}\sum_{k=j+1}^{N} V(x_i^j, x_i^k)$$

where $V(\cdot)$ is the external potential and $V(\cdot,\cdot)$ is the pair potential between particles. This is easily generalized to any potentials. It should be noted, that the potential between particles is between the same time slice beads, only. The path-integral formulation requires that $^{(1)}$ the potential is constant between two adjacent points, x_{n-1} and x_n, that $^{(2)}$ the potential is bounded from below and that $^{(3)}$ the error term $o(\tau)$ is negligible. For example, Coulomb[36] $-1/r$ potential does not satisfy this criterion.

Often, a somewhat different notation for the density matrices is used, and the path-integral is written as

$$\rho(x, y; \beta) = \int \exp\left[-\sum_{i=1}^{M} S(x_{i-1}, x_i; \tau)\right] \mathrm{d}x_1 \cdots \mathrm{d}x_{M-1}. \tag{1.29}$$

The short time action $S(x_{i-1}, x_i; \tau)$ is written explicitly as

$$S(x_{i-1}, x_i; \tau) = \frac{dN}{2}\ln(2\pi\hbar^2\tau/m) + \sum_{j=1}^{M}\Big[\tilde{T}_i + V_S(x_{i-1}, x_i; \tau)\Big]$$

with internal energy

$$\tilde{T}_i \equiv T(x_{i-1} - x_i) = \frac{m}{2\hbar^2\tau}(x_{i-1} - x_i)^2.$$

The Hermitian external potential V_S should contain quantum mechanical effects too, allowing the use of finite Trotter number M. To ensure hermiticity, it is written as $V_S(x_{i-1}, x_i; \tau) = \frac{\tau}{2}[U(x_{i-1}) + U(x_i)]$ containing the terms of external potential and interactions with other particles. The exact form of U depends on the system and the temperature considered. In the sc. *primitive approximation* the potential $U(x_i) \equiv V(x_i)$ is the external potential, as described earlier.

E.g. The Coulomb potential in *ab initio* calculations.

In some applications, when only pair potentials are needed, the short time density matrix $\rho(x, y; \tau)$, or $S(x_{i-1}, x_i; \tau)$, can be approximated with the sc. *pair potential form*. At sufficiently high temperature $\tau = \beta/M$, the short time density matrix in Eq. (1.29) for N particles can be written as

$$\rho(x, y; \tau) = \left[\prod_{i=1}^{N}\rho_0(x^i, y^i; \tau)\right]\left[\prod_{\substack{i,j=1\\ i<j}}^{N}\rho_2(x^i, y^i; \tau)\right]$$

with $\rho_2(x, y; \tau)$ being the pair potential density matrix which contains the temperature and Trotter number dependent potential and the effects arising from the finite Trotter number.

[36] Charles Augustin de Coulomb, 14 Jun 1736–23 Aug 1806 (Angoulême, France–Paris).

1.6 HARMONIC OSCILLATOR

The general considerations about path-integrals should be clear in mind at this stage. Thus, now it is time to extend the machinery from the free particle to harmonic oscillator. Let us calculate the harmonic oscillator in detail following the work of Schweizer et al. (1981). Also, the brick of Kleinert (2004, p. 128) should be beared in mind when studying this. For quadratic potentials $V(x) = \frac{1}{2}m\omega^2 x^2$, Eq.(1.25) can be done explicitly because it involves only Gaussian integrations, but to shorten the notation, we write $R = \hbar\omega\tau$ and $q_i = x_i(m\omega/(2\hbar))^{1/2}$, which gives for the differentials $\mathrm{d}q_i = (m\omega/(2\hbar))^{1/2}\mathrm{d}x_i$. We get for the discrete density matrix

$$\rho(x_0, x_M; \beta) = \int \left(\frac{m}{2\pi\hbar^2\tau}\right)^{1/2} (\pi R)^{-(M-1)/2} \times \exp\left[-\sum_{i=0}^{M}\left[(R + 2R^{-1})q_i^2 - 2R^{-1}q_{i-1}q_i\right]\right] \mathrm{d}q_1 \cdots \mathrm{d}q_{M-1}.$$

Because of periodicity with respect to the index i, the external potential term in the exponential can be written in a more symmetric form

$$-2R^{-1}\sum_{i=0}^{M} q_{i-1}q_i = -R^{-1}\sum_{i=0}^{M}(q_{i-1}q_i + q_i q_{i+1}).$$

Introduce two vectors in $\mathbb{R}^{M-1}$, $\vec{q} = [q_1, q_2, \ldots, q_{M-1}]^T$ for the integration variables, and $\vec{b} = 2R^{-1}[q_0, 0, \ldots, 0, q_M]^T$ for the coupling between integration variables q_1 and q_{M-1} with the fixed end-points, q_0 and q_M. Now the density matrix $\rho(x_0, x_M; \beta)$ can be written as shortly as

$$\rho(x_0, x_M; \beta) = \left(\frac{m}{2\pi\hbar^2\tau}\right)^{1/2} (\pi R)^{-(M-1)/2} \exp\left[-\tfrac{1}{2}(R + 2R^{-1})(q_0^2 + q_M^2)\right] I(\vec{q})$$

where integral $I(\vec{q})$ is defined by

$$I(\vec{q}) = \int \exp[-\vec{q}^T A\vec{q} + \vec{b}^T\vec{q}]\mathrm{d}\vec{q}$$

Let $A \in \mathbb{R}^{n\times n}$. Then $\int \exp(-\frac{1}{2}\vec{x}^T A\vec{x} + \vec{b}^T\vec{x})\mathrm{d}\vec{x} = [(2\pi)^n \det A^{-1}]^{1/2}\exp(\frac{1}{2}\vec{b}^T A^{-1}\vec{b})$. If $a \in \mathbb{R}$, $|aA| = a^n|A|$.

with $A \in \mathbb{R}^{(M-1)\times(M-1)}$ being a tridiagonal symmetric matrix whose elements are

$$A_{ij} = (R + 2R^{-1})\delta_{ij} - R^{-1}(\delta_{i-1,j} + \delta_{j,i+1}).$$

Because the matrix A is symmetric and positive definite, the integral may be immediately evaluated to give

A Hermitian (or symmetric) matrix is positive definite iff all its eigenvalues are positive.

$$I(\vec{q}) = (\pi^{M-1}\det A^{-1})^{1/2}\exp(\tfrac{1}{4}\vec{b}^T A^{-1}\vec{b}).$$

The determinant of the former form is *easily* evaluated and is given by

The eigenvalues of such a tridiagonal Toeplitz band matrix are $A_{ii} + 2\sqrt{A_{i,i-1}A_{i-1,i}}\cos(i\pi/M)$.

$$\det A = \prod_{i=1}^{M-1}\left(R + 2R^{-1} - 2R^{-1}\cos(i\pi/M)\right).$$

Comparing that and the one found from Gradshteyn and Ryzhik (1980, p. 34, Eq. 1.396.1 (KR 58 (28.1)))

$$\prod_{i=1}^{M-1} (f^2 + 1 - 2f\cos(i\pi/M)) = \frac{f^{2M}-1}{f^2-1}$$

we note that to get a correct factor in front of cosine term, take $1/R$ as a common factor

$$\begin{aligned}\det A &= \prod_{i=1}^{M-1} \frac{1}{R}\left(R^2 + 2 - 2\cos(i\pi/M)\right) \\ &= \prod_{i=1}^{M-1} \frac{1}{fR}\left(fR^2 + 2f - 2f\cos(i\pi/M)\right).\end{aligned}$$

Now, the cosine term is in the right form; we should choose f such that

$$fR^2 + 2f = f^2 + 1 \text{ which is reduces to } f = 1 + \tfrac{1}{2}\left(R^2 + R\sqrt{R^2+4}\right)$$

and the determinant can be written as

$$\det A = \frac{f^{2M}-1}{f^2-1}(fR)^{-M+1}.$$

$\frac{1}{4}R^2\vec{b}^T A^{-1}\vec{b} = (q_0,\ldots,q_M)^T A^{-1}(q_0,\ldots,q_M) = q_0^2(A^{-1})_{1,1} + q_0 q_M (A^{-1})_{M-1,1} + q_0 q_M (A^{-1})_{1,M-1} + q_M^2 (A^{-1})_{M-1,M-1} = (q_0^2+q_M^2)(A^{-1})_{1,1} + 2q_0 q_M (A^{-1})_{M-1,1}.$

Remember that $(A^T)^{-1} = (A^{-1})^T$ for any nonsingular matrix A.

Cramer's rule: $(A^{-1})_{ij} = (-1)^{i+j}|A_{ij}|/\det A$.

The determinant of a triangular matrix is the product of its diagonal elements.

To solve the integral, we need to find the inverse of A. However, the remaining quantity, $\vec{b}^T A^{-1}\vec{b}$, involves only four terms, $(A^{-1})_{ij}$ for i,j equal to 1 or $M-1$, since the vector $\vec{b}$ has only two nonzero components. Furthermore, because the inverse of a symmetric matrix is symmetric, the two diagonal elements are equal, as are two off diagonal elements. The determinants for the minors are already known, thus straightforwardly by Cramer's[37] rule we get

$$\begin{aligned}(A^{-1})_{1,1} &= Rf(f^{2M-2}-1)/(f^{2M}-1) \\ (A^{-1})_{1,M-1} &= Rf^{M-1}(f^2-1)/(f^{2M}-1).\end{aligned}$$

Together these results yield for the exponential part of the density matrix

$$\tfrac{1}{4}\vec{b}^T A^{-1}\vec{b} = R^{-1}\left((q_0^2+q_M^2)f(f^{2M-2}-1) + 2q_0 q_M f^{M-1}(f^2-1)\right)/(f^{2M}-1)$$

which may be combined with earlier equation, and after the substitution of constants q and R we get the result for the density matrix of a particle in a harmonic potential

$$\begin{aligned}\rho(x_0, x_M; \beta) = &\left(\frac{m}{2\pi\hbar^2\tau}\frac{f^2-1}{f^{2M}-1}f^{M-1}\right)^{1/2} \times \\ &\exp\left[\frac{m\omega}{2\hbar}\Big[\left(-\tfrac{1}{2}\hbar\omega\tau - \frac{(f^{2M-1}+1)(f-1)}{\hbar\omega\tau(f^{2M}-1)}\right)(x_0^2+x_M^2) + \right. \\ &\left. 2\frac{f^{M-1}(f^2-1)}{\hbar\omega\tau(f^{2M}-1)}x_0 x_M\Big]\right].\end{aligned}$$

Remember that $R^2+2 = (f^2+1)/f$ and thus $R^2+4 = (f+1)^2/f$ and R can be written as $R = \sqrt{f}(f-1)/f$.

For the diagonal density matrix, $x_M = x_0$, we find a shorter expression

[37] Gabriel Cramer, 31 July 1704–4 Jan 1752 (Geneva, Switzerland–Bagnols-sur-Cèze, France)

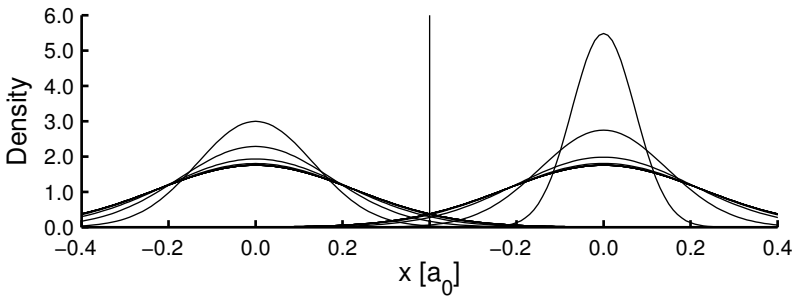

Figure 1.2: Diagonal density matrix for harmonic oscillator with $M = 2^i$, $i = 1, 2, \ldots, 11$ (left). The higher order approximations are also showed (right). Already with $M = 2^5$ the density matrix converge to the continuum case. Here, $T = 300$ K, $\omega = 0.0104816$ Ha a_0^{-2} and $m = 1836/2$.

$$\rho(x_0, x_0; \beta) = \left(\frac{m}{2\pi\hbar^2\tau} \frac{f^2 - 1}{f^{2M} - 1} f^{M-1} \right)^{1/2} \exp\Big[- \frac{m\omega}{2\hbar} \frac{\left(f^M - 1\right)(f+1)}{f^{1/2}(f^M + 1)} x_0^2 \Big]. \tag{1.30}$$

The normalization factor—or partition function—of the harmonic oscillator is easily seen to be

$$Q = \int \rho_{\text{ho}}(x_0, x_0; \beta) \mathrm{d}x_0 = \frac{f^{M/2}}{f^M - 1}. \tag{1.31}$$

By taking the limit $M \to \infty$ we find that $f \to 1$ and $f^M \to \exp(\beta\hbar\omega)$, and these gives the density matrix

$$\rho(x, y; \beta) = \left(\frac{m\omega}{2\pi\hbar \sinh \hbar\omega\beta} \right)^{1/2} \exp\left[\frac{-m\omega}{2\hbar \sinh \hbar\omega\beta} \left((x^2 + y^2) \cosh \hbar\omega\beta - 2xy \right) \right]$$

for the limiting case $\beta \to \infty$, or continuum case. This is exactly the same result shown earlier, see Eq. (1.14). Thus we note that the discrete path-integral yields exact results for harmonic potential.

Remember that $\exp(f(x)) = \lim_{M\to\infty}(1 + f(x)/M)^M$. The limits are $f^2 - 1 \to 2\hbar\omega\beta/M$ and $f - 1 \to \hbar\omega\beta/M$, and hyperbolic functions are defined as $\sinh x = \frac{1}{2}(\mathrm{e}^x - \mathrm{e}^{-x})$ and $\cosh$ as its symmetric counterpart.

The diagonal density is shown in Fig. 1.2 (left density). The Trotter numbers are $2, 4, 8, \ldots$ and the density is spreadening as more quantum mechanical behavior is obtained. Already at $M = 2^4$ the discretized diagonal density matrix coincides with the continuum case, red line. Furthermore, the use of higher order Trotter approximations, see Sec. 1.4.2, is shown on the right (blue). Thus, the harmonic frequency is temperature dependent, $\omega_{\text{eff}} = \omega(1 + \tau^2\omega^2/12)$. The density is totally different, but converges to the same continuous result.

EVALUATION OF PATH-INTEGRALS

...
Tuoll' lehdossa vaaran alla
oli kummia äskettäin,
niin vienoa, ihmeellistä
all' lehvien vehreäin.
...

There are only a small number of analytically solvable path-integrals—solutions to free particle and harmonic oscillator problems were given in Chapter 1—thus, numerical methods must be used to obtain density matrices of more complicated, or more realistic systems. Path-integrals, unfortunately, are rather expensive to solve numerically because the solution needs the evaluation of NMd-dimensional integral. In literature it can be found three main approaches of optimizing a path-integral algorithm: by using more accurate forms of the action (Sec 2.1), by sampling more efficiently (Sec 2.2) and by "estimating" the energy with lower variance (Sec 2.3), as described by Chakravarty et al. (1998)

N: number of particles, M: Trotter number, d: dimension.

The advantage of path-integral methods is that it includes the correlations between particles and the effects of finite temperature readily. Furthermore, it enables the study of the transition from classical systems to fully quantum mechanical systems by changing the the Trotter number, only. These phenomena are hard to study with other quantum mechanical formalisms, e.g. using density functional theory.

2.1 NUMERICAL APPROACHES

The quantum effects are temperature dependent. In the "action formalism", see Sec. 1.5 the idea is to find a numerically well behaving action $S(x_{i-1}, x_i; \tau)$, or potential $V_S(x_{i-1}, x_i; \tau)$ that gives the correct quantum mechanical density matrix with as small Trotter number M as possible, see Ceperley (1995, p. 309 and

forward).

Because evaluation of path-integrals involves integrations, usually *Monte Carlo* methods are established. However, for example, most one-body problems can be solved easier with s.c. *matrix squaring* methods, as will be described below. And, as in Car–Parrinello quantum dynamics scheme, also molecular dynamics can be used to evaluate quantum mechanical path-integrals.

The molecular dynamics method of solving path-integrals is somehow off the mainstream. It is based on the idea that the closed path of beads, also necklace, is influenced by the harmonic potential field generated by the neighbor beads and the external potential, and thus the dynamics for the beads can be simulated. This movement can be simulated by classical methods, or Newtonian[1] dynamics. By using Nosé–Hoover chains Tuckermann *et al* (Martyna et al., 1992) are able to get a canonical ensemble via continuous dynamics. However, the simple approach is rather inefficient, and thus by using the staging variables, introduced in Sec. 1.3.1, more efficiency is gained, see Tuckerman et al. (1993). The method is tested against harmonic oscillator and the excess of an electron in helium and in fluid xenon. The method is about as efficient as PIMC method, and about 200 times more efficient than the basic path-integral molecular dynamics method. However, usually exchange effects are neglected in PIMD schemes, which is, of course, a minor inaccuracy when dealing with atoms, see Eq. (1.19).

L–J potential with $\epsilon_{\mathrm{He}} = 10.22$ K, $\sigma_{\mathrm{He}} = 2.556$ Å, and $\epsilon_{\mathrm{Xe}} = 229.15$ K, $\sigma_{\mathrm{Xe}} = 4.332$ Å.

Furthermore, Tuckerman *et al* constructed an *ab initio* path-integral molecular dynamics method, where no model potentials, or pseudopotentials, are needed. It is based on Car–Parrinello type molecular dynamics (Car and Parrinello, 1985), where the interactions between the nuclei are obtained from electronic structure calculations carried out as the particles are propagated (Marx and Parrinello, 1996). The quantum nuclei are treated within the path-integral representation, and the electronic structure governing their interactions is described within density functional theory, or a similar robust method, see Marx and Parrinello (1996), Tuckerman et al. (1996) and references therein. Correlations between the electrons are included in some approximative method, e.g. LDA or GGA.

2.2 MATRIX SQUARING METHOD

The matrix squaring method is based on the convolution theorem of density matrices, see Eq. (1.15). It is easy to apply for pair potentials, and numerically exact density matrices are rather easy to generate. Those can be exploited when simulating larger systems. The matrix squaring method is a very applicaple method for generating U for V_S from the classical potential V, see Sec. 1.5.

The method is described well in Thirumai et al. (1983) and Whitfield and Straub (2001), also one of the earliest examples, Storer (1968), should be consulted at least

[1] Sir Isaac Newton, 4 Jan 1643–31 March 1727 (Woolsthorpe, Lincolnshire–London).

if working with the hydrogen atom. In addition, Ceperley (1995) shows the use of it, and Burghard et al. (1998) apply the method for evaluation of coherent-state path-integrals. We will give a brief summary with some examples.

Within the asumptions of Trotter expansion.

One-dimensional density matrices $\rho(x, y; \beta)$, with $x, y \in \mathbb{R}$, can be solved numerically exactly by noting that the product rule of density matrices

$$\rho(x, y; 2\tau) = \int \rho(x, x_1; \tau)\rho(x_1, y; \tau)\mathrm{d}x_1$$

with integration scheme approximated by trapezoid rule with uniform grid is actually a matrix multiplication of the matrix $\rho(x_i, y_j; \tau)$ with itself,

Trapezoid rule:

$$\int_x^y f(t)\mathrm{d}t \approx \tfrac{h}{2}(f(x) + f(y)) + h\sum_{i=1}^{n-1} f(x + ih)$$

with $h = |y - x|/n$ is the size of discretization.

$$\rho(x_i, y_j; 2\tau) \approx \Delta \sum_k \rho(x_i, x_k; \tau)\rho(x_k, y_j; \tau),$$

with x_i being the discretized version of continuous position variable x and Δ is the size of discretization. Thus, by squaring the density matrix k times, it will result in decrease of the temperature by a factor of 2^k. The requirement here is, that the starting temperature must be chosen such that the hermitian high temperature approximation

$$\rho(x, x'; \tau) = \exp[-\tfrac{\tau}{2}V(x)]\rho_0(x, x'; \tau)\exp[-\tfrac{\tau}{2}V(x')]$$

is valid. Thus, the procedure for evaluating one-dimensional density matrices is rather simple: Choose Trotter number $M = 2^k$, and discretization Δ such that the free particle inverse variance $m\Delta^2 M/(2\hbar^2\beta)$ is small enough, calculate high temperature density matrix $\rho(x, x'; \tau)$ and rise it to power k to get the final low temperature density matrix.

For a particle in a central potential, total energy depends only on ℓ, thus $E_{n\ell m} = E_\ell$. Expand the radial density matrix in spherical harmonics and remember the *addition theorem*.

Furthermore, because any central potential can be expanded into partial waves

$$\rho(\vec{x}, \vec{x}'; \beta) = \frac{1}{4\pi r r'}\sum_{\ell=0}^{\infty}(2\ell + 1)\tilde{\rho}_\ell(r, r'; \beta)P_l(\cos\theta), \tag{2.1}$$

the matrix squaring method can be applied to some 3-dimensional problems, too. Here $\tilde{\rho}_\ell(r, r'; \beta)$ is the ℓth partial wave and θ is the angle between $\vec{x}$ and $\vec{x}'$. The partial wave is a density matrix for one-dimensional potential $V(r)$ with an additional centrifugal term, and it satisfies the Bloch equation (see Eq. (1.10a))

$$\frac{\partial\tilde{\rho}_\ell(r, r'; \beta)}{\partial\beta} = -\left[-\frac{\hbar^2}{2m}\frac{\partial^2}{\partial r^2} + V_{\text{eff}}(r)\right]\tilde{\rho}_\ell(r, r'; \beta),$$

where

$$V_{\text{eff}} = \frac{\hbar^2\ell(\ell + 1)}{2mr^2} + V(r).$$

Thus, in 3D case a similar matrix squaring procedure as in 1-dimensional case can be used with $V(r)$ replaced by $V_{\text{eff}}(r)$. Furthermore, it must be beared in mind, that in radial problems, the particle is confined to areas where $r > 0$ only, thus the correct free-particle propagator is $\rho_{\text{b}}(r, r'; \beta)$, shown in Sec. 1.3.2, in Eq. (1.20),

$$\rho_{\text{b}}(r, r'; \beta) = \rho_0(r, r'; \beta) - \rho_0(r, -r'; \beta).$$

The number of partial waves, ℓ_{max}, needed is primarily dictated by temperature and the free-particle part of the system (Ceperley, 1995, p. 319). The higher the temperature, the more partial waves are needed. Ceperley states that 20–60 partial waves are needed for 40 K ^{4}He, and Thirumai et al. (1983) used $\ell_{\text{max}} = 100$ for Lennard–Jones 12–6 potential describing Ar_2 dimer at $T = 20$ K; for $T = 2$ K only 30 ℓ-waves were needed.

$V(r) = 4\epsilon((\sigma/r)^{12} - (\sigma/r)^6)$, where $\epsilon = 119.8$ K and $\sigma = 3.405$ Å.

The special case of a normalized radial distribution function $\rho(r)$ is easily obtained by this method. For a diagonal density, or distribution, we have $x = x'$ giving $\cos(\theta) = 1$, and thus

$$\rho(r) = \frac{4\pi r^2 \rho(r, r; \beta)}{Z} = \frac{\sum_{\ell=0}^{\infty}(2\ell+1)\tilde{\rho}_\ell(r, r; \beta)}{\sum_{\ell=0}^{\infty}(2\ell+1)\int_0^\infty \tilde{\rho}_\ell(r, r; \beta)\mathrm{d}r}.$$

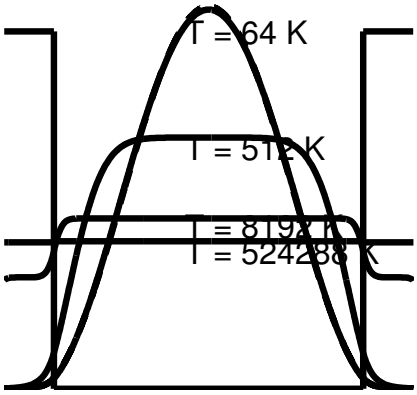

The single well from Paper II with effective mass $m^\star = 0.067m_e$, width $W = 12$ nm and potential $V = 300$ meV. The starting temperature was 524288 K which results in the free particle density matrix. At each iteration the temperature is halved, and finally at 64 K the NMM yields the zero-kelvin limit (black dashed line), already.

However, a uniform grid with no interpolation, that is trapezoid rule, causes difficulties when high accuracy is needed (Ceperley, 1995). The integrand is Gaussian-like, and thus Gauss–Hermite[2] integration scheme is a natural choice of numerical integration for gaining more accuracy.

2.2.1 EXAMPLES

The Coulomb density matrix has many interesting properties, see Storer (1968), Hostler and Pratt (1963) or Pollock (1988). The pair density matrix of the Coulomb potential in any dimensions depends on two scalar spatial variables only, which may be taken as $r_1 + r_2$ and $|\vec{r}_2 - \vec{r}_1|$, or the combination

$$\begin{aligned} x &= \tfrac{1}{2}(r_1 + r_2 + |\vec{r}_2 - \vec{r}_1|) \\ y &= \tfrac{1}{2}(r_1 + r_2 - |\vec{r}_2 - \vec{r}_1|), \end{aligned}$$

and with these variables thus a density matrix is given as

$$\rho(\vec{r}_1, \vec{r}_2; \beta) = -\frac{1}{4\pi(x-y)}\left(\frac{\partial}{\partial x} - \frac{\partial}{\partial y}\right)\tilde{\rho}_0(x, y; \beta)$$

for the Coulomb potential. In the above expression, $\tilde{\rho}_0(x, y; \beta)$ is the density matrix with $\ell = 0$, thus, s-waves only contribute to expansion shown in Eq. (2.1). The s-wave density matrix is easy to evaluate with the help of numerical matrix multiplication, and that is demonstrated in Fig. 2.1. Temperature $T = 300$ K and Trotter number $M = 2^{16}$ are used for each different $\tilde{\rho}_0(r)$. The singular Coulomb potential $-1/r$ and the pseudopotential used in Paper V are tested. We note that the hydrogen radial s-wave distribution, and the pseudopotential in Paper V both give satisfactory results. The Coulomb singularity problem is found, when the cut-off radius is $r_{\text{cut-off}} < 0.05\ a_0$. However, as the cut-off radius to avoid Coulomb collapse is very small, this suggests that we could use Coulomb potential with a small cut-off radius instead of the pseudopotential. This requires, however, use of approximately $M \approx 2^{14}$ to get the accurate hydrogen energy.

Note the more elegant method of Storer (1968) which takes the integration to infinite accurately into account.

Of course, there are many elegant approaches to solve the hydrogen singularity problem, see e.g. Kole and Raedt (2001) or cumulant approximant from Ceperley (1995) or Thijssen (2000).

[2] Charles Hermite, 24 Dec 1822–14 Jan 1901 (Dieuze, Lorraine, France–Paris)

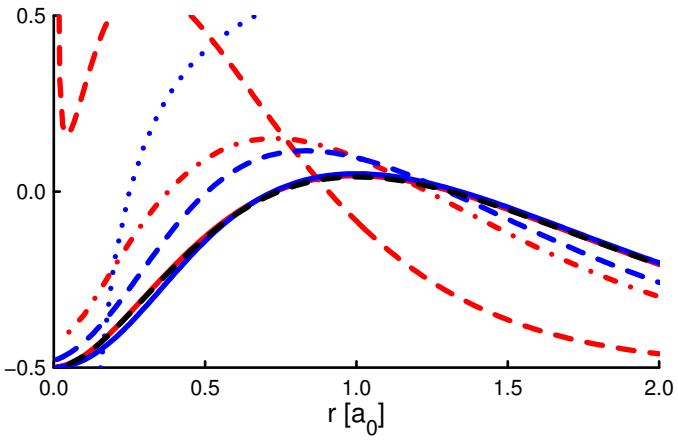

Figure 2.1: Coulomb density matrix with the correct free particle propagator, ρ_b (solid red) coincides with the square of $\psi_{1s} = r\exp(-r)$ wave function (black dashed). If the ρ_b is replaced with ρ_0 we find the Coulomb singularity problem (red dashed line). However, if using larger grid spacing, having a larger cut-off radius, we find that there is no singularity problem (red dash dotted), but the density at the origin fails. Furthermore, the pseudopotential used in Paper V is drawn in blue, solid is for ρ_b and dash dotted is for ρ_0. It has minor problems with smaller radius though the energetics is rather good. The hydrogen potential is also shown (dotted blue).

2.2.2 EFFECTIVE CLASSICAL POTENTIAL

The path-integral method is capable of simulating classical systems, too, when the Trotter number is set to one, $M = 1$, thus the density matrix is $\rho(x_0, x_0; \beta)$.

If $M = 1$, the internal energy, or free particle density matrix is just an identity operator. Thus, the quantum effects are mainly due to this kinetic energy, and the fully quantum mechanical behavior is obtained as $M \to \infty$ while the kinetic part dominates the Lagrangian, see Eq. (1.28) However, we may define such an effective classical potential V_{eff} that yields the same diagonal density as the quantum mechanical system $\rho(x_0, x_M; \beta)$,

The first Hohenberg–Kohn theorem states that the external potential $V(r)$ is a unique functional of the electron density $n(r)$.

$$\rho(x, x; \beta) \equiv N(\beta) \exp\left[-\beta V_{\text{eff}}(x_i)\right]$$

with normalization factor $N(\beta)$ chosen such that the classical partition function coincides with the quantum case, also $Z = Q$ (Janke and Kleinert, 1986). Clearly, the effective classical potential is temperature dependent, and it should contain the *quantum fluctuations* (or smearing).

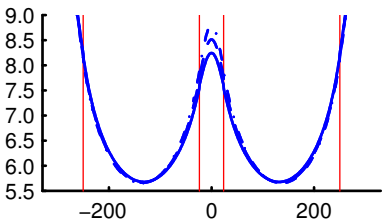

The effective potential times inverse temperature, βV_{eff} at $T = 1$ K, 32 K and 128 K (blue). The lower the temperature, the smoother potential. The classical potential is drawn with red line.

The effective potential arising from Coulomb density matrix is shown in Storer (1968). It is amazing that at high temperatures (about 10^4 K) V_{eff} is almost a straight line for small radial distances and joins the classical potential over quite a small range of r, thus the s-wave is important, only. Furthermore, it has been shown that at low temperatures (2 K), the ground state $1s$-wave function contains

all the information up to $r \approx 3\,a_0$.

In addition, the quantum effective potential obtained by matrix squaring method can be used to obtain smoother potential terms to use with path-integral Monte Carlo methods as described in Ceperley (1995, p. 309 and forward).

2.3 METROPOLIS MONTE CARLO METHOD

Let the quadrature error be $e \propto o(h^k)$ where h is the step length and $k \geq 1$. For the integration of hypercube, with volume L^M, there are totally $N = (L/h)^M$ integration points. Thus, the error in integration is $e \propto o((L/N^{1/M})^k) \propto o(N^{-k/M})$.

The traditional quadrature rules are not very efficient for many dimensional integrations, opposed to the previous example with one dimension. E.g. for Gaussian quadrature there is no general rule how to integrate over M-dimensional space. The simple error estimate gives that the error in integration is $e \propto o(N^{-k/M})$, where $k \geq 0$ is a constant. It can be argued that Monte Carlo methods are better than quadratures because the random distribution is more homogeneous than the regular grid (Thijssen, 2000, p. 273). For Monte Carlo integrations the error in integration is $e \propto o(N^{-1/2})$, independent of the dimensionality of the space. However, this error estimate requires statistically independent sampling, a requirement which is not fulfilled in the Metropolis[3] Monte Carlo method.

It was named Monte Carlo because of the element of chance, the production of random numbers with which to play suitable games. –Stanislaw Ulam.

Buffon's bin (or needle): G. Comte de Buffon, Essai d'arithmétique morale, Supplément à l'Histoire Naturelle, Vol. 4, 1777.

Monte Carlo is common sense applied to mathematical formulations of physical laws and processes. –Stanislaw Ulam.

This section is comprised of a brief introduction to Markov chain (or Metropolis) Monte Carlo (Metropolis et al., 1953), a short introduction to improved sampling methods that are required to find the equilibrium distribution in a reasonable time and also reliably, and lastly some error estimates are given.

2.3.1 MARKOV CHAIN

In pimc scheme $\Omega = \mathbb{R}^{dNM}$ if spin statistics is not included.

Most of the physical systems are continuous, including the Brownian path that is needed in path-integration, and thus it can be argued that by *not* using fully independent Monte Carlo integration schemes we can adopt better convergence. The Metropolis idea is to abandon the statistical uncorrelation and to generate the new random configuration $X_{t_i} \in \Omega$ from the old configuration $X_{t_{i-1}}$. The states X_t and the time t are usually discrete, and the configuration space Ω is usually $\mathbb{R}^{dN}$ but it is easily extended to include e.g. spin dynamics, giving $\Omega = \mathbb{R}^{dN} \times (\mathbb{Z}_2)^N$.

The dynamics is usually governed by a Newtonian equation $F = \frac{\mathrm{d}p}{\mathrm{d}t}$.

The dynamics of a stochastic process is understood as a stochastic transition that governs the evolution of the system. Let the conditional probability of being in state $X_{t_n} = S_j$ given it was on a previous step at $X_{t_{n-1}} = S_i$ be $P(X_{t_n} = S_j | X_{t_{n-1}} = S_i)$. This probability is the a transition probability from state i to state j, which is written as

$$W_{ij} \equiv W(S_i \to S_j) \equiv P(X_{t_n} = S_j | X_{t_{n-1}} = S_i).$$

[3] Nicholas Constantine Metropolis, 11 Jun 1915–17 Oct 1999 (Chicago–Los Alamos)

Because the evolution from state $X_{t_{n-1}}$ to X_{t_n} is dependent only on the previous step, this is known as a *Markov*[4] *process*. The corresponding sequence of states $\{X_t\}$ is called *Markov Chain*, and the process is a *random walk*. This process can be applied to many different problems, e.g. solving the Poisson equation.

W_{ij} is a stochastic rule, thus $W_{ij} \geq 0 \,\forall\, i, j$ and $\sum_j W_{ij} = 1 \,\forall\, i$.

Brownian motion is homogeneous in both time and space and is an example of Markovian process.

The states $\{X_t\}$ generate a distribution $\pi_n \equiv \pi(X_n)$ at the nth step of the random walk. The asymptotic distribution gives the unique equilibrium distribution $p = \lim_n \pi_n$ for arbitrary initial distribution π_1 or X_1, if the system is *ergodic*. An ergodic system is one in which the random walk may return to the neighborhood of X but does not do so periodically, see Kalos and Whitlock (1986, p. 77) or Feller (1950, p. 324).

Let ith element after n step be π_n^i, giving $\pi_{n+1}^j = \sum_j \pi_n^i W_{ij}$, and thus $\pi_{n+1} = \pi_n W = \pi_1 W^n$.

The Metropolis Monte Carlo method gives the *elegant device* for that (Kalos and Whitlock, 1986). Writing the transition probability as a product of the trial move T and the acceptance A, thus $W_{ij} = T_{ij}A_{ij}$, and requiring *detailed balance* criterion, $p(X_j)W_{ji} = p(X_i)W_{ij}$, for the equilibrium distribution p, we find that

Metropolis Monte Carlo is also called M(RT)^2 algorithm.

$$\frac{A_{ij}}{A_{ji}} = \frac{p(X_j)T_{ji}}{p(X_i)T_{ij}} \equiv q_{ij} \geq 0. \tag{2.2}$$

Detailed balance states ensures the equilibrium distribution. However, it is not a necessary condition to achieve correct distribution π.

Thus we sample the next state X_{n+1} with some distribution $T_{n,n+1}$ from state X_n and accept that "move" with a probability $A_{n,n+1} = \min(1, q_{n,n+1})$ or $A_{n,n+1} = 1/(1 + q_{n+1,n})$.

Now the Metropolis algorithm can be described concretely (Kalos and Whitlock, 1986). Let at step n of the random walk the state be X_n, and

- the possible new value X'_{n+1} is sampled from X_n with the help of $T_{n,n+1}$. Compute the probability of accepting X'_{n+1} from Eq. (2.2). If
  - $q_{n,n+1} > 1$ then $A_{n,n+1} = 1$
  - $q_{n,n+1} < 1$, then $A_{n,n+1} = q$
- With probability $A_{n,n+1} = \min(1, q_{n,n+1})$ we set $X_{n+1} = X'_{n+1}$; otherwise we set $X_{n+1} = X_n$
  - If $A_{n,n+1} > \xi$, where $\xi \in [0, 1]$ is a uniform distribution, the trial move is accepted.
  - Otherwise the trial move is rejected and we set $X_{n+1} = X_n$.

The associated probabilities $\pi_1, \ldots, \pi_n, \ldots$ of corresponding states $X_1, \ldots, X_n, \ldots$ are in a recursive relationship, and asymptotically $\lim_n \pi_n = p$. We find that the distribution after j steps is

$$\pi_j = \sum_i \pi_i A_{ij} T_{ij} + \pi_j \sum_i (1 - A_{ji}) T_{ji}$$

[4] Andrei Andreyevich Markov, 14 Jun 1856–20 Jul 1922 (Ryazan, Russia – Petrograd (St Petersburg))

because it may move from any state i to desired state j with probability A_{ij} or stay at j with probability $1 - A_{ji}$. If the random walk converges at some step j to the equilibrium distribution p, also $\pi_j = p$, then the distribution at the next step is clearly given by $\pi_{j+1} = p$ because of detailed balance and because of the normalization condition, $\sum_i T_{ji} = 1$.

However, as the Metropolis Monte Carlo is a powerful tool and easy to implement, there are major drawbacks. It samples the distribution p but only asymptotically. Thus, one must throw away huge amount of sampled random walks, or Markov chains, from the beginning of the simulation. There are a few means to reduce the amount of waste obtained with Monte Carlo methods. First, by selecting the initial distribution π_1 that is a good representative of p, and secondly choosing T_{ij} approximately as p, rapid convergence and a small autocorrelation is achieved (Kalos and Whitlock, 1986, p. 79). Furthermore, Kalos continues, that if we were able to sample $T_{ij} = p_i$ exactly, then $q = 1$ by Eq. (2.2) and all moves are accepted and the samples are independent.

2.3.2 SAMPLING METHODS

Kalos shows the details on M(RT)^2 algorithm by fully working out a one-dimensional example in which $p(x) = 2x$ on $(0, 1)$ and 0 elsewhere.

The original approach of Metropolis et al. (1953) is to use T_{ij} as trial moves for one particle from a uniform distribution within a cube of side length L and zero otherwise. Thus, they selected one particle x_i, and made a trial move $x_{i+1} \leftarrow x_i + L\xi$, where $\xi \in U([-1, 1])$ is from an uniform probability distribution. Furthermore, they studied canonical systems, for which

$$p(X_i) = \frac{1}{Q} \exp(-\beta V(X_i)),$$

and thus when calculating q, Eq. (2.2), the unknown and to-be-solved partition function Q is cancelled out. The side length L is adjusted to achieve the acceptance rate of 50%, approximately. However, there is no certainty in choosing the acceptance rate, it might be anything between 20% and 80%.

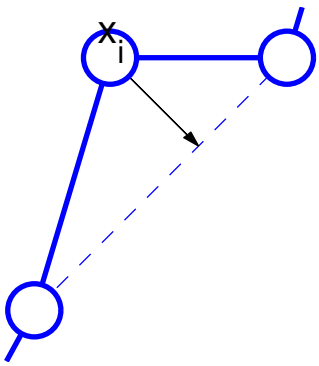

Metropolis move for the ith particle. In the next move it is inclining to come closer to the line between x_{i-1} and x_{i+1} due to the harmonic forces.

These s.c. Metropolis trial moves are not very efficient in path-integral Monte Carlo simulations, because of the stiff harmonic forces between adjacent beads in one necklace. When we move the ith bead, x_i, the beads x_{i-1} and x_{i+1} remain unchanged. To achieve approximately 50% acceptance, the side length should be about $L = \sqrt{\hbar^2 \tau / m}$ according to the variance in Eq. (1.19) and equations above. Therefore, the step length L is dependent on Trotter number $M = \beta/\tau$, and the sampling is very inefficient for large M. Furthermore, on the next move, this bead is inclined to return to the original position because of the harmonic forces caused by its neighbor beads.

The kinetic part of the action dominates at the quantum limit, and thus it is essential to sample that *stiff* part more efficiently. Because the adjacent beads are

connected, we should consider to move a chain of beads of length L. Instead of moving one bead ("single slice") per each sampling, we randomly choose some starting point i and move all the beads between i and $i+L$. The length of chain, L, is chosen such that the total probability of accepting the move of the chain is good, around 50%.

Remember

$$\exp\Big[-\beta\sum_{i=1}^{M}\Big(\frac{mM}{2\pi\hbar^2\beta^2}(x_{i-1}-x_i)^2 + V_S(x_i)/M\Big)\Big].$$

The staging method described in Chapter 1 while evaluating the free particle density matrix, is one good possibility. In this case, instead of moving all particles, choose the starting point i and ending point $i+L$ instead of 1 and Trotter number, M. Because, with the new *staging* variables $\widetilde{x}_j$, $j=i,\ldots,i+L$, the positions are not coupled anymore, the new positions can be sampled exactly by using normally distributed random numbers with variance $\sqrt{\hbar^2\tau/m_j}$ for all $\widetilde{x}_j$, see Sec. 1.3.1.

The other technique for sampling a chain of beads is called *bisection*, which is an multilevel method. It is based on the idea that because the imaginary time between the beads is τ, or the variance is $\sqrt{\hbar^2\tau/m}$, and sampling with larger imaginary time $L\tau/2$ we get larger variance $\sqrt{L\hbar^2\tau/2m}$. Thus, first fix the beads i and $i+L=i+2^k$, and then move the bead $i+2^{k-1}$ with variance $\sqrt{2^{k-1}\hbar^2\tau/m}$. Then, hold the beads i and $i+2^{k-1}$ fixed and move the bead $i+2^{k-2}$, and similarly for the beads $i+2^{k-1}$ and $i+2^k$. This should be done recursively, as is shown in Fig. 2.2. It resembles s.c. *Brownian bridge* process of stochastics, which is a Wiener process, an example of Lévy[5] processes, that is required to satisfy conditions at both ends of the fixed interval. These methods, staging and multilevel, sample the free-particle part of density matrix exactly.

The *Box–Muller algorithm* is the standard way of producing normally distributed random variables with zero mean and unit variance. Let x_1 and x_2 be two independent random variables that are uniformly distributed in $(0,1]$. Then $z_1 = R\cos(\theta) = \sqrt{-2\ln x_1}\cos(2\pi x_2)$ and $z_2 = R\sin(\theta) = \sqrt{-2\ln x_1}\sin(2\pi x_2)$ are independent random variables with a normal distribution of standard deviation 1. More efficient method of George Marsaglia's *ziggurat algorithm* can also be used.

The pseudocode for generating a multilevel transition is the following:
Choose $L=2^k$ and let $x'\leftarrow x$. Let $n\in U([0,M-1])$ and $\eta\in\mathbb{R}$ have standard normal distribution.

for $i\leftarrow k$ **to** 1
  $s\leftarrow 2^{i-1}$
  for $j\leftarrow 0$ **to** $L/(2s)-1$
    $b\leftarrow n+2js \mod M$
    $m\leftarrow n+(2j+1)s \mod M$
    $e\leftarrow n+2(j+1)s \mod M$
    Choose new η
    $x'_m\leftarrow\frac{1}{2}(x'_b+x'_e)+\eta\sqrt{s\tau\hbar^2/(2m)}$
  end j
end i
Calculate the new energy with new x'.

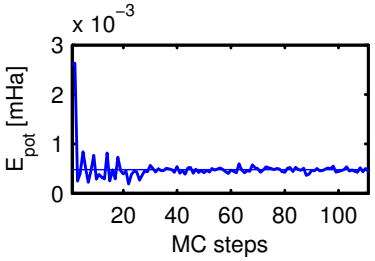

The potential energy for HO as a function of MC steps using multilevel sampling starting from zero Markov chain. The solid line represents the exact energy with $M=64$ exploiting the convergence. $\hbar\omega=0.3$ meV is a typical value for quantum dots, and $m=0.067\,m_e$ represents GaAs mesa.

Thus, in multilevel sampling the trial moves T_{ij} are more complicated than in the original version of Metropolis. However, it should be noted that *in principle* there is no difference which trial move T_{ij} is used, but as it was pointed out earlier, by choosing better trial moves faster convergence is obtained. We have found, that it was impossible (meaning that the convergence time is weeks or months with single processor) to sample with the single bead moves when $M>512$ or so, see Paper V. Furthermore, these two methods sample the kinetic part exactly, thus Metropolis acceptance–rejection scheme needs to be done only for the potential terms.

2.3.3 ERROR ESTIMATES

The successive steps in the process of generating samples of the random walk with MC methods appropriate to many-body systems are correlated, and this gives rise to the main complication in computing the statistical error (Chakravarty et al., 1998). Thus, we need to think of measuring the statistical dispersion of the outcome of a property, indicating how its possible values are spread around the

[5] Paul Pierre Lévy, 15 Sep 1886– 15 Dec 1971 (Paris–Paris)

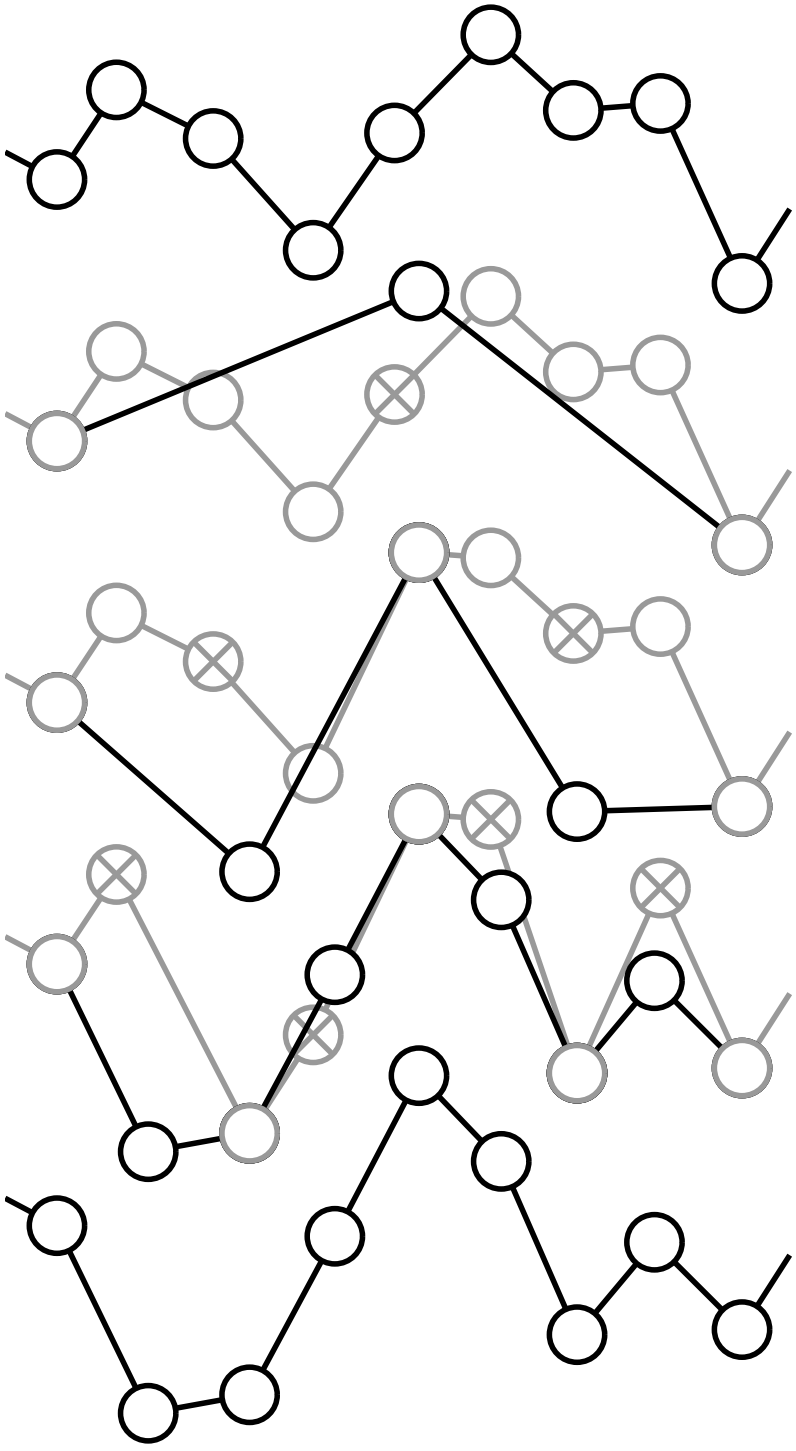

Figure 2.2: Bisection move for the chain of beads for $L = 2^3$. The uppermost figure is the original configuration of the beads. Then the middle bead (shown with gray $\times$) is moved, and this is repeated recursively. In the next step, beads i and $i + 2^1$ are held fixed and similarly $i + 2^2$ and $i + 2^3$. The last figure shows the new trial move, which is to be considered in Metropolis algorithm.

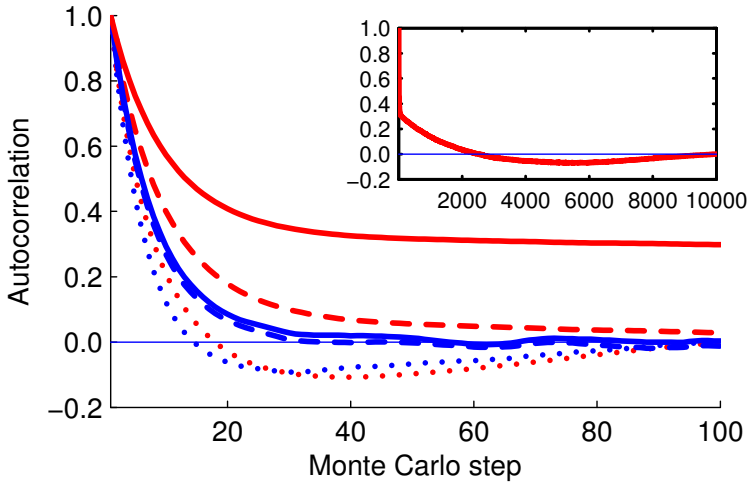

Figure 2.3: Autocorrelation data with three different lengths of autocorrelation window is plotted, see text. Dotted is for $N = 100$, dashed for $N = 1000$ and solid line $N = 10000$ data points. The autocorrelation is averaged for all data with respective N. The red line is for single bead and blue for multilevel sampling. The very beginning shows exponential decay, but soon the autocorrelation becomes linear and thus exploiting rather strong autocorrelation. It should be noted that the all data points in single bead simulation are correlated, see the inset.

expected value $\langle Q \rangle$,

$$\langle Q \rangle = \frac{1}{N} \sum_{k=1}^{N} Q_k.$$

The estimate for the deviation from the expectation value given by the unbiased sample average *formula*

$$s^2_{N-1} = \frac{1}{N-1} \sum_{i=1}^{N} (Q_i - \langle Q \rangle)^2$$

gives too small error estimates, because the data is correlated. The correlation between data points reduces the number of uncorrelated data points N, and thus it should be changed to some effective $N_{\text{eff}} < N$. The autocorrelation function for a quantity Q

$$A_Q(k) = \frac{\sum_{i=1}^{N-k} (Q_i - \langle Q_i \rangle)(Q_{i+k} - \langle Q_i \rangle)}{\sum_{i=1}^{N} (Q_i - \langle Q_i \rangle)^2} = \frac{\langle Q_{i+k} Q_i \rangle - \langle Q_i \rangle^2}{\langle Q_i^2 \rangle - \langle Q_i \rangle^2}$$

gives an estimate for the *autocorrelation length*, also if $A_Q(\ell) \approx 0$ for all $\ell > k$, then the correlation length is k and the data points Q_i and Q_{i+k} are not correlated. The effective number of data points is $N_{\text{eff}} = N/k$. To verify the correlation length, one may use smaller N, e.g. use a *window* on the data set and find the autocorrelation only for the data under the window. These should converge. See Fig. 2.3 for an example.

An estimator for a parameter $\widehat{\theta}$ is unbiased if $E(\widehat{\theta}) = \theta$, thus $E(s^2_{N-1}) = \sigma^2$.

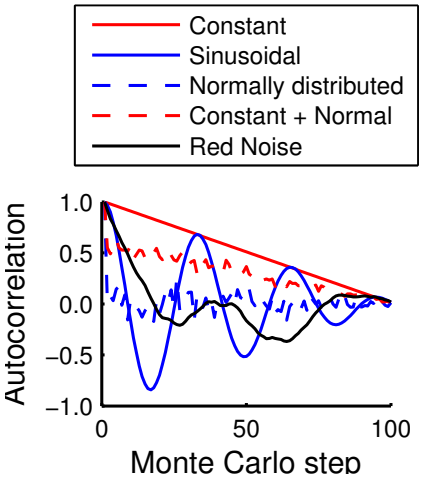

The autocorrelation function for the realization of a few different random functions. Note that even though there is full correlation in the constant case, the autocorrelation function still decays linearly.

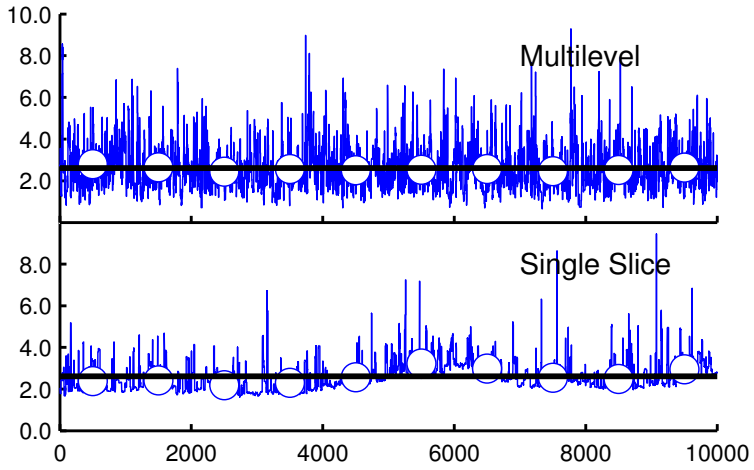

Figure 2.4: Data binning of multilevel and single bead external energetics. Here, the length of data is 10000 MC steps, and the size of a bin is 1000 steps. The 20000 first MC steps are left out to achieve equilibrium. The analytical energy, 2.6108 mHa, is drawn with black line. The corresponding MC energies are given in Table 2.1. See kinetic energy. The single bead energy looks similar to that of pure brownian noise with large a, and multilevel energy with small a.

For the *red (Brownian) noise*, $x(t) = ax(t - \Delta t) + (1 - a^2)^{1/2}\epsilon(t)$ where $a \in [0, 1]$ is the degree of memory from previous states the autocorrelation is of type $r(\tau) = \exp(-\tau/T_{\text{exp}})$ with $T_{\text{exp}} = -\Delta t/\ln a$ being the exp -folding decay time. For the *white noise*, where $a = 0$ we have $r(\tau) = \delta(\tau)$.

Another method to study the effect of statistical correlations is *data binning*. When using data binning the successive measurements are collected into N_B bins, giving $m = N/N_B$ measurements per bin. The bins should be selected such that the successive averages

$$\langle Q_k \rangle = \frac{1}{m} \sum_{i=1}^{m} Q_{m(k-1)+i}$$

for kth and $(k+1)$th bins are not correlated any more. The autocorrelation length k should be approximately the same as m here. Now the expected value and the variance are

$$\langle Q \rangle = \frac{1}{N_B} \sum_{k=1}^{N_B} \langle Q_k \rangle$$

$$s^2_{N_B-1} = \frac{1}{N_B - 1} \sum_{k=1}^{N_B} (\langle Q_k \rangle^2 - \langle Q \rangle^2).$$

The data binning of the total energy of harmonic oscillator is shown in Fig. 2.4 with both multilevel and single slice sampling methods. It should be noted that the successive bins with single slice sampling are still correlated, and that it does not yield the correct energy. The autocorrelation plots, Fig. 2.3, are generated from this data. It can be seen that the correlation length is larger for single bead than for multilevel sampling.

Furthermore, to estimate the *standard error of the mean*, the standard deviation of

	Multilevel $E \pm S$	Single bead $E \pm S$
	2.614 ± 0.003	2.733 ± 0.001
$N = 10000$		
$m = 100$	2.630 ± 0.042	3.284 ± 0.034
$m = 1000$	2.630 ± 0.034	3.284 ± 0.041
$N = 100000$		
$m = 100$	2.610 ± 0.013	3.300 ± 0.028
$m = 1000$	2.610 ± 0.013	3.300 ± 0.085
$m = 5000$	2.610 ± 0.014	3.300 ± 0.175
$m = 10000$	2.610 ± 0.015	3.300 ± 0.226

Table 2.1: External (potential) energy for the harmonic oscillator with $M = 2^6$ and $T = 300$ K. Here N refers to the number of data points and m is the size of the binning box. The first row contains the average of all data points. The analytic energy is 2.6108 mHa at Trotter number $M = 64$ and $T = 300$ K, and the full quantum energy is 2.6205 mHa.

the sampling distribution of the mean can be used,

$$s_E = \sqrt{\frac{s_{N-1}^2}{N}}.$$

The final result for property Q is then $\langle Q \rangle \pm s_E$ with one SEM. Note that the error in estimate is $s_E \propto N^{-1/2}$ and it can be made as small as needed by using large enough N while having small correlation. The comparison between multilevel and single bead energetics is collected in Table 2.1. Note that the single bead simulation has not yet converged though the simulation is rather long, 4096000 Monte Carlo steps.

The *central limit theorem* guarantees that the sampling distribution of the mean is asymptotically normal as the sample size N tends to infinity.

2.4 CALCULATION OF PROPERTIES

According to the Postulate 3 shown in Chapter 1, the average value of an observable $\widehat{A}$ in the state $\widehat{\rho}$ is given by $\langle \widehat{A} \rangle = \text{Tr}\,(\widehat{\rho}\widehat{A})$ where Tr $(\cdot)$ is the trace of the operator in the parentheses. In coordinate basis the trace is evaluated as an integral,

Note that Tr $(\widehat{\rho}\widehat{A}) = \sum_i \langle i|\widehat{\rho}\widehat{A}|i\rangle = \sum_{i,n} p_n \langle i|n\rangle\langle n\widehat{A}|i\rangle = \sum_n p_n \langle n|\widehat{A}|n\rangle$.

$$\text{Tr}\,(\widehat{\rho}\widehat{A}) = \int \rho(x, x; \beta) A(x) \mathrm{d}x$$

for diagonal operators $A(x)$. Thus, by introducing the path-integral representation for density matrix $\rho(x, y; \beta)$, we get

$$\langle \widehat{A} \rangle = \frac{1}{M} \int \exp\left[-\sum_{i=1}^{M} S(x_{i-1}, x_i; \tau)\right] \sum_{i=1}^{M} A(x_i) \mathrm{d}x_1 \cdots \mathrm{d}x_M \qquad (2.3)$$

with periodic boundary conditions in imaginary time, $x_0 = x_M$. Here, the symmetry of time slices is taken into account. Actually, Eq. (2.3) is only a multidimensional integral of $A(x)$ with the weight function $\exp\left[-\sum_{i=1}^{M} S(x_{i-1}, x_i; \tau)\right]$, and thus the Monte Carlo integration schemes with importance sampling are very powerful tools in calculating the quantum properties.

However, for a given property, it is possible to device more than one *estimator* such that the Monte Carlo average is the same for each choice (Herman et al., 1982). An estimator is characterized by its statistical error, efficiency (statistical error for a given length run), bias (nonlinear distortion), time-step error, and finite-size error (Ceperley, 1995), and those may be very different for different estimators of a given property. In addition, some estimators are easier physically to interpret or easier to program. The aim is to find an estimator that minizes the maximum of various errors.

In following subsections, some estimators to frequently used operators with their efficiencies are given. Of course, there are many other interesting properties that are not discussed here, e.g. pressure, heat capacity, magnetic susceptibility, exchange or correlation energies, position and momentum (Whitfield and Staub, 2001), partition function, $Q(\beta) = \int \rho(x, x; \beta)\mathrm{d}x$, or free energy (Schweizer et al., 1981).

2.4.1 DENSITY AND PAIR CORRELATION FUNCTIONS

The density of particle x_1 is a function of $x_1 - x_0$ where x_0 is the fixed origin; the pair correlation is a function of $|x_1 - x_2|$ where x_1 and x_2 are the positions of particles 1 and 2.

The diagonal density matrix, $\rho(x, x; \beta)$, itself is a density function. It is easy to obtain during the simulation process, simply by collecting the positions of all beads. Furthermore, because of the symmetry in imaginary time, all beads can be taken advantage of. The pair correlation function is a special case of density. Its formal definition is

$$g(x) = \int \delta(x - |x_1 - x_2|)\rho(x, x; \beta)\mathrm{d}x.$$

The pair correlation function is obtained during the simulation process, too.

2.4.2 POTENTIAL ENERGY

The estimator for potential energy $\langle \widehat{V} \rangle$ in PIMC simulations is easy to obtain during the simulation process, because $V(x)$ is needed in the Metropolis acceptance–rejection scheme. Because the potential energy is diagonal, we find directly by applying Eq. (2.3) that

$$E_V = \frac{1}{M} \sum_{i=1}^{M} V(x_i). \tag{2.4}$$

Thus, we find that as the number of beads grows, the potential energy fluctuations becomes smaller and averaged.

Furthermore, the one-particle potential energy is easy to obtain afterwards with the help of density matrix,

$$E_v = \langle V(\vec{x}) \rangle_\rho \tag{2.5}$$

with numerical integration schemes. The same integration technique can be applied to N-particle systems too, but it needs the knowledge of pair correlation function between particles, see e.g. Harting (2001) or some of his articles, e.g. Harting et al. (2000).

2.4.3 KINETIC ENERGY

Thermodynamic and *virial* estimators for the kinetic energy are the most popular ones. The thermodynamic estimator is the same that is obtained when estimating the thermodynamic total energy, see Sec. 2.4.4, but it suffers from convergence problems. The virial estimator is the one that is widely used.

In the following, only the special case of one particle in a confining potential $V(x)$ is considered, and the primitive approximation to the action is assumed. However, the generalization is straightforward, but yields rather cumbersome notation and is thus left out. This is shown in detail in Ceperley (1995, Appendix A).

The thermodynamic kinetic energy can be defined (Ceperley, 1995) as

$$E_k = \frac{m}{\beta Q}\frac{\mathrm{d}Q}{\mathrm{d}m} = \int \frac{m}{\beta Q}\frac{\partial \rho(x,x;\beta)}{\partial m}\mathrm{d}x. \tag{2.6}$$

The thermodynamic kinetic energy (2.6) for classical harmonic oscillator is as

$$E_k^{\mathrm{cl}} = \frac{m}{\beta Z}\frac{\mathrm{d}Z}{\mathrm{d}m} = \frac{1}{2}\beta^{-1} = \frac{1}{2}k_{\mathrm{B}}T.$$

When the density matrix in the path-integral formalism, Eq. (1.29), is substituted for ρ, and after differentiation we find that

$$\begin{aligned} E_k &= \int \frac{m}{\beta Q}\frac{\partial \rho(x,x;\beta)}{\partial m}\mathrm{d}x = \frac{m}{\beta Q}\int \frac{\partial}{\partial m}\exp\left[-\sum_{i=1}^{M} S(x_{i-1},x_i;\tau)\right]\mathrm{d}x\mathrm{d}x_1\cdots\mathrm{d}x_{M-1} \\ &= \frac{1}{Q}\int\left(\frac{dNM}{2\beta} - \sum_{i=1}^{M} T_i'\right)\exp[-S(x_{i-1},x_i,;\tau)]\mathrm{d}x_0\cdots\mathrm{d}x_{M-1} \end{aligned}$$

with the cyclic condition $x_0 = x_{M-1}$. The first part, $dNM/2\beta$, resembles the classical kinetic energy $1/(2\beta)$, and the second part can be thought as a quantum mechanical correction term. It should be noted, that if we were not using the primitive approximation, also the potential term would give rise to kinetic energy, as $\partial_m V_S(m)$. Finally, we have the estimator

$$E_k = \left\langle \frac{dNM}{2\beta} - \frac{mM}{2\hbar^2\beta^2}\sum_{i=1}^{M}(x_{i-1}-x_i)^2 \right\rangle_\rho \tag{2.7}$$

for the kinetic energy. Though it is impossible to collect and maintain all the positions during the simulation process, this kinetic energy estimator can be calculated after Metropolis acceptance. However, both terms diverge as $\tau = \beta/M \to 0$. Furthermore, the evaluation of kinetic energy with this estimator is difficult, because there is a subtraction of two large numbers, $\frac{dN}{2\tau}$ and $\sum_j \frac{m_j}{2\hbar^2\tau^2}(x_{i-1}^j - x_i^j)^2$. The variance of this estimator is badly behaving, as will be demonstrated in the next subsection with a special case of harmonic oscillator. Thus, a more refined estimator will be needed.

Monte Carlo can add but not subtract.

The average of a *virial* is defined as

$$\frac{1}{M}\sum_{i=1}^{M}\langle x_i \cdot \nabla V\rangle_\rho .$$

The *virial* originates from a Latin word vires, *"forces"*, and is defined as $\sum_i r_i \cdot p_i$.

Note that by differentiating the density matrix, $\exp(-S(x_{i-1}, x_i; \tau))$, with respect to x_i, we get the virial term,

$$x_i \cdot \nabla \exp[-\sum_i S_i] = -\sum_{i=1}^{M}\left(2\frac{mM}{2\hbar^2\tau^2}(x_{i-1}-x_i)^2 + \tau x_i \cdot \nabla V(x_i)\right)\exp[-\sum_i S_i]$$

and thus the average of the virial is given by

$$\frac{1}{M}\sum_{i=1}^{M}\langle x_i \cdot \nabla V(x_i)\rangle_\rho = \frac{-1}{\beta}\sum_{i=1}^{M}\left\langle 2\frac{mM}{2\hbar^2\tau^2}(x_{i-1}-x_i)^2 + x_i\cdot\nabla\right\rangle_\rho$$

because $\tau = \beta/M$. The partial derivative can be integrated by parts

$$\int x_i \cdot \nabla \mathrm{e}^{-\sum_i S}\mathrm{d}x_1\cdots\mathrm{d}x_{M-1} = -\left[(x_{x,i}+x_{y,i}+x_{z,i})\,\mathrm{e}^{-\sum_i S(x_{i-1},x_i;\tau)}\right]_{x_{i,\text{start}}}^{x_{i,\text{end}}} - \int \mathrm{e}^{-\sum_i S(x_{i,1},x_i;\tau)}\mathrm{d}x_1\cdots\mathrm{d}x_M .$$

The substitution part in the previous differs from case to case, and according to Tuckerman, there are five different possibilities, if

1. $V \to \infty$ when $x \to \pm\infty$: a bound system and $\exp(-S) \to 0$,
2. $V \to 0$ when $x \to \pm\infty$: an unbound system, and $\exp(-S) \to 1$,
3. V is periodic and the coordinates will take on the same value at the period boundaries,
4. the particle experience elastic collisions with the walls of the container, then there is an infinite potential at the walls

and the surface term vanishes. However,

5. if the particle is confined within a volume V with a reflected boundaries, then the surface contributions actually give rise to an observable pressure.

It is easy to show that (Euler's theorem)

$$\sum_{i=1}^{M} x_i \cdot \frac{\partial}{\partial x_i}(x_{i-1}-x_i)^2 = 2\sum_{i=1}^{M}(x_{i-1}-x_i)^2.$$

Consider the equation of motion for the virial, $\imath\hbar\frac{d}{dt}\langle r\cdot p\rangle = \langle[r\cdot p, H]\rangle$. For the x component we get

$$[r\cdot p, H]_x = [xp_x, H] = \left[xp_x, \frac{p_x^2}{2m}+V\right] = \imath\hbar\frac{p_x^2}{m} + x[p_x, V]$$

if $[x, V] = 0$. Thus, because $[\nabla, V] = \nabla V$ and by combining these and the *change-of-variable* results for y and z components, we find that

$$\imath\hbar\frac{d}{dt}\langle r\cdot p\rangle = \imath\hbar\left\langle\frac{p^2}{m}\right\rangle - \imath\hbar\langle r\cdot\nabla V\rangle$$

because $p = -\imath\hbar\nabla$. This gives for a stationary state (or for periodic motion, or for a bounded system)

$$2\left\langle\frac{p^2}{2m}\right\rangle = \langle r\cdot\nabla V\rangle,$$

which agrees with the result of path-integral formulation, Eq. (2.8).

Assuming the substitution part to vanish, we find that

$$\int \sum_{i=1}^{M} x_i \cdot \nabla \mathrm{e}^{-\sum S(x_{i-1},x_i)} \mathrm{d}x_1 \cdots \mathrm{d}x_{M-1} = -dMN.$$

Thus, we are left with

$$\frac{1}{M}\sum_{i=1}^{M} \langle x_i \cdot \nabla V \rangle_\rho = \frac{dMN}{\beta} - 2\sum_{i=1}^{M} \left\langle \frac{mM}{2\hbar^2\tau^2}(x_{i-1}-x_i)^2 \right\rangle_\rho$$

which gives us a hopefully less oscillating definition for the internal energy. After substituting this into Eq. (2.10), we find for the virial kinetic energy

For harmonic oscillator $V = \frac{1}{2}m\omega^2 x^2$ and thus $\frac{1}{2} r \cdot \nabla V = \frac{1}{2}m\omega^2 x^2 = V$.

$$E_k = \frac{1}{M}\sum_{i=1}^{M} \left\langle \tfrac{1}{2} x_i \cdot \nabla V \right\rangle_\rho . \tag{2.8}$$

The thermodynamic estimator, Eq. (2.7), is called the *Barker* estimator because Barker (1978) was one of the first to use it, and the later estimator, Eq. (2.8), is sometimes called *Herman* or *Berne* virial estimator, because of Herman et al. (1982) which is a continuation to the work of Schweizer et al. (1981). A more general derivation with N particles and general external potential V_S is shown in Ceperley (1995), in Appendix A. The performance of these kinetic energy estimators are shown below for the case of linear harmonic oscillator.

2.4.4 TOTAL ENERGY

As the total energy is considered to be one of the most important physical quantities, there are various estimators for it. The *direct*, or *Hamiltonian* estimator is obtained directly by calculating the expectation value of the Hamiltonian

$$\langle \widehat{H} \rangle = \mathrm{Tr}\ \widehat{H}\widehat{\rho},$$

but this is rather complicated, because it contains terms with $\langle \nabla^2 V \rangle$ etc. More convenient is the *thermodynamic* total energy

The classical total energy energy for harmonic oscillator is by (2.9)

$$E_T^{\mathrm{cl}} = -\frac{1}{Z}\frac{\mathrm{d}Z}{\mathrm{d}\beta} = \beta^{-1} = k_\mathrm{B}T.$$

$$E_T = -\frac{1}{Q}\frac{\mathrm{d}Q}{\mathrm{d}\beta} = -\frac{1}{Q}\int \frac{\partial \rho(x,x;\beta)}{\partial \beta}\mathrm{d}x. \tag{2.9}$$

When the density matrix in path-integral formalism, Eq. (1.29), is substituted for $\int \rho(x,x;\tau)\mathrm{d}x$, and after differentiation, we find, similarly as for the kinetic energy, that

$$\begin{aligned} E &= -\int \frac{1}{Q}\frac{\partial \rho(x,x;\beta)}{\partial \beta}\mathrm{d}x = -\frac{1}{Q}\int \frac{\partial}{M\partial\tau} \exp\left[-\sum_{i=1}^{M} S(x_{i-1},x_i;\tau)\right] \mathrm{d}x_0 \cdots x_{M-1} \\ &= \frac{1}{Q}\int \left[\frac{dNM}{2\beta} - \frac{mM}{2\hbar^2\beta^2}\sum_{i=1}^{M}(x_{i-1}-x_i)^2 + \frac{1}{M}\sum_{i=1}^{M} V(x_i)\right] \times \\ &\qquad \exp\left[-\sum_{i=1}^{M} S(x_{i-1},x_i;\tau)\right] \mathrm{d}x_0 \cdots x_{M-1} \end{aligned}$$

with cyclic condition in imaginary time $x_0 = x_M$. Thus, the thermodynamic estimator for the total energy can be calculated from

$$E = \left\langle \frac{dNM}{2\beta} - \frac{mM}{2\hbar^2\beta^2}\sum_{i=1}^{M}(x_{i-1}-x_i)^2 + \frac{1}{M}\sum_{i=1}^{M}V(x_i)\right\rangle_\rho \tag{2.10}$$

By equipartition theorem in classical system at temperature T, kinetic and potential energy terms are equal and $E^{\mathrm{cl}} = k_{\mathrm{B}}T = 1/\beta$.

However, this is plagued by the same subtraction problem as the kinetic energy; when subtracting $\frac{mM}{2\hbar^2\beta^2}\sum_{i=1}^{M}(x_{i-1}-x_i)^2$ from $dNM/2\beta$ we are left only with random noise giving a large variance while the expectation value is correct, for this estimator. The very same virial kinetic energy estimator can be used to obtain better behaving estimator. Thus, by replacing the thermodynamic kinetic part, Eq. (2.7), in Eq. (2.10) with virial kinetic part, Eq. (2.8), we get a better estimator

$$E_v = \frac{1}{M}\sum_{i=1}^{M}\left\langle \tfrac{1}{2}x_i\cdot\nabla V(x_i) + V(x_i)\right\rangle_\rho \tag{2.11}$$

which is, again, sometimes called the Hermann estimator.

Furthermore, the total energy can be calculated via the expansion, Eq. (1.27),

$$E(\beta) = \frac{\sum_i d_i E_i \exp(-\beta E_i)}{\sum_i d_i \exp(-\beta E_i)}, \tag{2.12}$$

which can not be used during the simulation process. Here, d_i is the degeneracy of energy E_i at state i.

2.4.5 EXTRAPOLATION TO HIGHER TROTTER NUMBERS

The path-integral density matrix is exact only in the limit $M \to \infty$. However, the integral that is supposed to be calculated is MNd-dimensional, and thus the larger M, the greater work need to be done to get a good density matrix or good enough estimators for different physical properties.

Following the higher order expansion, shown in Sec. 1.4.2, we note that the second order correction term is $\frac{1}{2}[\widehat{X},\widehat{Y}]/M^2$, thus it scales as M^{-2} (Binder and Heermann, 2001). To achieve better approximations, we could compute observables for several values of M and try an extrapolation of the results as an function of M^{-2}. This is done in Paper V for the hydrogen atom and hydrogen molecule.

2.5 HARMONIC OSCILLATOR

To get insight into the different estimators of energy, and into the discrete path-integral scheme with finite Trotter number M, we calculate the expectation values and variances of different estimators for the harmonic oscillator, $V(x_i) = \frac{1}{2}m\omega^2 x_i^2$, analyzed already in Sec. 1.6. To elucidate the differences between

The density matrix for classical oscillator is $\rho^{\mathrm{cl}}(p,x) = \mathrm{e}^{-\beta H(p,x)}$, where $H(p,x)$ is the Hamiltonian, $H(p,x) = p^2/(2m) + \frac{1}{2}kx^2$.

Table 2.2: First order differentials needed in linear harmonic oscillator.

$$\begin{aligned}\frac{1}{Q}\frac{\partial Q}{\partial f} &= \frac{-M}{2f}\frac{f^M+1}{f^M-1}\\ \frac{\partial f}{\partial R} &= \frac{2f\sqrt{f}}{f+1}\\ \frac{\partial R}{\partial s} &= \hbar\frac{\beta}{M}\frac{\partial\omega(s)}{\partial s}\end{aligned}$$

energy estimators, we apply thermodynamic and virial estimators to this system. Furthermore, the effect of using higher order Trotter approximations, see Sec. 1.4.2, can also be shown by using the effective frequency, $\omega \to \omega_{\text{eff}}$. This is also shown below.

2.5.1 THERMODYNAMIC ESTIMATOR

The partition function for the harmonic oscillator is $Q = f^{M/2}/(f^M - 1)$, see Eq. (1.31), and the thermodynamic total energy by applying Eq.(2.9) is

Remember that $f = 1 + \frac{1}{2}R^2 + \frac{1}{2}R(4+R^2)^{1/2}$ and $R = \hbar\omega\beta/M$.

$$\langle E_T\rangle_M = -\frac{1}{Q}\frac{\partial Q}{\partial\beta} = -\frac{1}{Q}\frac{\partial Q}{\partial f}\frac{\partial f}{\partial R}\frac{\partial R}{\partial\beta} = \hbar\omega\frac{\sqrt{f}}{f+1}\frac{f^{M/2}+f^{-M/2}}{f^{M/2}-f^{-M/2}}.$$

The differentials needed here are given in Table 2.2. By taking the limit $M \to \infty$ this finite-M energy reduces to that given by Feynman (1972, p. 52)

$$\langle E_T\rangle = \tfrac{1}{2}\hbar\omega\coth\frac{\hbar\omega\beta}{2}. \tag{2.13}$$

The finite-M approximation to the internal energy of the one-dimensional harmonic oscillator, for example, loses its ground state energy as $T \to 0$ (Whitfield and Staub, 2001).

2.5.2 ENERGETICS IN PATH-INTEGRAL SCHEME

To find the correct estimators and error estimates of the path-integral scheme, more elaborated methods must be employed to find the effect of time slices, or Trotter number. In probability theory, the characteristic function of any random variable x,

$$\varphi_x(s) = E(\exp(\imath sx)) = \int \mathrm{e}^{\imath sx} f(x)\mathrm{d}x$$

The potential energy can also be calculated as $\langle\widehat{V}\rangle = \int\rho\widehat{V}\mathrm{d}x$, thus now ρ for ho is given by Eq. (1.30), and the integral can be calculated straightforwardly giving $\langle\widehat{V}\rangle = \frac{1}{2}\langle E\rangle_M$ with the help of identity $\int x^2\exp(-ax^2)\mathrm{d}x = -\frac{\mathrm{d}}{\mathrm{d}a}\int\exp(-ax^2)\mathrm{d}x = \frac{1}{2a}\sqrt{\pi/a}$.

completely and uniquely defines its probability distribution $f(x)$. This is almost the same as Fourier[6] transform; the characteristic function of a probability density function $f(x)$ is the complex conjugate of the continuous Fourier transform of $f(x)$, according to the usual convention. Provided that nth moment exists, the characteristic function can be differentiated n times giving

Note that

$$\begin{aligned}\varphi_x(s) &= E(\exp(\imath s x)) \\ &= E\left(\sum_{n=0}^{\infty}\frac{(\imath s x)^n}{n!}\right) \\ &= \sum_{n=0}^{\infty}\frac{(\imath s)^n}{n!}E(x^n).\end{aligned}$$

$$\varphi_x^{(n)}(s) = \int (\imath x)^n \mathrm{e}^{\imath s x} f(x)\mathrm{d}x$$

and thus

$$\int x^n f(x)\mathrm{d}x = \imath^{-n}\varphi_x^{(n)}(0).$$

All the moments of the random variable can be derived from the characteristic function (Tan et al., 2006). Here we employ Laplace[7] transform to find the describing moments of Gaussian random variable needed for the harmonic oscillator. In the following, we use the abbreviations given below for internal energy, external energy and the difference

$$\begin{aligned}\alpha_M &\equiv \frac{Mm}{2\hbar^2\beta^2}\sum_{i=1}^{M}(x_{i-1}-x_i)^2 \\ \lambda_M &\equiv \frac{1}{M}\sum_{i=1}^{M}V(x_i) = \frac{1}{2M}m\omega^2\sum_{i=1}^{M}x_i^2 \\ \gamma_M &\equiv \alpha_M - \lambda_M,\end{aligned}$$

and Laplace transforming each term gives the corresponding characteristic function

$$\begin{aligned}P_\alpha(\alpha) &\equiv \langle\delta(\alpha-\alpha_M)\rangle_M \quad &\rightarrow \quad \widetilde{P}_\alpha(s) &= \langle\exp(-s\alpha_M)\rangle_M, \\ P_\lambda(\lambda) &\equiv \langle\delta(\lambda-\lambda_M)\rangle_M \quad &\rightarrow \quad \widetilde{P}_\lambda(s) &= \langle\exp(-s\lambda_M)\rangle_M, \\ P_\gamma(\gamma) &\equiv \langle\delta(\gamma-\gamma_M)\rangle_M \quad &\rightarrow \quad \widetilde{P}_\gamma(s) &= \langle\exp(-s\gamma_M)\rangle_M.\end{aligned}$$

$$\begin{aligned}E_k^{\mathrm{cl}} &= \frac{\frac{1}{2m}\int p^2\exp\left[-\beta\left(\frac{p^2}{2m}+\frac{1}{2}kx^2\right)\right]\mathrm{d}p}{\int\exp\left[-\beta\left(\frac{p^2}{2m}+\frac{1}{2}kx^2\right)\right]\mathrm{d}p} \\ &= \frac{1}{2m}\frac{\int p^2\exp\left(-\frac{1}{2m}\beta p^2\right)\mathrm{d}p}{\int\exp\left(-\frac{1}{2m}\beta p^2\right)\mathrm{d}p} \\ &= \frac{1}{2}\beta^{-1}.\end{aligned}$$

Thus we find that the transformed density is similar to the old one but with effective mass and frequency. For the internal energy the characteristic function becomes

$$\widetilde{P}_\alpha(s) = \left[\frac{2\pi\hbar^2\tau}{m}\right]^{M/2}\int\exp\left[-\beta\left(\frac{\beta+s}{\beta}\alpha_M+\lambda_M\right)\right]\mathrm{d}x_1\cdots\mathrm{d}x_{M-1}$$

and it is equivalent to the statement that we are using some effective mass $m_\alpha = m(\beta+s)/\beta$ and potential $\omega_\alpha = \omega(\beta/(\beta+s))^{1/2}$ instead of the old ones. The characteristic function can be written with the help of partition function as

$$\widetilde{P}_\alpha(s) = \left(\frac{m}{m_\alpha}\right)^{M/2}\frac{Q(M,\beta,m_\alpha(s),\omega_\alpha(s))}{Q(M,\beta,m,\omega)},$$

and the characteristic functions for external energy λ and the difference energy γ can be treated similarly. The frequencies ω_i and masses m_i are given in Tables 2.3 and 2.4.

Table 2.3: The effective masses for harmonic oscillator energetics and respective differentials.

$m_i(s)$	$\frac{1}{m_i}\frac{\partial m_i}{\partial s}$	$\frac{1}{m_i}\frac{\partial^2 m_i}{\partial s^2}$
$\alpha : \frac{\beta+s}{\beta}m$	$\frac{1}{\beta+s} \to \frac{1}{\beta}$	0
$\lambda : m$	0	0
$\gamma : \frac{\beta+s}{\beta}m$	$\frac{1}{\beta+s} \to \frac{1}{\beta}$	0

Table 2.4: The effective frequencies and differentials for harmonic oscillator energetics.

$\omega_i(s)$	$\frac{\beta}{\omega_i}\frac{\partial \omega_i}{\partial s}$	$\frac{\beta}{\omega_i}\frac{\partial^2 \omega_i}{\partial s^2}$
$\alpha : \sqrt{\frac{\beta}{\beta+s}}\omega$	$\frac{-\beta^2}{2(\beta+s)^2}\sqrt{\frac{\beta+s}{\beta}} \to -\frac{1}{2}$	$\frac{3\beta^2}{4(\beta+s)^3}\sqrt{\frac{\beta+s}{\beta}} \to \frac{3}{4\beta}$
$\lambda : \sqrt{\frac{\beta+s}{\beta}}\omega$	$\frac{1}{2}\sqrt{\frac{\beta}{\beta+s}} \to \frac{1}{2}$	$\frac{-1}{4(\beta+s)}\sqrt{\frac{\beta}{\beta+s}} \to \frac{-1}{4\beta}$
$\gamma : \sqrt{\frac{\beta-s}{\beta+s}}\omega$	$\frac{-\beta^2}{(\beta+s)^2}\sqrt{\frac{\beta+s}{\beta-s}} \to -1$	$\frac{\beta^2(\beta-2s)}{(\beta-s)(\beta+s)^3}\sqrt{\frac{\beta+s}{\beta-s}} \to \frac{1}{\beta}$

While we are studying the Gaussian probability distribution, the two first moments describe it. Thus, for the expectation value and variance of the internal energy, for example, we have

To shorten the calculations the logarithmic differential is used. Remember that $\frac{1}{Q(s)}\frac{\partial Q(s)}{\partial s} = \frac{\partial \ln Q(s)}{\partial s}$.

$$\langle \alpha_M \rangle = -\left(\frac{\partial \ln \widetilde{P}_{\alpha_M}(s)}{\partial s} \right)_{s\to 0}$$
$$\langle \delta\alpha_M^2 \rangle = \left(\frac{\partial^2 \ln \widetilde{P}_{\alpha_M}(s)}{\partial s^2} \right)_{s\to 0}.$$

The expectation value for internal energy, for example, is easily calculated as

$$-\frac{\partial \ln \widetilde{P}_{\alpha_M}(s)}{\partial s} = \frac{M}{2}\frac{1}{m_\alpha(s)}\frac{\partial m_\alpha(s)}{\partial s} + \frac{\beta}{\omega}\frac{\partial \omega_\alpha(s)}{\partial s}\langle E_T\rangle_M$$

by using the properties of logarithm. The differentials are given in Tables 2.2 and 2.3, and the expectation values are below.

Similar approach can be used for the variance, though now more complicated expression arise. The definition of the heat capacity should be taken into account to reduce the amount of calculations,

$\langle \delta E_T^2 \rangle = \frac{\partial^2 \ln Q}{\partial \beta^2} = -\frac{\partial \langle E\rangle}{\partial T}\frac{\partial T}{\partial \beta} = k_\mathrm{B}T^2 C_V.$

$$\langle \delta E_T^2 \rangle = \frac{\partial^2 \ln Q(\beta)}{\partial \beta^2} = k_\mathrm{B}T^2 C_V$$

and then we find

$$\langle \delta\alpha_M^2 \rangle = \frac{M}{2}\left[\left(\frac{1}{m_\alpha}\frac{\partial m_\alpha}{\partial s} \right)^2 - \frac{1}{m_\alpha}\frac{\partial^2 m_\alpha}{\partial s^2} \right] + \langle \delta E_T^2\rangle_M \left(\frac{\beta}{\omega}\frac{\partial \omega(s)}{\partial s} \right)^2 - \langle E_T\rangle_M \frac{\beta}{\omega}\frac{\partial^2 \omega(s)}{\partial s^2}$$

with similar expressions to λ and γ. Finally, the expectation values and variances are (Herman et al., 1982, note the misprints there)

$$\langle \alpha_M \rangle = \frac{M}{2\beta} - \tfrac{1}{2}\langle E_T\rangle_M \qquad \langle \delta\alpha_M^2 \rangle = \frac{M}{2\beta^2} + \tfrac{1}{4}\langle \delta E_T^2\rangle_M - \frac{3}{4\beta}\langle E_T\rangle_M$$
$$\langle \lambda_M \rangle = \tfrac{1}{2}\langle E_T\rangle_M \qquad \langle \delta\lambda_M^2 \rangle = \tfrac{1}{4}\langle \delta E_T^2\rangle_M + \frac{1}{4\beta}\langle E_T\rangle_M$$
$$\langle \gamma_M \rangle = \frac{M}{2\beta} - \langle E_T\rangle_M \qquad \langle \delta\gamma_M^2 \rangle = \frac{M}{2\beta^2} + \langle \delta E_T^2\rangle_M - \frac{1}{\beta}\langle E_T\rangle_M.$$

First we note that $\langle E_T\rangle_M = M/(2\beta) - \langle \gamma_M\rangle$ as required by Eqs. (2.9) and (2.10). Furthermore, because $\langle \alpha_M\rangle = M/(2\beta) - \frac{1}{2}\langle E_T\rangle_M$ and $\langle \lambda_M\rangle = \frac{1}{2}\langle E_T\rangle_M$, this satisfies the virial theorem for the harmonic oscillator, $\langle M/(2\beta) - \alpha_M\rangle = \frac{1}{2}\langle E_T\rangle_M = \langle \lambda_M\rangle$, see Eq. (2.11). Because the total energy estimator, Eq. (2.10), is $\langle E\rangle_M = M/(2\beta) - \langle \gamma_M\rangle$, its variance is dependent only on the variance of γ_M, that is $\langle \delta\gamma_M^2\rangle$. Thus,

$\langle \delta E_T^2\rangle_M = \frac{\partial^2 \ln Q}{\partial f^2}\left(\frac{\partial f}{\partial R}\right)^2\left(\frac{\partial R}{\partial \beta}\right)^2 + \frac{\partial \ln Q}{\partial f}\left(\frac{\partial^2 f}{\partial R^2}\right)\left(\frac{\partial R}{\partial \beta}\right)^2.$

$$\langle \delta E^2\rangle_M = \frac{M}{2\beta^2} + \langle \delta E_T^2\rangle_M - \frac{\langle E_T\rangle_M}{\beta},$$

shows that the mean square fluctuation in the energy estimator, Eq. (2.10), as well as the kinetic energy, Eq. (2.7), increases as $o(M)$. This is because both $\langle \delta E_T\rangle_M$ and $\langle \delta E_T^2\rangle_M$ becomes independent of M when $M \to \infty$, as indicated in Fig. 2.5.

[6] Jean Baptiste Joseph Fourier, 21 Mar 1768– 16 May 1830 (Auxerre, Bourgogne, France–Paris).
[7] Pierre-Simon Laplace, 23 Mar 1749–5 Mar 1827 (Beaumont-en-Auge, Normandy, France–Paris)

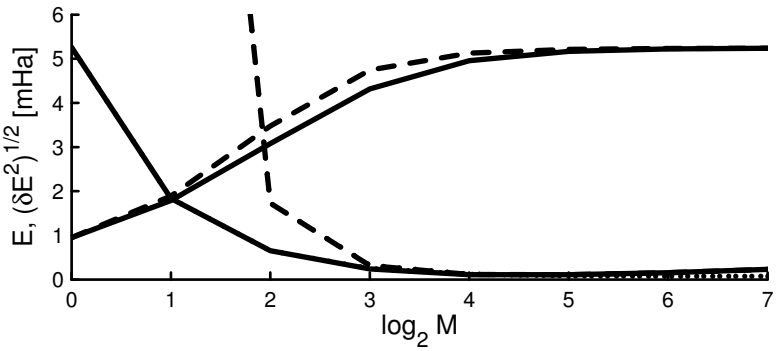

Figure 2.5: The energetics of harmonic oscillator (solid line), $T = 300$ K and $\omega = 0.0104816$ Ha$/a_0^2$. For the Trotter number $M = 1$ we find the energetics described by the classical equipartition theorem, $\langle E \rangle = 1/\beta$ and for approximately $M = 2^6$ we the fully converged quantum limit, given by Eq. (2.13). The standard deviation, $\sqrt{\langle \delta E^2 \rangle_M}$ is also drawn. Note that the standard deviation is increasing as $M \to \infty$. Furthermore, the same results with effective ω_{eff} are drawn (dashed line). The behavior is similar, but it reaches the quantum limit faster. The fluctuations of virial estimator (dotted line), however, seems to be bounded.

For the virial estimator we find that $\langle E_v \rangle_M = 2\langle \lambda_M \rangle$ and thus the fluctuations are

$$\langle \delta E_v^2 \rangle_M = 4\langle \lambda_M \rangle = \langle \delta E_T^2 \rangle_M + \frac{1}{\beta} \langle E_T \rangle_M .$$

This estimator is not so sensitive to Trotter number M, as indicated in Fig. 2.5, because the problem of subtracting two large numbers does not plague here anymore.

Fig. 2.5 shows also the benefit of using higher order Trotter expansion, as described in Sec. 1.4.2. It was shown that higher order expansion affects as a correction to the frequency in harmonic oscillator,

$$\omega_{\text{eff}} = \left(1 + \tfrac{1}{12}\tau^2\omega^2\right)\omega.$$

The effect is clearly visible but small.

The efficiency of estimators is widely studied. Giansati and Jacucci (1988) revisited the harmonic oscillator specially in Metropolis Monte Carlo scheme and found out that the correlation length is greatly dependent on the form of the estimator chosen. Cao and Berne (1989) studies further the efficiency between the energy estimators and between the different sampling methods. Chakravarty et al. (1998) compares the primitive and pair actions for more realistic cluster of 22 H_2 molecules, and Whitfield and Staub (2001) studies the uncertainty of path-integral averages. Thus, one should be careful when choosing the estimators, and be aware of the different problems that might arise.

TEMPERATURE EFFECTS IN FEW-PARTICLE SYSTEMS

...
Minä miekkonen vain sen tiedän
minä vain sekä muuan muu
ja lehdon lempivä kerttu
ja tuoksuva tuomipuu.
— Eino Leino

The last part of this thesis consists of the published papers concerning properties of electrons in quantum dots, Papers I and II (Sec. 3.1), some applications to surface physics with hydrogen atoms, Papers III and IV (Sec. 3.2), and molecular physics including quantum features with both, electrons and protons simultaneously, Paper V (Sec. 3.3). We have dealt mostly with temperature and quantum effects—effects that can be treated with path-integrals and that are hard to consider with other theoretical methods. Furthermore, we have been studied how the excited states can be extracted from finite temperature density matrix. Finally, we analyzed the validity of Born[1] –Oppenheimer[2] and non-adiabatic approximations.

3.1 DIMENSIONALITY EFFECT

Quantum dots are small man-made artificial atoms made usually from semiconducting materials. The size and shape of the confining potential can be adjusted to a large extent, and thus they might be important in novel semiconductor technology, also. Quantum dots consist of 10^3–10^9 atoms with possibly only a few charge carriers. These are subject to strong many-body effects.

[1]Max Born, Dec 11, 1882–Jan 5, 1970 (Breslau, Germany–Göttingen)
[2]J. Robert Oppenheimer, April 22, 1904–Feb 18, 1967 (New York–Princeton)

"How many bodies we need to have a *problem*? In Newtonian mechanics 3-body system was insoluble. General relativity and quantum electrodynamics proved that 2- and 1-body problems are insoluble. Within quantum field theories, the problem of 0-body became insoluble." (Mattuck, 1992, p. 1)

Note the method of Lyubartsev (2005) for the resolution of excited states.

The two electron system, considered in Papers I and II, is one of the simplest nontrivial quantum mechanical system. Nevertheless, some analytical results exist for the electrons in a symmetrical enough quantum dot, see Taut (1993) and Dineykhan and Nazmitdinov (1997). In addition to analytical results, there are a number of numerical results for harmonic two-electron quantum dots.

We studied how to extract the pure states from the thermally averaged density matrix that is obtained with path-integral method. Also, we studied the effect of dimensionality, that is how much the third dimension influences to the properties of quantum dots. This study is extended to the case of surfaces in Papers III and IV.

In Papers I and II, the quantum dot is assumed to be made of GaAs, with the electron effective mass $m^\star = 0.067 m_e$, with m_e being the free electron mass, and the dielectric constant $\epsilon = 12.4$ everywhere in the structure. Paper I describes a 2-dimensional harmonic quantum dot with confining strength $\hbar\omega = 1$ eV. Thus, the confinement is very strong corresponding to a QD of a few nanometers and a few hundreds of atoms, only. This servers, however, as a nice model and might even be realistic with new fabrication technologies.

The vertical unnormalized wave function for symmetrical double quantum well is (Gasiorowicz, 1996)

$$u(z)=\begin{cases}\cosh kz \text{ or } \sinh kz, \text{if } 0 < z < \frac{1}{2}b \\ A\sin qz + B\cos qz, \text{if } 0 < z - \frac{1}{2}b < W \\ C\mathrm{e}^{-kz}, \text{if } z > \frac{1}{2}b + W\end{cases}$$

where $k^2 = |E_z|/\lambda$, $q^2 = (V - |E_z|)/\lambda$, $\lambda = \hbar^2/2m^\star$, and the constants A, B and C are chosen to make the wave function and its derivative continuous and to normalize $u(z)$.

In the next paper, Paper II, the 2-dimensional system is enhanced by adding a double quantum well structure in the third dimension. The confining potential in the third dimension consists of two quantum wells of depth 300 meV, width of $W = 12$ nm and a barrier in between of width $b = 2.4$ nm. The confining strength was $\hbar\omega = 5$ meV, substantially lower than in the first paper. This system is taken from the experimental work of Pi et al. (2001).

Furthermore, in both cases, the exact Hamiltonian reduces to the center of mass and relative motion, and the relative motion must be determined numerically. The motion of CM is of the free-particle type, as usual, and thus the solution is known analytically.

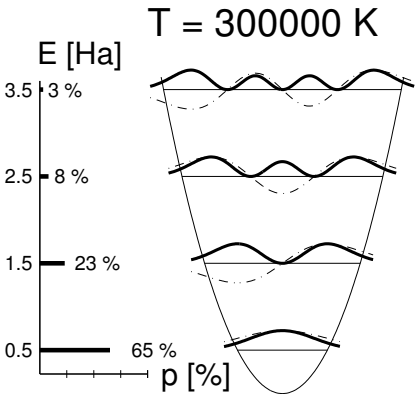

Energy states of harmonic oscillator ($m = 1$ and $k = 1$) together with respective Boltzmann probabilities at very high temperature.

3.1.1 FINDING PURE STATES

The path-integral density matrix is a finite temperature, mixed state, description of the quantum system. Thus, the mixed state energy $\langle E(\beta)\rangle$ at temperature $T = 1/(k_\mathrm{B}\beta)$, Eq. (2.9), is the Boltzmann weighted mean value of pure state eigenenergies E_i given in Eq. (2.12),

$$E(\beta) = \frac{\sum_i d_i E_i \mathrm{e}^{-\beta E_i}}{\sum_i d_i \mathrm{e}^{-\beta E_i}}.$$

This summation suggests, that the contribution of excited state energies E_i can be separated from the finite temperature energy, $\langle E(\beta)\rangle$ by some fitting procedure, assuming that the function $\langle E(\beta)\rangle$ is known.

See Grosche and Steiner (1995) for the list of systems for which $\langle E(\beta)\rangle$ is known.

Only for a few systems is $\langle E(\beta)\rangle$ known analytically; the free particle and har-

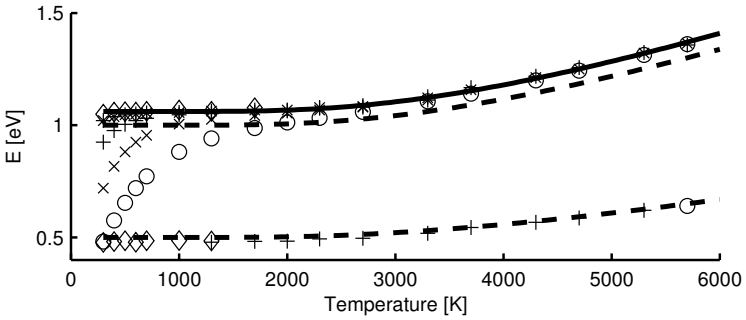

Figure 3.1: Mixed state energy as a function of temperature of the correlated two-electron system, simulated with Trotter numbers 8 ($\circ$), 16 ($\times$), 32 ($+$), 64 ($*$) and 128 ($\diamond$). The solid line is a fit to the functional form of $\frac{1}{2}\hbar\omega\coth\frac{1}{2}\hbar\omega\beta$ and the dashed lines show analytical single electron total and kinetic (potential) energies, respectively.

monic oscillator are shown in Part I. However, if we are able to simulate $\langle E(\beta)\rangle$ accurately enough, this should give us the pure state energies E_i. In principle, it should be possible to find the pure state densities $\rho_i(\mathbf{r})$ independently with the same procedure, and thus, find a verification of pure state energies E_i obtained here.

At low enough temperature we get only one or two states that contribute to the total energy, according to the Boltzmann factor. It implies that the fitting needs physically too high temperatures to obtain nonzero probabilities for higher states. However, when extracting more states, the lowest states can be fixed and thus resulting in a easier optimazion task.

One should note that the high temperature here is a computational tool, only, and have nothing to do with any realistic temperature related to quantum dots.

For the fitting procedure, we used Levenberg–Marquardt algorithm, which is explained in any textbook on optimization, or see Fletcher (1978) or Nash and Sofer (1996); the Gauss–Newton algorithm was not good enough. It is possible to find a few first pure states with G–N, but Levenberq–Marquardt was much simpler to use and more eigenenergies were found. L–M is so called trusted region algorithm, i.e., its trajectory stays in the region where the fit is good, discarding too long steps. This is achieved by choosing μ_k such that the coefficient matrix for $\boldsymbol{d}_k$ is positive definite and thus the quadratic approximation to nonlinear residual vector is valid.

The L–M-algorithm is following:
Minimize $||\boldsymbol{y}-\boldsymbol{g}(\boldsymbol{\theta})||^2$ where $\boldsymbol{y}$ is the $\boldsymbol{g}(\boldsymbol{\theta})$ is the model function with parameters $\boldsymbol{\theta}$.
First, linearize $\boldsymbol{g}(\boldsymbol{\theta})$ around point $\boldsymbol{\theta}_k$. Then
1. Choose the initial point $\boldsymbol{\theta}_0$
2. Solve $\boldsymbol{d}_k$ from
$\boldsymbol{g}'(\boldsymbol{\theta}_k)^T[\boldsymbol{y}-\boldsymbol{g}(\boldsymbol{\theta}_k)] =$
$[\boldsymbol{g}'(\boldsymbol{\theta}_k)^T\boldsymbol{g}'(\boldsymbol{\theta}_k)+\mu_k\boldsymbol{I}]\boldsymbol{d}_k$
3. Set $\boldsymbol{\theta}_{k+1}=\boldsymbol{\theta}_k+\boldsymbol{d}_k$
4. If the error is small enough quit, otherwise goto step 2.

The L–M algorithm is stable with respect to changes in starting point and temperature in the one-electron case. Thus, if the simulated energy $\langle E(\beta)\rangle$ is replaced by the analytical formula $\langle E\rangle = \frac{1}{2}\hbar\omega\coth(\frac{1}{2}\hbar\omega\beta)$ in optimization procedure, the pure one-electron eigenstates E_i can be found easily until $i\approx 7$. However, the optimization is sensitive to the accuracy of mixed state energy: if the analytical energies are rounded to two decimals, the fitting procedure does not work reliably anymore.

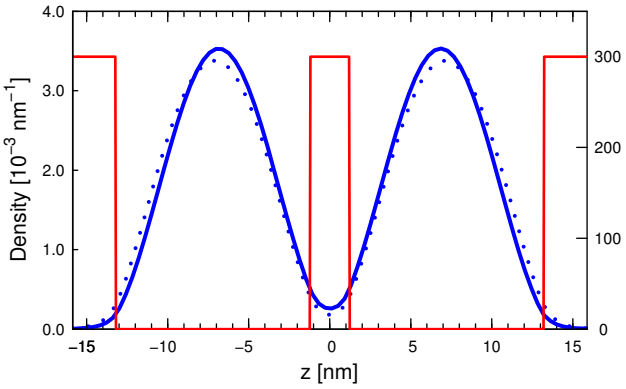

Figure 3.2: Analytical vertical (z) one-particle distribution functions at different temperatures in the confining potential of 300 meV. The probability distributions $\rho(z)$ are in arbitrary units but normalized to the same constant. The shown distributions are 10 K (solid) and 300 K (dotted).

The small M energies becomes zero at low T, thus failing in describing the quantum (kinetic) energy.

The fitting procedure leads to the two first excited energies 1.00 eV and 1.9 eV above the ground state.

The simulated interacting case energies are shown in Fig. 3.1 for different Trotter numbers $M = 8, \ldots, 128$ and temperatures. Also the equal contributions from the kinetic and potential energies are shown. From low-T fitting the ground state energy 1.06 eV is found for 2 interacting electrons in a 2 dimensional harmonic quantum dot with $\hbar\omega = 1$ eV. The high-T behavior is seen to be similar to the single electron case, though the analytical single-particle form probably cannot be assumed. However, a fit to that results in a scaling factor 0.48 for β.

3.1.2 DISTRIBUTIONS AND ENERGETICS

While the level spacing in vertical quantum problem is about 50 meV, in the horizontal harmonic oscillator it is 5 meV with the degeneracy increasing linearly in energy.

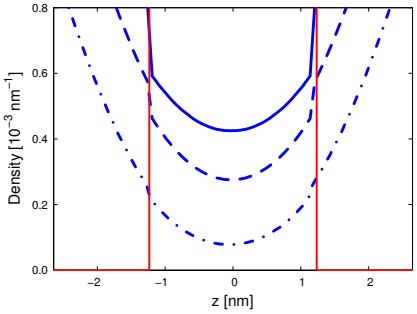

Trotter extrapolation error from simulations of a single electron with $(k_B\tau)^{-1} = (T \times M)$ = 6144 K, 20480 K and 61440 K. The distributions are from 3 K (solid), 10 K (dashed) 30 (dash-dotted).

The vertical confining potential together with density distributions are shown in Fig. 3.2. The confinement is one to two orders in magnitude stronger in vertical direction, resulting in essential differences in temperature response of the one-particle density. In Fig. 3.2 it is seen that only at 300 K a small shift of the density away from the center barrier takes place, resulting in decrease of tunneling there. The horizontal distribution, on the contrary, shows the strong temperature broadening, as expected.

The classical-to-quantum transition is clearly visible in projected one-particle distribution functions in the vertical (z) direction. The simulation is carried out at fixed temperature T with different Trotter number M, thus using various $\tau = \beta/M$. In the limit $\tau \to 0$ the path-integral formalism is exact, and when $\tau = \beta$, classical description is used, as explained in Part I. The quantum mechanics softens the external potential, as described in Part II, which is observed as discontinuities in the classical distributions. Similar behavior was observed in studies related to Paper V.

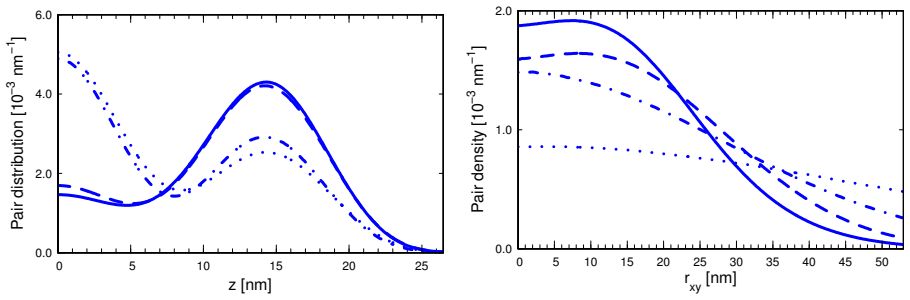

Figure 3.3: Projected horizontal (z) and vertical (xy) pair correlation function at various temperatures.

Turning the electron–electron repulsion on, i.e. adding one additional electron to the quantum dot, two expected main features emerges. First, the repulsion decreases the density, where it is high, by shifting it to the less occupied regions of space. Secondly, the correlation effects are the larger the lower the temperature.

Two effects should be seen. First, the temperature broadening, and second, the weak modifications due to the Coulomb repulsion, which tends to keep the electrons apart from each other.

The dimensionality effect or separability of the three dimensional system to one and two dimensional subsystems is now considered. The main question is: does the small but finite vertical extension (z) have an essential effect on the electronic structure in the lateral (xy) plane (Pi et al., 2001, Rontani et al., 1999). For the one-particle distribution the answer is obviously "no", because the one-particle distributions of the two-electron case and the single electron case do not differ and the latter is analytically separable to three dimensions. However, for the detailed two-electron distribution the answer is different as indicated by the low temperature pair correlation functions. Clearly, at low temperatures where the electrons occupy the center of the disc, see Figs. 3.3, the third dimension allows more freedom for both of the electrons simultaneously. However, increase of temperature allows occupation of lateral space further away, which seems to cover the quantum and correlation effects.

The same conclusions can be drawn from the correlation holes shown in Paper II, only, where the case is even more transparent: at temperatures 100 K and 300 K the presence of the second electron does not essentially effect on the dynamics of the first one. At lower temperatures (10 K and 30 K), however, a more conventional correlation hole is seen, both vertically and laterally.

ENERGETICS

The computational capacity becomes a limitation, at lower temperatures in particular.

Though we were able to reach sufficient convergence for the distributions, regarding the energetics we are only able to give rough estimates for some contributions.

Within the statistics, we are not able to find differences in the external potential

Table 3.1: Potential and interaction energetics for two interacting electrons in a quantum dot.

T [K]	$V_{\rm pot}$ [meV]	$V_{\rm vrk}$ [meV]
3	33.2	4.0
10	31.4	4.4
30	18.0	4.2
100	29.0	4.0
300	59.0	2.5

energies of one of the interacting electrons and one of the two noninteracting, see Table 3.1. The mutual Coulomb (repulsion) energy of the two electrons is about 4.0 meV independent of temperature. Surprisingly, this very same value is found for two interacting electrons and two noninteracting, We are not able to obtain estimates for kinetic energies, the main reason being the discontinuous external potential function.

3.2 TEMPERATURE AND COVERAGE EFFECTS OF H ATOMS ON NI SURFACE

E.g. peculiar adsorbate diffusion, EELS, LEED, photoemission or He scattering.

Hydrogen motion and interactions on metal surfaces are of interest both technologically and fundamentally. Hydrogen, being the lightest atom apparently seems to be simple, but it emphasizes the quantum effects. Furthermore, the mutual interaction between adsorbed hydrogen atoms may significantly alter the apparent temperature dependent properties of the system.

Impurities in the lattice, vacancies, other defects, relaxations or reconstructions, and most importantly at higher temperatures the thermal motion of the surface need to be taken into account in studies of real surfaces, see Auerbach et al. (1987), Daw and Baskes (1984), Jena et al. (1985), Puska et al. (1987).

Diffusion is convenient to study with path-integrals because the temperature is easily taken into account. However, this requires somehow different formulation than described here.

One of the early pioneers in applying PIMC to metals is Gillan (1987). However, most path-integral studies are formulated differently to study diffusion-related topics,see e.g. Mattsson and Wahnström (1997), Mattsson et al. (1993), Mattsson and Wahnström (1995).

3.2.1 MANY-BODY ALLOY POTENTIAL

The complexity of hydrogen behavior on a nickel surface arises from the explicit involvement of energy exchange due to phonons and other forms of excitations, defects, and strong interaction between the hydrogen and metal atoms. Only a

few theoretical methods are capable of treating these problems.

We adopt the many-body alloy (MBA) potential, see Zhong et al. (1991), derived from tight-binding theory of bulk materials as a starting point for the adsorbate–surface interaction. It offers a possibility for extensions to a description of both adsorbate–adsorbate interactions and metal surface dynamics at finite temperature. MBA is well suited for both single component and alloy bulk materials. The needed parameters can be fitted to *ab initio* or experimental data.

Other useful methods are *ab initio* DFT, EAM and TBTE, (Tersoff).

MBA has been used for H/Pd systems and for studies of the electronic and structural properties of small clusters (Grönbeck et al., 1997a,b), surfaces of metals, and dilute metal alloys (Zhong et al., 1992, and references therein).

The total (cohesive) energy of a crystal or a cluster is decomposed into individual atomic contributions E_i as

$$E_{\mathrm{T}} = \sum_i E_i, \tag{3.1}$$

where i runs over all atoms in the system and

$$E_i = E_i^{\mathrm{mb}} + E_i^{\mathrm{r}}$$

with E_i^{mb} being the many-body term and E_i^{r} is the (repulsive) pair potential. Several parametrizations can be found for the many-body term, see Brenner (1989) for examples. Zhong et al. (1991) based their expression on a parametrized tight-binding Hamiltonian: in a *one-electron* picture, the binding energy of atom i is given by

$$E_i^{\mathrm{mb}} = -\int_{-\infty}^{E_{\mathrm{F}}} (E - E_0) N_i(E) \mathrm{d}E$$

where N_i is the local density of states. Higher-order moments cannot be expressed in analytic form (Cleri and Rosato, 1993), and thus this is usually simplified by the second-moment approximation. The cohesive properties of transition metals originate from the d-band density of states, and it is assumed that these bands can be described by a s.c. *hopping* or *overlap integrals*. The hopping integrals are functions of the radial distance between atoms i and j, only, and thus the same holds for the band energies also. We may write

The experimental binding energies of transition metals appear to be roughly proportional to the average width of the DOS, $\sqrt{M_2}$.

$$E_i^{\mathrm{mb}} \propto M_2(i)^{1/2} = \left(\sum_{j \neq i} t_{ij}^2 \right)^{1/2} = \left(\sum_{j \neq i} \xi^2 \exp(-2q r_{ij}) \right)^{1/2}$$

where an exponential distance dependence of *screened* or *effective* hopping integral is assumed. The parameter ξ is an effective hopping integral and q describes its dependence on the relative interatomic distance. Both parameters are assumed to depend only on the interacting atomic species α and β.

The pair potential term (repulsive part), E_i^{r}, is parametrized as a pair-wise Born–Mayer potential

$$E_i^{\mathrm{r}} = \sum_{j \neq i} \epsilon \exp(-p r_{ij})$$

Born–Mayer form assumes that the internuclear potential U is $U(r) = a \exp(-br)$, $R_1 \leq r \leq R_2$ which is an experimental observation (Abrahamson, 1969).

Table 3.2: Many-body alloy (MBA) potential parameters for all atom pairs in Eq. (3.2).

X_α–X_β	$q_{\alpha\beta}$	$p_{\alpha\beta}$	$r_{0,\alpha\beta}$ [Å]	$\epsilon_{\alpha\beta}$ [eV]	$\xi_{\alpha\beta}$ [eV]
H–H	3.22	5.28	2.30	0.16	0.91
H–Ni	2.87	5.87	1.44	2.70	5.52
Ni–Ni	3.00	8.62	2.49	0.20	1.97

with an exponential distance dependence. This ensures the stability of the crystal together with the bonding term, E_i^{mb}. The parameter ϵ is related to the repulsion energy between two atoms and p should be related to the compressibility of the bulk metal, see (Cleri and Rosato, 1993) and Appendix A in Paper III.

Thus, we may conclude that the MBA total cohesive energy to be used in PIMC simulations as external potential is given by

The MBA cohesive energy resembles the more popular Sutton–Chen potential

$$E_i = -\epsilon c_i \sqrt{\sum_{j\neq i}\left(\frac{r_0}{r_{ij}}\right)^m} + \tfrac{1}{2}\sum_{j\neq i}\epsilon\left(\frac{r_0}{r_{ij}}\right)^n$$

as $r_{ij} \approx r_0$ because $\exp[-a(r_{ij}/r_0 - 1)] \approx (r_0/r_{ij})^a$.

$$E_i = -\sqrt{\sum_{j\neq i}\xi_{\alpha\beta}^2 \exp\left[-2q_{\alpha\beta}\Big(\frac{r_{ij}}{r_{0,\alpha\beta}} - 1\Big)\right]} + \sum_{j\neq i}\epsilon_{\alpha\beta}\exp\left[-p_{\alpha\beta}\Big(\frac{r_{ij}}{r_{0,\alpha\beta}} - 1\Big)\right]. \tag{3.2}$$

The more accurate model, the more parameters are needed. Groß et al. (1999) fitted 53 parameters in TBTE potential function to reproduce the *ab initio* PES and the qm nature of bonding properly.

The parameters are defined for atom pairs (i, j) of elements α and β, and are dependent on the interacting atomic species, only. Five parameters for each different pair are needed. These are the attraction due to overlapping orbitals $\xi_{\alpha\beta}$ and the pair-wise repulsion energy $\epsilon_{\alpha\beta}$, both given at the equilibrium distance $r_{0,\alpha\beta}$. The distance dependence of attractive and repulsive parts are scaled by the parameters $p_{\alpha\beta}$ and $q_{\alpha\beta}$, respectively.

MBA PARAMETERS FOR NI–NI, NI–H AND H–H INTERACTIONS

$a = 3.52$ Å, $r_0 = 2.49$ Å, $E_{\mathrm{coh}} = -4.44$ eV and $B = 1.17$ eV/Å^3.

The Ni–Ni fitting can be done to bulk properties, for which we use the data adopted from Sutton and Chen (1990) with the supplement that the coordination number in the fcc lattice is $z = 12$. Since this set of data still leaves us with one free parameter, we utilize the Sutton–Chen parametrization to start with, see Sutton and Chen (1990) for details. The scaling parameter for attraction is $m = 6$, which corresponds to $q = 3.0$, see Appendix in Paper III. Using this value for q and bulk fitting, we obtain p, ξ and ϵ. The values are given in Table 3.2.

$E_{\mathrm{ads}} = 2.8$ eV, $r_a = 0.5$ Å, $E_{\mathrm{barr}} = 0.14$ eV.

We fit the Ni–H MBA potential to the data given by Mattsson et al. (1997), where adsorption of H on Ni(001) surface has been studied with an EMT-type model potential whose parameters are fitted to *ab initio* potential energy surface. The fitted quantities are the adsorption energy of the hollow site, the equilibrium distance from the surface at hollow site and the energy barrier between the hollow sites through the bridge site.

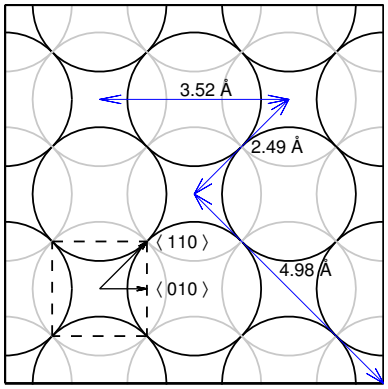

Figure 3.4: Simulation supercell of Ni(001) surface (of FCC lattice, $a = 3.52$ Å) schematically, surface and subsurface layer atoms indicated by black and grey circles, respectively. One of the 4-fold hollow sites is designated by the dashed square and the high symmetry directions along the surface are shown. The three possible hollow site distances (within the "periodical" simulation cell) are depicted.

The fitted parameters for H–Ni interaction are given in Table 3.2. These give exact values for the chosen adsorption properties, but rather useless values for the dissociation energy and the force constant of the free HNi molecule; the *ab initio* calculations of Bagus and Björkman (1981) give somehow different results. Thus, fitting the surface properties leads to a parametrization that does not describe satisfactorily the HNi molecule.

$E_d = 5.6390$ eV, $k = 45.7780$ eV/Å^2. *Ab initio* values are $E_d = 3.1$ eV, $r_0 = 1.47$ Å and $k = 13.67$ eV/Å^2.

For the H_2 dimer in the MBA scheme we adopt the parameters from Zhong et al. (1991), giving the binding energy as -4.95 eV at bond length 0.9 Å. We note, that the parameters are not fitted to describe the free H_2 molecule but the one adsorbing onto on a transition metal surface.

For the free hydrogen molecule $E_{\text{bind}} = -4.747734185194$ eV and $r_0 = 0.74143$ Å (Sims and Hagstrom, 2006).

PERFORMANCE OF THE MBA POTENTIAL

First, we used a model consisting of N atoms with one quantum mechanically behaving hydrogen adsorbate on a surface of $N-1$ classical nickel atoms at either zero or at finite temperature, see Paper III. The hydrogen cut-off radius for MBA potential is essentially 8 Å, corresponding to $N \approx 100$. For nickel atom dynamics some finite-size effects may remain as a compromise with computational labor.

We take N large enough to give the hydrogen energetics from Eqs (3.1) and (3.2) on an infinite Ni substrate.

However, for Paper IV, when more hydrogen atoms and thus hydrogen–hydrogen interaction is taken into account, our model was changed to a periodic slab of six layers of Ni atoms, eight atoms in each layer. The lateral periodicity is two lattice constants, $2a$, see Fig. 3.4 for more details.

Due to the finite-size supercell, in $\langle 100 \rangle$ and $\langle 110 \rangle$ directions there are only two and one hollow site distances, respectively. Thus, the finite simulation cell is different from the infinite one.

Fig. 3.5 shows the classical hydrogen equipotential curves at zero temperature in

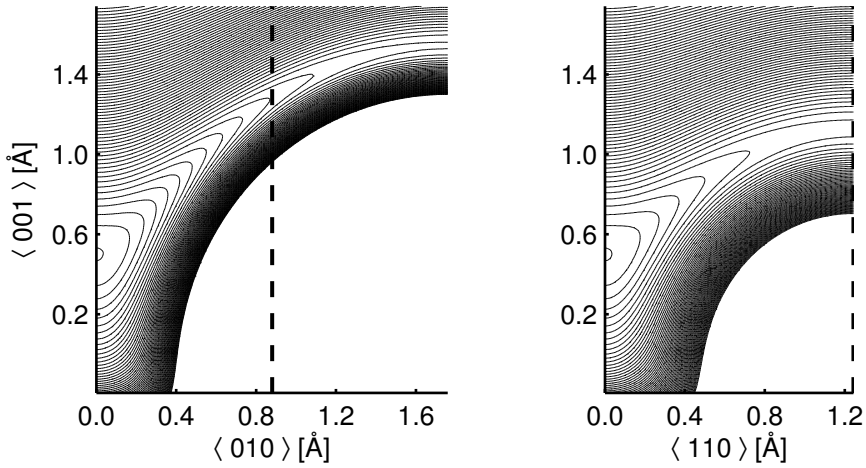

Figure 3.5: Equipotential contour lines of the H atom MBA potential energy hypersurface in two perpendicular planes of rigid (001) surface of Fig. 3.4. from the hollow site to (a) the top site direction $\langle 010 \rangle$ and (b) the bridge site direction $\langle 110 \rangle$. The minimum at z = 0.5 Å corresponds to the adsorption energy 2.8 eV and line spacing is 25 meV.

two high-symmetry planes perpendicular to the surface. Potential to the $\langle 110 \rangle$ direction is identical with that of Mattsson et al. (1997). We see that the topsite barrier between hollow sites is about a double (0.3 eV) of that of the bridge site (0.14 eV). Thus, the H–Ni interaction is described satisfactory.

As a good reference test for the MBA parameters of H–H interactions we consider the high-symmetry potential-energy hypersurfaces conventionally used to illustrate the dissociation dynamics of H_2 molecule coming down to the perfect and rigid surface. Due to their typical shape they are called *elbow plot*s. We choose the DFT calculations of Kresse and Hafner (2000) to compare with.

We present some of MBA elbow plots in Fig. 3.6. These should be compared to those of Kresse *et al*, and also, to the equipotential contour lines of single hydrogen atom on Ni surface, Fig. 3.5. We see that MBA surprisingly successfully transforms the single atom *potential energy surface* (PES) to the various elbow plots as a consequence of H–H interaction.

In our case the most important regions of the elbow plots to consider are the hollow sites shown in Fig. 3.6, where hydrogen adsorbates almost exclusively dwell in thermal equilibrium. Fig. 3.6a shows the PES for H_2 molecule dissociation above the bridge site towards the hollow sites (HBH). A small physisorption energy minimum of 20 meV is found in agreement with DFT data of Kresse (2000). We evaluate for the dissociation barrier a value of 140 meV, as the DFT barrier is 110 meV.

The dissociation energy of free H_2 is too large by about 0.5 eV. Therefore, the chemisorption energy becomes too small by about the same amount.

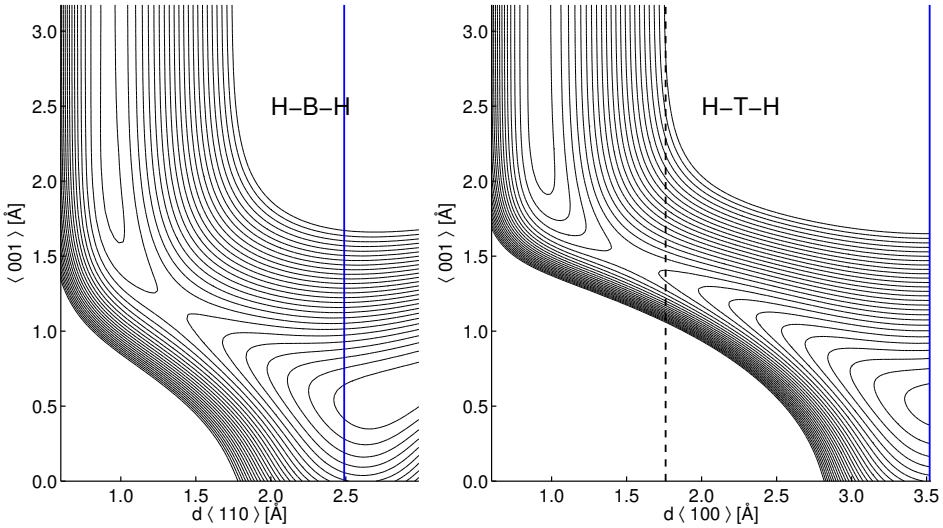

Figure 3.6: Elbow plots for H_2 dissociation to hollow sites from MBA potential. High symmetry cases in planes {110} (on bridge site) and {010} (on top site) are shown on the left and right, respectively. Line spacing is 100 meV. Note, that the minimum is about 100 meV higher in the former case due to the difference in remaining indirect H–H interaction, see text.

The elbow plot above the top site towards hollow sites (HTH), Fig. 3.6b, presents the same features as HBH. The only essential difference in these two cases is the H–H repulsion. H atoms in hollow sites further apart do not essential interact. We note that the dissociation barrier is not described correctly but it is not relevant for the equilibrium distribution of H adsorbates at low coverages. For a collection of H_2 molecule physisorption, dissociation barrier and chemisorption energetics for the elbow plots see Table 3 from Paper III.

The effect of wrong dissociation energy of H_2 molecule is clearly seen in Fig. 3.6b (hth) where a dissociation barrier of 350 meV emerges, opposed to DFT data, which shows a -230 meV dissociation barrier.

It is interesting to test MBA performance in the description of surface relaxation. By allowing the two uppermost Ni layers to relax, their separation is changed by $\Delta z_{12} = -0.120$ Å, which is close to the DFT result -0.116 Å (Kresse and Hafner, 2000). Also, for the second layer separation change we get $\Delta z_{23} = -0.08$ Å, a negative value indicating a smaller layer separation. The corresponding DFT value is $\Delta z_{23} = 0.04$.

As a conclusion, we find MBA with the given parameters capable of describing a single and two interacting H atoms on a Ni surface. Furthermore, it seems to describe correctly many other features of the system that are not relevant or needed in the present study.

We assume the validity of MBA for higher coverages.

3.2.2 ADSORBATE DISTRIBUTIONS

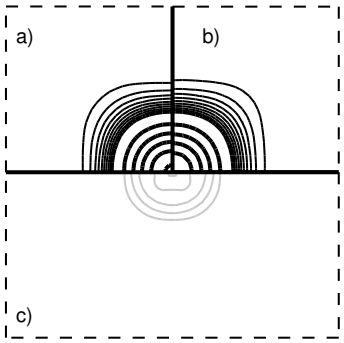

H distributions at the hollow site of rigid substrate shown in Fig. 3.4. The contours present the density projected onto the surface plane at (a) 100 K, (b) 300 K and (c) the difference of the two ((b)−(a)). The thin and thick lines show densities $0.5, 1.0, \ldots$ and $5, 10, \ldots$ atoms/(surface unit cell); and the black and grey lines stand for positive and negative values, respectively.

The hydrogen quantum distribution in the hollow site at low coverages and low temperatures does not strongly depend on the actual temperature or the coverage. It has been found to be rather similar to that at zero Kelvin, see Mattsson et al. (1997), Puska et al. (1983) or Puska and Nieminen (1985). Indeed, rise of the temperature just slightly spreads out the distribution and the difference between the two almost vanishes. Also the isotope effect is studied. Deuterium is clearly more localized and behaving more "classical".

The classical distribution and its temperature dependence is demonstrated in the figure. The quantum delocalization is substantial, and relatively the larger the lower the temperature, as expected. We see that only at 300 K the classical thermal spreading conceals the quantum delocalization. Furthermore, the classical distributions are more bridge direction oriented compared with the quantum case, where tunneling allows more circular shape.

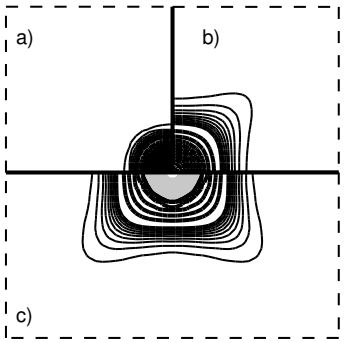

The "classical H atom" distributions.

The case of finite temperature substrate in thermal equilibrium with the adsorbate is also considered. Though, the RMS displacements of substrate atoms do not differ too much at 100 K and 300 K temperatures, the resulting adsorbate distributions do, as is seen by comparison of Figs 3 and 6 in Paper III. At 100 K the distributions seem to be almost identical, whereas at 300 K they are clearly different. This reveals strong temperature dependence of the distribution, that can be expected to influence the adsorbate diffusion dynamics.

On the rigid surface the temperature dependence is weaker than the isotope effect, whereas it is strong for the classical adsorbate, but the largest effect on distributions arises from the finite temperature substrate dynamics in all cases as can be seen from the vertical distributions, shown in Paper IV. These turn out to be modified Gaussians with the width of about 0.4 Å and mean values being equal to the maxima at around 0.5 to 0.65 Å, except for some of the classical cases. The mean height coincides with the previously reported results, 0.6 Å Puska and Nieminen (1985) and Mattsson and Wahnström (1995). Furthermore, we obtained similar results with higher hydrogen coverages, too.

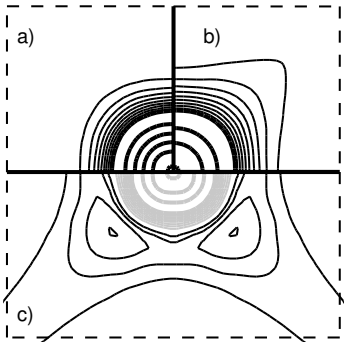

The hydrogen atom distributions in thermal equilibrium with the same finite temperature Ni surface.

Thus, as a conclusion for one-hydrogen distributions, we might say that we find a strong quantum delocalization of the adsorbate at 100 K, and that the finite-temperature surface dynamics effects only little on distribution of the quantum adsorbate at 100 K. At room temperature the case is totally different. In the following, the quantum case with higher coverages is considered in more detail. Temperature and quantum effects and also the H–H interactions are considered. The study for the classical case can be found from Paper IV.

At $T = 100$ K, the adsorbates are lying in the "circular ground state", exhibiting harmonic confinement. It should be noted, that at $T = 100$ K the distributions of coverages $\theta = 2/8$ and $\theta = 3/8$ are almost identical. Thus, the adsorbate–

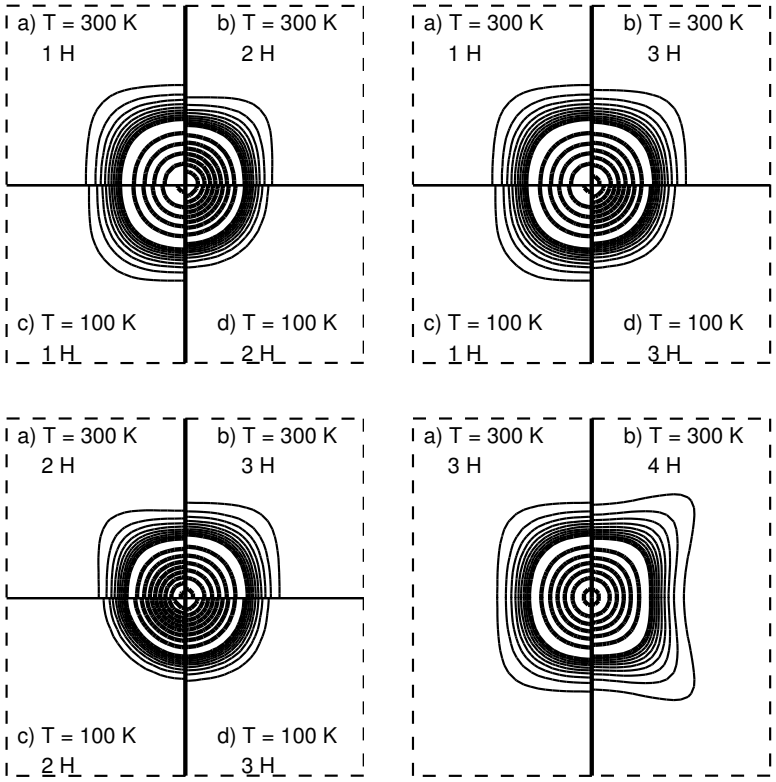

Figure 3.7: One-particle quantum distribution in the hollow site in case of adsorbate coverages $\theta = 1/8, 2/8, 3/8$ and $4/8$ in the simulation cell and for temperatures 100 K and 300K. The equidensity contours present the three dimensional density projected onto the surface plane. The thin and thick lines show densities $0.5, 1.0, 1.5, \ldots$ and $5, 10, 15, \ldots$ atoms/(surface) unit cell.

adsorbate interaction is rather small in both cases, though the pair correlation function differs.

The "classical hydrogen adsorbates" show more pronounced temperature effect. It is due to the absence of zero-point vibration. The lateral distributions of quantum and classical adsorbates at room temperature are quite similar, the largest difference being that the classical distributions are more bridge-direction oriented.

Only at coverages $\theta \geq 4/8$ the lateral distribution of quantum adsorbates is profoundly different from zero-kelvin distributions, see subfigure in low-right corner in Fig. 3.7, showing more towards bridge-site orientation. This may be a reflection of attractive interaction, see Wong et al. (1995) of H adsorbates at HTH configuration, already depicted in Fig. 3.6b.

The classical hydrogen pair correlation distributions are similar to those of quantum adsorbates, the only essential difference being that classical peaks are broader.

The pair correlation functions of the distributions, see Paper IV, show that all hydrogen adsorbates tend to reside apart from each other which, again, is an indication of H–H repulsion. There is no molecular adsorption state at $T = 300$ K or $T = 100$ K, a result observed for $T = 80$ K by Mårtensson et al. (1986). The maximum values of pair correlation functions are obtained at hollow-site distances, 3.5 Å and 5.0 Å.

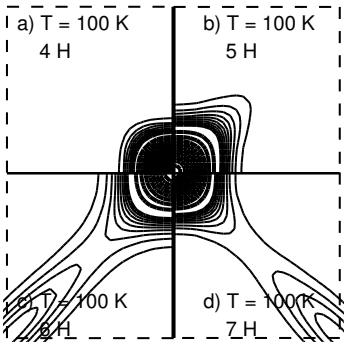

"Classical hydrogen" distributions of higher coverages. Here, only temperature $T = 100$ K is shown, because at higher temperatures the system becomes unstable. This is the case for coverage $\theta = 7/8$ even at $T = 100$ K.

3.2.3 ADSORBATE ENERGETICS

Evaluation of energetics turns out to be a real computational challenge. Although, the distributions seem to converge faster by visual judgment, those above have been evaluated from the fully converged equilibrium. For the energetics, below, with chosen Trotter number $M = 64$ we were able to acquire data enough to make the statistical error bars negligible with respect to the convergence in Trotter number.

For the case described in Paper III, that is, with one hydrogen atom only, the PIMC potential and kinetic energies are relatively close to each other in both cases pointing to the harmonic oscillator like potential with $\hbar\omega = 120$ meV. However, the potential is flat in all directions at its minimum with smaller force constants where $\hbar\omega$ is below 100 meV, see Fig. 3.6.

This gives energies 180 meV and 183 meV, with $\langle E \rangle = \frac{1}{2}\hbar\omega \coth(\frac{1}{2}\hbar\omega\beta)$, Eq. (2.13).

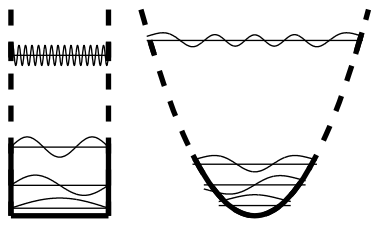

Energetics of potential well and harmonic oscillator compared. For H/Ni system, the force constant is below $\hbar\omega = 100$ meV in all directions expressing a potential between these two.

The interaction energy between hydrogen atoms is more difficult to estimate, because the MBA potential does not involve pair interactions. To estimate that, we used the total MBA potential of N hydrogen adsorbates energy obtained directly from simulations, by Eq. (2.4), and the single-adsorbate potential energy $E_{\mathrm{pot},1}$ of the 3-dimensional density function $\rho(\mathbf{r})$ of N hydrogen adsorbates as described in Eq. (2.5) where $V(\mathbf{r})$ is taken to be single-adsorbate energy term, see Eq. (3.2). By comparing these two estimates we are able to find an approximation to the interaction energy between H adsorbates.

The kinetic energy is estimated via virial the theorem, but as a simplification, we

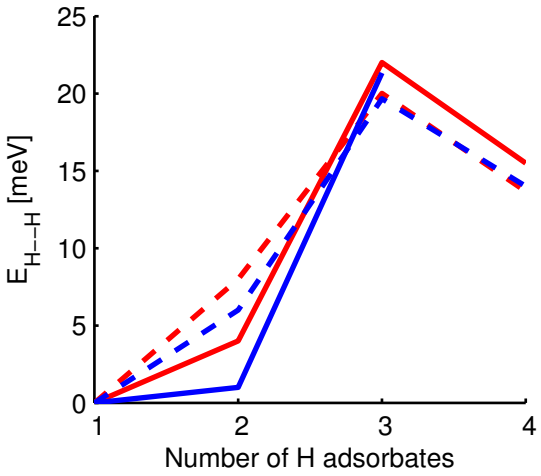

Figure 3.8: Total interaction energy of the hydrogen adsorbates on Ni surface. The solid line is for $T = 100$ K and the dashed for $T = 300$ K. Classical results are the lower (red), quantum statistical results are the upper (blue). The statistical error bars are hidden in the line width.

neglected the H–H interaction. Thus, the approximation is written as

$$E_{\text{vir},1}(\beta) = \frac{1}{2}\langle \mathbf{r} \cdot \nabla V_1(\mathbf{r}) \rangle_{\rho(\mathbf{r})}.$$

This gives a good approximation as long as the H–H interaction is small, which is true for long-distance adsorbates on surface. From the pair correlation function, we conclude that the energetic estimates here are valid for at least H_2 and H_3. The total energy for single-adsorbate system is then $E_{\text{tot},1} = E_{\text{pot},1} + E_{\text{vir},1}$. For the interacting system, by replacing the kinetic energy term with its single-adsorbate counterpart, we get the total energy

$$E_{\text{tot},N} = E_{\text{T}} + E_{\text{vir}} \approx E_{\text{T}} + E_{\text{vir},1},$$

where E_{T} is given in Eq. (3.2), and thus, by writing the total energy in the form $E_{\text{T}} = E_{\text{pot},1} + \frac{1}{2}(N-1)NE_{\text{H–H}}$ we get an approximation for the interaction energy $E_{\text{H–H}}$ of hydrogen adsorbates.

The interaction part of the potential term, Fig. 3.8 strongly depends on the number of adsorbates. The interaction energy increases from a few meV with 2 adsorbates to 22 meV with 3 hydrogen adsorbates in accordance with the above discussion of pair correlation function and energies in Paper IV. Only a small temperature dependence can be found. Quantum and classical interaction energies are rather similar.

3.3 ELECTRON–PROTON COUPLING

There is a number of phenomena in molecular and chemical physics which are influenced by the quantum behavior of both nuclei and electrons, rovibrational dynamics being a good example. In case of light-mass nuclei, protons in particular, treatment of the quantum nature of the nuclei is essential. The last paper of this sheaf, Paper V, shows how the quantum mechanics with path-integrals can be applied to both, nuclei and electrons simultaneously.

The path-integral formalism allows us to evaluate the density matrix of the full three-body quantum dynamics in a stationary state and finite-temperature. This is what we call "all-quantum" (AQ) simulation. Furthermore, the electronic part only is evaluated as a function of internuclear distance in the spirit of BO approximation, and the adiabatic nuclear dynamics is evaluated in the BO potential curve. Also, we have demonstrated the use of method of extrapolating the finite Trotter number M to infinite.

3.3.1 PSEUDOPOTENTIAL OF THE ELECTRON

Note the remarks in Fig. 2.1. It was shown that by using high enough Trotter number, $M \approx 2^{15}$, the cut-off radius of hydrogen potential can be made rather small, and the pseudo-potential can be neglected.

The attractive Coulomb potential makes some problems in path-integral scheme, as described earlier, and thus we choose to use a pseudopotential instead of true Coulombic. The pseudopotential is described in Corso et al. (1996) and is of the form

$$V_{\mathrm{PP}}(r) = -\frac{\mathrm{erf}(\alpha_c r)}{r} + (a + br^2)e^{-\alpha r^2}. \tag{3.3}$$

Note that the erf function is the cumulant version of hydrogen atom potential, see Thijssen (2000) or Ceperley (1995) with proper choice of α_c. Here, however, α_c and other parameter are fitted to generate the exact ground state energy of hydrogen atom and the wave function accurately outside a cut-off radius of about $0.6\,a_0$. The parameters are $\alpha_c = 3.8638$, $\alpha = 7.8857$, $a = 1.6617$ and $b = -18.2913$. Because the bond length of H_2^+ is about $2\,a_0$, it is expected that bonding of the hydrogen molecule ion becomes properly described.

3.3.2 SPECTROSCOPIC CONSTANTS

The spectroscopic constants of H_2^+ and D_2^+ are obtained as introduced in Alexander and Coldwell (2005). In atomic units they read

$$B_{\mathrm{e}} = \frac{1}{2\mathrm{I}} = \frac{1}{2\mu R^2},$$
$$\omega_{\mathrm{e}} = \Big(\frac{1}{\mu}\frac{\mathrm{d}^2 E}{\mathrm{d}R^2}\Big)^{1/2},$$

$$\omega_{\mathrm{e}} x_{\mathrm{e}} = \frac{1}{48\mu}\Big[5\Big(\frac{\mathrm{d}^3E/\mathrm{d}R^3}{\mathrm{d}^2E/\mathrm{d}R^2}\Big)^2 - 3\frac{\mathrm{d}^4E/\mathrm{d}R^4}{\mathrm{d}^2E/\mathrm{d}R^2}\Big]$$

and

$$\alpha_{\mathrm{e}} = -\frac{6B_{\mathrm{e}}^2}{\omega_{\mathrm{e}}}\Big[\frac{R}{3}\frac{\mathrm{d}^3E/\mathrm{d}R^3}{\mathrm{d}^2E/\mathrm{d}R^2} + 1\Big].$$

Insteadof determining these constants at the equilibrium distance only, as is done in Alexander and Coldwell (2005), we evaluate expectation values from the distribution of nuclei, e.g. for the rotational constant,

$$B_{\mathrm{e}} = \frac{1}{2\mu}\int g(R)\frac{1}{R^2}\mathrm{d}R,$$

where the pair correlation function $g(R)$ is normalized to unity. The other spectroscopic constants are evaluated similarly.

Within the BO approximation of diatomic molecules the corrections to electronic energies due to rovibrational motion of the nuclei can be evaluated from a Dunham polynomial (Dunham, 1932)

$$E_{vJ} = -D_e + \omega_{\mathrm{e}}(v+\frac{1}{2}) - \omega_{\mathrm{e}}x_{\mathrm{e}}(v+\frac{1}{2})^2$$
$$+B_{\mathrm{e}}J(J+1) - \alpha_{\mathrm{e}}J(J+1)(v+\frac{1}{2}) + \ldots,$$

where v and J are vibrational and rotational quantum numbers, respectively, and B_{e}, ω_{e}, $\omega_{\mathrm{e}}x_{\mathrm{e}}$ and α_{e} are the spectroscopic constants.

3.3.3 RESULTS

First, the electronic part only is evaluated as a function of internuclear distance in the spirit of BO approximation. Secondly, the adiabatic nuclear dynamics is evaluated in the BO potential curve. Finally, H_2^+ is treated fully non-adiabatically with the AQ simulation. These allow us to demonstrate the non-adiabatic electron–nuclei coupling by a projection of the AQ dynamics onto the adiabatic approximations.

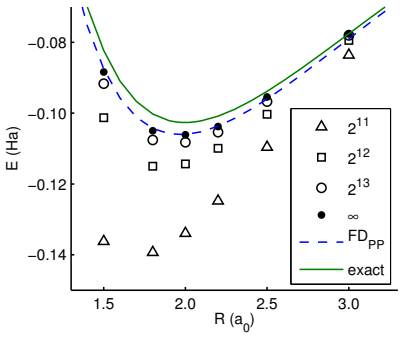

H_2^+ potential curves with different Trotter numbers, finite difference calculation with the pseudopotential and with exact e^-–p^+ potential. The PP reproduces the hydrogen atom energy exactly, a small error results in binding of another proton to form H_2^+.

First, we demonstrate that path-integral Monte Carlo method and the pseudopotential reproduces the potential curve of H_2^+. Thus, the nuclei are held fixed, i.e. the Born–Oppenheimer approximation, during the simulation process. We note that the Trotter number has to be at least 2^{13} in order to find the minimum of the potential curve at the nuclear separation $R = 2.0\ a_0$. The extrapolated values are in good agreement with the potential curve $\mathrm{FD_{PP}}$, and there is almost a perfect match at $R = 2.0\ a_0$, where the value of the extrapolated dissociation energy is $0.1061(2)$ Ha.

Second, we consider the quantum dynamics of the nuclei only (QN), for which convergence with respect to Trotter number is found at $M \geq 2^6$. Average nuclear separation of $2.019(1)\ a_0$ for H_2^+ and $2.007(2)\ a_0$ for the isotope D_2^+ is found with $M \geq 2^6$.

Difference in the bond length of H_2^+ between the adiabatic electron and adiabatic nuclei simulations is $0.019\ a_0$. Centrifugal contribution to this, the difference between one and three dimensional simulations of the nuclei, is $0.009(1)\ a_0$, which unexpectedly is about twice as much as the harmonic approximation. The anharmonic contribution, i.e. difference between total and centrifugal distortions, is $0.010(1)\ a_0$. Lounila and Rantala (1991) showed that anharmonic effects in the H_2 molecule contribute about the same amount to total distortion as the centrifugal force, which turns out to be the case here, too.

By inspecting the extremum values of the energy of harmonic oscillator $E_J(r) = \frac{1}{2}k(r-r_{\mathrm{e}})^2 + J(J+1)/2\mu r^2$ the effects of centrifugal distortion can be seen. Thus, $\Delta R = 4B_{\mathrm{e}}J(J+1)/(\mu\omega_{\mathrm{e}}^2 R_{\mathrm{e}}^2)$, where R_{e} is the equilibrium distance. At finite temperature the rotational energy states should be weighted by the Boltzmann factor. Using the spectroscopic constants (Alexander and Coldwell, 2005) and temperature of 300 K we obtain $\Delta R = 0.0043\ a_0$.

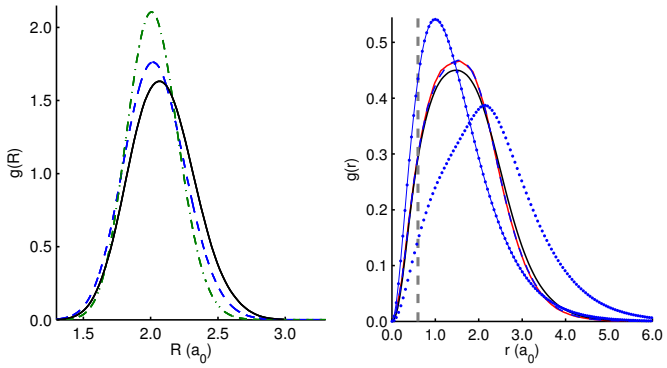

Figure 3.9: (Color online) Nuclear and electron–nucleus pair correlation functions: Left: H_2^+ AQ (solid), H_2^+ QN (dashed) and D_2^+ QN (dash-dotted). Right: AQ (solid, second lowest curve), AQ projection to $R \approx 2.0\ a_0$ (solid) and BO at $R = 2.0\ a_0$ (dashed). The latter two almost coincide. Dashed vertical line indicates the size of the pseudopotential core, $r = 0.6\ a_0$. Corresponding pair correlation functions for hydrogen atom (dotted line) and H_2^+ (dotted) obtained by using the analytical ground state wave function of hydrogen atom are also shown.

A Morse potential, Morse (1929), fitted to the FD_{PP} potential curve is used in the evaluation of the spectroscopic constants. This is justified because the nuclear simulations and analytical Morse wave function (ter Haar, 1946) calculations coincide. The spectroscopic constants of H_2^+ are close to those given by Alexander and Coldwell (2005), which have been determined at the equilibrium distance of the nuclei, only. We note that the spectroscopic constant obtained from PIMC simulations are close to those "exact" values, see Alexander and Coldwell (2005) for example.

One should note that variational and diffusion Monte Carlo methods are used when high accuracy in energy is needed, see Sims and Hagstrom (2006) for example.

Third, the non-adiabatic "all quantum" dynamics is considered. The finite size of quantum nuclei affects to the dissociation energy; the difference in dissociation energies of AQ and the 3D QN H_2^+ simulations is 0.00097 Ha, which is about $k_B T$ revealing additional electronic energy degrees of freedom in the first. Furthermore, the average nuclear separation is $0.056\ a_0$ larger than that in the QN simulation.

In Fig. 3.9 BO and AQ electron–nucleus pair correlation functions are compared. AQ projection onto the BO bond length, $R = 2.0\ a_0$, and BO results coincide, which indicates that the adiabatic BO approach for the electron dynamics is sufficient. Thus, it seems that the electron–nuclei coupling effects are more clearly seen in the dynamics of the nuclei. As one might expect, there is a noticeable difference between the AQ and the BO electron–nucleus pair correlation functions due to varying bond length.

A projection of the AQ simulation to a potential curve of the nuclei is constructed with the help of the known solutions to the Morse potential. The distribution

from the Morse wave function is fitted to the pair correlation function of the AQ simulation. The three-body system is then presented by an effective two-body potential. The projected potential curve shows clear differences in the dynamics of the nuclei between BO and AQ simulations. The minima of the potentials are set to zero: the difference in the dissociation energies between BO and the AQ projection is about 0.036 Ha and the shift in the equilibrium distance is $0.036\ a_0$. All this indicates that an effective Morse potential is not capable of describing non-adiabatic effects correctly.

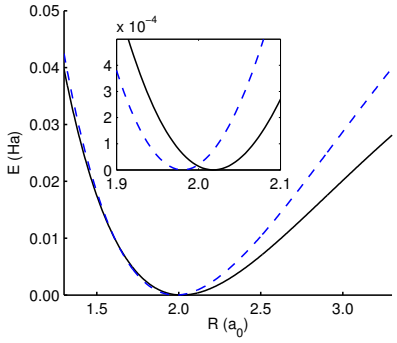

H_2^+ potential curves: Morse potential fitted to FD_{PP} (dashed) and the effective Morse potential obtained from the projection of the AQ simulation (solid), see the text for details. Corresponding nuclear pair correlation functions are shown in Fig. 3.9. The shift in the bond length is $0.036\ a_0$.

CONCLUSIONS

The path-integral Monte Carlo method is shown to be applicable to a wide variety of quantum mechanical problems. The method implicitly includes the Boltzmann summation, resulting in a finite temperature density matrix. Furthermore, the correlation between the particles are readily taken into account. PIMC offers a finite-temperature approach together with a transparent tool to describe the correlations between the particles involved. This method is applied the to nanophysics, surface science and molecular physics, and used to extract the finite temperature behavior and correlation effects between particles in those systems.

First, in the case of quantum dots, an expected temperature broadening of the one-electron distribution is found, the effect being slightly smaller for correlated electrons than for the single one. Coulomb correlation of the two electrons is analyzed in terms of pair correlation functions and correlation holes. A detailed inspection of these reveals differences in the nature of correlation at different temperatures. Generally, the correlations become more important at lower temperatures. At higher temperatures the thermal broadening in the mixed quantum state description screens the correlation effect efficiently. Furthermore, it is also demonstrated how (physically unreasonably) high temperature simulations and the resulting mixed state data can be used to resolve the pure quantum state properties.

Second, adsorbate distributions and energetics of hydrogen adsorbates at nickel surface are determined at two temperatures, 100 K and 300 K, to trace the temperature dependencies. To describe the adsorbate–substrate interaction and those between substrate atoms we use the tight binding derived many-body-alloy potential. The few parameters of the potential are fitted to the adsorption energetics and geometries from DFT calculations.

On the rigid Ni surface, we find strong quantum delocalization of the adsorbate at 100 K, the classical adsorbate being significantly more localized in terms of distribution and energetics. At room temperature the extent of classical distribution approaches that of the quantum case, but a clear difference in energetics remains. For low coverages, $\theta \leq 3/8$, the distributions of classical adsorbates are more bridge-site oriented, but at coverage $\theta = 4/8$ the lateral distribution of classical and quantum cases are rather similar. The quantum effect is mainly due to zero point effects and tunneling towards Ni atoms in $\langle 100 \rangle$ directions.

The finite temperature surface dynamics seems to affect only a little the distri-

bution of the quantum adsorbate at 100 K. At room temperature the substrate dynamics has a clear effect on both as compared to the rigid surface case. Furthermore, the substrate atom dynamics seems to make the strongest contribution to the temperature dependence of the H/Ni(001) system properties and phenomena considered here.

Third, a three-body quantum system, the hydrogen molecule ion, is revisited, once again. We aim at tracing the electron–nuclei coupling effects in the three-body all-quantum, i.e. non-adiabatic, molecule. Among others we have evaluated spectroscopic constants and molecular deformation. Quantum dynamics of the system is well described and distinct features of coupling are observed for the nuclei: shift in the equilibrium bond length, increase in the width of the pair correlation function of the nuclei, and non-adiabatic correction to dissociation energy.

The electronic distribution, however, is less influenced by the coupling, and therefore, we could say that the adiabatic approximation is better for the electron than for the nuclei. Projection of the non-adiabatic three-body system with the help of Morse wave functions onto two-body nuclei-only subsystem indicates that Morse potential is not capable of describing non-adiabatic effects accurately.

Finally, though the path-integral Monte Carlo method is straightforward, the simplest approach is not suitable if accurate results is desired. Also, the 0 K quantum state can be obtained as an extrapolation from finite temperatures, only. On the other hand, the classical representation can be nicely found within the same formalism. We find that computational capacity becomes the limiting factor in simulations with increasing accuracy or with increasing number of particles. Path integral Monte Carlo method is shown to be straightforward but computationally intensive approach to find the finite temperature mixed quantum state even for a single particle.

INDEX

BIBLIOGRAPHY

L. F. Abbot and M. B. Wise. Dimension of a quantum-mechanical path. *Am. J. Phys.*, 49(1):37–39, Jan. 1981. 25

A. A. Abrahamson. Born–Mayer-type interatomic potential for neutral ground-state atoms with $Z = 2$ to $Z = 105$. *Phys. Rev.*, 178(1):76–79, Feb 1969. 63

S. A. Alexander and R. L. Coldwell. Spectroscopic constans of H_2^+ using Monte Carlo methods. *Chem. Phys. Lett.*, 413:253, 2005. 72, 73, 74

S. A. Ali and A. Inomata. Note on path integration in a space with a dispiration. Google. iii

L. Andersson and B. K. Driver. Finite dimensional approximations to Wiener measure and path integral formulas on manifolds. *Journal of Functional Analysis*, 165:430–498, Feb. 1999. 24, 25

J. Arponen. *Statistinen fysiikka*. Limes ry, 1994. 7

P. Atkins and R. Friedman. *Molecular Quantum Mechanics*. Oxford University Press, 1997 edition, 1970. 1

A. Auerbach, K. F. Freed, and R. Gomer. Effective medium potentials for molecule-surface interactions: H_2 on Cu and Ni surfaces. *J. Chem. Phys.*, 86 (4):2356–2361, 1987. 62

P. Bagus and C. Björkman. Electronic structure of transition-metal hydrides: NiH and PdH. *Phys. Rev. A*, 23:461, 1981. 65

L. E. Ballentine. The statistical interpretation of quantum mechanics. *Rev. Mod. Phys.*, 42(4):358–381, October 1970. 1, 3

L. E. Ballentine. *Quantum Mechanics: A Modern Development*. World Scientific Publishing Co. Pte. Ltd., 2000 edition, 1999. iii, 1, 2

J. A. Barker. A quantum-statistical Monte Carlo method; path integrals with boundary conditions. *J. Chem. Phys.*, 70(06):2914–2918, March 1978. 7, 14, 49

F. A. Barone, H. Boschi-Filho, and C. Farina. Three methods for calculating the Feynman propagator. *Am. J. Phys.*, 71(5):483–491, May 2003. 9

K. Binder and D. W. Heermann. *The Monte Carlo Method in Statistical Physics*. Springer-Verlag, 2001. iii, 50

B. Bodmann, H. Leschke, and S. Warzel. Wiener integration for quantum systems: A unified approach to the Feynman–Kac formula. *arXiv:quant-ph/9703031 v1*, pages 95–106, March 1997. 25, 26

D. W. Brenner. Relationship between the embedded-atom method and Tersoff potentials. *Phys. Rev. Lett.*, 63(9):1022–1022, Aug. 1989. 63

L. M. Brown, editor. *Feynman's Thesis: A New Approach to Quantum Theory*. World Scientific Publishing, 2005. iii

B. Burghard, J. Eicke, and J. Stolze. Evaluation of coherent-state path integrals in statistical mechanics by matrix multiplication. *J. Chem. Phys.*, 108(4):1562–1569, 1998. 24, 35

J. Cao and B. J. Berne. On energy estimators in path integral Monte Carlo simulations: Dependence of accuracy on algorithm. *J. Chem. Phys.*, 91(10):6359–6366, Nov. 1989. 55

R. Car and M. Parrinello. Unified approach for molecular dynamics and density-functional theory. *Phys. Rev. Lett.*, 55(22):2471–2474, Nov 1985. 34

P. Cartier and C. DeWitt-Morette. A new perspective on functional integration. *J. Math. Phys.*, 36:2137–2340, 1995. 26

D. M. Ceperley. Path integrals in the theory of condensed helium. *Rev. Mod. Phys*, 67(2):279, 1995. 8, 33, 35, 36, 38, 46, 47, 49, 72

C. Chakravarty, M. C. Gordillo, and D. M. Ceperley. A comparision of the efficiency of Fourier- and discrete time-path integral Monte Carlo. *J. Chem. Phys.*, 109(6):2123–2134, Aug. 1998. 33, 41, 55

S. A. Chin and C. R. Chen. Fourth order symplectic integrator methods for solving the time-dependent Schrödinger equation. *J. Chem. Phys*, 114(17):7338–7341, May 2001. 23

F. Cleri and V. Rosato. Tight-binding potentials for transition metals and alloys. *Phys. Rev. B*, 48(1):22–33, Jul 1993. 63, 64

A. D. Corso, A. Pasquarello, and A. Baldereschi. Generalized-gradient approximations to density-functional theory: A comparative study for atoms and solids. *Phys. Rev. B*, 53(3):1180, 1996. 72

C. Cronström and C. Montonen. *Johdatus kvanttimekaniikkaan*. Limes ry, 1991. 1

M. S. Daw and M. I. Baskes. Embedded-atom method: Derivation and application to impurities, surfaces, and other defects in metals. *Phys. Rev. B*, 29(12):6443–6453, 1984. 62

H. De Raedt and B. De Raedt. Applications of the generalized Trotter formula. *Phys. Rev. A*, 28(6):3775–3580, Dec. 1983. 23

C. M. DeWitt. Feynman's path integral — definition without limiting procedure. *Commun. math. Phys.*, 28:47–67, 1972. 26

M. Dineykhan and R. Nazmitdinov. Two-electron quantum dot in a magnetic field: Analytical results. *Phys. Rev. B*, 55(20):13707, 1997. 58

J. L. Dunham. The energy levels of a rotating vibrator. *Phys. Rev.*, 41(6):721–731, Sep 1932. 73

W. Feller. *An introduction to probability theory and its applications, Vol 1*. John Wiley & Sons, 1950. 39

R. P. Feynman. Space-time approach to non-relativistic quantum mechanics. *Rev. Mod. Phys.*, 20(2):367–387, April 1948. iii

R. P. Feynman. *Statistical Mechanics*. Addison Wesley, 1998 edition, 1972. iii, 8, 9, 10, 11, 20, 21, 51

R. P. Feynman and A. R. Hibbs. *Quantum Mechanics and Path Integrals*. New York: McGraw-Hill, 1965. iii, 8, 9, 11, 12, 13, 24

R. Fletcher. *Practical methods of optimization*. John Wiley & Sons Ltd, 1978. 59

S. A. Fulling and K. S. Güntürk. Exploring the propagator of a particle in a box. URL `http://www.math.tamu.edu/~fulling/`. electric, 2003. 14, 16

R. F. Gariepy and W. Ziemer. *Modern Real Analysis*. Boston: PWS Pub., 1995. 2

S. Gasiorowicz. *Quantum Physics*. John Wiley & Sons, 1996. 58

A. Giansati and G. Jacucci. Variance and correlation length of energy estimators in Metropolis path integral Monte Carlo. *J. Chem. Phys.*, 89(12):7454–7456, Dec. 1988. 55

M. J. Gillan. Quantum simulation of hydrogen in metals. *Phys. Rev. Lett.*, 58(6): 563–566, 1987. 62

M. Goodman. Path integral solution to the infinite square well. *Am. J. Phys.*, 49 (9):843–847, Sept. 1981. 14, 15, 16, 17, 18

I. S. Gradshteyn and I. M. Ryzhik. *Table of Integrals, Series and Products*. Academic Press, 1980. 30

H. Grönbeck, D. Tománek, S. G. Kim, and A. Rosén. Does hydrogen pre-melt palladium clusters? *Chem. Phys. Lett.*, 264:39–43, 1997a. 63

H. Grönbeck, D. Tománek, S. G. Kim, and A. Rosén. Hydrogen induced melting of Palladium clusters. *Z. Phys. D*, 40:469–471, 1997b. 63

C. Grosche. Path integration via summation of perturbation expansions and applications to totally reflecting boundaries, and potential steps. *Phys. Rev. Lett*, 71(1):1–4, July 1993. 14, 15

C. Grosche and F. Steiner. How to solve path integrals in quantum mechanics. *J. Math. Phys.*, 36(5):2354–2385, May 1995. iii, 27, 58

A. Groß, M. Scheffler, M. J. Mehl, and D. A. Papaconstantopoulos. *Ab initio* based tight-binding Hamiltonian for the dissociation of molecules at surfaces. *Phys. Rev. Lett.*, 82(6):1209–1212, 1999. 64

J. Harting. *Path integral Monte Carlo simulations and their relation to recent advances in nanophysics*. PhD thesis, University of Oldenburg, December 2001. 47

J. Harting, O. Mülken, and P. Borrmann. Interplay between shell effects and electron correlation in quantum dots. *Phys. Rev. B*, 62(15):10207, 2000. 47

M. F. Herman, E. J. Bruskin, and B. J. Berne. On path integral Monte Carlo simulations. *J. Chem. Phys.*, 76(10):5150–5155, May 1982. 46, 49, 54

L. Hostler and R. H. Pratt. Coulomb Green's function in closed form. *Phys. Rev. Lett.*, 10(11):469, 1963. 36

L. B. i Barberà. *Path integral Monte Carlo*. PhD thesis, Universitat Politècnica de Catalunya, July 2002. 12, 24

G.-L. Ingold. 1. path integrals and their application to dissipative quantum systems. Springer Verlag Berlin Heidelberg. iii

W. Janke and H. Kleinert. Effective classical potential and particle distribution of a Coulomb system. *Phys. Lett. A*, 118(8):371–374, Nov. 1986. 37

P. Jena, R. M. Nieminen, M. J. Puska, and M. Manninen. Role of elastic and electronic interactions in trapping of hydrogen by impurities in transition metals. *Phys. Rev. B*, 31(12):7612–7616, 1985. 62

L. Kahanpää. Suoraviivaista ajattelua, II osa: Funktionaalianalyysi. URL `http://www.math.jyu.fi/~kahanpaa/`. 2005. 2

M. H. Kalos and P. A. Whitlock. *Monte Carlo Methods. Volume I: Basics*. John Wiley & Sons, 1986. 39, 40

J. B. Keller and D. W. McLaughlin. The Feynman integral. *The American Monthly*, 82(5):451–465, May 1975. 7, 14, 26, 27

H. Kleinert. *Path Integrals in Quantum Mechanics, Statistics, Polymer Physics, and Financial Markets*. World Scientific Publishing Co. Pte. Ltd, Singapore, 2004. See his `www`-pages. iii, 23, 29

J. S. Kole and H. D. Raedt. Quantum Monte Carlo method for attractive Coulomb potentials. *Phys. Rev. E*, 64(1):016704–(6), June 2001. 36

G. Kresse. Dissociation and sticking of H_2 in the Ni(111), (100) and (110) substrate. *Phys. Rev. B*, 62(12):8295–8305, 2000. 66

G. Kresse and J. Hafner. First-principles study of the adsorption of atomic H on Ni(111), (100) and (110). *Surf. Sci.*, 459:287–302, 2000. 66, 67

V. Kurlin. Exponential Baker-Campbell-Hausdorff formula, Jul 2006. URL `http://arxiv.org/abs/math.QA/0606330`. 23

I. Kylänpää, M. Leino, and T. T. Rantala. Hydrogen molecule ion: Path integral Monte Carlo approach. *Accepted to Phys. Rev. A*, 2007. v, 36, 37, 41, 50, 57, 60, 72, 101

P. Lahti. *Kvanttimekaniikka III*. Turun Yliopisto — Luentomuistiinpanot, 2005. 1, 4, 6

P. J. Lahti and K. Ylinen. *Johdatus kvanttimekaniikkaan*. Fysiikan Kustannus Oy, 1989. 3

M. G. G. Laidlaw and C. M. DeWitt. Feynman functional integrals for systems of indistinguishable particles. *Phys. Rev. D*, 3(6):1375–1378, March 1971. 26

M. Leino, I. Kylänpää, and T. T. Rantala. Coverage dependence of finite temperature quantum distribution of hydrogen on nickel (001) surface. *Surf. Sci.*, 601: 1246–1254, March 2007. v, 65, 68, 70, 71, 99

M. Leino, J. Nieminen, and T. T. Rantala. Finite temperature quantum distribution of hydrogen adsorbate on nickel (001) surface. *Surf. Sci.*, 600:1860–1869, March 2006. v, 64, 65, 67, 68, 70, 97

M. Leino and T. T. Rantala. Finite-temperature effects on correlation of electrons in quantum dots. *Physica Scripta*, T114:44–48, 2004. v, 58, 93

M. Leino and T. T. Rantala. Temperature effects on electron correlations in two coupled quantum dots. *Few Body Systems*, 40(3–4):237–252, June 2007. v, 36, 58, 61, 95

X.-P. Li and J. Q. Broughton. High-order correction to the Trotter expansion for use in computer simulation. *J. Chem. Phys*, 86(9):5094–5100, May 1987. 24

J. Lounila and T. T. Rantala. Effects of repulsion and dispersion forces in liquid crystals: Alignment and deformation of H_2 solute. *Phys. Rev. A*, 44(10):6641–6651, Nov. 1991. 73

A. P. Lyubartsev. Simulation of excited states and the sign problem in the path integral Monte Carlo method. *J. Phys. A: Math. Gen.*, 38:6659–6674, July 2005. 58

A. S. Mårtensson, C. Nyberg, and S. Andersson. Observation of molecular H_2 chemisorption on a nickel surface. *Phys. Rev. Lett.*, 57(16):2045–2048, 1986. 70

G. J. Martyna, A. Hughes, and M. E. Tuckerman. Molecular dynamics algorithms for path integrals at constant pressure. *J. Chem. Phys*, 110(7):3275–3290, 1999. 12

G. J. Martyna, M. L. Klein, and M. E. Tuckerman. Nosé–hoover chains: The canonical ensemble via continuous dynamics. *J. Chem. Phys.*, 97(4):2635–2643, Aug. 1992. 34

D. Marx and M. Parrinello. *Ab initio* path integral molecular dynamcis: Basic ideas. *J. Chem. Phys.*, 104(11):4077–4082, March 1996. 34

T. Mattsson and G. Wahnström. Isotope effect in hydrogen surface diffusion. *Phys. Rev. B*, 56(23):14944–14947, 1997. 62

T. Mattsson, G. Wahnström, L. Bengtsson, and B. Hammer. Quantum-mechanical calculation of H on Ni(001) using a model potential on first-principles calculations. *Phys. Rev. B*, 56:2258–2266, 1997. 64, 66, 68

T. R. Mattsson, U. Engberg, and G. Wahnström. H diffusion on Ni(100): A quantum monte carlo simulation. *Phys. Rev. Lett.*, 71(16):2615–2618, 1993. 62

T. R. Mattsson and G. Wahnström. Quantum Monte Carlo study of surface diffusion. *Phys. Rev. B*, 31(3):1885, 1995. 62, 68

R. D. Mattuck. *A Guide to Feynman Diagrams in the Many-Body Problem*. Dover, 1992. 58

N. Metropolis, A. W. Rosenbluth, M. N. Rosenbluth, and A. H. Teller. Equation of state calculations by fast computing machines. *J. Chem. Phys.*, 21(6):1087–1092, Jun. 1953. 38, 40

P. M. Morse. Diatomic molecules according to the wave mechanics. II. Vibrational levels. *Phys. Rev.*, 34:57–64, July 1929. 74

H. J. W. Müller-Kirsten. *Introduction to Quantum Mechanics: Schrodinger Equation And Path Integral*. World Scientific Publishing Co Ltd, 2006. iii

S. G. Nash and A. Sofer. *Linear and Nonlinear Programming*. MacGraw-Hill, 1996. 59

R. D. Nevels, Z. Wu, and C. Huang. Feynman path integral for an infinite potential barrier. *Phys. Rev. A*, 48(5):3445–3451, Nov. 1993. 14

M. A. Nielsen and I. L. Chuang. *Quantum Computation and Quantum Information*. The Press Syndicate of the University of Cambridge, 2002. 2, 3

M. Pedersen. *Functional Analysis in Applied Mathematics and Engineering*. Chapman & Hall /CRC, 2000. 2

M. Pi, A. Emperador, M. Barranco, and F. Garcias. Vertically coupled quantum dots in the local spin-density functional theory. *Phys. RB*, 63:115316, 2001. 58, 61

E. L. Pollock. Properties and computation of the Coulomb pair density matrix. *Comp. Phys. Commun.*, 52(1):49–60, 1988. 36

E. L. Pollock and D. M. Ceperley. Simulation of quantum many-body systems by path-integral methods. *Phys. Rev. B*, 30(5):2555–2568, 1984. 12

E. Prugovecki. *Quantum mechanics in Hilbert space*. Academic Press, 1971. 14

M. J. Puska and R. M. Nieminen. Hydrogen chemisorbed on nickel surfaces: A wave mechanical treatment of proton motion. *Surf. Sci*, 157:413–435, 1985. 68

M. J. Puska, R. M. Nieminen, and P. Jena. Hydrogen and deuterium decoration of In-vacancy complexes in nickel. *Phys. Rev. B*, 35(12):6059–6063, 1987. 62

M. J. Puska, R. M. Nieminen, M. Manninen, B. Chakraborty, S. Holloway, and J. K. Nørskov. Quantum motion of chemisorbed hydrogen on Ni surfaces. *Phys. Rev. Lett.*, 51:1081–1084, 1983. 68

M. Rontani, F. Rossi, F. Manghi, and E. Molinari. Coulomb correlation effects in semiconductor quantum dots: The role of dimensionality. *Phys. Rev. B*, 59(15): 10165–10175, 1999. 61

L. S. Schulman. *Techniques and Applications of Path Integration*. Dover, 2005 edition, 1981. iii, 10, 14, 15, 19, 22, 26

K. S. Schweizer, R. M. Stratt, D. Chandler, and P. G. Wolynes. Convenient and accurate discretized path integral methods for equilibrium quantum mechanical calculations. *J. Chem. Phys.*, 75(3):1347–1364, Aug. 1981. 29, 46, 49

B. Simmons. Quantum condensed matter field theory. URL `http://www.tcm.phy.cam.ac.uk/~bds10/tp3.html`. Chapter 3: Feynman Path Integral. iii

J. S. Sims and S. A. Hagstrom. High precision variational calculations for the Born-Oppenheimer energies of the ground state of the hydrogen molecule. *J. Chem. Phys.*, 124(9):094101(7), March 2006. 65, 74

M. Sprik, M. L. Klein, and D. Chandler. Computer simulation of a quantum particle in a quenched disordered system: Direct observation of Lifshitz traps. *Phys. Rev. B*, 32(1):545–547, July 1985a. 12

M. Sprik, M. L. Klein, and D. Chandler. Staging: A sampling techniques for the Monte Carlo evaluation of path integrals. *Phys. Rev. B*, 31(7):4234–4244, April 1985b. 12

R. G. Storer. Path-integral calculation of the quantum-statistical density matrix for attractive Coulomb forces. *J. Math. Phys.*, 9(6):964–970, 1968. 34, 36, 37

W. A. Strauss. *Partial Differential Equations: An Introduction*. John Wiley & Sons, Inc, 1992. 8

A. P. Sutton and J. Chen. Long-range Finnis–Sinclair potentials. *Philos. Mag. Lett.*, 61(3):139–146, 1990. 64

S. Tan, C. Fox, and G. Nicholls. Inverse problems. URL `http://www.math.auckland.ac.nz/%7Ephy707/`. Lecture notes, part 4, 2006. 52

M. Taut. Two electrons in an external oscillator potential: Particular analytical solutions of a Coulomb correlation problem. *Phys. Rev. A*, 48(5):3561, 1993. 58

M. Tegmark. Anything goes. *New Scientist*, 158(2137):26–30, June 1998. 1

D. ter Haar. The Vibrational Levels of an Anharmonic Oscillator. *Phys. Rev.*, 70: 222, 1946. 74

J. Tervo. *Osittaisdifferentiaaliyhtälöt — Johdatus teoriaan ja ratkaisumenetelmät*. Kuopion yliopiston ylioppilaskunta, 2000. 8

J. M. Thijssen. *Computational Physics*. Cambridge, 2000. 36, 38, 72

D. Thirumai, E. J. Bruskin, and B. J. Berne. An iterative scheme for the evaluation of discretized path integrals. *J. Chem. Phys.*, 79(10):5063–5069, Nov. 1983. 34, 36

H. F. Trotter. On the product of semi-groups of operators. *Proc. Am. Math. Soc.*, 10:545–551, 1959. 21, 22

M. Tuckerman. Statistical mechanics. Lecture notes. 48

M. E. Tuckerman, B. J. Berne, G. J. Martyna, and M. L. Klein. Efficient molecular dynamics and hybrid Monte Carlo algorithms for path integrals. *J. Chem. Phys.*, 99(4):2796–2808, Aug. 1993. 12, 34

M. E. Tuckerman, D. Marx, M. L. Klein, and M. Parrinello. Efficient and general algorithms for path integral Car–Parrinello molecular dynamics. *J. Chem. Phys.*, 104(14):5579–5588, March 1996. 12, 34

A. Valtakoski. Mathematical aspects of functional integration. Master's thesis, Helsinki University, 2000. URL `www.helsinki.fi/`. 24, 26

J. von Neumann. *Mathematical Foundations of Quantum Mechanics*. Princeton University Press, 1983 edition, 1955. 2

C. Wetterich. Quantum field theory I. URL `http://www.thphys.uni-heidelberg.de/~cosmo/view/Main/QFTWetteric`. Aug 2006. iii

T. W. Whitfield and J. E. Staub. Uncertainty of path integral averages at low temperature. *J. Chem. Phys.*, 115(15):6834–6840, Oct. 2001. 46, 51, 55

T. W. Whitfield and J. E. Straub. Enhanced sampling in numerical path integration: An approximation for the quantum statistical density matrix based on the nonextensive thermostatics. *Phys. Rev. E*, 64(6):066115, Nov. 2001. 34

A. Wong, A. Lee, and X. D. Zhu. Coverage dependence of quantum tunneling diffusion of hydrogen and deuterium on Ni(111). *Phys. Rev. B*, 51(7):4418–4425, 1995. 70

W. Zhong, Y. Cai, and D. Tománek. Mechanical stability of Pd-H systems: A molecular-dynamics study. *Phys. Rev. B*, 46:8099–8108, 1992. 63

W. Zhong, Y. S. Li, and D. Tománek. Effect on adsorbates on surface phono modes: H on Pd(001) and Pd(110). *Phys. Rev. B*, 44(23):13053–13062, 1991. 63, 65

PAPER I

Paper I: Leino and Rantala (2004)

M. Leino and T. T. Rantala,

Finite-temperature effects on correlation of electrons in quantum dots,

Physica Scripta, T114, 44–48, 2004.

Physica Scripta. Vol. T114, 44–48, 2004

Finite-Temperature Effects on Correlation of Electrons in Quantum Dots

Markku Leino and Tapio T. Rantala*

Institute of Physics, Tampere University of Technology, P.O. Box 692, FIN-33101 Tampere, Finland

Received September 2, 2003; accepted October 22, 2003

PACS number: 73.21.La

Abstract

The path-integral Monte Carlo method is used to examine the two-electron state of a model quantum dot. Electrons in the two-dimensional quantum dot are confined by a harmonic oscillator potential of strength $\hbar\omega = 1$ eV. Mixed state densities, energies and pair correlation functions are evaluated at various temperatures, and their temperature dependencies are analyzed. Also, the two-electron pure state energetics is resolved and the correlation induced shifts of the first and second excited states are evaluated.

1. Introduction

Quantum dots are small man-made structures in a solid, typically with sizes ranging from nanometers to a few micrometers. They consist of 10^3–10^9 atoms with an equivalent number of bound electrons. Electrons are tightly bound to the atomic cores and bonds except for a small fraction of free charge carriers [1]. Current nanofabrication technology allows precise control of the size and shape of these dots. Thus, the size and shape of the confining potential and the effective mass of charge carriers can be adjusted to tune the electronic structure and the excitation spectrum, in particular [2].

Properties of few-electron quantum dots, e.g. at heterojunction interfaces, are important to understand for the development of novel semiconductor technology. In semiconductor laser technology, quantum dots may provide unique opportunities in developments and advance the applications [3]. Thus, the quantum dots are convenient for optoelectronic device design and fascinating for theoretical studies. From the theoretical point of view the quantum dots are atomic-like systems with localized electronic states. Thus, atomic physics can be applied here to the field of semiconductor devices.

The two-electron system is one of the simplest non-trivial quantum mechanical systems. Nevertheless, some analytical results exist for two electrons in a symmetrical enough quantum dot. Taut [4] reduced the problem of solving a six-dimensional partial differential equation to finding the real roots of a polynomial, and thus, gave analytic solutions to particular oscillator frequencies of two interacting electrons in an external harmonic oscillator potential. Dineykhan and Nazmitdinov [5] found analytic expressions for the ground state energy for 2D and 3D harmonic oscillators in external magnetic fields.

In addition to analytical results, there are a number of numerical results for two-electron quantum dots. A numerically exact calculation for the energy spectra of two electrons in a finite height cylindrical quantum dot by a coupled-channel method is presented in details by Lin and Jiang [6]. Harju *et al*. [7] studied the ground state of parabolically confined electrons in a quantum dot by both direct numerical diagonalization and variational Quantum Monte Carlo methods. In an older paper Harju *et al*. [8] applied the Quantum Monte Carlo technique to a two-electron quantum dot. Merkt, Huser and Wagner [9] have calculated the discrete energy spectra for two electrons in a two-dimensional harmonic well in the effective-mass approximation as a function of the dot size and the strength of a magnetic field directed perpendicular to the dot plane using first order perturbation theory. Furthermore, the states of two-electron paired quantum well quantum dots [10] were calculated with diagonalization and the variational principle.

More complicated quantumd dots have been studied by many methods: Perturbation theory [11], numerical diagonalization [12], density-functional theory [13, 14], unrestricted Hartree-Fock [15], diffusion Monte Carlo [16] and path-integral Monte Carlo [17, 18, 19, 20, 21, 22, 23] methods. In these studies electronic structure, addition spectra, electronic states, Fermi liquid and Wigner molecule behaviour, ground and excited state energies, shell effects, electron correlations and low-energy states were examined.

Even for the correlation energy in a quantum dot a simple but accurate analytic expression can be found in Wentzel–Kramers–Brilloun approximation [24]. The behavior of 3D exchange–correlation energy functional approximation of DFT in anisotropic systems with 2D character is investigated by Kim *et al*. [25]. They pointed out a fundamental limitation of LDA, due to the nonlocal nature of exchange–correlation hole.

The physics of interactions becomes especially interesting in zero external magnetic field, when electron spins are not polarized and are active players in the game [26].

In this study, we apply the path-integral Monte Carlo simulation method [27] to investigate the properties of a two-electron quantum dot. We evaluate the one-electron distributions and two-electron correlation functions, and temperature effects on both. Furthermore, we resolve the finite-temperature mixed states to the contributing pure states, and by that, we are able to consider the transition energies, and thus, the optical response of charge carriers. Also, the correlation effect on transition energies is discussed.

In the next chapter we briefly review the theoretical concepts of Monte Carlo methods and the optimization algorithm needed here. Then, in chapter 3 we give the simulation results and compare those to the analytical one-electron results. Chapter 4 is devoted to the case of two correlated electrons, and conclusions are given in chapter 5.

2. Method

In this chapter we briefly describe the basic concepts of PIMC method, the Monte Carlo simulation procedure we used and the

*email: Tapio.Rantala@tut.fi

optimization scheme that was used to resolve the pure many-body eigenstates from the mixed state.

2.1. *Path-Integral Monte Carlo method*

All stationary properties of a d-dimensional quantum N-body system with Hamiltonian $\widehat{H} = \widehat{T} + \widehat{V}$ in thermal equilibrium at temperature $\beta \equiv 1/k_B T$ are obtained from the density matrix $Z = \mathrm{Tr}\, \mathrm{e}^{\beta \widehat{H}}$ [28]. Here, $\widehat{T} = \sum_{i=1}^{N} \widehat{\boldsymbol{p}}_i^2/2m_i$ is the kinetic energy operator and $\widehat{V}$ includes the external potential and interactions between particles.

2.1.1. *Path-Integral Formalism.* In discrete path-integral representation the density matrix is

$$Z = \left(\frac{mM}{2\pi\hbar^2\beta}\right)^{dN/2} \int \exp\left[-\beta \sum_{n=1}^{M} (K_n + U_n)\right] \mathrm{d}\boldsymbol{r}_0 \cdots \mathrm{d}\boldsymbol{r}_{M-1}, \tag{1}$$

where operators K_n and U_n define internal and external energies of the system. In the primitive approximation [27] they are written as

$$K_n = \frac{mM}{2\hbar^2\beta^2}(\boldsymbol{r}_{n-1} - \boldsymbol{r}_n)^2, \tag{2a}$$

$$U_n = \frac{1}{2M}(V(\boldsymbol{r}_{n-1}) + V(\boldsymbol{r}_n)), \tag{2b}$$

where m is the effective mass of the electrons and M is called the Trotter number, and $\boldsymbol{r}_0 = \boldsymbol{r}_M$. The primitive approximation, where the external energy coincides with potential energy, contains all the physics and converges to the correct limit, given a small enough β/M [27]. Furthermore, it is simple and well defined, and at the limit $M \to \infty$ the true many-body description (1) is exact.

It is straightforward to calculate scalar operators, such as density, potential energy, and the pair correlation functions; they are simply averages over the paths [27]. Use can be made of the symmetry in imaginary time, since all time slices t are equivalent. Thus, the average density and pair correlation functions are

$$\rho(\boldsymbol{r}) = N_\rho \sum_{n,t} \langle \delta(\boldsymbol{r} - \boldsymbol{r}_{nt}) \rangle \tag{3a}$$

and

$$g(\boldsymbol{r}) = N_g \sum_{n,i,j,t} \langle \delta(\boldsymbol{r} - (\boldsymbol{r}_{nit} - \boldsymbol{r}_{njt})) \rangle, \tag{3b}$$

where N_ρ and N_g are proper normalization factors, i and j refer to different particles, and n and t are as above.

The nondiagonal properties in coordinate basis, such as the energy, free energy, and momentum distribution, are not so straightforward to calculate. A thermodynamic estimate of the energy is obtained by differentiating the partition function with respect to the inverse temperature [27] as

$$E(\beta) = -\frac{1}{Z}\frac{\mathrm{d}Z}{\mathrm{d}\beta} = M\langle dN/(2\beta) - K_n + U_n/M \rangle. \tag{4}$$

Path-integral Monte Carlo (PIMC) simulation method is a "numerically exact" finite-temperature approach, the only limiting factor being computational capacity, for evaluation of the density matrix (1).

2.1.2. *Monte Carlo simulation procedure.* The quantum-mechanical approximation of the finite temperature density matrix of the N-particle system, Eq (1), is a multidimensional integral [29, 28], which turns out to be a partition function of a classical $M \times N$-particle canonical ensemble or NVT-system. This specific classical system consists of N closed chains or "polymers" of M knots or "beads" in a necklace with a certain special description of interactions among the particles and between the external potential. Thus, quantum-mechanical density matrix can be evaluated using classical formalism.

We use the Metropolis Monte Carlo scheme to evaluate the integral (1). With this technique all the approximations in integration scheme and in path-integral formulation are controllable. The Metropolis algorithm samples very effectivitely the correct distribution of beads and thus the correct density matrix Z using the integrand in (1) as the weight for the importance sampling process. The main issue is whether the configuration space is explored thoroughly in a reasonable amount of computer time. Including many types of Monte Carlo moves makes the algorithm more robust, since before doing a calculation one does not necessarily know which type of moves will lead to a balanced sampling of the phase space and rapid convergence of expectation values. We used two types of moves: one randomly selected bead in one random necklace and the center of mass of a random necklace.

Distribution of steps in the phase space was taken to be Gaussian such that the total Metropolis acceptance rate is about 70% and the frequency of each move is about the same. This is called the *classic rule* [27].

2.2. *Finding the pure states*

The density matrix (1) is a finite temperature, mixed state, description of the quantum system. Thus, the mixed state energy $E(\beta)$ at temperature T, Eq (4), is the Boltzmann weighted mean value of pure state eigenenergies E_i

$$E(\beta) = \frac{\sum_i d_i E_i \mathrm{e}^{-\beta E_i}}{\sum_i d_i \mathrm{e}^{-\beta E_i}}, \tag{5}$$

where the summation is done over all states i weighted by the degeneracy d_i. In principle, the contribution of excited state energies E_i can be separated from equation (5) by fitting, if the function $E(\beta)$, Eq (4), is known analytically or can be simulated accurately enough. In finding the pure states, the infinite summation (5) is approximated by a function $f(\beta, \boldsymbol{E}) = \sum_{i=0}^{m} d_i E_i \exp(-\beta E_i)/\sum_{i=0}^{m} d_i \exp(-\beta E_i)$, where $\boldsymbol{E}$ is a finite (truncated) vector containing the pure state energies E_i, $i = 0, 1, \ldots, m$. In principle, it should be possible to find the pure state densities $\rho_i(\boldsymbol{r})$ independently with the same procedure, and thus, find a verification of pure state energies E_i obtained here.

From simulations at various temperatures T_j we sampled the mean energy function, and found it very similar to the one-electron mixed state energy function, see below. The differences in ground state energy E_0 and scaling with respect to β were determined. We found the excited state eigenenergies E_i by fitting the energy formula (5) in the least squares sense. Two optimization methods for fitting were tested, Gauss–Newton and Levenberg–Marquardt algorithms [30, 31]. Both use quadratic approximations to nonlinear residual vector, but L–M is so called trusted region algorithm, i.e., it moves only in the region where the fit is good, discarding too long steps.

Actually, the Gauss–Newton method was not good enough. It is possible to find a few first pure states with that method,

but Levenberq–Marquardt was much simpler to use and more eigenenergies were found, and the algorithm is almost as simple.

The optimization can be simplified because of Boltzmann distribution: at low enough temperature we get only one or two states that contribute to the total energy. Thus, we can find easily a few lowest eigenenergies and when purifying more states, the lowest states can be fixed.

One should note that the high temperature here is a computational tool, only, and has nothing to do with any realistic temperature related to quantum dots.

3. Single electron case

The one-electron harmonic oscillator is analytically solvable in any dimensions. The eigenenergies of the 2D harmonic oscillator are $E_i = \hbar\omega(1 + i)$, where $i = 0, 1, \ldots$. The degeneracy d_i of the state i is $i + 1$ for a 2D harmonic oscillator. The same degeneracy is assumed for the two-electron case. When all states weighted by the respective Boltzmannian probality are summed, Eq (5), we get the temperature dependent energy [28] per dimension

$$\langle E\rangle = \frac{\hbar\omega}{2}\coth\frac{\hbar\omega\beta}{2}, \tag{6}$$

which explicitly shows how the temperature and the confining potential are related. Similarly, the electron densities of pure states can be summed up to give the temperature dependent density and by convolution we obtain the pair correlation function for the non-interacting particles.

Thus, we can test the path-integral Monte Carlo code and optimization methods for the single electron case with analytical energies and electron densities. Both methods turned out to work fine. In figure 1, the one-electron states (energies, wavefunctions, occupations and probabilities) are demonstrated. Note that this one-electron energy diagram is identical with the excited states diagram of the non-interacting N-electron quantum dot.

The L–M algorithm is stable with respect to changes in starting point and temperature in the one-electron case. Thus, the pure one-electron eigenstates E_i can be found until $i \approx 7$ easily, if replacing simulated (4) by the analytical formula (6) in fitting. However, the optimization is sensitive to the accuracy in mixed state energy: if the analytical energies are rounded to two decimals, the fitting procedure does not work reliably.

4. Two-electron correlations

The system we consider is two Coulomb-interacting opposite spin electrons in a two-dimensional quantum dot. The lateral confinement is approximated by a harmonic potential assuming circular symmetry and "strength" $\hbar\omega = 1$ eV. Thus, the confinement is very strong corresponding to a QD of a few nanometers and a few hundreds atoms, only. This serves, however, as a nice model and may be realistic with new fabrication technologies. Assuming GaAs as the material we use the electron effective mass $m = 0.067m_e$ and the dielectric constant $\epsilon = 12.4$.

The two-electron case with Coulomb interaction looses the full separability, and the Hamiltonian can be reduced to center-of-mass and relative motion, only. The wave function for the center-of-mass can be solved analytically, but that describing the relative motion must be solved using numerical methods. With the PIMC method we treat the full Hamiltonian numerically, too.

4.1. *Distributions*

In fig 2 we compare the one-electron densities of the non-interacting or the single electron case to the case of two interacting electrons, at two different temperatures. In the upper panel we see the temperature broadening clearly but hardly any correlation effects. However, the difference curves in the lower panel reveal the weak modifications due to the Coulomb repulsion, which tends to keep the electrons apart from each other. The resulting balance seems to be: one at the center of QD and the other away, rather than both slightly off from the center. Surprisingly, the difference is larger at the higher temperature. We do not expect Wigner crystallization type of electron localization in our case, because the effective density parameter here is $r_s^* \approx 0.15$, the threshold being $r_s \geq 7.5$ [32].

Figure 3 shows the pair correlation functions for these two cases together with the corresponding non-interacting case Gaussian reference function. Changes in pair correlation functions due to the Coulomb interactions are illustrated in Fig 4. In addition to temperature broadening the correlation effects are clearly seen,

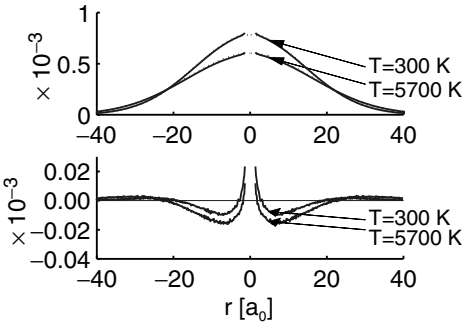

Fig. 2. One-electron densities for non-interacting or single- (dashed) and two-electron (solid) systems, upper panel. Also, the differences of correlated and non-interacting case densities are shown in the lower panel (r in atomic units, $a_0 \approx 0.52$ Å).

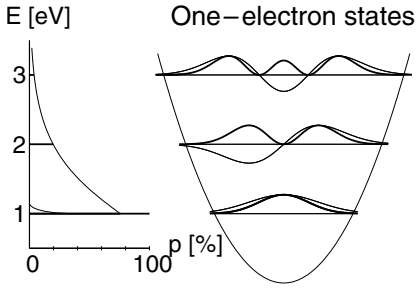

Fig. 1. One-electron states for the 2D harmonic oscillator with $\hbar\omega = 1$ eV. The energy levels, with wavefunctions, densities and probabilities are shown with Boltzmann distribution for $T = 300$ K and $T = 5700$ K.

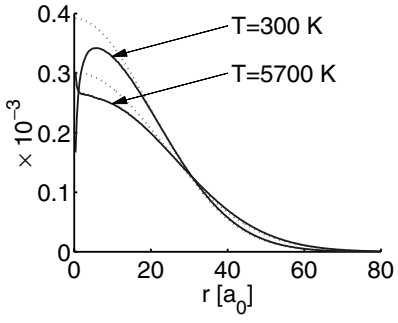

Fig. 3. Pair correlation functions $g(r)$ of the two interacting electrons. Normalization with weight $2\pi r$ is adjusted to unity.

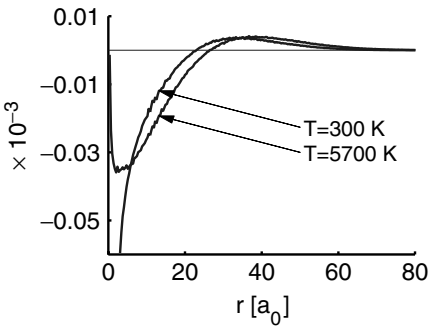

Fig. 4. Difference of pair correlation functions of the interacting and non-interacting electrons, evaluated from the functions in Fig 3.

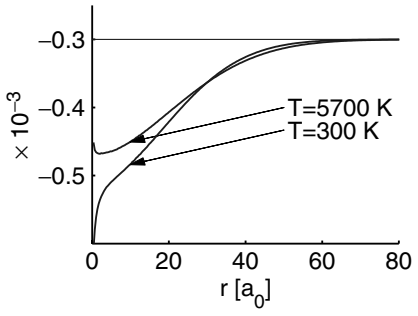

Fig. 5. The average Coulomb correlation hole. Normalization to unity with the weight factor $2\pi r$.

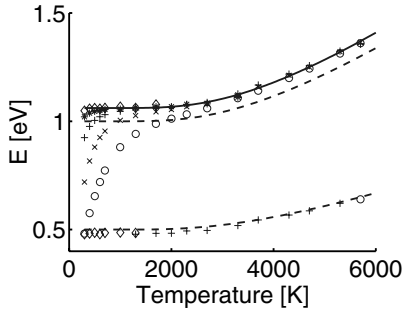

Fig. 6. Mixed state energy as a function of temperature of the correlated two-electron system, simulated with Trotter numbers 8 (○), 16 (×), 32 (+), 64 (∗) and 128 (◇). Solid line is a fit with functional form (6) and dashed lines show analytical single electron total and kinetic (potential) energies, respectively. The high temperatures are only a computational tool to make the resolution of the mixed state to pure states and, of course, have nothing to do with any realistic temperatures of any QDs.

too. The short range repulsive correlation (at a few a.u.) is strong at room temperature, whereas it becomes weaker further away (from 10 a.u.), as compared to the 5700 K case. At the $r \to \infty$ limit the behavior is remarkably different. That however, may not be relevant in any real 2D system, where the third dimension is inevitably present.

We define the average correlation hole as $g(r) - 2g_1(r)$ where $g_1(r)$ is the non-interacting case (Gaussian shaped) pair correlation function. This is shown in Fig 5. It supports the conclusions above, except for the range: the room temperature repulsive Coulomb correlation hole is more pronounced, as expected.

4.2. *Excitation energetics*

The analytical average energy of the single electron mixed state as a function of T, Eq (6), is shown in Fig 6. Also the equal contributions from the kinetic and potential energies are shown. The low temperature limit is 1 eV (0.5 eV) and contributions from lowest excitation appear just below 2000 K.

The simulated interacting case energies are shown for different Trotter numbers $M = 8, \ldots, 128$ and temperatures. The asymptotic low temperature limit should be similar to the single-electron case: contribution from the ground state, only. It is nicely seen how the small M energies deviate from this at low T, thus failing in describing the quantum (kinetic) energy. However, from low-T fitting the ground state energy 1.06 eV is found. Contributions from kinetic, external and Coulomb repulsion are 0.48 eV, 0.52 eV and 0.06 eV, respectively.

The Coulomb interaction keeps the electrons more apart than the noninteracting counterparts, which decreases the kinetic energy but increases potential energy [25]. In Fig 6, it can be seen that the kinetic energy decreases some 0.02 eV at low temperature, that is, in quantum regime, but the effect becomes smaller with increasing temperature.

The high-T behavior is seen to be similar to the single electron case, though the analytical form (6) probably cannot be assumed. However, a fit to (6) results in a scaling factor 0.48 for β.

Resolution of the excited states by fitting $f(\beta, \boldsymbol{E})$ to simulated $\{E(\beta_j)\}$, as described above, leads to the two first excited energies 1.00 eV and 1.9 eV above the ground state. Thus, the correlation has an equal effect on the two lowest state energies but less on the third, the second excited state. This probably can be related to decreasing Coulomb energy with increasing excitation energy.

As a QD becomes larger, the energy difference between single-particle quantum states in the QD becomes smaller and the single-particle quantum states can mix thoroughly to construct many-body quantum states at low-T, already. In general, many-body quantum states are determined by competition between single-particle energy spacing and Coulomb interaction [33, 25, 10].

5. Conclusions

We have shown that the path-integral Monte Carlo method is suitable for the study of two-dimensional two-electron quantum dot. The temperature effects and role of electron-electron correlations, in particular, are nicely demonstrated.

An expected temperature broadening of one-electron distribution was found. However, a detailed inspection of correlations in terms of pair correlation functions and correlation hole reveales differences in the nature of correlation in two different temperatures.

It is also demonstrated how (unreasonably) high temperature simulations and the resulting mixed state data can be used to resolve the pure quantum state properties. This was applied here to determine the excited state energetics, but the related densities or wavefunctions could be found similarly. In the present case, two-dimensional quantum dot with harmonic ($\hbar\omega = 1$ eV) confining potential, the two lowest two-electron states shift by 0.06 eV, 0.06 eV up and the third 0.1 eV down in energy as a result from electron-electron Coulomb correlation.

References

1. Kouwenhoven, L., Austing, D. and Tarucha, S., Rep. Prog. Phys. **64**, 701 (2001).
2. Reimann, S. M. and Manninen, M., Rev. Mod. Phys. **74**, 1283 (2002).
3. Ledentsov, N. N., Grundmann, M., Heinrichsdorff, F. and Bimberg, D., IEEE J. Selected Topics Quant. Electron. **6**, 439 (2000).
4. Taut, M., Phys. Rev. A. **48**, 3561 (1993).

5. Dineykhan, M. and Nazmitdinov, R., Phys. Rev. B **55**, 13707 (1997).
6. Lin, J. T. and Jiang, T. F., Phys. Rev. B **64**, 195323 (2001).
7. Harju, A., Sverdlov, V. and Nieminen, R., Phys. Rev. B **59**, 5622 (1999).
8. Harju, A., Sverdlov, V., Barbiellini, B. and Nieminen, R., Physica B **255**, 145 (1998).
9. Merkt, U., Huser, J. and Wagner, M., Phys. Rev. B **43**, 7320 (1991).
10. Ugajin, R., Suzuki, T., Nomoto, K. and Hase, I., J. Appl. Phys. **76**, 1041 (1994).
11. Rontani, M., Rossi, F., Manghi, F. and Molinari, E., APL **72**, 957 (1998).
12. Ezaki, T., Mori, N. and Hamaguchi, C., Phys. Rev. B **56**, 6428 (1997).
13. Lee, I.-H., Rao, V., Martin, R. M. and Leburton, J.-P., Phys. Rev. B **57**, 9035 (1998).
14. Hirose, K. and Wingreen, N. S., Phys. Rev. B **59**, 4604 (1999).
15. Reusch, B., Häusler, W. and Grabert, H., Phys. Rev. B **63**, 113313 (2001).
16. Pederiva, F., Umrigar, C. J. and Lipparini, E., Phys. Rev. B **62**, 8120 (2000).
17. Harting, J., Mülken, O. and Borrman, P., Phys. Rev. B **62**, 10207 (2000).
18. Häusler, W., Reusch, B., Egger, R. and Grabert, H., Physica B **284**, 1772 (2000).
19. Mak, C., Egger, R. and Weber-Gottschick, H., Phys. Rev. Lett. **81**, 4533 (1998).
20. Egger, R., Häusler, W., Mak, C. and Grabert, H., Phys. Rev. Lett. **82**, 3320 (1999).
21. Dikovsky, M. V. and Mak, C. H., Phys. Rev. B **63**, 235105 (2001).
22. Sundqvist, P. A., Volkov, S. Y., Lozovik, Y. E. and Willander, M., Phys. Rev. B **66**, 075335 (2002).
23. Lozovik, Y. E., Volkov, S. Y. and Willander, M., Solid State Commun. **125**, 127 (2003).
24. García-Castelán, R. M. G., Choe, W. S. and Lee, Y. C., Phys. Rev. B **57**, 9792 (1998).
25. Kim, Y.-H. *et al*., Phys. Rev. B **61**, 5202 (2000).
26. Mikhailov, S. A., Phys. Rev. B **66**, 153313 (2002).
27. Ceperley, D. M., Rev. Mod. Phys. **67**, 279 (1995).
28. Feynman, R. P., "Statistical Mechanics" (Addison Wesley, 1972, 1988).
29. Feynman, R. P. and Hibbs, A. R., "Quantum Mechanics and Path Integrals" (New York: McGraw-Hill, 1965).
30. Fletcher, R., "Practical methods of optimization" (John Wiley & Sons Ltd, 1978).
31. Nash, S. G. and Sofer, A., "Linear and Nonlinear Programming" (MacGraw-Hill, 1996).
32. Chui, S. T. and Tanatar, B., Phys. Rev. Lett. **74**, 458 (1995).
33. Bryant, G. W., Phys. Rev. Lett. **59**, 1140 (1987).

PAPER II

Paper II: Leino and Rantala (2007)

M. Leino and T. T. Rantala,

Temperature effects on electron correlations in two coupled quantum dots,

Few Body Systems, 40(3–4), 237–252, June 2007.

Few-Body Systems 40, 237–252 (2007)
DOI 10.1007/s00601-007-0175-5
Printed in The Netherlands

Few-Body Systems

Temperature Effects on Electron Correlations in Two Coupled Quantum Dots

M. Leino* and T. T. Rantala**

Institute of Physics, Tampere University of Technology, P.O. Box 692,
FI-33101 Tampere, Finland

Received February 9, 2007; accepted April 19, 2007
Published online May 25, 2007;

Abstract. The path-integral Monte Carlo simulation method is used to examine one and two electrons in a system of two coupled disc-like quantum dots (QD) in a zero magnetic field. With this approach we are able to evaluate the one-electron distributions and two-electron correlation functions, and finite temperature effects on both. Increase of temperature broadens the distributions as expected, the effect being smaller for correlated electrons than for single ones. The simulated one- and two-particle distributions of a single and two coupled quantum dots are also compared to those from other theoretical methods. For the one-particle distributions we find a good agreement with those from the DFT approach. The effect of the third dimension or the thickness of the almost two-dimensional disc-like QDs is small for the one-particle distributions, but it is clearly seen in the electron-electron correlation or the two-particle distribution function at low temperatures. The mutual Coulomb energy of the two electrons is found to be temperature-independent, and also, independent of the correlation effects on the dynamics. Computational capacity is found to become the limiting factor in simulations with increasing accuracy or increasing number of particles, and in case of fermions in particular. This and other aspects of PIMC and its capability for this type of calculations are also discussed.

1 Introduction

Special features of the electronic structure of small quantum-confined systems has drawn much attention during the last years. This is largely a consequence of developments in semiconductor technology, where it has become possible to devise

* *E-mail address*: Markku.Leino@tut.fi
** *E-mail address*: Tapio.Rantala@tut.fi

nanometer scale confinement in one, two or three dimensions [1–4]. Confinement in three dimensions leads to smallest systems, quantum dots (QD), containing possibly only a few charge carriers. The electronic structure of a few-electron system is subject to strong many-body effects, and therefore makes a distinctive challenge to the conventional density-functional (DFT) approach, the standard formalism of theoretical solid-state and semiconductor physics. Emanation of the finite-temperature effects is another challenge beyond the standard approaches.

Quantum Monte Carlo methods offer a possibility to treat the many-body correlations exactly with an accuracy depending on the available computing power only. On the other hand, the path-integral formalism of quantum statistics allows one to include finite temperature using a description with mixed states. The combination of these two, the path-integral Monte Carlo (PIMC) approach, permits inspection of the interplay of both, i.e., the temperature effects in many-body correlations. Earlier, we have used this approach to study two electrons in a strongly confining model QD [5]. Mixed state densities, energies and pair correlation functions and their temperature dependencies were evaluated. We also showed how pure states can be searched using the density matrices from several different temperatures. In this paper we report a PIMC study of a system consisting of two coupled QDs, a system which has also been studied experimentally [4].

As QDs are sometimes called artificial atoms, the coupled QDs have been considered as molecules with delocalized electronic states. The electronic properties of single and coupled QDs created with layer-by-layer semiconductor growth can be selected with some freedom by tailoring the shape of a lateral confining potential and the range of vertical confinement [4]. The grown QDs are usually confined vertically in nanometer scale, but laterally in a one to two orders of magnitude larger range. Such dots can be approximately treated as two-dimensional disk-like electronic systems [6]. The ‘‘dimensionality effect’’ or separability of such systems to one- and two-dimensional subsystems is still considered to be an open question. Thus, the effect of a small but finite vertical extension on the QD structure is worth studying [4, 6].

We restrict our present study to systems with one or two electrons, only. By separating the vertical and lateral electronic wave functions the single electron case can be treated analytically. It then serves as a reference case to study the dimensionality effect or separability in the two-electron system. On the other hand, the two-electron system is also the simplest system to study the correlations and its dependence on temperature. With the two-electron system we do not involve the exchange interaction by restricting ourselves to two ‘‘spinless electrons’’ only.

The two-electron system is one of the simplest non-trivial quantum mechanical systems. Nevertheless, some analytical results exist for two electrons in a symmetrical enough quantum dot. Taut [7] reduced the problem of solving a six-dimensional partial differential equation to finding the real roots of a polynomial, and thus gave analytic solutions to particular oscillator frequencies of two interacting electrons in an external harmonic oscillator potential. Dineykhan and Nazmitdinov [8] found analytical expressions for the ground-state energy for 2D and 3D harmonic oscillators in an external magnetic field.

In addition to analytical results, there are a number of numerical results for (harmonic) two-electron quantum dots. A numerically exact calculation for the

energy spectra of two electrons in a finite-height cylindrical quantum dot by a coupled-channel method is presented in details by Lin and Jiang [9]. Harju et al. [10] studied the ground state of parabolically confined electrons in a quantum dot by both direct numerical diagonalization and variational quantum Monte Carlo methods. In an older paper Harju et al. [11] applied the quantum Monte Carlo technique to a two-electron quantum dot. Merkt, Huser, and Wagner [12] have calculated the discrete energy spectra for two electrons in a two-dimensional harmonic well in the effective-mass approximation as a function of the dot size and the strength of a magnetic field directed perpendicular to the dot plane using the first-order perturbation theory. Furthermore, the states of two-electron paired quantum-well quantum dots [13, 14] were calculated with diagonalization and the variational principle. A spin-exchange coupling J between two electrons in tunnel-coupled quantum dots is determined by Burkard et al. [15] by the Heitler-London and Hund-Mulliken techniques.

The ground-state behavior of a 3D quantum dot with square well in z-dimension is studied by Lee et al. [16]. The coupled quantum dots are studied by Partoens and Peeters [17] and Pi et al. [4] within the spin-density functional theory. The latter one serves as reference approach to ours as the studied system is similar. Wensauer et al. [18] present ground-state calculations for laterally coupled quantum dots containing two, four and eight electrons using the spin-density functional theory. Pi et al. [19] investigate computationally and experimentally the dissociation of few-electron circular vertical-semiconductor double-quantum-dot artificial molecules at 0 K as a function of the interdot distance. Excited-state properties of vertically coupled double quantum dots are studied by Imamura et al. [20] by exact diagonalization. Tanaka and Akera [21] calculated the exact many-body eigenstates in a quantum dot formed in double-barrier heterostructures, and they studied coherent transport through the states.

More complicated quantum dots have been studied by many methods: perturbation theory [22], numerical diagonalization [23], density-functional theory [24, 25], unrestricted Hartree-Fock [26], diffusion Monte Carlo [27] and path-integral Monte Carlo [3, 28–31] methods. In these studies the electronic structure, addition spectra, electronic states, Fermi liquid and Wigner molecule behaviour, ground and excited state energies, shell effects, electron correlations and low-energy states were examined.

The next section briefly presents the PIMC method and details of our simulation procedure. In Sect. 3 we describe the two-coupled-dots system that we are interested in, with the relevant analytical one-particle distributions and energetics. The two last sections report the simulation results and our conclusions for the two-electron system.

2 Method

2.1 Path-Integral Monte Carlo Method

All stationary properties of a quantum many-body system with Hamiltonian $\widehat{H}$ in thermal equilibrium are obtained from the density matrix [32] $\hat{\rho} = \exp(-\beta\widehat{H})$ as expectation values $\langle\widehat{A}\rangle = Z^{-1}\,\mathrm{Tr}(\hat{\rho}\widehat{A})$, where $\beta \equiv (k_\mathrm{B}T)^{-1}$ is the inverse tem-

perature, $\widehat{A}$ is the operator of the property in question and $Z = \mathrm{Tr}(\hat{\rho})$ is the partition function.

In the position representation the density matrix $\hat{\rho}$ reads as

$$\rho(\boldsymbol{R}, \boldsymbol{R}'; \beta) = \langle \boldsymbol{R} | \exp(-\beta \widehat{H}) | \boldsymbol{R}' \rangle, \tag{1}$$

where $\boldsymbol{R} = (\boldsymbol{r}_1, \boldsymbol{r}_2, \ldots, \boldsymbol{r}_N)$ are the coordinates of the N particles. Thus, the one-particle distribution is

$$\begin{aligned} \rho(\boldsymbol{r}) &= \int \rho(\boldsymbol{R}, \boldsymbol{R}; \beta)\, d\boldsymbol{r}_2\, d\boldsymbol{r}_3 \cdots d\boldsymbol{r}_N \big|_{\boldsymbol{r}_1 = \boldsymbol{r}} \\ &= \int \delta(\boldsymbol{r} - \boldsymbol{r}_1) \rho(\boldsymbol{R}, \boldsymbol{R}; \beta)\, d\boldsymbol{R} \end{aligned} \tag{2}$$

and the simple 1D pair-correlation function for two particles is

$$g(r) = \int \delta(r - |\boldsymbol{r}_1 - \boldsymbol{r}_2|) \rho(\boldsymbol{R}, \boldsymbol{R}; \beta)\, d\boldsymbol{R}, \tag{3}$$

assuming normalization of the density by

$$\int \rho(\boldsymbol{R}, \boldsymbol{R}; \beta)\ d\boldsymbol{R} = 1. \tag{4}$$

The path-integral representation of the density matrix discretized in the primitive approximation [33] is a multidimensional integral [34, 35], which turns out to be a partition function of one specific classical many-particle canonical ensemble or NVT-system with

$$Z = N_Z \int \exp\left[-\beta \sum_{n=1}^{M} (K_n + U_n) \right] d\boldsymbol{r}_1 \cdots d\boldsymbol{r}_M, \tag{5}$$

where the normalization constant $N_Z = (mM/(2\pi\hbar^2\beta))^{dN/2}$ and internal and external energies of the system are described by K_n and U_n, respectively. They are written as

$$K_n = \frac{mM}{2\hbar^2\beta^2} (\boldsymbol{r}_{n-1} - \boldsymbol{r}_n)^2, \tag{6}$$

$$U_n = \frac{1}{2M} (V(\boldsymbol{r}_{n-1}) + V(\boldsymbol{r}_n)), \tag{7}$$

and $V(\boldsymbol{r})$ is a local external potential, and we require periodic boundary conditions in imaginary time τ, i.e., all paths have to be closed, and thus, $\boldsymbol{r}_0 = \boldsymbol{r}_M$. The primitive approximation is exact at the limit $\tau = \beta/M \to 0$, and thus it will converge to the correct description, given small enough τ. Furthermore, it ''contains all the physics'' and it is simple and well defined [33].

This specific classical system consists of N closed chains or ''polymers'' or ''necklaces'' of M knots or ''beads'' with a certain special description of interactions among the N particles and between the external potential. The Trotter number M is the degree of discretization. This is the famous mapping from a quantum system to a classical system [33].

The quantum kinetic energy part corresponds to a classical spring potential connecting neighbouring beads representing the same particle. The interbead

potential (spring constant) depends on both M and $\beta = 1/k_{\mathrm{B}}T$. It is easier to obtain a good approximation to the high-temperature density matrix with respect to M, since the high-temperature behavior is more classical-like [36]. The lower the temperature, the more beads on the necklace are needed for the proper quantum description. We will demonstrate this below.

In summary, the description of a finite-temperature quantum statistical system is reduced to that of one specific classical NVT-system. For simulation of this there is the powerful Metropolis Monte Carlo (MMC) algorithm [37]. Thus, PIMC is a combined path-integral formalism and MMC, that has shown to be a powerful computational technique, capable of simulating boson systems exactly and fermions accurately [36]. Furthermore, with this technique all the approximations are controllable.

It is straightforward to calculate scalar operators, such as density, the potential energy, and the pair correlation functions as they are simply averages over the paths [33]. Use can be made of the symmetry in imaginary time, since all time slices are equivalent. Thus, the average density is

$$\rho(\boldsymbol{r}) = N_\rho \sum_{n,i,t} \langle \delta(\boldsymbol{r} - \boldsymbol{r}_{nit}) \rangle \tag{8}$$

where n refers to different beads of particles, i and t to MMC steps. This can be evaluated directly during the stationary simulation process. Similarly, data for the 3D pair correlation function

$$g(\boldsymbol{r}) = N_g \sum_{n,i\neq j,t} \langle \delta(\boldsymbol{r} - (\boldsymbol{r}_{nit} - \boldsymbol{r}_{njt}) \rangle \tag{9}$$

can be collected from the MMC path.

The nondiagonal properties in coordinate basis, such as the energy, the free energy, and the momentum distribution, are not so straightforward to calculate. The thermodynamic estimator of the energy is obtained by differentiating the partition function with respect to the inverse temperature [33]

$$E_T = -\frac{1}{Z}\frac{dZ}{d\beta} = M\langle dN/(2\beta) - K_n + V_n/M \rangle. \tag{10}$$

So, the path-integral Monte Carlo simulation method is a formally exact finite-temperature approach, where the only limiting factor is the computational capacity needed for evaluation of the density matrix $\rho(\boldsymbol{R}, \boldsymbol{R}'; \beta)$ with large enough Trotter number M.

2.2 Simulation Procedure and Parameters

We run Metropolis Monte Carlo in its standard form, only searching for the effective algorithm for random sampling of the configuration space.

In the simplest choice for the transition probability, *the classic rule*, a single particle at a single time slice is displaced uniformly inside a cube of side length Δ, adjusted to achieve 50% acceptance rate. This is inefficient at very large particle numbers: Interactions prevent sizeable displacements of a single particle [38]. As

the main issue is whether the configuration space is explored thoroughly in a reasonable amount of computing time obeying the principle of detailed balance, we do the following.

We include many types of moves, which makes the algorithm more robust. We separate the steps in the *xy*-plane and *z*-direction. We have two types of steps, one for a randomly selected bead in one random necklace and another for the centre of mass of the necklace. We use the classic rule such that the acceptance frequency of each move is about the same. The step lengths vary from 0.5 to 9 nm in both the *z*-direction and the *xy*-plane for one bead and for the centre of mass from 0.05 to 3 nm in the *z*-direction and from 10 to 50 nm in the *xy*-plane.

We choose the Trotter numbers in powers of 2. Using small Trotter numbers, the stationary state can be achieved more easily. Therefore, we found it useful to take the initial configuration for the case $M = 2^n$ from the $M = 2^{n-1}$ case by doubling the number of beads: inserting one more between the existing ones. The above choice of moves prevents us using too large Trotter numbers (larger than 2^{11}) because the configuration space should be explored thoroughly in a reasonable amount of computer time.

To check out the choice of parameters and the numerical scheme we have carried out extensive and systematic tests.

3 Two Coupled Quantum Dots

3.1 Structure Parameters

The system of two vertically coupled QDs is taken from Pi et al. [4]. They have considered it experimentally and realized by semiconductor technology as a layered circular mesa with two axially symmetric GaAs QDs with electrodes to control the number of trapped electrons. Thus, the vertical confining potential consists of two quantum wells of depth 300 meV and width of $W = 12$ nm and a barrier in between of width $b = 2.4$ nm. The potential profile is shown in Figs. 1 and 2, below.

In this two-electron problem the exact Hamiltonian reduces to the centre of mass (CM) and the relative motion [6]. The CM solutions are known analytically, but the relative motion must be determined numerically.

The two-dimensional lateral confinement is approximated by a harmonic potential assuming circular symmetry and ''strength'' $\hbar\omega = 5$ meV. Thus, the system consists of two disc-like QDs axially on top of each other, with the disc diameter an order of magnitude larger than the disc thickness.

Assuming GaAs material parameters throughout the structure, we use the electron effective mass $m^\star = 0.067 \times$ free electron mass and the dielectric constant $\epsilon = 12.4$ everywhere.

3.2 Analytical Distribution Functions

The three-dimensional wavefunction and distributions of a single electron are separable to three one-dimensional contributions in this geometry. In the present case, however, we find it more representative to project out the one-dimensional vertical

and the two-dimensional lateral contributions. Thus, we define the projected one-particle densities

$$\rho_z(z) = \int \rho(\boldsymbol{r})\, dx\, dy \tag{11}$$

and

$$\rho_{xy}(r_{xy}) = \int \rho(\boldsymbol{r})\, dz, \tag{12}$$

where $r^2 = r_{xy}^2 + z^2 = x^2 + y^2 + z^2$. Similarly we define for the pair correlation functions

$$g_z(z) = \int \delta(z - |z_1 - z_2|)\rho(\boldsymbol{R}, \boldsymbol{R}; \beta)\, d\boldsymbol{R} \tag{13}$$

and

$$g_{xy}(r_{xy}) = \int \delta(r_{xy} - |r_{1xy} - r_{2xy}|)\rho(\boldsymbol{R}, \boldsymbol{R}; \beta)\ d\boldsymbol{R}. \tag{14}$$

These can be readily evaluated from the analytical one-electron distributions for a single electron (or two noninteracting electrons) in our coupled QD model. The vertical unnormalized wave function for the symmetrical double quantum well is [39]

$$u(z) = \begin{cases} \cosh kz \quad \text{or} \quad \sinh kz, & \text{for} \quad 0 < z < b/2, \\ A \sin qz + B \cos qz, & \text{for} \quad b/2 < z < b/2 + W, \\ Ce^{-kz}, & \text{for} \quad z > b/2 + W, \end{cases} \tag{15}$$

where $k^2 = |E_z|/\lambda$, $q^2 = (V - |E_z|)/\lambda$, $\lambda = \hbar^2/2m^\star$, E_z is the (quantized) eigenenergy and the constants A, B, and C are chosen to make the wave function and its derivative continuous. The functions $\cosh(kz)$ and $\sinh(kz)$ are the even and odd parity solutions, respectively, implying an obvious behavior of $u(z)$ at $z < 0$, not written in Eq. (15), explicitly.

The finite-temperature density matrix can be written now as

$$\rho(z, z'; \beta) = N(\beta) \sum_i u_i^*(z) u_i(z') \exp[-\beta E_{iz}], \tag{16}$$

where at low temperatures we can restrict to the sum over a finite number of lowest quantum states and $N(\beta) = \left\{\sum_i \exp[-\beta E_{iz}]\right\}^{-1}$. Similarly the energy expectation value is obtained from

$$\langle E_z \rangle = \sum_i E_{iz} \exp[-\beta E_{iz}], \tag{17}$$

which should be evaluated numerically as the eigenenergies are solved from implicit equations.

Note that there is only a finite number of bound states in the potential well of finite depth V, over which the summing is carried out. Omission of the continuum states introduces an error, which is, however, negligible at such low temperatures considered here.

In the horizontal plane the case is a simple two-dimensional harmonic oscillator, found in good text books of quantum mechanics. The two-dimensional one-electron finite-temperature electron distribution is

$$\rho_{xy}(\boldsymbol{r}_{xy}, \boldsymbol{r}'_{xy}) \propto \exp\left[\frac{-m\omega}{2\hbar \sinh(\hbar\omega\beta)} \times ((\boldsymbol{r}_{xy}^2 + \boldsymbol{r}_{xy}'^2)\cosh\hbar\omega\beta - 2\boldsymbol{r}'_{xy} \cdot \boldsymbol{r}_{xy})\right] \tag{18}$$

and the energetics can be summed up, giving

$$\langle E_{xy} \rangle = 2\frac{\hbar\omega}{2}\coth\frac{\hbar\omega\beta}{2}. \tag{19}$$

While the level spacing in the vertical quantum problem is about 50 meV, in the horizontal harmonic oscillator it is 5 meV with the degeneracy increasing linearly

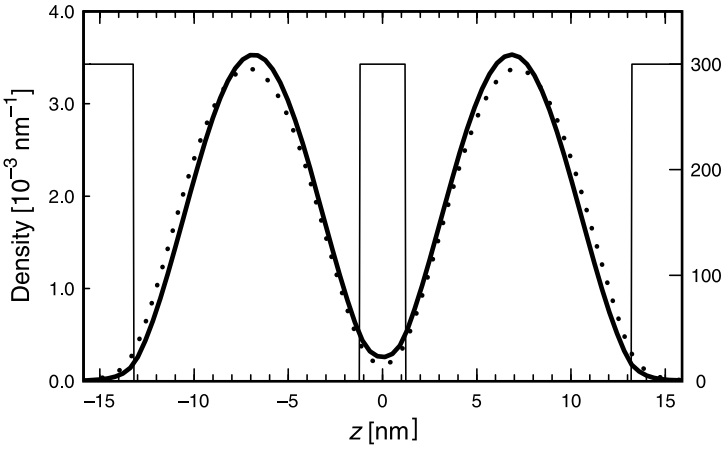

Fig. 1. Analytical vertical (z) one-particle distribution functions at different temperatures in the confining potential of 300 meV. The probability distributions $\rho(z)$ are in arbitrary units but normalized to the same constant. The shown distributions are 10 K (solid) and 300 K (dotted)

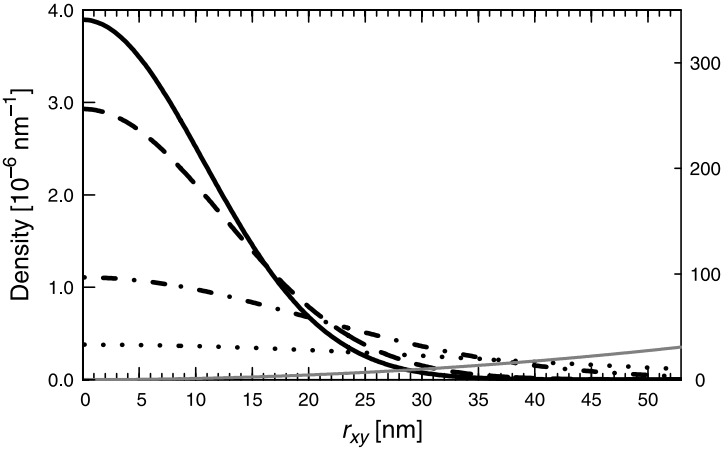

Fig. 2. Analytical horizontal (xy) one-particle distribution functions at different temperatures and the confining potential with $\hbar\omega = 5$ meV (~ 30 meV at 50 nm). The two-dimensional integrals (with a weight $4\pi r^2$) of shown distributions are normalized to the same constant. The distributions are from 10 K (solid), 30 K (dashed), 100 K (dash-dotted), and 300 K (dotted)

in energy. The separable energy contributions from the z confinement and xy harmonic potential simply add up.

The vertical and horizontal confining potentials and distributions are shown in Figs. 1 and 2, respectively. The confinement is seen to be one to two orders of magnitudes stronger in the vertical direction, resulting in essential differences in the temperature response of the one-particle density.

In Fig. 1 it is seen that only at 300 K a small shift of the density away from the centre barrier takes place, resulting in a decrease of tunneling there. This is probably a contribution from the continuum states. Fig. 2, on the contrary, shows the strong temperature broadening, as expected.

Like the energies, the densities of separable dimension simply ''add up'', too. From these one-particle densities we have calculated the pair correlation functions of the two noninteracting electrons, to be used as a reference in search of the two-electron correlation effects, later. The two-noninteracting-electron pair correlation function is a simple convolution-like distribution.

4 Simulation Results

4.1 Single Electron Distributions and Energies

Simulations with large enough Trotter numbers accurately reproduce the analytical one-particle distributions of the single-electron system (or two noninteracting electrons) shown in Figs. 1 and 2 both as vertical (z) and lateral (xy) projections of the three-dimensional distribution, respectively. Due to the limited computing capacity we were able to verify this at higher temperatures, $T \geq 10$ K, only.

The analytical temperature-dependent energies are easily obtained from Eqs. (17) and (19). The 2D harmonic oscillator energy raises from the zero-Kelvin quantum limit 5 meV to about 18 and 52 meV at 100 and 300 K, respectively. The corresponding energies for the 1D ''vertical'' double QD are about 24, 25, and 30 meV, in the same order. Whereas the contributions from the kinetic and potential energies are equal in case of the harmonic oscillator, the 1D ''vertical potential energy'' is about 6 meV at all temperatures. The sum of the 1D and 2D contributions yields the total energies 29, 43, and 82 meV, for the zero-Kelvin quantum limit, 100 and 300 K, respectively.

At lower temperatures higher Trotter numbers are required to reach the quantum statistical limit. Below this limit the correct quantum statistical behavior is not found, but classical-like features emerge. For example, discontinuous distributions at potential discontinuities are seen. On the other hand, this can be used to demonstrate the classical-to-quantum transition, see Fig. 3, where for the lowest temperature $T = 3$ K the Trotter number $M = 2048$ is clearly too small, or correspondingly, $\tau = \beta/M$ is too large.

Discontinuities in classical distributions emerge, of course, in cases of discontinuous confining potentials only. These are more critical at the quantum limit and more different from the classical system, too. Thus, in our case in the horizontal harmonic potential the quantum limit is reached already with smaller Trotter numbers.

We should note that these distributions are essentially the same as those of Pi et al. [4] for the similar system. In their DFT study the number of electrons

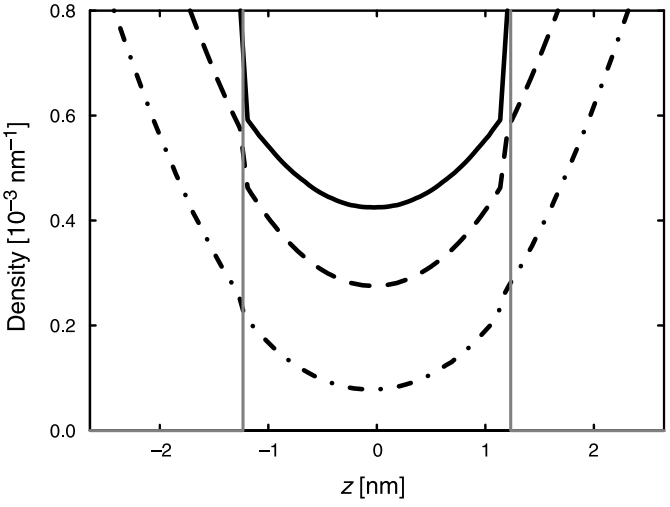

Fig. 3. Projected one-particle distribution functions in vertical (z) direction from simulations of a single electron with $(k_B\tau)^{-1} = (T \times M) = 3\,\mathrm{K} \times 2048 = 6144\,\mathrm{K}$, $10\,\mathrm{K} \times 2048 = 20480\,\mathrm{K}$, and $30\,\mathrm{K} \times 2048 = 61440\,\mathrm{K}$. The distributions are from 3 K (solid), 10 K (dashed), 30 (dash-dotted)

occupying the QDs was not found to essentially effect on the one-electron distributions, and our results for the two-electron case, below, support this general conclusion. However, there are small effects from electron-electron correlations, which we will analyze in what follows.

4.2 Two Interacting Electrons

Let us consider the system of two correlated electrons next and start by comparing the ''correlated'' one-electron distributions to the uncorrelated ones, i.e., to the single-electron distributions shown in Figs. 1 and 2. As the distributions are rather similar, we show the differences of those only in Figs. 4 and 5, respectively.

In both cases we see two expected main features. First, turning on electron-electron repulsion decreases the density where it is high, by shifting it to the less

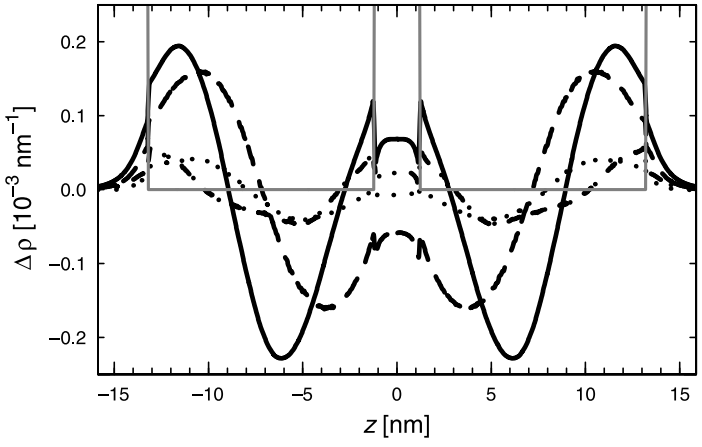

Fig. 4. Difference of the vertical (z) one-particle distribution function between the ''correlated'' two-electron and single-electron case. Thus, the two-electron distribution is a sum of the contributions given in Fig. 1 and this one. Note the different scaling of vertical axes in these figures. The notation for different temperatures is the same as in Fig. 1

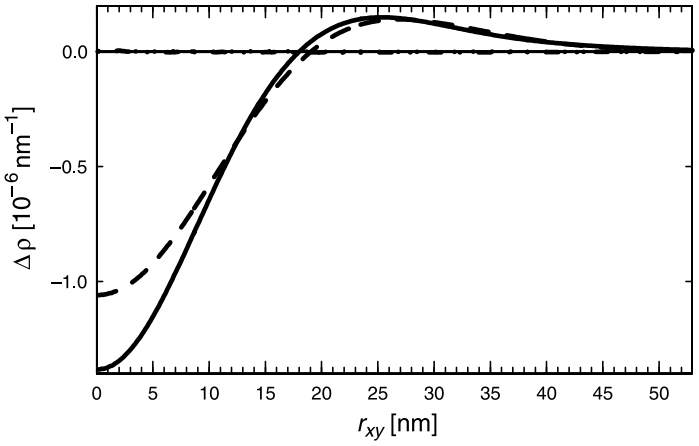

Fig. 5. Difference of the horizontal (*xy*) one-particle distribution function between the "correlated" two-electron and single-electron case. Again, the two-electron distribution is a sum of the contributions given in Fig. 2 and this one. The notation for different temperatures is the same as in Fig. 2

occupied regions of space. Secondly, the correlation effects are the larger the lower the temperature is.

In Fig. 4 the fine scaling zooms in the small discontinuities, which are visible at lower temperatures only, revealing that even larger Trotter numbers should be used to reach the quantum description limit more accurately. Fig. 5 shows that correlation effects are negligible in the horizontal distribution at the two highest temperatures, but essential at the two lower ones.

In Figs. 6 and 7 the two relevant projections of the pair correlation function in our case are shown, whereas Fig. 8 presents the conventional radial pair correlation function, good in characterizing isotropic systems. Clearly the vertical and radial functions reflect the same feature natural for a double QD: The electron correlation from repulsive interaction favors the case of one electron in each QD. This effect is stronger at the two lowest temperatures, as is seen in Fig. 6.

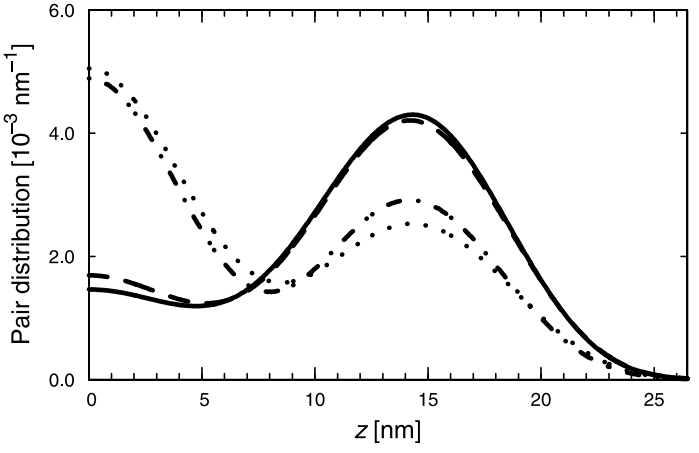

Fig. 6. Projected vertical (*z*) pair correlation function at various temperatures. The notation for different temperatures is the same as in Fig. 4

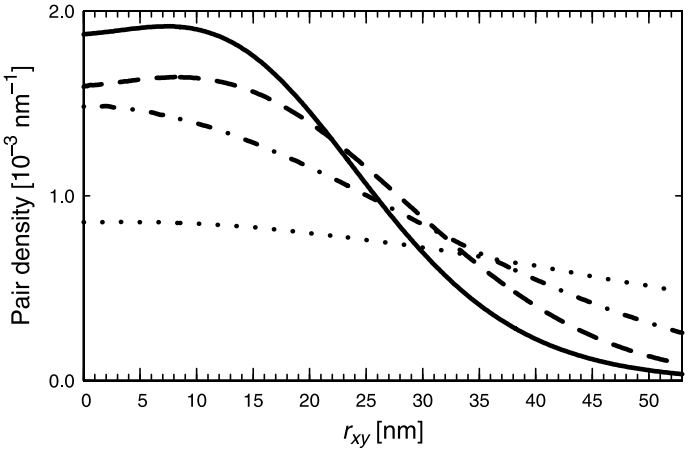

Fig. 7. Projected horizontal (xy) pair correlation function at various temperatures. The notation for different temperatures is the same as in Fig. 4

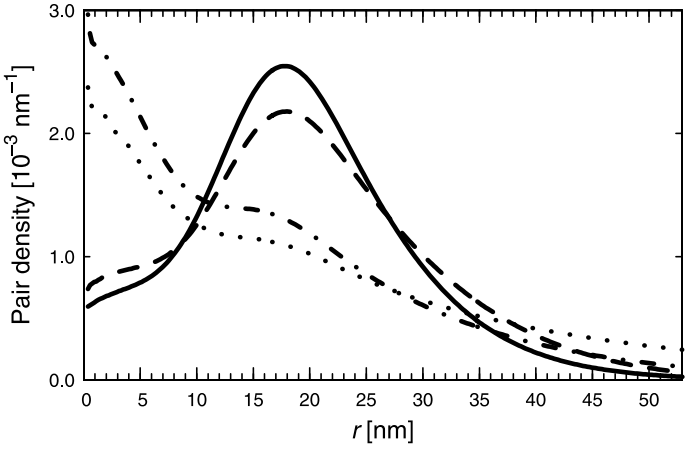

Fig. 8. (Radial) pair correlation function at various temperatures. The notation for different temperatures is the same as in Figs. 6 and 7

The dimensionality effect or separability of the three-dimensional system to the one- and two-dimensional subsystems can now be considered. The main question is: Does the small but finite vertical extension (z) have an essential effect on the electronic structure in the lateral (xy) plane [4, 6]? For the one-particle distribution the answer is obviously ''no'', because the one-particle distributions of the two-electron case and the single-electron case do not essentially differ and the latter is analytically separable to three dimensions. However, for the detailed two-electron distribution the answer is different as indicated by the low-temperature pair correlation functions. Clearly, at low temperatures where the electrons occupy the centre of the disc, see Figs. 7 and 6, the third dimension allows more freedom for this for both of the electrons simultaneously. However, the increase of temperature allows an occupation of the lateral space further away, which seems to cover the quantum and correlation effects.

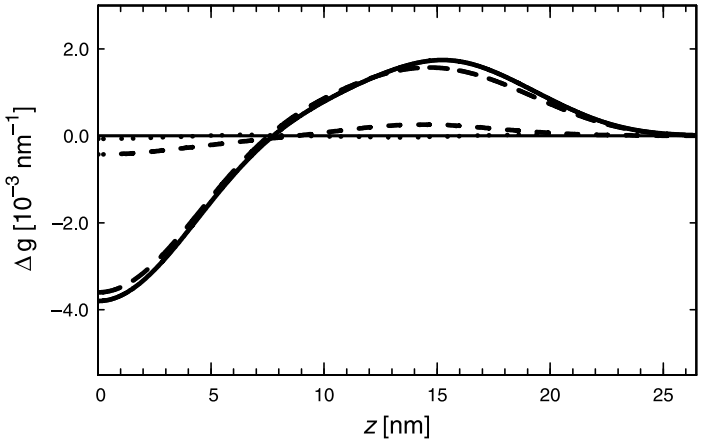

Fig. 9. Projected vertical (z) correlation hole at various temperatures

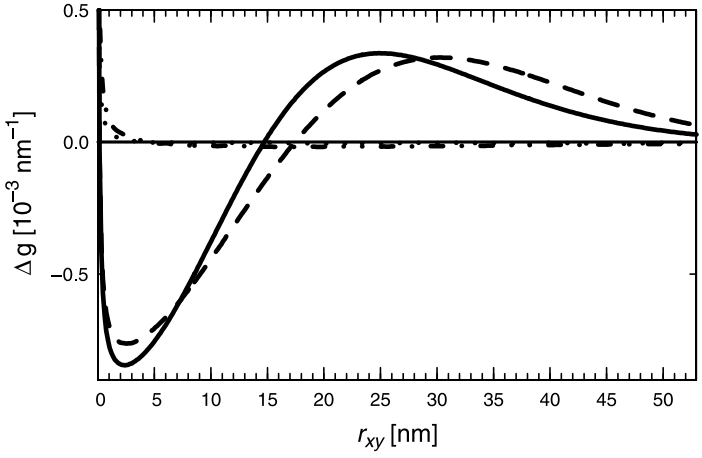

Fig. 10. Projected horizontal (xy) correlation hole at various temperatures

The same conclusions can be drawn from the correlation holes shown in Figs. 9 and 10. Here, the case is even more clear: At temperatures 100 and 300 K the presence of the second electron does not essentially effect on the dynamics of the first one. At lower temperatures 10 and 30 K, however, a more conventional correlation hole is seen, both vertically and laterally.

Table 1. Energetics of the two interacting electrons in the double quantum dot given per one electron. Uncertainty for the potential energy V_{pot} and mutual interaction energy V_{ee} are at least 5 and 0.5 meV, respectively

T [K]	V_{pot} [meV]	V_{ee} [meV]
3	15	2
10	15	2
30	10	2
100	15	2
300	30	1

Though we were able to reach a sufficient convergence for the distributions, regarding the energetics we are able to give rough estimates for some contributions only. These are presented in Table 1. The computational capacity gets a limitation, at lower temperatures in particular. Within the statistics, we are not able to find differences in the external potential energies of one of the interacting electrons and a single electron (or one of the two noninteracting ones). In both cases this potential-energy contribution grows from the zero-Kelvin quantum limit of about 15 meV to about 30 meV at 300 K, in fair agreement with the analytical single-electron case, where the total energies are 29 and 82 eV. The mutual Coulomb (repulsion) energy of the two electrons is about 1–2.5 meV, see Table 1. Surprisingly, only a small difference is found for two interacting electrons and two noninteracting ones, the latter one evaluated from the simulated noninteracting electron ''dynamics''. We are not able to obtain estimates for kinetic energies, the main reason being the discontinuous external potential function.

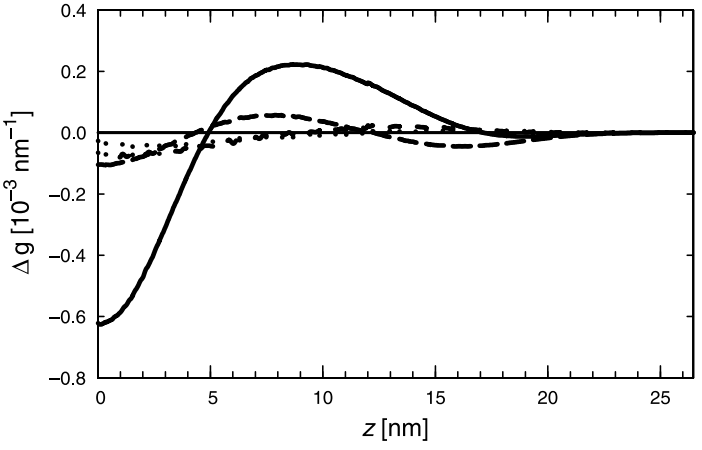

Fig. 11. Single QD case: Projected vertical (z) correlation hole

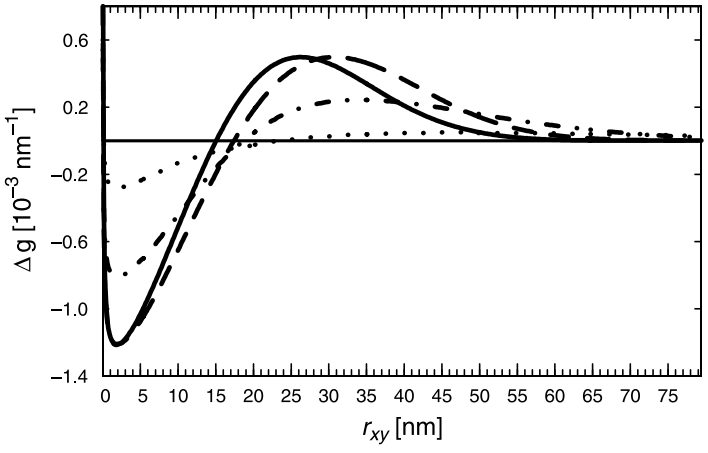

Fig. 12. Single QD case: Projected horizontal (xy) correlation hole

Finally, just for comparison, we consider the case of two electrons in *a single QD*, one of those coupled ones considered above. The projected correlation holes for this case are shown in Figs. 11 and 12 to be compared with Figs. 9 and 10. The stronger confinement in the vertical direction is seen directly in the vertical projection and indirectly in the horizontal projection. In the horizontal correlation this implies the temperature dependence even at higher temperatures. This is expected as there is less spatial freedom for electrons to occupy, unless thermally activated to higher quantum states.

5 Conclusions

We have shown that path-integral Monte Carlo (PIMC) simulations can be successfully carried out for one and two correlated electrons in a model quantum dot (QD). The case of ''spinless electrons'' of the two is considered only, and no magnetic field is applied in the studies reported here, either. We have considered disc-like, almost two-dimensional ''harmonic confinement QDs''. The main interest is in two QDs on top of each other and coupled through a narrow barrier, but a single one is considered for comparison.

The simulated one-particle distributions are very similar to those from the DFT calculations for the same system. With PIMC we find that the one-particle distributions for a single electron and for two electrons are almost identical in all cases independent of the temperature. Increase of temperature just broadens the distributions as expected, the effect being slightly smaller for correlated electrons than for the single one.

The Coulomb correlation of the two electrons is analyzed in terms of pair correlation functions and correlation holes. The perpendicular to the discs (vertical) and horizontal contributions are projected out from the fully 3D functions. This allows us to analyze the semiconductor dimensionality effect: Is the third dimension or the thickness of the almost two-dimensional disc-like QD essential for the horizontal distribution in the disc plane? The one-particle distributions are trivially separable to the vertical and horizontal contributions, but this turns out not to be the case for the two-particle distributions.

Generally, the correlations become more important at lower temperatures (10 and 30 K). At higher temperatures (100 and 300 K) the thermal broadening in the mixed quantum state description screens the correlation effect efficiently. For this reason, also the finite thickness of the QD disc is essential at the lower temperatures only, and also for the two-particle distribution only.

Evaluation of accurate energies takes more computational capacity than there is available today. This is true for the low-temperature quantum statistics in particular. Therefore, we are able to give rough estimates for some of the energy contributions only. We are able to predict that in case of our double QD structure the external potential energy is not strongly dependent on the temperature or correlation effects. Similarly, the mutual Coulomb energy seems to be constant throughout the various conditions of our system that we have considered.

We find that computational capacity becomes the limiting factor in simulations with increasing accuracy or with an increasing number of particles. In particular, this is true for fermion systems.

References

1. Kouwenhoven, L., Austing, D., Tarucha, S.: Rep. Prog. Phys. **64**, 701 (2001)
2. Reimann, S. M., Manninen, M.: Rev. Mod. Phys. **74**, 1283 (2002)
3. Harting, J.: PhD Thesis. University of Oldenburg 2001 (unpublished)
4. Pi, M., et al.: Phys. Rev. **B63**, 115316 (2001)
5. Leino, M., Rantala, T. T.: Physics Scripta **T114**, 44 (2004)
6. Rontani, M., et al.: Phys. Rev. **B59**, 10165 (1999)
7. Taut, M.: Phys. Rev. **A48**, 3561 (1993)
8. Dineykhan, M., Nazmitdinov, R.: Phys. Rev. **B55**, 13707 (1997)
9. Lin, J. T., Jiang, T. F.: Phys. Rev. **B64**, 195323 (2001)
10. Harju, A., Sverdlov, V., Nieminen, R.: Phys. Rev. **B59**, 5622 (1999)
11. Harju, A., et al.: Physica **B255**, 145 (1998)
12. Merkt, U., Huser, J., Wagner, M.: Phys. Rev. **B43**, 7320 (1991)
13. Ugajin, R., et al.: J. Appl. Phys. **76**, 1041 (1994)
14. Rontani, M., et al.: Solid State Commun. **119**, 309 (2001)
15. Burkard, G., Seelig, G., Loss, D.: Phys. Rev. **B62**, 2581 (2000)
16. Lee, E., et al.: Phys. Rev. **B57**, 12281 (1998)
17. Partoens, B., Peeters, F. M.: Phys. Rev. Lett. **84**, 4433 (2000)
18. Wensauer, A., et al.: Phys. Rev. **B62**, 2605 (2000)
19. Pi, M., et al.: Phys. Rev. Lett. **87**, 066801 (2001)
20. Imamura, H., Maksym, P. A., Aoki, H.: Phys. Rev. **B59**, 5817 (1999)
21. Tanaka, Y., Akera, H.: Phys. Rev. **B53**, 3901 (1996)
22. Rontani, M., et al.: Appl. Phys. Lett. **72**, 957 (1998)
23. Ezaki, T., Mori, N., Hamaguchi, C.: Phys. Rev. **B56**, 6428 (1997)
24. Lee, I.-H., et al.: Phys. Rev. **B57**, 9035 (1998)
25. Hirose, K., Wingreen, N. S.: Phys. Rev. **B59**, 4604 (1999)
26. Reusch, B., Häusler, W., Grabert, H.: Phys. Rev. **B63**, 113313 (2001)
27. Pederiva, F., Umrigar, C. J., Lipparini, E.: Phys. Rev. **B62**, 8120 (2000)
28. Häusler, W., et al.: Physica **B284**, 1772 (2000)
29. Mak, C., Egger, R., Weber-Gottschick, H.: Phys. Rev. Lett. **81**, 4533 (1998)
30. Egger, R., et al.: Phys. Rev. Lett. **82**, 3320 (1999)
31. Dikovsky, M. V., Mak, C. H.: Phys. Rev. **B63**, 235105 (2001)
32. Pollock, E. L., Ceperley, D. M.: Phys. Rev. **B30**, 2555 (1984)
33. Ceperley, D. M.: Rev. Mod. Phys. **67**, 279 (1995)
34. Feynman, R. P., Hibbs, A. R.: Quantum Mechanics and Path Integrals. New York: McGraw-Hill 1965
35. Feynman, R. P.: Statistical Mechanics. Reading, MA: Addison-Wesley 1972, 1988
36. Zong, F., Ceperley, D.: Phys. Rev. **E58**, 5123 (1998)
37. Harting, J., Mülken, O., Borrman, P.: Phys. Rev. **B62**, 10207 (2000)
38. Knoll, L., Marx, D.: Eur. Phys. J. **D10**, 353 (2000)
39. Gasiorowicz, S.: Quantum Physics. New York: Wiley 1996

Verleger: Springer-Verlag GmbH, Sachsenplatz 4–6, 1201 Wien, Austria. – Herausgeber: Prof. Dr. B. L. G. Bakker, Theoretical Physics Group, Department of Physics and Astronomy, Vrije Universiteit, De Boelelaan 1081, 1081 HV Amsterdam, The Netherlands. – Redaktion: De Boelelaan 1081, 1081 HV Amsterdam, The Netherlands. – Satz und Umbruch: Thomson Press (India) Ltd., Chennai. – Offsetdruck: Krips bv, Kaapweg 6, 7944 HV Meppel, The Netherlands. – Verlagsort: Wien. – Herstellungsort: Meppel. – Printed in The Netherlands.

PAPER III

Paper III: Leino et al. (2006)

M. Leino, J. Nieminen, and T. T. Rantala,

Finite temperature quantum distribution of hydrogen adsorbate on nickel (001) surface,

Surface Science, 600, 1860–1869, March 2006.

Available online at www.sciencedirect.com
SCIENCE DIRECT
Surface Science 600 (2006) 1860–1869
SURFACE SCIENCE
www.elsevier.com/locate/susc

Finite temperature quantum distribution of hydrogen adsorbate on nickel (0 0 1) surface

Markku Leino *, Jouko Nieminen, Tapio T. Rantala

Institute of Physics, Tampere University of Technology, P.O. Box 692, FI–33101 Tampere, Finland

Received 27 December 2005; accepted for publication 10 February 2006
Available online 3 March 2006

Abstract

Finite temperature quantum behavior of hydrogen and deuterium adsorbates on Ni(0 0 1) surface has been simulated using path-integral Monte Carlo technique. The adsorbate–surface interaction is described by the many-body alloy potential form, fitted to the adsorption parameters from DFT calculations. This allows consideration of substrate atom dynamics. Temperatures 100 K and 300 K have been considered and contribution of the thermal motion of Ni surface atoms is analyzed.

At low temperatures the quantum delocalization of the adsorbate is considerable, and therefore, temperature dependence of distributions is weak. In this case, the isotope effect is larger. At higher temperatures, however, the thermal dynamics of the substrate dominates all studied phenomena and classical description may be sufficient. By using a semi-classical description of the hydrogen adsorbate temperature dependence of the distributions and energetics becomes strong at all temperatures, providing that quantum description is necessary for the correct picture of H/Ni(0 0 1) system.

Keywords: Monte Carlo simulations; Nickel; Hydrogen atom

1. Introduction

Quantum behavior of H adsorbate on Ni and other metal surfaces has been of interest both experimentally [1,2] and theoretically [3–13]. It has been used to explain peculiar adsorbate diffusion [3–10], vibrational observations [3], electron-energy loss spectra [11,12], low-energy electron diffraction [11,12], photoemission [12], helium scattering [13], thermal desorption [4], linear optical diffraction [2] and field emission [1,2]. Most of the interesting quantum states relate to Ni(0 0 1) surface, where H adsorbate is known to delocalize and develop a two-dimensional band structure.

Quantum mechanical tunneling of a hydrogen atom between adjacent binding sites dominates diffusion at low temperatures, which is revealed by the fact that the diffusion constant is temperature independent [1–10,14]. The usual method for considering the temperature dependence of the diffusion constant from theoretical point of view is the path-centroid formulation, as proposed by Gillan [15,16], and further developed by Voth et al. [17,18]. Mattsson et al. has applied it widely [7–9]. Also quantum mechanical transition state theory [3,13,19] has been in extensive use in studies of hydrogen diffusion on a nickel surface.

The impurities of lattice, vacancies, other defects, relaxations or reconstructions, and most importantly at higher temperatures, the thermal motion of the surface need to be taken into account in studies of real surfaces [20–23]. Thus, for theoretical studies an accurate model for the interatomic interactions is required. Pair potentials cannot be expected to be successful. Therefore, several more sophisticated model potentials have been proposed, including semi-empirical potentials, embedded atom model, effective medium theory but also ab initio calculations for the

* Corresponding author. Tel.: +358 50 363 8659; fax: +358 3 3115 2600.
E-mail addresses: Markku.Leino@tut.fi (M. Leino), Tapio.Rantala@tut.fi (T.T. Rantala).

0039-6028/$ - see front matter © 2006 Elsevier B.V. All rights reserved.
doi:10.1016/j.susc.2006.02.017

potential energy surfaces have been carried out [6,7,10–12,15,24,25].

Furthermore, the complexity of hydrogen behavior on a nickel surface arises from the explicit involvement of dissipative forces due to phonons and other forms of excitations, defects, and strong interaction between the hydrogen and metal atoms. Only a few theoretical methods are capable of treating these problems.

We adopt the many-body alloy (MBA) potential [26] derived from tight-binding theory as a starting point for the adsorbate–surface interaction. It offers a possibility for extensions to description of both adsorbate–adsorbate interactions and metal surface dynamics at the finite temperature. Here, we first make the parametrization and assess the quality of resulting potential against chemisorption energies of ab initio DFT calculations and the spectroscopic observations mentioned above.

We then report fully quantum mechanical and thermally averaged constant temperature simulation of hydrogen atom on a rigid Ni(1 0 0) surface using path-integral Monte Carlo (PIMC) technique [27]. It implicitly includes thermal averaging over the quantum states of the hydrogen. Thus, we obtain the equilibrium energetics that is not provided by the path-centroid method used for evaluation of the diffusion constant. Next, we include the dynamics of the substrate nickel atoms. The thermal dynamics of Ni surface is taken into account classically and simulated with Metropolis Monte Carlo method (MMC).

Thus, we combine the PIMC for the H atom and MMC for Ni atoms into the same simulation to evaluate the finite temperature density matrix and the related distributions for the quantum adsorbed hydrogen under the influence of thermally distributed Ni surface atoms. We compare the results to the semi-classical "atoms at the adsorption sites" picture. We assess the quantum nature and temperature dependencies of the hydrogen distribution and differences with the semi-classical picture. We also consider the isotope effect by comparing distributions of hydrogen to those of deuterium.

This report is organized as follows. Section 2 describes the many-body alloy potential, in Section 3 is the path-integral formalism described, and the results are given in the Section 4. Finally, Section 5 collects the conclusions.

2. Many-body alloy potential

The analytical form of the many-body alloy potential is based on the tight-binding formalism [26,28] of bulk materials. The needed parameters can be fitted to ab initio or experimental data. It suits well for both single component and alloy bulk materials. It has been used for H/Pd systems and for studies of the electronic and structural properties of small clusters [29,30], surfaces of metals, and dilute metal alloys [28, and references therein]. Whether the same set of parameters is useful for different configurations—dimers, surfaces, bulk etc.—must be checked separately in each case.

The total (cohesive) energy of a crystal or a cluster is decomposed [26] into individual atomic contributions E_i as

$$E_{\mathrm{T}} = \sum_i E_i, \tag{1}$$

where i runs over all atoms in the system and

$$E_i = -\sqrt{\sum_{j\neq i} \xi_{\alpha\beta}^2 \exp\left[-2q_{\alpha\beta}\left(\frac{r_{ij}}{r_{0,\alpha\beta}}-1\right)\right]} + \sum_{j\neq i} \epsilon_{\alpha\beta} \exp\left[-p_{\alpha\beta}\left(\frac{r_{ij}}{r_{0,\alpha\beta}}-1\right)\right]. \tag{2}$$

The attractive part (first term) is due to the hybridization of orbitals. It is based on a parameterized tight-binding Hamiltonian and the second-moment approximation. The repulsive part (second term) is parameterized as a pair-wise Born–Mayer potential with an exponential distance dependence [26].

The parameters are defined for atom pairs (i,j) of elements α and β. Five parameters for each different pair are needed. These are the attraction due to overlapping orbitals $\xi_{\alpha\beta}$ and the pair-wise repulsion energy $\epsilon_{\alpha\beta}$, both given at the equilibrium distance $r_{0,\alpha\beta}$. The distance dependence of attractive and repulsive parts are scaled by the parameters $p_{\alpha\beta}$ and $q_{\alpha\beta}$, respectively.

Next, we consider the parameters for hydrogen on nickel. The parameters used for Ni–Ni interactions are fitted to bulk properties, and H–Ni parameters fitted to adsorption properties. General principles based on atom pair interactions and bulk cohesion are outlined in Appendix A.

2.1. Ni–Ni bulk

First, we discuss the interaction between metal atoms, since they are needed in fitting the H–Ni parameters to the adsorption data. The fitting can be done to bulk properties, for which we use the following data [31]: $a = 3.52$ Å, $r_0 = 2.49$ Å, $E_{\mathrm{coh}} = -4.44$ eV and $B = 1.17$ eV/Å^3. In addition, the coordination number in the fcc lattice is $z = 12$.

Since this set of data still leaves us with one free parameter, we utilize the Sutton–Chen parameterization to start with [31] (see Appendix A). The scaling parameter for attraction is $m = 6$, which corresponds to $q = 3.0$. Using this value for q and bulk fitting, we obtain $p = 8.6197$, $\xi = 1.9659$ eV and $\epsilon = 0.1975$ eV.

2.2. Fitting H–Ni

We attempt to fit the H/Ni(0 0 1) MBA potential to the data given by Mattsson et al. [10], where adsorption of H on Ni(0 0 1) surface has been studied with an EMT-type model potential whose parameters are fitted to ab initio potential energy surface. The fitted quantities are the adsorption energy of the hollow site, $E_{\mathrm{ads}} = 2.8$ eV, the equilibrium distance from the surface at hollow site $r_{\mathrm{a}} = 0.5$ Å and the energy barrier between the hollow sites through the bridge site, $E_{\mathrm{barr}} = 0.14$ eV, see Ref. [10].

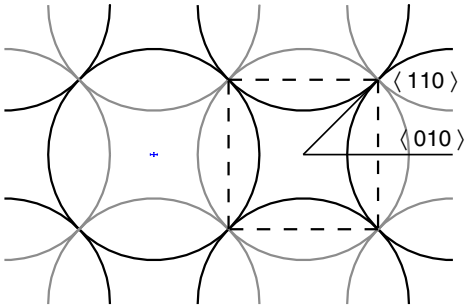

Fig. 1. Nickel (001) surface (of FCC lattice, $a = 3.52$ Å) schematically, surface and sub-surface layer atoms indicated by black and grey circles, respectively. The 4-fold hollow site is designated by the dashed square. The high-symmetry directions $\langle 010\rangle$ and $\langle 110\rangle$ along the surface are also shown. The RMS displacements related to the Ni atom thermal motion at the two temperatures, are also indicated on the left, see text.

This fitting gives parameters $q = 2.8698$, $p = 5.8659$, $r_0 = 1.4400$ Å, $\epsilon = 2.7006$ eV and $\xi = 5.5201$ eV. These give exact values for the chosen adsorption properties, but rather useless values for the dissociation energy ($E_d = 5.6390$ eV) and the force constant of the HNi molecule ($k = 45.7780$ eV/Å^2); the ab initio calculations [32] give $E_d = 3.1$ eV, $r_0 = 1.47$ Å and $k = 13.67$ eV/Å^2. Thus, fitting the surface properties leads to a parameterization that does not describe satisfactorily the HNi molecule.

2.3. H/Ni(001) model

The (001) surface of fcc nickel is illustrated in Fig. 1. The most relevant region for hydrogen adsorption is the 4-fold hollow site and the bridge site that presents the barrier between the adjacent hollow sites. The H and D distributions are given for the region depicted in Fig. 1.

In the present model consisting of N atoms, we have one quantum mechanically behaving hydrogen adsorbate on a surface of $N-1$ classical nickel atoms at either zero or at finite temperature. We take N large enough to give the hydrogen energetics from Eqs. (1) and (2) on an infinite Ni substrate. The hydrogen cut-off radius for MBA potential is essentially 8 Å, corresponding to $N \approx 100$.

It should be noted that the Ni surface seen by the hydrogen atom is perfectly periodical in two dimensions, expect for the thermal motion of Ni atoms. For nickel atom dynamics some finite-size effects may remain as a compromise with computational labour.

Fig. 2 shows the hydrogen equipotential curves at zero temperature in two high-symmetry planes perpendicular to the surface. Potential to the $\langle 1\,1\,0\rangle$ direction is identical with that of Mattsson et al. [10]. We see that the topsite barrier between hollow sites is about a double (0.3 eV) of that of the bridge site (0.14 eV).

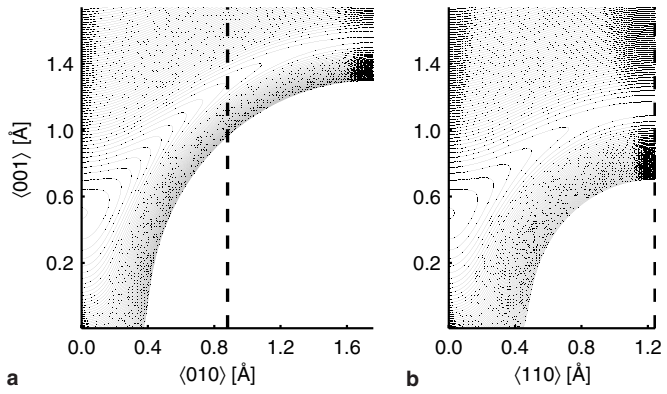

Fig. 2. Equipotential contour lines of the H atom MBA potential energy hypersurface in two surface perpendicular planes of rigid (001) surface of Fig. 1 from the hollow site to (a) the top site direction $\langle 010\rangle$ and (b) the bridge site direction $\langle 110\rangle$. The minimum at $z = 0.5$ Å corresponds to the adsorption energy 2.8 eV and line spacing is 25 meV.

3. Path-integral Monte Carlo method

All stationary properties of a quantum system with Hamiltonian $\widehat{H} = \widehat{T} + \widehat{V}$ in thermal equilibrium at temperature $\beta \equiv 1/k_B T$ are obtained from the density matrix $Z = \mathrm{Tr}\, e^{\beta \widehat{H}}$ [33]. Here, $\widehat{T} = \sum_{i=1}^{N} \hat{\mathbf{p}}_i^2/2m_i$ is the kinetic energy operator and $\widehat{V}$ includes the external potential and interactions between the quantum particles.

Obviously, quantum statistics is not important for nickel atoms at high temperatures. Even at $T = 100$ K the thermal wavelength [27] $\Lambda_\beta = (\hbar^2\beta/m)^{1/2} \approx 0.01$ Å is negligible compared to the interatomic spacing, 2.4 Å. Thus, the quantum statistics of nickel atoms becomes important only at sub-Kelvin temperatures.

3.1. Path-integral formalism

In the discrete path-integral representation partition function Z is the trace of the density matrix $\rho(\mathbf{r}', \mathbf{r})$ of one quantum particle in a d-dimensional space, given by

$$Z = \left(\frac{mM}{2\pi\hbar^2\beta}\right)^{d/2} \int \exp\left[-\beta \sum_{n=1}^{M} (K_n + U_n)\right] \mathrm{d}\mathbf{r}_0 \cdots \mathrm{d}\mathbf{r}_{M-1}, \tag{3}$$

where functions K_n and U_n define internal and external energies of the system. In the primitive approximation [27] they are written as

$$K_n = \frac{mM}{2\hbar^2\beta^2} (\mathbf{r}_{n-1} - \mathbf{r}_n)^2 \tag{4a}$$

and

$$U_n = \frac{1}{2M} (V(\mathbf{r}_{n-1}) + V(\mathbf{r}_n)), \tag{4b}$$

where m is the mass of the particle and M is called the Trotter number, and the periodic boundary conditions in imaginary time are taken into use, i.e. $\mathbf{r}_0 = \mathbf{r}_M$. The primitive approximation, where the external energy coincides with classical potential energy of the distribution, contains all the physics and converges to the correct limit, given a small enough β/M [27]. Furthermore, it is simple and well

defined, and at the limit $M \to \infty$ the exact many-body description of quantum system is obtained.

It is straightforward to calculate scalar operators, such as density and potential energy; they are simply averages over the path [27]. Use can be made of the symmetry in imaginary time, since all time slices n are equivalent. Thus, the average one-particle density is

$$\rho(\mathbf{r}) = N_\rho \sum_{i=1}^{N} \sum_{n=1}^{M} \delta(\mathbf{r} - \mathbf{r}_{i,n}), \tag{5}$$

where $\rho(\mathbf{r})$ is the diagonal part of the density matrix, $\rho(\mathbf{r}) = \rho(\mathbf{r},\mathbf{r})$, and N_ρ is a proper normalization factor for the total number of particles. N should be large enough for good sampling of the phase space at the temperature $T = 1/k_B\beta$.

The nondiagonal properties in coordinate basis, such as the energy, free energy, and momentum distribution, are not so straightforward to evaluate. The thermodynamic estimator of the energy is obtained by differentiating the partition function with respect to the inverse temperature [27] as

$$E_T(\beta) = -\frac{1}{Z}\frac{dZ}{d\beta} = M\langle dN/(2\beta) - K_n + U_n/M\rangle,$$

but this is not a useful estimator because of large fluctuations and statistical noise. Total energy can be approximated more accurately by using the virial theorem for kinetic energy

$$T_{vir}(\beta) = \tfrac{1}{2}\langle \mathbf{r}\cdot\nabla V(\mathbf{r})\rangle \tag{6}$$

and by calculating the potential energy by a scalar operator

$$E_{pot}(\beta) = \langle V(\mathbf{r})\rangle, \tag{7}$$

where the averages $\langle\cdot\rangle$ are evaluated with the density $\rho(\mathbf{r})$ as a weight function. The total energy is a sum of the two, $E_{tot}(\beta) = E_{pot}(\beta) + T_{vir}(\beta)$.

Path-integral Monte Carlo (PIMC) simulation method is a "formally exact" finite temperature approach for a quantum particle, the only limiting factor in accuracy being the computational capacity, for evaluation of the density matrix (3).

3.2. Monte Carlo simulation procedure

Conventionally, the Metropolis Monte Carlo scheme is used to evaluate the integral (3). With this technique all the approximations in the integration scheme and in path-integral formulation are controllable. The Metropolis algorithm samples effectively the one-particle distribution, and thus, the partition function Z using the integrand in (3) as the weight for the importance sampling process. The main issue is whether the configuration space is explored thoroughly in a reasonable amount of computing time. Inclusion of several types of Monte Carlo moves makes the algorithm more robust, since before calculation one does not necessarily know which type of moves will lead to a balanced sampling of the phase space and rapid convergence of expectation values. Therefore, we have used two types of moves: Some for one randomly selected "knot of the path", and another for the center-of-mass of the path.

Distribution of steps in the phase space was taken to be Gaussian such that the total Metropolis acceptance rate is about 40% and the frequency of each different type of move is about the same. This is called the *classic rule* [27] for sampling of the phase space.

Simulation is exact at the limit, where the Trotter number $M \to \infty$. However, usually the distributions and expectation values converge at some finite Trotter number, which depends on temperature and potential. This is clearly seen from the plots of adsorbate distribution at different Trotter numbers, and by testing the procedure for analytically solvable systems. We found sufficient convergence in our case with Trotter number $M = 64$. At 100 K this can be considered as a compromise with computational labour. The typical number of sufficient Monte Carlo steps is about 10^8.

4. Results

First, we describe the adsorbate distributions for the rigid and the finite temperature Ni surfaces, and then, we consider the energetics.

4.1. Adsorbate distributions

The hydrogen quantum distribution in the hollow site at low temperatures does not strongly depend on the actual temperature. It has been found to be rather similar to that at zero Kelvin [10–12]. We confirm the fact and illustrate it in Fig. 3 with the distributions from 100 K and 300 K. Indeed, rise of the temperature just slightly spreads out the distribution and the difference between the shown two almost vanishes.

The isotope effect in the distribution is more pronounced as seen in Fig. 4. Deuterium is clearly more localized: within the radius of 0.2 Å the probability density is higher and outside it is lower than that of hydrogen. A weak top-bridge direction difference is seen at the lower temperature, compare Fig. 4a and b, indicating that deuterium distribution is less circular or more classical, see below. Stensgaard and Jakobsen, cited in Ref. [10], have measured the spatial width $d = \sqrt{\langle x^2 + y^2\rangle}$ of deuterium on Ni(0 0 1) and found 0.20 Å in a nice agreement with our simulation.

It should be noted that the isotope effect is of quantum nature, as "classical" hydrogen and deuterium present identical distributions. The classical distribution and its temperature dependence is demonstrated in Fig. 5. It shows, first, the development of classical distribution from a delta function (a point) at 0 K to the extensive thermal distribution at 300 K, which is quite similar to that of quantum case. Second, comparison of Figs. 3 and 5 shows that the quantum delocalization is substantial, and relatively the

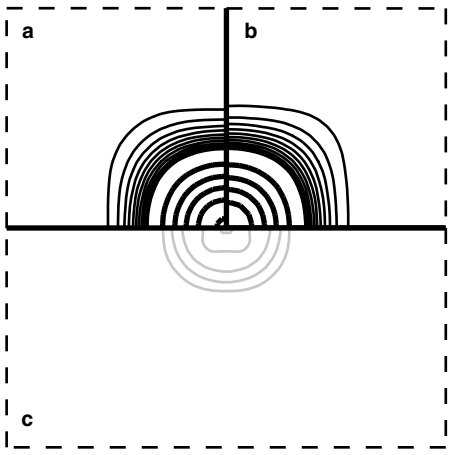

Fig. 3. Hydrogen adsorbate distributions at the hollow site of rigid substrate depicted in Fig. 1 (1.76 Å × 1.76 Å square). The equidensity contours present the three-dimensional density projected onto the surface plane, i.e., integrated over z-direction, at (a) 100 K, (b) 300 K and (c) the difference of the two ((b) − (a)). The thin and thick lines show densities $0.5, 1.0, 1.5, \ldots$ and $5, 10, 15, \ldots$ atoms/(surface unit cell); and the black and grey lines in (c) stand for positive and negative values, respectively. Here, the positive density difference is everywhere less than 0.5 atoms/(surface unit cell).

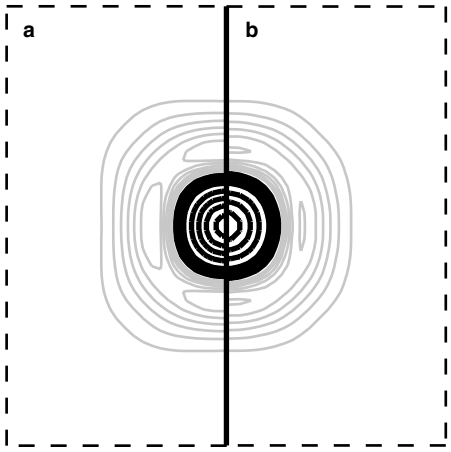

Fig. 4. Isotope effect at (a) 100 K and (b) 300 K. Differences between the deuterium and hydrogen distributions are shown, black and gray lines for positive and negative values, respectively. The equidensity curves are as defined in Fig. 3.

larger the lower the temperature. We see that only at 300 K the classical thermal spreading conceals the quantum delocalization. Instead, the thermal effect on quantum delocalization in the studies of hydrogen diffusion dynamics on Ni(0 0 1) [7,8] turns on at about 40 K, already. Third, the classical distributions are more bridge direction oriented compared with the quantum case, where tunneling allows more circular shape.

Next, we consider the case of finite temperature substrate in thermal equilibrium with the adsorbate. The substrate Ni atoms are found to have thermal fluctuation around their equilibrium positions with RMS displacements 0.05 Å and 0.08 Å at the temperatures 100 K and

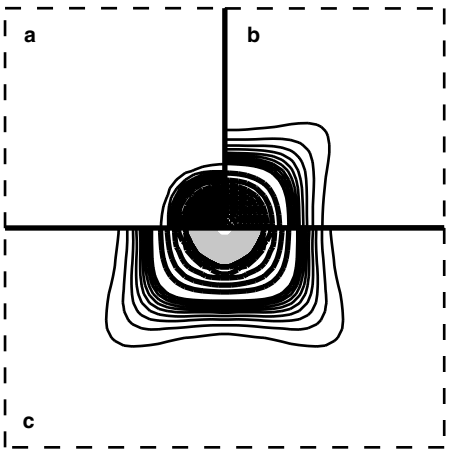

Fig. 5. The "classical hydrogen atom" distributions presented the same way as in the quantum case in Fig. 3, (a) 100 K, (b) 300 K and (c) the difference of the two ((b) − (a)).

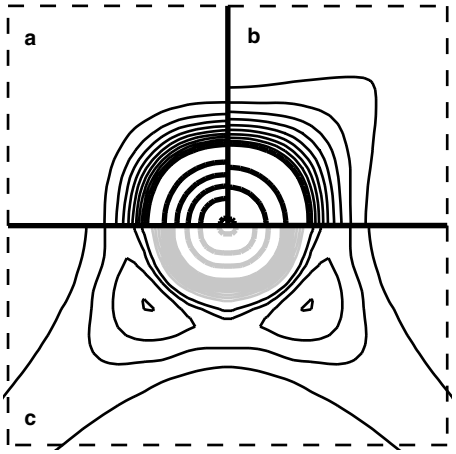

Fig. 6. The hydrogen atom distributions as in Fig. 3 but in thermal equilibrium with the same finite temperature Ni surface. Again, (a) 100 K, (b) 300 K and (c) the difference of the two ((b) − (a)).

300 K, respectively, shown in Fig. 1. In Fig. 6 we present the consequent adsorbed hydrogen atom distributions. Though, the RMS displacements of substrate atoms do not differ too much at these temperatures, the resulting adsorbate distributions do, as seen by comparison of Figs. 3 and 6. At 100 K the distributions seem to be almost identical (Figs. a), whereas at 300 K they look clearly different (Figs. b).

Fig. 6c reveals strong temperature dependence of the distribution, that can be expected to influence on the adsorbate diffusion dynamics. Although, we have not evaluated the diffusion constants, this leads us to suggest that the temperature dependence in hydrogen diffusion on Ni(0 0 1) surface is a consequence of substrate dynamics, above 100 K. This can be contrasted with the suggestion of temperature independence arising from quantum delocalization or tunneling, below 100 K [7].

The vertical adsorbate distributions shown in Fig. 7 support the ideas and conclusions, above: On the rigid surface

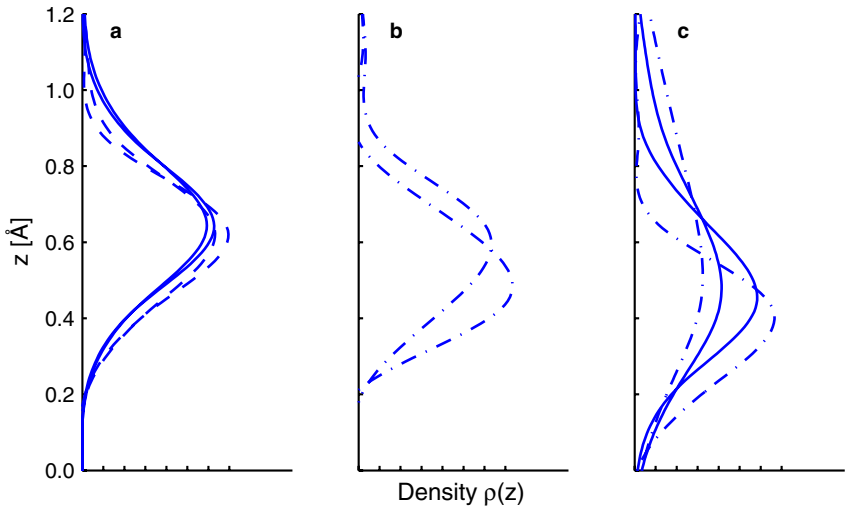

Fig. 7. Hydrogen atom distributions perpendicular to the surface, (a) quantum hydrogen (solid line) and deuterium (dashed), (b) classical hydrogen (dash-dotted) and (c) with substrate at finite temperature, hydrogen (solid line) and "classical hydrogen" (dash-dotted). All distributions are evaluated at 300 K (the one with maximum at higher z) and at 100 K (the one with maximum at lower z) temperatures.

the temperature dependence is weaker than the isotope effect, whereas it is strong for the classical adsorbate, but the largest effect on distributions arises from the finite temperature substrate dynamics in all cases. All of the vertical distributions turn out to be modified Gaussians with the width of about 0.4 Å and mean values being equal to the maxima at around 0.5–0.65 Å, except for some of the classical cases. The mean height coincides with the previously reported results, 0.6 Å [12,8].

4.2. Adsorbate energetics

Evaluation of energetics turns out to be a real computational challenge even in our case of a single quantum particle. This is due to the extremely slow convergence of statistics, although the distributions presented above have reached convergence by visual judgement. In the present case, we are able to present reliable estimates to the energy contributions in case of the rigid substrate, only.

Puska et al. [11,12] used the effective medium theory for interaction of the adsorbed hydrogen atom on Ni(0 0 1) and numerical solutions for the band structure was calculated. Mattsson et al. [8] solved the hydrogen energy levels in the ab initio DFT potential. In Table 1, a summary of these results is given. As the common basic features we can point out the lowest excited state at about 45–70 meV above the ground state and several below 100 meV.

We give the hydrogen and deuterium energetics from our PIMC simulations in Tables 2 and 3. The potential energies are referred to the bottom of the hollow site minimum. The standard error of mean is about 5 meV in all cases. Let us consider the hydrogen adsorbate first.

The potential energies are found to be about 85 meV and 90 meV for the two temperatures 100 K and 300 K, respectively. The corresponding kinetic energies evaluated from the virial formula are given as 95 meV and 100 meV, yielding the total energies as 180 meV and 190 meV. We find that our mixed state total energies are higher than those evaluated from the data in Table 1, properly weighting with the temperature. Thus, we note that the energies found here are higher than the barrier 140 meV at the bridge site between two adjacent hollow sites. But this is true for the quantum hydrogen, only, as the classical hydrogen energies, see Table 2, are 50 meV and 100 meV at 100 K and 300 K, respectively.

Table 1
Hydrogen atom energy "levels" on Ni(0 0 1) surface from the band structure calculations of Puska et al. [12] and Mattsson et al. [8] referred to the ground state

	A_1^0	A_1^1	E^1	E^2	A_1^2	100 K	300 K
Puska et al. (band center)	0	62	45	80	95	0.6	27
Mattsson et al. (Γ)	0		68		86	0.06	11

The energies are given in meV. The energy difference between potential minimum and ground state is 121 meV for Mattsson's data. The thermal averages, two last columns, for Puska et al. are estimated from the full data given in Ref. [12], including levels of B_1 and B_2 symmetry below 100 meV, whereas for Mattsson et al. only the data given in this table is used.

Table 2
Energetics for hydrogen on a rigid Ni(0 0 1) surface

	$T = 100$ K		$T = 300$ K		
	Classical	Quantum	Classical	Quantum	
Mattsson et al. [8]		121		132	E_{tot}
PIMC	25	85	49	91	E_{pot}
	24	95	48	102	T_{vir}
	49	179	97	193	E_{tot}
$\frac{3}{2}k_BT$	12.9		38.8		

All energies are given in meV.

Table 3
Energetics for deuterium

	$T = 100$ K		$T = 300$ K		
	Classical	Quantum	Classical	Quantum	
Mattsson et al. [8]		84		99	E_{tot}
PIMC	22	60	48	69	E_{pot}
	23	70	49	76	E_{kin}
	45	130	97	145	E_{tot}

HO-energetics at $\omega = \sqrt{k/m}$, thus $\sqrt{2}\omega_D = \omega_H$. All energies are given in meV.

Table 4
Energetics of hydrogen on thermally vibrating Ni surface

	$T = 100$ K		$T = 300$ K		
	Classical	Quantum	Classical	Quantum	
PIMC	116	160	330	276	E_{pot}
	208	207	578	524	E_{kin}
	324	367	908	800	E_{tot}

All energies are given in meV.

The PIMC potential and kinetic energies are relatively close to each other in both cases pointing to the harmonic oscillator like potential. The energies we obtain are close to those of a simple three-dimensional harmonic oscillator with $\hbar\omega = 120$ meV. The quantum mechanical total energy of harmonic oscillator is $\langle E\rangle = \frac{3\hbar\omega}{2}\coth\frac{1}{2}\hbar\omega\beta$, giving energies of 180 meV and 183 meV at temperatures 100 K and 300 K, respectively, when applied to this system. However, the potential is flat in all directions at its minimum with smaller force constants, $\hbar\omega$ below 100 meV.

The shape of the hollow potential and the excited state structure can be further analyzed by noting that we find the difference in the total energies in the two temperatures to be about 10 meV. This is what can be estimated from the data of Mattsson et al., as well, indicating that our potential function produce similar level structure. The absolute values, however, differ significantly, theirs being closer to the average of our classical and quantum energies. Overall, our potential is more confined at the hollow site than the one in Ref. [8]. This explains the difference of about 50 meV in the absolute values in Table 2. This also explains the difference between the classical and quantum case in Table 2: The confinement pushes the quantum hydrogen to higher potential energy region, see Fig. 7.

At this point, it is also instructive to remind about the classical simple harmonic oscillator energetics that is given independent of harmonic force constant by $\frac{3}{2}k_BT + \frac{3}{2}k_BT = 3k_BT = 26$ meV and 78 meV for the considered temperatures 100 K and 300 K, respectively.

For the deuterium we obtain 60 meV and 70 meV for potential energies, 70 meV and 75 meV for kinetic energies, and finally, 130 meV and 145 meV for the total energies in the two temperatures 100 K and 300 K, respectively. Thus, we nicely find the scaling down of energies in the quantum case by a factor $\sqrt{2}$. The difference in classical H and D reflect the statistical error, as these should be equal with large enough statistics.

Finally, we can briefly consider the energetics of hydrogen adsorbate on thermally fluctuating Ni surface. There, from the adsorbate-contribution-only calculation for the expression $E_{pot} + E_{kin} = E_{tot}$ we find $0.15\,\text{eV} + 0.2\,\text{eV} = 0.35\,\text{eV}$ and $0.3\,\text{eV} + 0.5\,\text{eV} = 0.8\,\text{eV}$ for the quantum hydrogen at 100 K and 300 K, respectively. In these cases, the classical hydrogen adsorbate takes on essentially the same energetics. This gives further support to our suggestion of the role of substrate dynamics in the temperature dependence of the adsorbate diffusion, and also, the classical nature of adsorbate properties at room temperature (Table 4).

5. Conclusions

We have carried out a study of hydrogen quantum delocalization on Ni(0 0 1) surface at finite temperatures. Adsorbate distributions and energetics were determined in two temperatures, 100 K and 300 K, to trace the temperature dependencies, and deuterium was considered to find the isotope effect. The finite temperature quantum and classical hydrogen adsorbates were considered both on a rigid substrate and one in thermal equilibrium with the adsorbate.

To flexibly describe the adsorbate–substrate interaction and those between substrate atoms we use the tight binding derived many-body alloy (MBA) potential, which contains only a few parameters. The parameters were fitted to the adsorption energetics and geometries from DFT calculations. The fit was shown to be perfect for the considered H/Ni(0 0 1) case, but lacking the universality to describe the extreme case of HNi molecule.

By comparing MBA to Sutton–Chen potential, we find that the two potentials have a one-to-one correspondence. The terms of the potentials can be attributed to different functional forms of hopping integrals in tight-binding formalism and it is possible to derive a unique connection between the parameter sets of these two.

Path-integral Monte Carlo method is shown to be straightforward but computationally intensive approach to find the finite temperature mixed quantum state even for a single particle. Also, the 0 K quantum state can be obtained as an extrapolation from finite temperatures, only, and time dependent dynamics cannot be assessed, either. On the other hand, the classical limit can be nicely found within the same formalism.

On the rigid Ni surface, we find strong quantum delocalization of the adsorbate at 100 K, the classical adsorbate being significantly more localized in terms of distribution and energetics. The 100 K mixed state energy turns out be larger than the bridge site barrier between the hollow sites. As this is obviously true down to 0 K, as well, it can be expected to be an important factor in surface diffusion dynamics.

At room temperature the extent of classical distribution approaches to that of quantum case, but a clear difference in energetics remains, 100 meV compared to 190 meV. The corresponding simple harmonic oscillator energy is 78 meV indicating the difference (or similarity) of the adsorbate potential and harmonic potential.

The isotope effect is, as expected, localization of the distributions and scaling down the energetics by a factor of $\sqrt{2}$.

The finite temperature surface dynamics seems to effect only little on distribution of the quantum adsorbate at 100 K. The energies increase somewhat, however. At room temperature the case is different, the substrate dynamics has a clear effect on both as compared to the rigid surface case. Furthermore, the substrate atom dynamics seems to make the strongest contribution to the temperature dependence of the H/Ni(0 0 1) system properties and phenomena considered here.

Acknowledgements

For financial support we thank Graduate School of Tampere University of Technology and the Academy of Finland, and for computational resources CSC, Center of Scientific Computing, Finland.

Appendix A. General aspects in MBA potential parameter fitting

Let us consider a cluster with N atoms, each of which with a coordination number z. If the equilibrium distance of the nearest neighbours is r_0, the total cohesive energy of the N-cluster from the MBA potential (1) and (2) is

$$E_N = N(-\sqrt{z}\xi + z\epsilon). \tag{A.1}$$

If we remove one atom and assume no relaxation of the cluster, there is one atom without neighbours, z atoms with a coordination number $z-1$, and $N-(z+1)$ atoms with a coordination number z. Thus, the energy of a $(N-1)$-cluster is

$$E_{N-1} = (N-(z+1))(-\sqrt{z}\xi + z\epsilon) + z(-\sqrt{z-1}\xi + (z-1)\epsilon). \tag{A.2}$$

Thus, by neglecting the lattice relaxation *the defect formation energy* is

$$\Delta E = E_N - E_{N-1} = -((1+z)\sqrt{z} - z\sqrt{z-1})\xi + 2z\epsilon. \tag{A.3}$$

It is useful to consider the limits of this result. For a pair of atoms, the defect formation energy is the same as the dissociation energy. In this case, $z=1$ and $\Delta E = -2\xi + 2\epsilon$.

In the limit of large coordination, i.e., $z \gg 1$, we find that $(z-1)^{1/2} \approx \sqrt{z}(1-1/(2z))$ and after some algebra we find $\Delta E \approx -\frac{3}{2}\sqrt{z}\xi + 2z\epsilon$.

In order to obtain *the cohesion energy,* we must allow relaxations, and assume that after removing one atom, all the remaining atoms in the $(N-1)$-cluster have a coordination number z. Hence the energy is

$$E_{N-1} = (N-1)(-\sqrt{z}\xi + z\epsilon) \tag{A.4}$$

and the cohesion energy is

$$\Delta E = E_N - E_{N-1} = -\sqrt{z}\xi + z\epsilon, \tag{A.5}$$

and this is the formula to be used in fitting parameters to the cohesion energy.

A.1. Fitting to dimer properties

Let us consider a pair of atoms with an equilibrium distance r_0. The total binding energy from (1) and (2) for the pair is

$$E_T(r) = -2\xi \exp\left[-q\left(\frac{r}{r_0}-1\right)\right] + 2\epsilon \exp\left[-p\left(\frac{r}{r_0}-1\right)\right]. \tag{A.6}$$

This couples the two energy parameters to the dissociation energy:

$$E_T(r_0) = -E_d = -2\xi + 2\epsilon. \tag{A.7}$$

The first derivative of the energy E_T at r_0 gives the condition for the equilibrium distance. This yields

$$q\xi = p\epsilon. \tag{A.8}$$

The second derivative at the r_0 is the harmonic force constant

$$k = \left.\frac{\partial^2 E_T}{\partial r^2}\right|_{r_0} = -2\left(\frac{q}{r_0}\right)^2\xi + 2\left(\frac{p}{r_0}\right)^2\epsilon. \tag{A.9}$$

Thus, given the equilibrium bond length r_0, dissociation energy E_d and harmonic force constant k, the four parameters are bound by three equations

$$\begin{aligned} pq &= \frac{kr_0^2}{E_d}, \\ \xi &= \frac{E_d}{2(p-q)}p, \\ \epsilon &= \frac{E_d}{2(p-q)}q, \end{aligned} \tag{A.10}$$

leaving one of the parameters free. Obviously, one free parameter cannot be expected to be sufficient to fit the adsorption data.

A.2. Fitting parameters to bulk properties

For bulk fitting, it is useful to scale the bond lengths as $r_{ij} = xr_0$, or $V = x^3V_0$. This transforms the equation for the energy to a form which is independent from the equilibrium bond length:

$$E_T = N\left(-\sqrt{z}\xi\exp(-q(x-1)) + z\epsilon\exp(-p(x-1))\right).$$

Since the equilibrium is obtained at $x = 1$, the total energy is

$$E_T = N(-\sqrt{z}\xi + z\epsilon). \tag{A.11}$$

Naturally, the cohesion energy is

$$E_{coh} = E_T/N = -\sqrt{z}\xi + z\epsilon.$$

Now the equilibrium condition is obtained from the derivative with respect to the scaling factor x, and it gives a condition

$$q\xi = \sqrt{z}p\epsilon. \tag{A.12}$$

A third condition is obtained from the bulk modulus

$$B = V\left.\frac{\partial^2 E_T}{\partial V^2}\right|_{r_0}.$$

We will need the following three results:

$$\left.\frac{\partial E_T}{\partial x}\right|_{r_0} = 0,\ \left.\frac{\partial^2 E_T}{\partial x^2}\right|_{r_0} = N(-\sqrt{z}q^2\xi + zp^2\epsilon),\ \text{and}$$

$$\frac{\partial V}{\partial x} = 3x^2 V_0.$$

Those results are used in the following lines

$$\frac{\partial E_T}{\partial V} = \frac{\partial x}{\partial V}\frac{\partial E_T}{\partial x} = \frac{1}{3x^2 V_0}\frac{\partial E_T}{\partial x}$$

and

$$\left.\frac{\partial^2 E_T}{\partial V^2}\right|_{r_0} = \left(\frac{1}{3x^2 V_0}\right)^2 \frac{\partial^2 E_T}{\partial x^2}.$$

Thus the bulk modulus is

$$B = \frac{N}{9V}(-\sqrt{z}q^2\xi + zp^2\epsilon).$$

This can be further simplified for fcc-crystals which have a density $N/V = a^3/4$ and thus

$$B = \frac{4}{9a^3}(-\sqrt{z}q^2\xi + zp^2\epsilon). \tag{A.13}$$

In the same way as for the pair, we obtain conditions:

$$\begin{aligned} pq &= -\frac{9Ba^3}{4E_{coh}}, \\ \xi &= -\frac{E_{coh}}{\sqrt{z}(p-q)}p, \\ \epsilon &= -\frac{E_{coh}}{z(p-q)}q. \end{aligned} \tag{A.14}$$

A.3. Comparison to Sutton–Chen potential

Sutton–Chen potential (SCP) is of the Finnis–Sinclair family, and also derived using tight-binding arguments. It can be written as a sum of cohesion energies of single atoms:

$$E_T = \sum_i E_i,$$

where

$$E_i = -\epsilon c_i \sqrt{\sum_{j\neq i}\left(\frac{r_0}{r_{ij}}\right)^m} + \frac{1}{2}\sum_{j\neq i}\epsilon\left(\frac{r_0}{r_{ij}}\right)^n.$$

Thus there is an apparent resemblance between MBA and SCP.

It is easy to show that at the limit $r_{ij} \to r_0$, there exists a more definite correspondence. Noticing that

$$\exp\left[-a\left(\frac{r_{ij}}{r_0} - 1\right)\right] = \left(\exp\left[\frac{r_{ij}}{r_0} - 1\right]\right)^{-a} \approx \left(\frac{r_0}{r_{ij}}\right)^a,$$

as $r_{ij} \approx r_0$, MBA has an approximate form

$$E_c(i) \approx -\xi\sqrt{\sum_{j\neq i}\left(\frac{r_0}{r_{ij}}\right)^{2q}} + \sum_{j\neq i}\epsilon\left(\frac{r_0}{r_{ij}}\right)^p.$$

Thus there we have a correspondence

$p \to n$	
$2q \to m$	
$\xi^2 r_0^{2q} \to (\epsilon c_i)^2 a^m$	
$2\epsilon r_0^p \to \epsilon a^n$	

For *Ni*, the SCP-parameters are $m = 6$, $n = 9$, $\epsilon = 1.5707 \times 10^{-2}$ eV, $c_i = 39.432$ and $a = 3.52$ Å. In terms of MBA, this would correspond to $q = 3.0$ and $p = 9.0$. If we choose the nearest neighbour distance for $r_0 = 2.49$ Å, the remaining parameters would be $\epsilon = 0.1771$ eV and $\xi = 1.752$ eV. As is shown in the text, the choice $q = 3.0$ and bulk fitting for MBA gives the parameters: $q = 3.0$ and $p = 8.6197$, $r_0 = 2.49$ Å, $\epsilon = 0.1975$ eV and $\xi = 1.9659$ eV. The difference between the two sets of parameters is due to different second derivative of the potential at the equilibrium position. In simulations, we utilize the latter set of parameters.

References

[1] A. Lee, X.D. Zhu, L. Deng, Phys. Rev. B 46 (23) (1992) 15472.
[2] X.D. Zhu, A. Lee, A. Wong, U. Linke, Phys. Rev. Lett. 68 (12) (1992) 1862.
[3] B.M. Rice, B.C. Garrett, M.L. Koszykowski, S.M. Foiles, M.S. Daw, J. Chem. Phys. 92 (1990) 775.
[4] S.E. Wonchoba, W.-P. Hu, D.G. Truhlar, Phys. Rev. B 51 (15) (1995) 9985.
[5] L.Y. Chen, S.C. Ying, Phys. Rev. Lett. 73 (5) (1994) 700.
[6] S. Badescu, S.C. Ying, T. Ala-Nissilä, Phys. Rev. Lett. 86 (22) (2001) 5092.
[7] T.R. Mattsson, U. Engberg, G. Wahnström, Phys. Rev. Lett. 71 (16) (1993) 2615.
[8] T.R. Mattsson, G. Wahnström, Phys. Rev. B 31 (3) (1995) 1885.
[9] T. Mattsson, G. Wahnström, Phys. Rev. B 56 (23) (1997) 14944.
[10] T. Mattsson, G. Wahnström, L. Bengtsson, B. Hammer, Phys. Rev. B 56 (1997) 2258.
[11] M.J. Puska, R.M. Nieminen, M. Manninen, B. Chakraborty, S. Holloway, J.K. Nørskov, Phys. Rev. Lett. 51 (1983) 1081.
[12] M.J. Puska, R.M. Nieminen, Surf. Sci. 157 (1985) 413.
[13] S.W. Rick, D.L. Lynch, J.D. Doll, J. Chem. Phys. 99 (10) (1993) 8183.
[14] K.A. Muttalib, J. Sethna, Phys. Rev. B 32 (6) (1985) 3462.

[15] M.J. Gillan, Phys. Rev. Lett. 58 (6) (1987) 563.
[16] M.J. Gillan, J. Phys. C 20 (1987) 3621.
[17] G.A. Voth, D. Chandler, W.H. Miller, J. Phys. Chem. 93 (1989) 7009.
[18] G.A. Voth, D. Chandler, W.H. Miller, J. Chem. Phys. 12 (1989) 7749.
[19] Y.-C. Sun, G.A. Voth, J. Chem. Phys. 98 (9) (1993) 7451.
[20] M.S. Daw, M.I. Baskes, Phys. Rev. B 29 (1984) 6443.
[21] P. Jena, R.M. Nieminen, M.J. Puska, M. Manninen, Phys. Rev. B 31 (12) (1985) 7612.
[22] M.J. Puska, R.M. Nieminen, P. Jena, Phys. Rev. B 35 (12) (1987) 6059.
[23] K.F.F. Assa Auerbach, R. Gomer, J. Chem. Phys. 86 (4) (1987) 2356.
[24] G. Mills, H. Jónsson, Phys. Rev. Lett. 72 (7) (1994) 1124.
[25] J.K. Nørskov, J. Chem. Phys. 12 (1989) 7461.
[26] W.Z.Y.S. Li, D. Tománek, Phys. Rev. B 44 (23) (1991) 13053.
[27] D.M. Ceperley, Rev. Mod. Phys. 67 (2) (1995) 279.
[28] W. Zhong, Y. Cai, D. Tománek, Phys. Rev. B 46 (1992) 8099.
[29] H. Grönbeck, D. Tománek, S.G. Kim, A. Rosén, Chem. Phys. Lett. 264 (1997) 39.
[30] H. Grönbeck, D. Tománek, S.G. Kim, A. Rosén, Z. Phys. D 40 (1997) 469.
[31] A. Sutton, J. Chen, Philos. Mag. Lett. 61 (3) (1990) 139.
[32] P. Bagus, C. Björkman, Phys. Rev. A 23 (1981) 461.
[33] R.P. Feynman, Statistical Mechanics, Addison-Wesley, 1972, 1988.

PAPER IV

Paper IV: Leino et al. (2007)

M. Leino, I. Kylänpää, and T. T. Rantala,

Coverage dependence of finite temperature quantum distribution of hydrogen on nickel (001) surface,

Surface Science, 601, 1246–1254, March 2007.

Available online at www.sciencedirect.com
ScienceDirect
Surface Science 601 (2007) 1246–1254
SURFACE SCIENCE
www.elsevier.com/locate/susc

Coverage dependence of finite temperature quantum distribution of hydrogen on nickel(0 0 1) surface

Markku Leino *, Ilkka Kylänpää, Tapio T. Rantala

Institute of Physics, Tampere University of Technology, P.O. Box 692, FI-33101 Tampere, Finland

Received 25 September 2006; accepted for publication 12 December 2006
Available online 30 December 2006

Abstract

Finite temperature quantum behavior of hydrogen adsorbates on Ni(0 0 1) surface is simulated using path-integral Monte Carlo technique. The adsorbate–surface and adsorbate–adsorbate interactions are described by the many-body alloy potential form, fitted to the adsorption parameters from DFT calculations. Temperatures 100 K and 300 K and coverages from 1/8 to 7/8 are considered. Also quantum and classical adsorbate behavior is compared.

At low temperatures, the quantum delocalization of the adsorbates is considerable with all studied coverages, and therefore, temperature dependence of distributions is weak. At $T = 300$ K, however, the H–H interaction energy has a considerable effect on distributions and energetics. By using a semi-classical description of the hydrogen adsorbates both temperature and coverage dependencies become strong at both temperatures.

Keywords: Monte Carlo simulations; Nickel; Construction and use of effective interatomic interactions; Equilibrium thermodynamics and statistical mechanics; Quantum effects; Hydrogen molecule

1. Introduction

Hydrogen motion and interactions on metal surfaces are of interest both technologically and fundamentally. Hydrogen interactions are considered to be simple and therefore well suited for fundamental research [1]. In particular, the light mass of hydrogen emphasizes quantum effects [2–5], which are used to explain peculiar adsorbate diffusion [6–12], vibrational observations [6], electron-energy loss spectra [13,14], low-energy electron diffraction [13,14], photoemission [14], helium scattering [15], thermal desorption [7], linear optical diffraction [16] and field emission [16,17]. Furthermore, it has been shown that quantum effects are essential in understanding the phenomena of H interactions on Ni surface [11,13,18], and, H on metal surfaces provides a unique opportunity to observe the crossover from quantum to classical dynamics at elevated temperatures [5]. Finally, combination of the many-body aspect of the interactions and the quantum nature of hydrogen dynamics at low temperatures [2] makes this system even more interesting.

Many of the interesting quantum states relate to Ni(0 0 1) surface, where H adsorbate is known to delocalize and develop a two-dimensional band structure. Thus, the protonic band structure may be important [4,19] in order to understand hydrogen reactions on metal surfaces. Many questions are still open, e.g., to what extent the electronic structure of the surface influences the reaction of atomic H (D) with adsorbed H or D [20]. Also, it is known, that presence of an adsorbate on a surface can profoundly change the surface reactivity [21]. The dissociative adsorption of molecules on surfaces of solids is of central importance in surface catalysis and has been extensively studied both experimentally and theoretically [22].

At low temperatures, the quantum delocalization of the hydrogen adsorbate on a Ni(1 0 0) surface is considerable,

* Corresponding author. Tel.: +358 50 363 8659; fax: +358 3 3115 2600.
E-mail addresses: Markku.Leino@tut.fi (M. Leino), Tapio.Rantala@tut.fi (T.T. Rantala).

0039-6028/$ - see front matter © 2006 Elsevier B.V. All rights reserved.
doi:10.1016/j.susc.2006.12.068

as we have shown earlier, see Ref. [18], and therefore, temperature dependence of distributions is weak. By using a classical description of the hydrogen adsorbate temperature dependence of the distributions and energetics becomes strong at all temperatures, proving that quantum description is necessary for the correct picture of H/Ni(0 0 1) system. At room temperature, $T = 300$ K, the extensive classical distribution is quite similar to that of quantum case and the classical thermal spreading conceals the quantum delocalization. It was found that the classical distributions are more bridge-direction oriented compared with the quantum case, where tunneling allows more circular shape.

Mutual interaction between adsorbed hydrogen atoms may significantly alter the apparent temperature dependence of the diffusion [23], and thus, other properties of the system. Two of the interaction mechanisms are direct, through space, and two are indirect, through substrate [24]: dipole–dipole interaction, direct overlap between adsorbate electronic levels, indirect interaction mediated by the non-rigid substrate ion cores and indirect interaction mediated by the metal electrons. The electrostatic interaction is assumed to be repulsive between hydrogen adatoms at Ni surface [25].

Some Ni surfaces exhibit ordered superstructures for H_n [26], but none is found for (1 0 0) surface [1,25]. On some surfaces, a molecular adsorbate is observed, e.g., Ni(5 1 0) surface covered with a dense atomic-hydrogen layer [27], but as Mårtensson et al. [27] pointed out, EELS studies of hydrogen adsorption on the flat Ni(1 0 0) surface shows that there is no molecular adsorption state populated at 80 K substrate temperature.

We report here fully quantum mechanical and thermally averaged constant temperature path-integral Monte Carlo simulation (PIMC) of hydrogen atoms on a rigid Ni(1 0 0) surface. The method is described in detail in Ref. [18] for the case of single H atom. Here we consider the coverages from 1/8 to 7/8. By employing PIMC method, we evaluate the finite temperature many-body density distributions and related energetics for quantum mechanical and classical cases. We compare the results to the semi-classical "atoms at the adsorption sites" picture. We assess the quantum nature and temperature dependencies of the hydrogen distribution and differences with the semi-classical picture. In particular, hydrogen–hydrogen interactions are considered in terms of pair correlation functions and energetics.

In the next chapter, the many-body alloy potential and PIMC are briefly described, chapter 3 gathers the results together and, finally, the last chapter presents the conclusions.

2. Computational methods

For the simulation, we need the full many-dimensional potential-energy hypersurface for several interacting H atoms at the surface. Therefore, we have chosen MBA potential, reviewed in Subsection 2.1, to describe Ni–Ni, Ni–H and H–H interactions. In Subsection 2.2 the path-integral method is described.

2.1. Many-body alloy potential

MBA has been succesfully used for H/Pd systems and for studies of the electronic and structural properties of small clusters [28,29], surfaces of metals, dilute metal alloys, see Ref. [30] and references therein, and the finite temperature quantum distribution of H adsorbate on Ni(0 0 1) surface [18].

The total (cohesive) energy of a crystal or a cluster in MBA description is decomposed [30,31] into individual atomic contributions E_i as

$$E_{\mathrm{T}} = \sum_i E_i, \tag{1}$$

where i runs over all atoms in the system and

$$E_i = -\sqrt{\sum_{j\neq i} \xi_{\alpha\beta}^2 \exp\left[-2q_{\alpha\beta}\left(\frac{r_{ij}}{r_{0,\alpha\beta}} - 1\right)\right]} + \sum_{j\neq i} \epsilon_{\alpha\beta} \exp\left[-p_{\alpha\beta}\left(\frac{r_{ij}}{r_{0,\alpha\beta}} - 1\right)\right]. \tag{2}$$

The attractive part (first term) is due to the hybridization of orbitals. It is based on a parametrized tight-binding Hamiltonian and the second-moment approximation. The repulsive part (second term) is parametrized as a pair-wise Born–Mayer potential with an exponential distance dependence [31].

We have fitted MBA potential to describe interactions between H adsorbate and Ni atoms [18]. The bulk Ni–Ni parameters were fitted to the lattice constant $a = 3.52$ Å, the nearest neighbour distance $r_0 = 2.49$ Å, cohesive energy $E_{\mathrm{coh}} = -4.44$ eV and bulk modulus $B = 1.17$ eV/Å^3. The H–Ni parameters of MBA potential were fitted to the DFT data given by Mattsson et al. [12]. The fitted quantities are the adsorption energy of the hollow site, $E_{\mathrm{ads}} = 2.8$ eV, the equilibrium distance from the surface at hollow site $r_a = 0.5$ Å and the energy barrier between the hollow sites through the bridge site, $E_{\mathrm{barr}} = 0.14$ eV. For DFT details, see Ref. [12].

For the H_2 dimer in MBA scheme we adopt the parameters from Ref. [31], giving the binding energy as -4.95 eV at bond length 0.9 Å. We note that the parameters are not fitted to describe the free H_2 molecule but the one adsorbing onto on a transition metal surface.

All of the MBA parameters that are used in simulations of this paper are given in Table 1.

Table 1
Many-body alloy (MBA) potential parameters for all atom pairs in Eq. (2)

X_α–X_β	$q_{\alpha\beta}$	$p_{\alpha\beta}$	$r_{0,\alpha\beta}$ [Å]	$\epsilon_{\alpha\beta}$ [eV]	$\xi_{\alpha\beta}$ [eV]
H–H	3.22	5.28	2.30	0.16	0.91
H–Ni	2.87	5.87	1.44	2.70	5.52
Ni–Ni	3.00	8.62	2.49	0.20	1.97

2.2. Path-integral Monte Carlo method

Quantum treatment at the finite temperature is included by using path-integral formalism for hydrogen atoms with Monte Carlo scheme, and by calculating the trace of finite temperature quantum density matrix

$$Z = \left(\frac{mM}{2\pi\hbar^2\beta}\right)^{d/2} \int \exp\left[-\beta \sum_{n=1}^{M} (K(r_{n-1}, r_n) + U(r_{n-1}, r_n))\right] \mathrm{d}r_0 \ldots \mathrm{d}r_{M-1}, \tag{3}$$

where functions K and U define internal and external energies of the system. In the primitive approximation [32,33] they are written as

$$K(r_{n-1}, r_n) = \frac{mM}{2\hbar^2\beta^2}(r_{n-1} - r_n)^2 \tag{4a}$$

and

$$U(r_{n-1}, r_n) = \frac{1}{2M}(V(r_{n-1}) + V(r_n)), \tag{4b}$$

where m is the mass of the particle and M, large enough integer, is called the Trotter number. The periodic boundary conditions in imaginary time are taken into use, i.e., $r_0 = r_M$ [18].

Quantum description is complete at the limit, where the Trotter number $M \to \infty$. However, the distributions and expectation values converge at some finite Trotter number, which depends on the temperature and external potential. This is clearly seen from the quantum distributions at different Trotter numbers, and by testing the procedure for analytically solvable systems. We found sufficient convergence in our case with Trotter number $M = 64$. At 100 K, this can be considered as a compromise with computational labour, but shows good convergence at 300 K. The typical number of sufficient Monte Carlo steps is about 10^8 for classical simulations and 2×10^9 for $T = 100$ and 4×10^8 for $T = 300$ K quantum simulations. Also, a similar sampling is needed in quantum cases to reach the equilibrium states. For higher H coverages, we are not able to use high enough Trotter numbers. Therefore, we choose $M = 1$ that returns the PIMC to classical Metropolis Monte Carlo approach. On the other hand, this allows us to compare classical and quantum hydrogen adsorbates.

Our surface model is a periodic slab of six layers of Ni atoms, eight atoms in each layer, including total of 48 atoms. The lateral periodicity is two lattice constants, $2a$. See Fig. 1. Some structure related data of the model is collected into Table 2.

3. Results

First, we test the performance of MBA potential in the present case, which now involves H–H interaction at the surface, in addition to previously reported H–Ni and Ni–Ni parametrizations [18]. This is done by considering the s.c. H_2 molecule dissociation elbow plots. Also, surface relaxation is considered, though computing capacity does not allow us to include Ni atom dynamics here, as was done in our previous study with the single hydrogen atom [18]. Then, we consider the equilibrium distributions and pair correlation functions of hydrogen atoms as a function of coverage. For lower coverages, we are able to consider both quantum and classical hydrogen and compare these, whereas, for higher coverages, we simulate the classical hydrogen only. Finally, we discuss the energetics in the above cases.

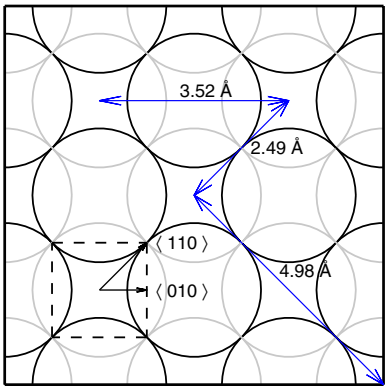

Fig. 1. Simulation supercell of Ni(001) surface (of FCC lattice, $a = 3.52$ Å) schematically, surface and subsurface layer atoms indicated by black and grey circles, respectively. One of the four-fold hollow sites is designated by the dashed square and the high symmetry directions along the surface are shown. The three possible hollow site distances (within the "periodical" simulation cell) are depicted.

Table 2
Comparison of hollow site pairs defined in Fig. 1

		R [a]	R [Å]	N_{fcc}	N_{sim}	ΔE [meV]
HBH	⟨110⟩	$\sqrt{1/2}$	2.49	4	4	199
HTH	⟨100⟩	1	3.52	4	2	99
	⟨110⟩	$\sqrt{2}$	4.98	4	1	1

N_{sim} and N_{fcc} give the statistical weight of the pairs in case of our periodic model and real (001) surface of FCC lattice, respectively, as seen in the pair correlation function of H atoms in hollow sites. HBH and HTH refer to the related elbow plots in Fig. 2.

3.1. H–H interaction in MBA

The MBA parameters for H–Ni were fitted to the case of single hydrogen atom adsorption in our previous study [18] using the DFT data of Mattson et al. [12], while the H–H parameters are taken directly from Ref. [31]. Thus, the combination should be tested against a good reference before use. For this purpose, we consider the high-symmetry potential-energy hypersurfaces conventionally used to illustrate the dissociation dynamics of H_2 molecule coming down to the perfect and rigid surface. Due to their typical shape, they are called "elbow plots". We choose the DFT calculations of Kresse et al. [25] to compare with.

It should be pointed out that description of such indirect interactions are not straightforward, as H–H interactions may be sensitive to the character of the H-induced surface

electronic structure involving the transition-metal d states [24]. On the other hand, the detailed form of the metal DOS was shown to be not important for a description of adsorbate photoemission [34]. However, different binding energies of H atoms at different sites on the surface due to the H–H interactions [26] put forward a challenge for MBA.

We present a set of MBA elbow plots in Figs. 2–4. These should be compared to those of Kresse et al., and also, to the equipotential contour lines of single hydrogen atom on Ni surface [18]. We see that MBA surprisingly successfully transforms the single atom PES to the various elbow plots as a consequence of H–H interaction.

In our case, the most important regions of the elbow plots to consider are the hollow sites shown in Fig. 2, where hydrogen adsorbates almost exclusively dwell in thermal equilibrium. Fig. 2a shows the PES for H_2 molecule dissociation above the bridge site towards the hollow sites (HBH). A small physisorption energy minimum of 20 meV is found in agreement with DFT data of Kresse [35]. We evaluate for the dissociation barrier a value of 140 meV, as the DFT barrier is 110 meV.

The chemisorption minimum is at 0.5 Å, the same as in the single-adsorbate case. The distance between adsorbed hydrogen atoms at the chemisorption minimum is 2.7 Å, expressing a repulsion between adjacent adsorbates. This repulsion is about 200 meV, see Table 3, and it is not present in DFT results.

The H–H MBA parameters are not intended for description of free H_2 molecule: the dissociation energy is too large

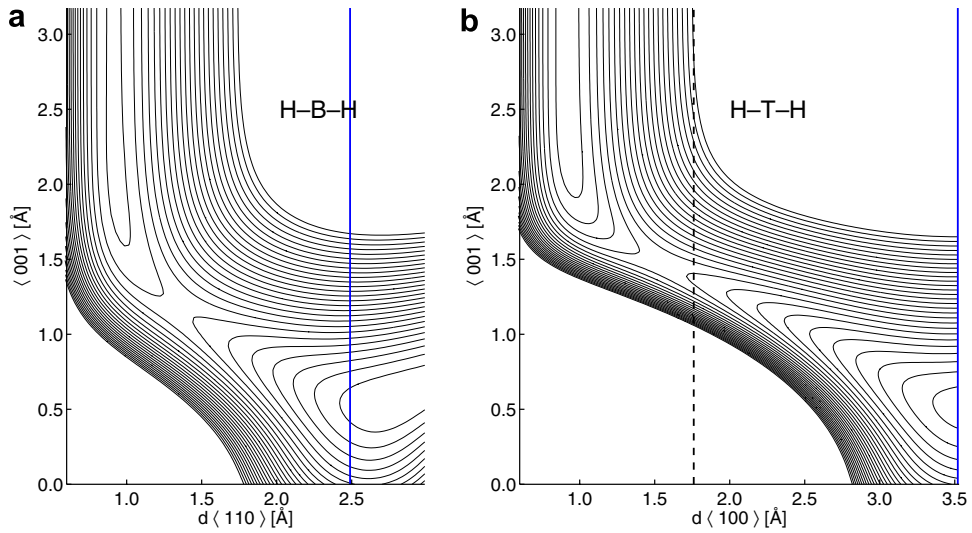

Fig. 2. Elbow plots for H_2 dissociation to hollow sites from MBA potential. High symmetry cases in planes {1 1 0} (on bridge site) and {0 1 0} (on top site) are shown on the left and right, respectively. Line spacing is 100 meV. Note that the minimum is about 100 meV higher in the former case due to the difference in remaining indirect H–H interation; see text.

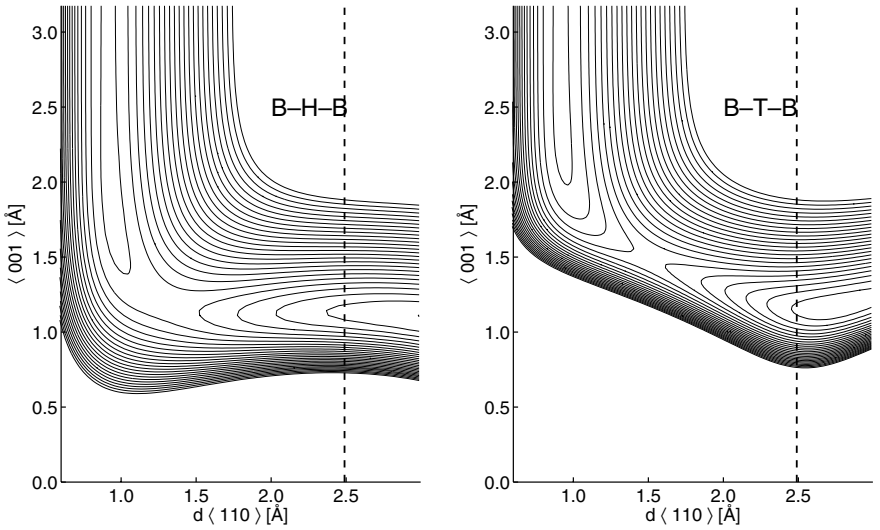

Fig. 3. Elbow plots for H_2 dissociation to bridge sites from MBA potential. High symmetry cases in planes {1 1 0} (on hollow site) and {1 1 0} (on top site) are shown on the left and right, respectively. Line spacing is 100 meV. Again, the minima differ due to the difference in remaining indirect H–H interation.

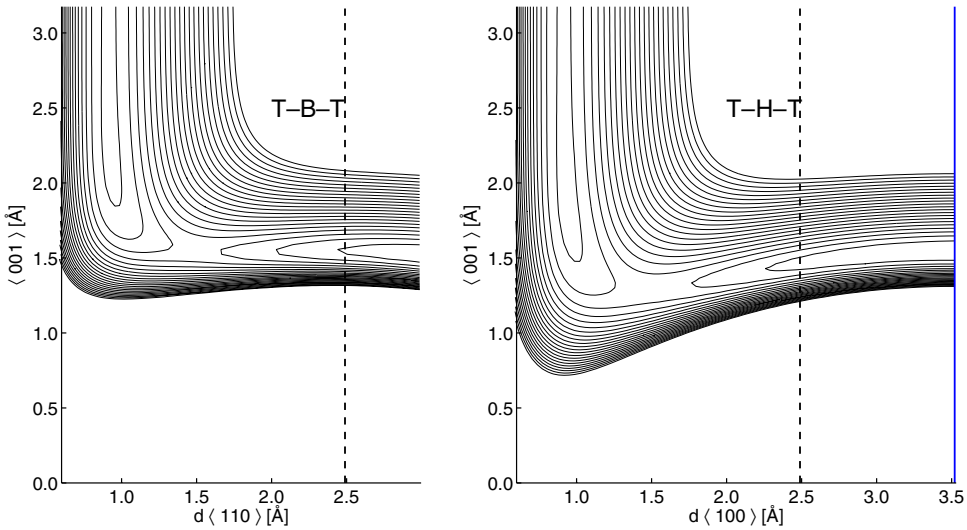

Fig. 4. Elbow plots for H_2 dissociation to top sites from MBA potential. High symmetry cases in planes {1 1 0} (on bridge site) and {1 0 0} (on hollow site) are shown on the left and right, respectively. Line spacing is 100 meV.

Table 3
MBA H_2 molecule physisorption, dissociation barrier and chemisorption energetics for the elbow plots in Fig. 2, compared to the DFT energetics from Ref. [35]

		Physisorption			Chemisorption	
		(d, z) [Å]	E [meV]	E_{dis} [meV]	(d, z) [Å]	E [eV]
MBA	hbh	(0.9,–)	25	140	(2.8,0.5)	0.5
	hth	(0.9,–)	50	350		0.6
DFT	hbh	(0.8,–)	20	110	(2.5,0.5)	1.1
	hth		20	0		

by about 0.5 eV. Therefore, the chemisorption energy becomes too small by about the same amount.

The elbow plot above the top site towards hollow sites (HTH), Fig. 2b, presents the same features as HBH. The only essentially difference in these two cases is the H–H repulsion, see Table 3. H atoms in hollow sites further apart do not essential interact, see ΔE in Table 3. We note that the dissociation barrier is not described correctly, but it is not relevant for the equilibrium distribution of H adsorbates at low coverages.

The four elbow plots in Figs. 3 and 4 are shown to illustrate performance of MBA, though they are not essential in our room temperature equilibrium simulations.

It is interesting to test MBA performance in description of surface relaxation. By allowing two uppermost Ni layers to relax, their separation is changed by $\Delta z_{12} = -0.120$ Å, which is close to the DFT result [25] −0.116 Å. Also, for the second layer separation change we get $\Delta z_{23} = -0.08$ Å, a negative value indicating a smaller layer separation. The corresponding DFT value is $\Delta z_{23} = 0.04$ Å.

As a conclusion, we find MBA with the given parameters capable of describing a single and two interacting H atoms on a Ni surface, and assume its validity for higher coverages too. Furthermore, it seems to describe correctly many other features of the system that are not relevant or needed in the present study.

3.2. Hydrogen adsorbates on nickel surface

First, we describe the adsorbate distributions for hydrogen coverages from 1/8 to 7/8 on Ni(1 0 0) surface. Temperature and quantum effects and also the H–H interactions are considered. The adsorbate energetics are estimated in the next section.

As was pointed out earlier, the simulation cell is of finite size and periodic, with periodicity of $2a$, see Fig. 1. Due to this, in ⟨1 0 0⟩ and ⟨1 1 0⟩ directions there are only two and one hollow site distances, respectively, see Fig. 1. Thus, the finite simulation cell is different from the infinite one, as indicated in Table 2.

The hydrogen quantum distribution in the hollow site at low coverages and low temperatures does not strongly depend on the coverage nor on the actual temperature. It is rather similar to that at zero Kelvin [12–14]. We confirm this fact and illustrate it in Fig. 5 with the distributions from 100 K and 300 K with hydrogen adsorbate coverages varying from 1/8 to 4/8. Indeed, only a slight spreading of the distributions can be observed when increasing the temperature, and thus, the difference between the shown two is almost insignificant.

At $T = 100$ K, the adsorbates are lying in the "circular ground state", exhibiting harmonic confinement. It should be noted that at $T = 100$ K, the distributions of coverages $\theta = 2/8$ and $\theta = 3/8$ are almost identical. Thus, the adsorbate–adsorbate interaction is rather small in both cases, though the pair correlation function differs, see below. At coverage $\theta = 2/8$, the spatial width of distribution is smallest; the hydrogen is most localized.

Only at coverages $\theta \geqslant 4/8$ the lateral distribution of quantum adsorbates is profoundly different from zero-

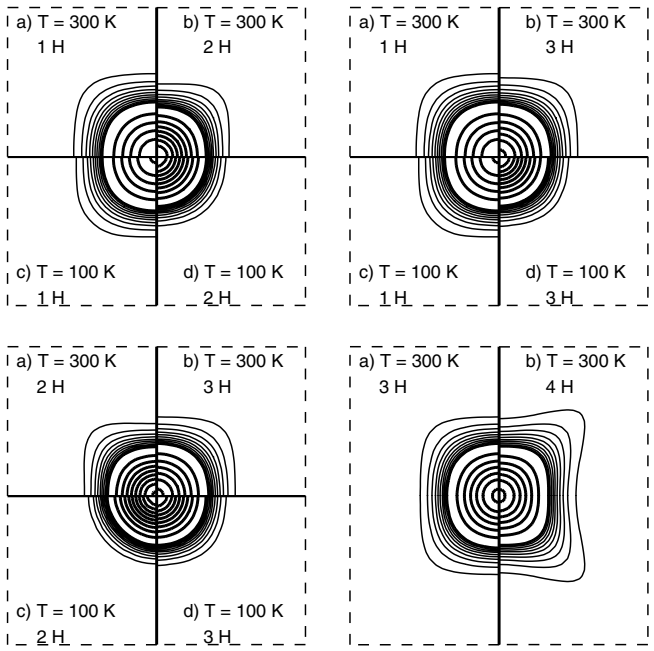

Fig. 5. One-particle quantum distribution in the hollow site, see Fig. 1, in case of adsorbate covarages $\theta = 1/8$, 2/8, 3/8, and 4/8 in the simulation cell and for temperatures 100 K and 300 K. The equidensity contours present the three-dimensional density projected onto the surface plane, i.e., integrated over z-direction. The thin and thick lines show densities 0.5, 1.0, 1.5, ... and 5, 10, 15, ... atoms/(surface) unit cell.

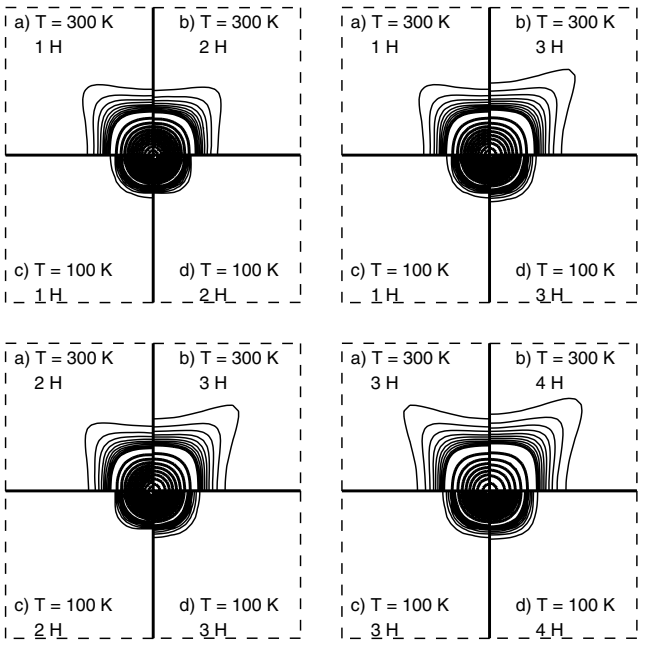

Fig. 6. "Classical hydrogen" distributions corresponding to those of quantum hydrogen in Fig. 5. Notations are the same as in Fig. 5.

Kelvin distributions, see subfigure in low-right corner in Fig. 5, showing more towards bridge-site orientation. This may be a reflection of attractive interaction [23] of H adsorbates at HTH configuration, see Fig. 2b. We have not been conducted the simulations at $T = 100$ K for coverages $\theta > 3/8$ due to the required computer capacity.

The "classical hydrogen adsorbates" show more pronounced temperature effect, see Fig. 6. It is due to the absence of zero-point vibration at $T = 100$ K, the distribution is spherical (harmonic confinement) and at room temperature, it is oriented towards bridge site. At $T = 300$ K, the thermal spreading conceals the classical in all studied coverages. Here too, the coverage $\theta = 2/8$ exhibits minimum in spatial width, following from the repulsive interaction of the H adsorbates. The lateral distributions of quantum and classical adsorbates at room temperature are quite similar, the largest difference being that the classical distributions are more bridge-direction oriented.

The pair correlation functions of the distributions, (see Fig. 7), show that all hydrogen adsorbates tend to reside apart from each other, which, again, is an indication of H–H repulsion. Thus, there is no molecular adsorption state at $T = 300$ K or $T = 100$ K, a result observed for $T = 80$ K by Mårtensson et al. [27]. The maximum values of pair correlation functions are obtained at hollow-site distances, 3.5 Å and 5.0 Å.

At higher coverages, $\theta \geqslant 3/8$, the hydrogen adsorbates are compelled to be closer to others, leading to a large peak at the distance of 3.5 Å. The difference on the quantum pair correlation functions for $\theta = 2/8$ and $\theta = 3/8$ in Fig. 7 reveals the origin of stronger localization of lateral distributions (Fig. 5). In comparison of $\theta = 3/8$ and $\theta = 4/8$ the statistical factor, $N_{\text{sim}}/N_{\text{fcc}}$ in Table 2 should be taken into account. At coverage $\theta = 3/8$, the temperature dependence is relatively small.

The pair correlation function in the non-periodic z-direction shows only Gaussian type behavior, similar to that of the case of single-adsorbate [18].

The classical hydrogen pair correlation distributions are similar to those of quantum adsorbates, the only

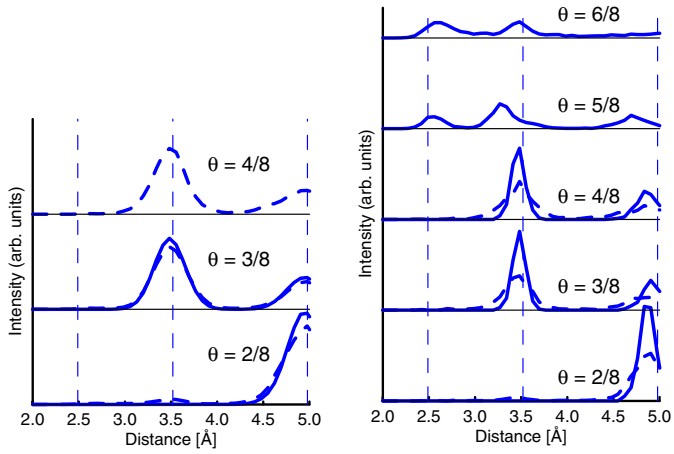

Fig. 7. Pair correlation function of H adsorbates corresponding to the one-particle distributions in Figs. 5 and 6, quantum case to the left and classical to the right. The two temperatures $T = 100$ K (solid line) and at $T = 300$ K (dashed line) are shown. Vertical dashed lines indicate the three hollow site distances, shown in Fig. 1.

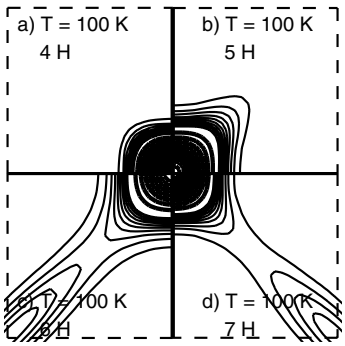

Fig. 8. "Classical hydrogen" distributions of higher coverages. Here, only temperature $T = 100$ K is shown, because at higher temperatures, the system becomes unstable. This is the case for coverage $\theta = 7/8$ even at $T = 100$ K.

essential difference being that quantum peaks are broader than classical peaks, see Fig. 7, revealing the quantum delocalization.

The hydrogen lateral distributions of higher coverages, $\theta = 4/8$–$7/8$, are shown in Fig. 8. We considered these with classical adsorbates only. For coverages $\theta > 4/8$, the hydrogen adsorbates are recombined and desorption of H_2 molecule occurs at $T = 300$ K. This may be an artifact of too small chemisorption energy of MBA, as higher coverages of quantum adsorbates are observed [1,16,17,36] and used in DFT calculations [12,25]. At $T = 100$ K, the coverages $\theta < 7/8$ are stable. The pair correlation functions of higher coverages (Fig. 7) show that adsorbates start to occupy the nearest hollow sites too.

Here, the location of maximum in z-distribution gets higher from 0.47 Å for 2 H atoms via 0.58 Å for 5 H adsorbates to 0.64 Å for 6 and 7 adsorbates. The z-distribution is not Gaussian for high coverages, as for the lower coverages, but reveals also another peak at a potential-energy minimum, $z = 1.1$ Å, which can be identified in the elbow plots in Fig. 3.

3.3. Energetics

Evaluation of energetics turns out to be a real computational challenge. This is due to extremely slow convergence to equilibrium with stationary energetics. Although, the distributions seem to converge faster by visual judgement, those above have been evaluated from the fully converged equilibrium. For the energetics below, with chosen Trotter number $M = 64$, we were able to acquire data, enough to make the statistical error bars negligible with respect to the convergence in Trotter number. In case of several H adsorbates, we are not able to evaluate the latter, but from the case of a single adsorbate [18], we estimate this "systematic error" to be of the order of a few meV.

As the MBA potential does not involve pair interactions, the interaction energy between two atoms, e.g., H–H interaction, cannot be evaluated directly. To estimate that, we used the total MBA potential of N hydrogen adsorbates energy

$$E_{\mathrm{pot},N}(\beta) = E_{\mathrm{T}} \tag{5a}$$

obtained directly from simulations, by Eq. (1), and the single-adsorbate potential energy $E_{\mathrm{pot},1}$ of the three-dimensional density function $\rho(r)$ of N hydrogen adsorbates as

$$E_{\mathrm{pot},1}(\beta) = \langle V_1(r)\rangle_{\rho(r)}, \tag{5b}$$

where $V_1(r)$ is taken to be single-adsorbate energy term, see Eq. (1). By comparing these two Eqs. (5a) and (5b), we are able to find an approximation to the interaction energy between H adsorbates.

We evaluated the kinetic energy via virial theorem, and only an approximation to that is used by assuming only single-hydrogen adsorbate, thus

$$E_{\mathrm{vir},1}(\beta) = \frac{1}{2}\langle r \cdot \nabla V_1(r)\rangle_{\rho(r)}.$$

This gives a good approximation as long as the H–H interaction is small, which is true for long-distance adsorbates on surface. From the pair correlation function, we conclude that the energetic estimates here are valid for at least H_2 and H_3. The total energy for single-adsorbate system is then

$$E_{\mathrm{tot},1} = E_{\mathrm{pot},1} + E_{\mathrm{vir},1}.$$

For the interacting system, by replacing the kinetic energy term with its single-adsorbate counterpart, we get the total energy

$$E_{\mathrm{tot},N} = E_{\mathrm{T}} + E_{\mathrm{vir}} \approx E_{\mathrm{T}} + E_{\mathrm{vir},1},$$

where E_{T} is given in Eq. (1), and thus, by writing the total energy in the form $E_{\mathrm{T}} = E_{\mathrm{pot},1} + E_{\mathrm{H\text{–}H}}$, we get an approximation for the interaction energy $E_{\mathrm{H\text{–}H}}$ of hydrogen adsorbates.

Next, we consider the energetics of hydrogen adsorbates on nickel surface.

Fig. 9a shows the variation of one-hydrogen potential energy $E_{\mathrm{pot},1}$ as a function of coverage θ. The potential energies for the quantum distributions are larger and the temperature effect is smaller compared to classical, as was pointed out earlier in discussion about the distributions. The maximum value is 90 meV at coverage 1/8. As was earlier pointed out, the H–H interaction pushes the lateral distributions smaller resulting in a smaller potential energy. The minimum potential energy of 75 meV is reached at coverage $\theta = 4/8$ for $T = 300$ K and 65 meV at $\theta = 3/8$ for $T = 100$ K.

The classical simulation shows considerable temperature effect. The single-particle potential energy of classical simulations with coverage 4/8 gives almost the same result than the quantum case. Here, it should be noticed that the lateral distributions of those two cases are very similar.

The single-adsorbate kinetic energy estimator is shown in Fig. 9b. The maximum value 100 meV is obtained at $\theta = 1/8$ and the energy is getting lower as the coverage is increasing. The minimum value is 60 meV for $T = 300$ K at $\theta = 4/8$. The quantum effect is rather large for kinetic energy also. At coverage of 4/8, the classical kinetic energy

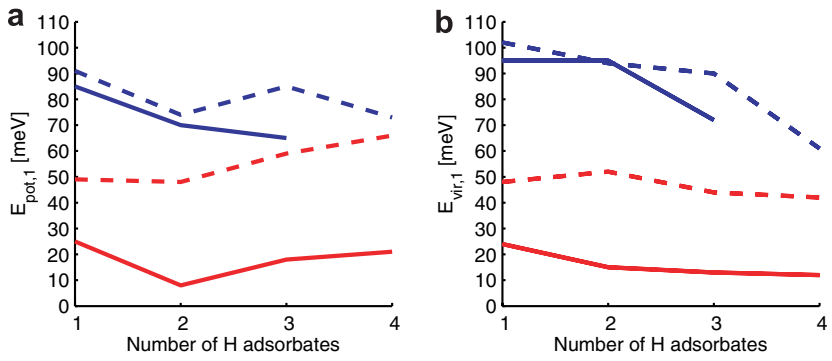

Fig. 9. Single-adsorbate approximation of potential energy (left) and kinetic energy (right) of hydrogen adsorbates on Ni surface. Solid line is for $T = 100$ K and dashed line for $T = 300$ K. Classical results are the lower (red), quantum statistical results are the upper (blue). The statistical error bars are hidden in the line width. (For interpretation of the references in colour in this figure legend, the reader is referred to the web version of this article.)

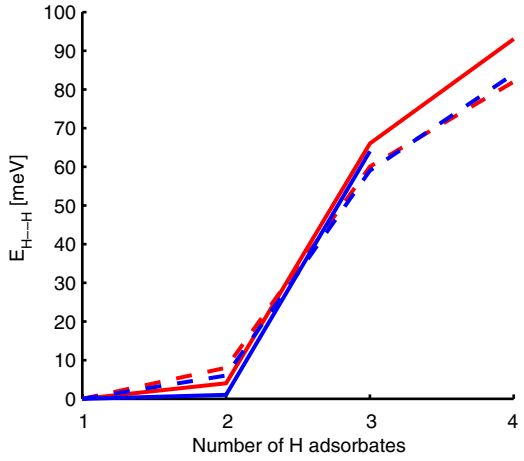

Fig. 10. Total interaction energy of the hydrogen adsorbates on Ni surface. Notations are the same as in Fig. 9.

is near to the quantum kinetic energy, when both are evaluated as a single-adsorbate approximation.

The interaction part of the potential term, Fig. 10 strongly depends on the number of adsorbates. The interaction energy increases from a few meV with two adsorbates to 100 meV with four hydrogen adsorbates in accordance with the above discussion of pair correlation function in Fig. 7 and energies given in Table 2. Only a small temperature dependence can be found. Quantum and classical interaction energies are rather similar.

4. Conclusions

We have carried out a study of quantum delocalization of hydrogen adsorbates on rigid Ni(0 0 1) surface at finite temperatures. Adsorbate distributions and energetics were determined at two temperatures, 100 K and 300 K, to trace the temperature dependencies.

To flexibly describe the adsorbate–substrate interaction and those between substrate and adsorbate atoms, we use the tight-binding derived MBA potential, which contains only a few parameters for atom pairs. The parameters were fitted to the adsorption energetics and geometries from DFT calculations. Path-integral Monte Carlo method is used, as it is a straightforward but computationally intensive approach to find the finite temperature mixed quantum state. The classical limit can be nicely found within the same formalism too.

We find strong quantum delocalization of the adsorbates at 100 K, the classical adsorbate being significantly more localized in terms of distribution and energetics. At this low temperature, the adsorbates are residing in the lateral "circular ground state", thus, showing harmonic confinement. For low coverages, $\theta \leqslant 3/8$, the distributions of classical adsorbates are more bridge-site oriented but for the coverage $\theta = 4/8$, the lateral distribution of classical and quantum cases are rather similar.

The hydrogen adsorbates have a repulsive interaction as they tend to reside apart from each other. No molecular H_2 state was found with the considered coverages. The quantum effect is mainly due to zero-point effects and tunneling towards Ni atoms in $\langle 1\,0\,0 \rangle$ directions.

The single-adsorbate potential and kinetic energies are not very sensitive to the hydrogen adsorbate coverage. Opposed to quantum case, the energetics of classical adsorbates have a considerable temperature effect, as is presumed from the distributions, already. The interaction energy of adsorbates has a strong dependence on hydrogen coverage. The interaction energy is independent of temperature and the type of the adsorbates, quantum or classical.

Acknowledgements

For financial support, the authors thank Graduate School of Tampere University of Technology and the Academy of Finland, and for computational resources, CSC, Center of Scientific Computing, Finland, and the M-grid facilities.

References

[1] K. Christmann, O. Schober, G. Ertl, M. Neumann, Adsorption of hydrogen on nickel single crystal surfaces, J. Chem. Phys. 60 (11) (1974) 4528.

[2] R. Baer, Y. Zeiri, R. Kosloff, Hydrogen transport in nickel(1 1 1), Phys. Rev. B 55 (16) (1997) 10952.
[3] B. Jackson, M. Persson, A quantum mechanical study of recombinative desorption of atomic hydrogen on a metal surface, J. Chem. Phys. 96 (3) (1992) 2378.
[4] G. Källén, G. Wahnström, Quantum treatment of H adsorbed on a Pt(1 1 1) surface, Phys. Rev. B 65 (3) (2002) 033406(4).
[5] Ş.C. Bădescu, P. Salo, T. Ala-Nissilä, S.C. Ying, K. Jacobi, Y. Wang, K. Bedürftig, G. Ertl, Energetics and vibrational states for hydrogen monolayer on Pt(1 1 1), Phys. Rev. Lett. 88 (13) (2002) 136101(4).
[6] B.M. Rice, B.C. Garrett, M.L. Koszykowski, S.M. Foiles, M.S. Daw, Kinetic isotope effects for hydrogen diffusion in bulk nickel and on nickel surfaces, J. Chem. Phys. 92 (1990) 775.
[7] S.E. Wonchoba, W.-P. Hu, D.G. Truhlar, Surface diffusion of H on Ni(1 0 0): Interpretation of the transition temperature, Phys. Rev. B 51 (15) (1995) 9985.
[8] L.Y. Chen, S.C. Ying, Theory of surface diffusion: Crossover from classical to quantum regime, Phys. Rev. Lett. 73 (5) (1994) 700.
[9] Ş.C. Bădescu, S.C. Ying, T. Ala-Nissilä, Quantum diffusion of H/Ni(1 1 1) through a Monte Carlo wave function formalism, Phys. Rev. Lett. 86 (22) (2001) 5092.
[10] T.R. Mattsson, U. Engberg, G. Wahnström, H diffusion on Ni(1 0 0): A quantum Monte Carlo simulation, Phys. Rev. Lett. 71 (16) (1993) 2615.
[11] T.R. Mattsson, G. Wahnström, Quantum Monte Carlo study of surface diffusion, Phys. Rev. B 31 (3) (1995) 1885.
[12] T. Mattsson, G. Wahnström, L. Bengtsson, B. Hammer, Quantum-mechanical calculation of H on Ni(0 0 1) using a model potential on first-principles calculations, Phys. Rev. B 56 (1997) 2258.
[13] M.J. Puska, R.M. Nieminen, M. Manninen, B. Chakraborty, S. Holloway, J.K. Nørskov, Quantum motion of chemisorbed hydrogen on Ni surfaces, Phys. Rev. Lett. 51 (1983) 1081.
[14] M.J. Puska, R.M. Nieminen, Hydrogen chemisorbed on nickel surfaces: A wave mechanical treatment of proton motion, Surf. Sci. 157 (1985) 413.
[15] S.W. Rick, D.L. Lynch, J.D. Doll, The quantum dynamics of hydrogen and deuterium on the Pd(1 1 1) surface: a path integral transition state theory study, J. Chem. Phys. 99 (10) (1993) 8183.
[16] X.D. Zhu, A. Lee, A. Wong, U. Linke, Surface diffusion of hydrogen on Ni(1 0 0): An experimental observation of quantum tunneling diffusion, Phys. Rev. Lett. 68 (12) (1992) 1862.
[17] A. Lee, X.D. Zhu, L. Deng, Observation of transition from over-barrier hopping to activated tunneling diffusion: H and D on Ni(1 0 0), Phys. Rev. B 46 (23) (1992) 15472.
[18] M. Leino, J. Nieminen, T. Rantala, Finite temperature quantum distribution of hydrogen adsorbate on nickel(0 0 1) surface, Surf. Sci. 600 (2006) 1860.
[19] Ş.C. Bădescu, K. Jacobi, Y. Wang, K. Bedürftig, G. Ertl, P. Salo, T. Ala-Nissilä, S.C. Ying, Vibrational states of a H monolayer on the Pt(1 1 1) surface, Phys. Rev. B 68 (2003) 205401(6).
[20] A. Winkler, Interaction of atomic hydrogen with metal surfaces, Appl. Phys. A 67 (1998) 637.
[21] A. Groß, C.M. Wei, M. Scheffler, Poisoning of hydrogen dissociation at Pd(1 0 0) by adsorbed sulfur studied by ab-initio quantum dynamics and ab-initio molecular dynamics, Surf. Sci. Lett. 416 (1998) L1095.
[22] G. Mills, H. Jónsson, Quantum and thermal effects in H_2 dissociative adsorption: evaluation of free energy barriers in multidimensional quantum systems, Phys. Rev. Lett. 72 (7) (1994) 1124.
[23] A. Wong, A. Lee, X.D. Zhu, Coverage dependence of quantum tunneling diffusion of hydrogen and deuterium on Ni(1 1 1), Phys. Rev. B 51 (7) (1995) 4418.
[24] C. Nyberg, C.G. Tengstål, Vibrational interaction between hydrogen atoms adsorbed on Pd(1 0 0), Phys. Rev. Lett. 50 (21) (1983) 1680.
[25] G. Kresse, J. Hafner, First-principles study of the adsorption of atomic H on Ni(1 1 1), (1 0 0) and (1 1 0), Surf. Sci. 459 (2000) 287.
[26] J.P. Muscat, Ordering of hydrogen overlayers on the (1 1 0) surfaces of nickel and palladium, Phys. Rev. B 34 (12) (1986) 8863.
[27] A.S. Mårtensson, C. Nyberg, S. Andersson, Observation of molecular H_2 chemisorption on a nickel surface, Phys. Rev. Lett. 57 (16) (1986) 2045.
[28] H. Grönbeck, D. Tománek, S.G. Kim, A. Rosén, Does hydrogen premelt palladium clusters? Chem. Phys. Lett. 264 (1997) 39.
[29] H. Grönbeck, D. Tománek, S.G. Kim, A. Rosén, Hydrogen induced melting of palladium clusters, Z. Phys. D 40 (1997) 469.
[30] W. Zhong, Y. Cai, D. Tománek, Mechanical stability of Pd–H systems: A molecular-dynamics study, Phys. Rev. B 46 (1992) 8099.
[31] W. Zhong, Y.S. Li, D. Tománek, Effect on adsorbates on surface phono modes: H on Pd(0 0 1) and Pd(1 1 0), Phys. Rev. B 44 (23) (1991) 13053.
[32] D.M. Ceperley, Path integrals in the theory of condensed helium, Rev. Mod. Phys. 67 (2) (1995) 279.
[33] M. Wagner, D.M. Ceperley, Path integral Monte Carlo simulations of thin ^{4}He films on a H_2 surface, J. Low Temp. Phys. 89 (3/4) (1992) 581.
[34] J. Rubio, M.C. Refolio, M.P.L. Sancho, J.M.L. Sancho, Correlation effects in photoemission from adsorbates: hydrogen on narrow-band metals, Phys. Rev. B 38 (5) (1988) 3142.
[35] G. Kresse, Dissociation and sticking of H_2 in the Ni(1 1 1), (1 0 0) and (1 1 0) substrate, Phys. Rev. B 62 (12) (2000) 8295.
[36] T. Kammler, S. Wehner, J. Küppers, Interaction of thermal H atoms with Ni(1 0 0)–H surfaces; through surface penetration and adsorbed hydrogen abstraction, Surf. Sci. 339 (1995) 125.

PAPER V

Paper V: Kylänpää et al. (2007)

I. Kylänpää, M. Leino, and T. T. Rantala,

Hydrogen molecule ion: Path integral Monte Carlo approach,

Accepted to Physical Review A, 2007.

Hydrogen molecule ion: Path integral Monte Carlo approach

I. Kylänpää, M. Leino and T. T. Rantala
Institute of Physics, Tampere University of Technology, P.O. Box 692, FI-33101 Tampere, Finland
(Dated: August 17, 2007)

Path integral Monte Carlo approach is used to study the coupled quantum dynamics of the electron and nuclei in hydrogen molecule ion. The coupling effects are demonstrated by comparing differences in adiabatic Born–Oppenheimer and non-adiabatic simulations, and inspecting projections of the full three-body dynamics onto adiabatic Born–Oppenheimer approximation. Coupling of electron and nuclear quantum dynamics is clearly seen. Nuclear pair correlation function is found to broaden by 0.040 a_0 and average bond length is larger by 0.056 a_0. Also, non-adiabatic correction to the binding energy is found. Electronic distribution is affected less than the nuclear one upon the inclusion of non-adiabatic effects.

I. INTRODUCTION

There is a number of phenomena in molecular and chemical physics which are influenced by the quantum behavior of both nuclei and electrons, rovibrational dynamics being a good example, see Refs. [1–3] and references therein. In case of light-mass nuclei, protons in particular, treatment of the quantum nature of the nuclei is essential [4–6]. This has proven to be important in the description of hydrogen bond, for example [7].

Hydrogen molecule ion (H_2^+), being the simplest molecule, has been studied extensively [8] and it has often been used as an example or a test case for an improved method or accuracy [9–14]. In addition to the free molecule, H_2^+ influenced by an electric or magnetic field is a well-studied subject [15–21]. Furthermore, there is interest in descriptions that do not restrict to Born–Oppenheimer (BO) or other adiabatic approximations [22–28]. Such extensions can be easily realized by using quantum Monte Carlo (QMC) methods [29, 30], for example.

Among the QMC methods the path integral formalism (PIMC) offers a finite temperature approach together with a transparent tool to trace the correlations between the particles involved. Though computationally extremely demanding, with some approximations it is capable of treating low-dimensional systems, such as small molecules or clusters accurately enough. Some examples found in literature are H [31], HD^+ and H_3^+ [32], H_2 clusters [33–37] with special attention laid on ^{4}He [38–42]. The approximations in these approaches relate to the *ad hoc* type potentials describing the interactions between particles.

In this work we evaluate the density matrix of the full three-body quantum dynamics in a stationary state and finite temperature. This is what we call "all-quantum" (AQ) simulation. Secondly, the electronic part only is evaluated as a function of internuclear distance in the spirit of BO approximation, and thirdly, the adiabatic nuclear dynamics is evaluated in the BO potential curve. These allow us to demonstrate the non-adiabatic electron–nuclei coupling by a projection of the AQ dynamics onto the adiabatic approximations.

We need to approximate the $-1/r$ Coulomb potential of electron–nucleus interaction at short range to make calculations feasible. We realize this with a carefully tested pseudopotential (PP). Also, the absent (ortho) or negligible (para) exchange interaction of nuclei is not taken into account. Finally, we want to emphasize that our purpose is to simulate a finite temperature mixed state including correlations exactly, which is a challenging task for other methods. However, if high-accuracy zero–Kelvin computations are preferred one should turn to other methods such as Variational Monte Carlo (VMC), for example. For convenience, we have chosen 300 K, which essentially, but not exactly, restricts the system to its electronic ground state.

We begin with a brief introduction to the theory and methods in the next section. This includes description of the PP, and tools and concepts for the analysis in the following section. Then we carry on to the results.

II. THEORY AND METHODS

For a quantum many-body system in thermal equilibrium the partition function contains all the information of the system [43]. The local thermodynamical properties, however, are included in the density matrix from which all the properties of the quantum system may be derived [44]. The non-adiabatic effects are directly taken into account in PIMC. In addition, finite temperature and correlation effects are exactly included.

A. Path integral Monte Carlo approach

According to the Feynman formulation of the statistical quantum mechanics [45] the partition function for interacting distinguishable particles is given by the trace of the density matrix,

$$\begin{aligned} Z &= \mathrm{Tr}\ \hat{\rho}(\beta) \\ &= \lim_{M\to\infty} \int \mathrm{d}R_0 \mathrm{d}R_1 \mathrm{d}R_2 \ldots \mathrm{d}R_{M-1} \prod_{i=0}^{M-1} e^{-S(R_i,R_{i+1};\tau)}, \end{aligned} \tag{1}$$

where $\hat{\rho}(\beta) = e^{-\beta\hat{H}}$, S is the action, $\beta = 1/k_{\mathrm{B}}T$, $\tau = \beta/M$ and $R_M = R_0$. M is called the Trotter number and it characterizes the accuracy of the discretized path. In the limit $M \to \infty$ we are ensured to get the correct partition function Z, but in practice sufficient convergence at some finite M is found, depending on the steepness of the Hamiltonian $\hat{H}$.

In the primitive approximation scheme of the PIMC formalism the action is written as [46]

$$S(R_i, R_{i+1}; \tau) = \frac{3N}{2} \ln(4\pi\lambda\tau) + \frac{(R_i - R_{i+1})^2}{4\lambda\tau} + U(R_i, R_{i+1}; \tau), \quad (2)$$

where $U(R_i, R_{i+1}; \tau) = \frac{\tau}{2}[V(R_i) + V(R_{i+1})]$ and $\lambda = \hbar^2/2m$.

Sampling of the configuration space is carried out using the Metropolis procedure [47] with the bisection moves [48]. This way the kinetic part of the action is sampled exactly and only the interaction part is needed in the Metropolis algorithm. Level of the bisection sampling ranges from 3 to 6 in our simulations, respectively with the increase in the Trotter number. The bisection sampling turns out to be essential with large Trotter numbers to achieve feasible convergence, for nuclei in particular. Total energy is calculated using the virial estimator [49].

B. Extrapolation of expectation values

The Trotter scaling procedure [32] for expectation values is used to obtain estimates for energetics in the limit $M \to \infty$. To use this procedure one needs expectation values with several different Trotter numbers. For the Trotter number M the scaling scheme is

$$\langle \widehat{A} \rangle_\infty = \langle \widehat{A} \rangle_M + \sum_{i=1}^{N} \frac{c_{2i}}{M^{2i}}, \quad (3)$$

where coefficients c_{2i} are constants for a given temperature and N represents the order of extrapolation. In this paper $N = 2$ has been used for the energies of H_2^+, and $N = 3$ for hydrogen atom energies, see Figs. 1 and 2.

C. Pseudopotential of the electron

For the hydrogen molecule ion the potential energy is

$$V(\mathbf{r}_1, \mathbf{r}_2, \mathbf{R}) = -\frac{1}{r_1} - \frac{1}{r_2} + \frac{1}{R}, \quad (4)$$

where $r_i = |\mathbf{r} - \mathbf{R}_i|$, $R = |\mathbf{R}_1 - \mathbf{R}_2|$, $\mathbf{r}$ being the coordinates of the electron and R the internuclear distance. Eq. (4) sets challenges for PIMC arising from the singularity of the attractive Coulomb interaction [50, 51], which in this work is replaced by a PP of the form [52]

$$V_{\mathrm{PP}}(r) = -\frac{\mathrm{erf}(\alpha_c r)}{r} + (a + br^2)e^{-\alpha r^2}. \quad (5)$$

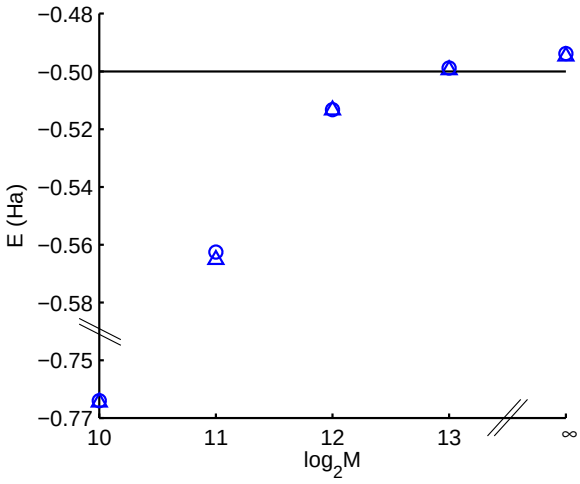

Figure 1: (Color online) Hydrogen atom total energies with different Trotter numbers: infinite nuclear mass (triangle) and AQ (circle). Extrapolated ground state energies are −0.4947(1) Ha and −0.4938(3) Ha for infinite nuclear mass and AQ simulations, respectively.

The parametres $\alpha_c = 3.8638$, $\alpha = 7.8857$, $a = 1.6617$ and $b = -18.2913$ were fitted using direct numerical solution to give the exact ground state energy of hydrogen atom and the wave function accurately outside a cut-off radius of about 0.6 a_0. Also, a number of lowest energy orbitals of the hydrogen atom are obtained accurately outside the same cut-off radius [53]. Because the bond length of H_2^+ is about 2 a_0, it is expected that bonding of the hydrogen molecule ion becomes properly described.

Hydrogen atom reference energies for different Trotter numbers are shown in Fig 1, where triangles are obtained from infinite nuclear mass and circles are from AQ simulations. Extrapolated ground state values are −0.4947(1) Ha and −0.4938(3) Ha for infinite nuclear mass and AQ simulations, respectively, statistical standard error of mean (SEM) given as uncertainty in parenthesis. We can note that within 2SEM limits proportion of these energies 0.9982 reproduces that of Rydberg constants, $R_{\mathrm{H}}/R_\infty = 0.9995$.

D. Spectroscopic constants

Within the BO approximation of diatomic molecules the corrections to electronic energies due to rovibrational motion of the nuclei can be evaluated from a Dunham polynomial [54]

$$E_{vJ} = -D_e + \omega_{\mathrm{e}}(v + \frac{1}{2}) - \omega_{\mathrm{e}}x_{\mathrm{e}}(v + \frac{1}{2})^2 + B_{\mathrm{e}}J(J+1) - \alpha_{\mathrm{e}}J(J+1)(v + \frac{1}{2}) + \ldots, \quad (6)$$

where v and J are vibrational and rotational quantum numbers, respectively, and B_e, ω_e, $\omega_\mathrm{e}x_\mathrm{e}$ and α_e are the spectroscopic constants.

The spectroscopic constants of H_2^+ and D_2^+ are obtained as introduced in Ref. [54]. In atomic units

$$B_\mathrm{e} = \frac{1}{2\mathrm{I}} = \frac{1}{2\mu R^2}, \tag{7}$$

$$\omega_\mathrm{e} = \Big(\frac{1}{\mu}\frac{\mathrm{d}^2E}{\mathrm{d}R^2}\Big)^{1/2}, \tag{8}$$

$$\omega_\mathrm{e}x_\mathrm{e} = \frac{1}{48\mu}\Big[5\Big(\frac{\mathrm{d}^3E/\mathrm{d}R^3}{\mathrm{d}^2E/\mathrm{d}R^2}\Big)^2 - 3\frac{\mathrm{d}^4E/\mathrm{d}R^4}{\mathrm{d}^2E/\mathrm{d}R^2}\Big] \tag{9}$$

and

$$\alpha_\mathrm{e} = -\frac{6B_\mathrm{e}^2}{\omega_\mathrm{e}}\Big[\frac{R}{3}\frac{\mathrm{d}^3E/\mathrm{d}R^3}{\mathrm{d}^2E/\mathrm{d}R^2} + 1\Big]. \tag{10}$$

Instead of determining these constants at the equilibrium distance only, as in Ref. [54], we evaluate expectation values from the distribution of nuclei, e.g. for the rotational constant,

$$B_\mathrm{e} = \frac{1}{2\mu}\int g(R)\frac{1}{R^2}\mathrm{d}R, \tag{11}$$

where the pair correlation function $g(R)$ is normalized to unity. The other constants, Eqs. (8)–(10), are evaluated similarly.

E. Centrifugal distortion

Effects caused by the centrifugal distortion, arising from rotational motion of the nuclei, on the equilibrium distance can be assessed by inspecting the extremum values of the energy of harmonic oscillator in rotational motion: $E_J(r) = \frac{1}{2}k(r-r_\mathrm{e})^2 + J(J+1)/2\mu r^2$. We find an approximate equation

$$\Delta R = \frac{4B_\mathrm{e}}{\mu\omega_\mathrm{e}^2 R_\mathrm{e}^2}J(J+1), \tag{12}$$

where R_e is the equilibrium distance. Eq. (12), however, does not include the anharmonic effects shown in Eq. (6), which evidently increase the bond length.

At finite temperature the rotational energy states should be weighted by the Boltzmann factor, which leads to

$$\Delta R = \frac{4B_\mathrm{e}}{\mu\omega_\mathrm{e}^2 R_\mathrm{e}^2}\frac{\sum_J J(J+1)\exp(-\beta B_\mathrm{e}J(J+1))}{\sum_J \exp(-\beta B_\mathrm{e}J(J+1))}, \tag{13}$$

where $J = 0,\ 1,\ 2, \ldots$. Using the spectroscopic constants from Ref. [54], see Table I, and temperature of 300 K we obtain $\Delta R = 0.0043\ a_0$. This approximation will be compared to our direct evaluation, below.

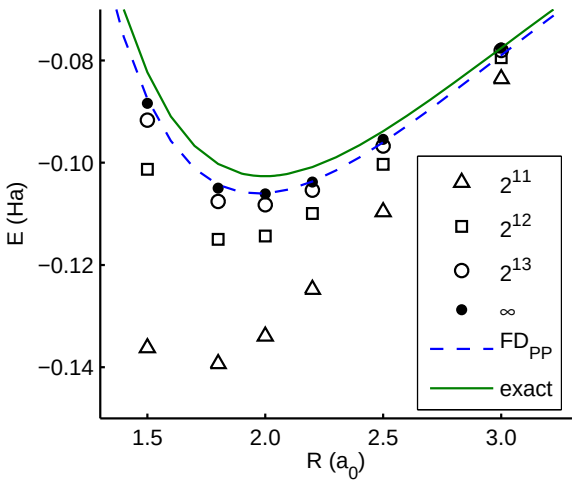

Figure 2: (Color online) H_2^+ potential curves with different Trotter numbers: $M = 2^{11}$ (square), $M = 2^{12}$ (triangle), $M = 2^{13}$ (circle), extrapolated values (dot), finite difference calculation with the pseudopotential (dashed) and with exact e^-–p^+ potential (solid).

III. RESULTS

We consider three different cases separately in order to demonstrate the non-adiabatic effects. First, the electronic part only is evaluated as a function of internuclear distance in the spirit of BO approximation. Secondly, the adiabatic nuclear dynamics is evaluated in the BO potential curve. Finally, H_2^+ is treated fully non-adiabatically with the AQ simulation. These allow us to demonstrate the non-adiabatic electron–nuclei coupling by a projection of the AQ dynamics onto the adiabatic approximations. In addition, spectroscopic constants and isotope effects are looked into.

A. Adiabatic electron dynamics

Though the PP, Eq. (5), reproduces the hydrogen atom energy exactly, an error of −0.00342 Ha from the exact value −0.10263 Ha results in binding of another proton to form H_2^+. This is demonstrated in Fig. 2, where potential curves of H_2^+ from finite difference calculations with V_PP from Eq. (5) and exact $V(r) = -r^{-1}$ are shown.

Our PIMC energies with increasing Trotter number M and the extrapolation to $M = \infty$ using Eq. (3) are shown in the same figure. These indicate clearly that the Trotter number has to be at least 2^{13} in order to find the minimum of the potential curve at the nuclear separation $R = 2.0\ a_0$. The extrapolated values are in good agreement with the potential curve $\mathrm{FD_{PP}}$, and there is almost a perfect match at $R = 2.0\ a_0$, where the value of the extrapolated dissociation energy is 0.1061(2) Ha.

For larger nuclear separations than $3.5\ a_0$, however, we are not able to reproduce the potential curve with these

Table I: Expectation values of spectroscopic constants, Eqs. (7)–(11). A Morse potential [55] fitted to the FD_{PP} potential curve is used in the evaluation of the energy derivatives. Corresponding pair correlation functions are shown in Fig. 3. First two columns are adiabatic nuclear dynamics results and AQ results are in the third column.

	H_2^+		D_2^+	H_2^+ (AQ)	
	Ha	cm^{-1}	cm^{-1}	cm^{-1}	
B_e	0.0001366	30.35	15.24	29.26	This work
	0.0001344	29.85705			Ref. [54]
ω_e	0.0104816	2328.96	1668.25	2229.77	This work
	0.0104201	2315.3		(2232)[a]	Ref. [54]
$\omega_e x_e$	0.0003552	78.92	35.33	90.73	This work
	0.0003029	67.3			Ref. [54]
α_e	6.445×10^{-6}	1.432	0.45	1.636	This work
	7.201×10^{-6}	1.600			Ref. [54]

[a]MCDFT, non-adiabatic [28]

Trotter numbers: we get too weakly binding molecule. This is assumed to be a consequence of the electronic wave function becoming more delocalized as the internuclear distance increases, and thus the "polymer ring" representing the electron is not capable of sufficient sampling of configuration space. This error should diminish with increasing M.

The electron–nucleus pair correlation function is shown in Fig. 4 and will be discussed below.

B. Adiabatic nuclear dynamics

For the quantum dynamics of the nuclei only (QN) we consider both H_2^+ and D_2^+ to see the isotope effect, too. The FD_{PP} potential curve in Fig. 2 is used, for which convergence with respect to Trotter number is found at $M \geq 2^6$ for both isotopes. Resulting pair correlation functions are shown in Fig. 3.

Average nuclear separation of 2.019(1) a_0 for H_2^+ and 2.007(2) a_0 for the isotope D_2^+ is found with $M \geq 2^6$. The full width at half maximum (FWHM) of the pair correlation functions are 0.539(1) a_0 and 0.454(1) a_0 for these isotopes, respectively.

Difference in the bond length of H_2^+ between the adiabatic electron and adiabatic nuclei simulations, i.e total distortion, is 0.019 a_0. Centrifugal contribution to this, the difference between one and three dimensional simulations of the nuclei, is 0.009(1) a_0, which unexpectedly is about twice as much as the value 0.0043 a_0 evaluated from the approximate Eq. (13). The anharmonic contribution, i.e. difference between total and centrifugal distortions, is 0.010(1) a_0. In Ref. [56] it was shown that anharmonic effects in H_2 molecule contribute about the same amount to total distortion as centrifugal force, which turns out to be the case here, too.

Difference between the total energies of the previous simulations (3D vs. 1D) is 0.0009383(2) Ha, which is close to $k_B T \approx 0.00095$ Ha as expected due to the presence of the two rotational degrees of freedom in 3D. Difference between the dissociation energies of adiabatic electron and nuclear simulations, i.e. the zero-point vibrational energy, is 0.0064(2) Ha.

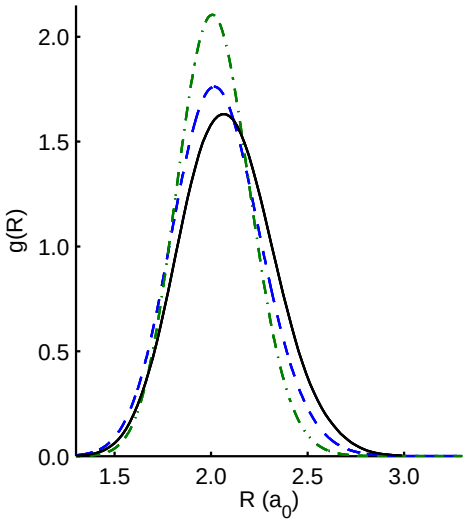

Figure 3: (Color online) Nuclear pair correlation functions: H_2^+ AQ (solid), H_2^+ QN (dashed) and D_2^+ QN (dash-dotted). The difference in the average nuclear separation between QN and AQ H_2^+ is 0.056(3) a_0.

A Morse potential [55] fitted to the FD_{PP} potential curve is used in the evaluation of the spectroscopic constants, see Table I. This is justified because the nuclear simulations and analytical Morse wave function [57] calculations coincide. The spectroscopic constants of H_2^+ are close to those given in Ref. [54], which have been determined at the equilibrium distance of the nuclei, only. Same procedure is used for the spectroscopic constants of the other isotope. In Table I the same constants evaluated using the AQ instead of BO nuclear pair correlation function are also shown.

C. Non-adiabatic "all-quantum" dynamics

For H_2^+ the total energy of AQ simulation with the Trotter number $M = 2^{13}$ is $-0.60159(3)$ Ha. The extrapolation procedure yields total energy $-0.59872(3)$ Ha, which is only 0.0016 Ha more binding than the value -0.5971 Ha from VMC simulation [30]. The zero-point energy obtained from simulations is $D_e - D_0^0 = 0.0074$ Ha, see Table II. It should be pointed out that the error due to the pseudopotential in the AQ total energy is only about half of that found for the BO total energies.

Difference in dissociation energies of AQ and the 3D QN H_2^+ simulations is 0.00097 Ha, which is about $k_B T$ revealing additional electronic energy degrees of freedom in the first. AQ simulation for H_2^+ gives for the average

Table II: H_2^+ energetics (atomic units). First three are BO and the next three are non-adiabatic values. For high-accuracy energetics see for example Ref. [14].

Method	$E_{\rm tot}$	D_e	D_0^0	R
HF[a]	−0.6026	0.1026		2.000
VMC[b]	−0.6026	0.1026		2.000
PIMC[e]	−0.6061(2)	0.1061(2)	0.0997(1)	2.0
VMC[c]	−0.5971		0.0971	2.064
MCDFT[d]	−0.581		0.081	2.08
PIMC[e]	−0.59872(3)		0.09872(3)	2.075(2)

[a]Hartree–Fock [58]
[b]VMC, Born–Oppenheimer [54]
[c]VMC, non-adiabatic[30]
[d]MCDFT, non-adiabatic (*SAO*) [28]
[e]This work

nuclear separation $R = 2.075(2)$ a_0, which is 0.056 a_0 larger than that in the QN simulation. The AQ FWHM of the nuclear pair correlation function is 0.5785(2) a_0, which shows a spreading of 0.040 a_0 compared to the QN results, see Fig. 3. With the Trotter number $M = 2^{13}$ we find the AQ nuclear pair correlation function sufficiently converged.

In Fig. 4 BO and AQ electron–nucleus pair correlation functions are compared. AQ projection onto the BO bond length, $R = 2.0$ a_0, and BO results coincide, which indicates that the adiabatic BO approach for the electron dynamics is sufficient. Thus, it seems that the electron–nuclei coupling effects are more clearly seen in the dynamics of the nuclei, see Fig. 3. As one might expect, there is a noticeable difference between the AQ and the BO electron–nucleus pair correlation functions due to varying bond length, see Fig. 4.

The AQ average nuclear separation is close to the value 2.064 a_0 obtained by a non-adiabatic VMC simulation [30]. The AQ pair correlation function of the nuclei, see Fig. 3, coincides with the *SAO* (Scaled Atomic Orbital) one in Ref. [28] computed within the Multicomponent Density Functional Theory (MCDFT) scheme, not shown here.

All the spectroscopic constants in Table I are defined using the derivatives from a fitted Morse potential, i.e. BO potential energy surface. Thus, the "AQ spectroscopic constants" should be interpreted mainly as the direction of change in the values, except for $B_{\rm e}$. The expectation values of the spectroscopic constants are obtained by weighting the equations by the nuclear pair correlation function from the corresponding simulation.

A projection of the AQ simulation to a potential curve of the nuclei is constructed with the help of the known solutions to the Morse potential. Distribution from the Morse wave function is fitted to the pair correlation function of the AQ simulation. The three-body system is then presented by an effective two-body potential. The projected potential curve shows clear differences in the dynamics of the nuclei between BO and AQ simulations, see Fig. 5. The minima of the potentials are set to zero: the difference in the dissociation energies between BO and the AQ projection is about 0.036 Ha and the shift in the equilibrium distance is 0.036 a_0. The spectroscopic constants with the projected potential curve are $B_{\rm e} = 29.26$ cm^{-1}, $\omega_{\rm e} = 2047.94$ cm^{-1},

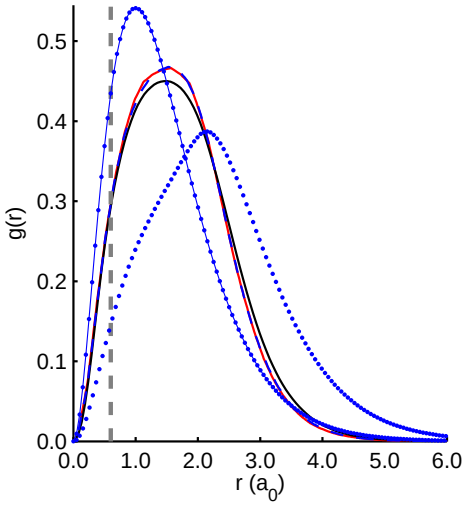

Figure 4: (Color online) H_2^+ electron–nucleus pair correlation functions: AQ (solid, second lowest curve), AQ projection to $R \approx 2.0$ a_0 (solid) and BO at $R = 2.0$ a_0 (dashed). The latter two almost coincide. Dashed vertical line indicates the size of the pseudopotential core, $r = 0.6$ a_0. For comparison corresponding pair correlation functions for hydrogen atom (dotted line) and H_2^+ (dotted) obtained by using the analytical ground state wave function of hydrogen atom are also shown.

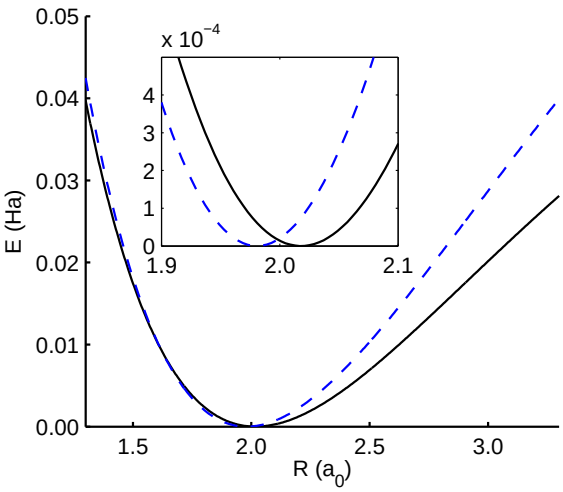

Figure 5: (Color online) H_2^+ potential curves: Morse potential fitted to FD_{PP} (dashed) and the effective Morse potential obtained from the projection of the AQ simulation (solid), see the text for details. Corresponding nuclear pair correlation functions are shown in Fig. 3. The shift in the bond length is 0.036 a_0.

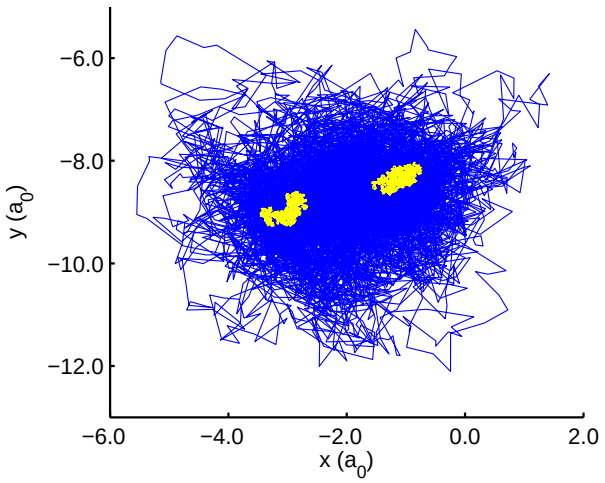

Figure 6: (Color online) xy-plane (z-projection) snapshot from AQ simulation with Trotter number 2^{13} for all particles. "Polymer ring" describing the electron is in the background and those of the nuclei are placed on top.

$\omega_e x_e = 78.12$ cm^{-1} and $\alpha_e = 2.110$ cm^{-1}. All this indicates that an effective Morse potential is not capable of describing non-adiabatic effects correctly.

Finally, it may be of interest to see a visualization of the "polymer rings" representing the quantum particles in the PIMC simulation. So, Fig. 6 presents the xy-plane (z-projection) snapshot from AQ simulation with Trotter number 2^{13} for all three particles. "Polymer ring" describing the electron is in the background and those of the nuclei are placed on top.

IV. CONCLUSIONS

The three-body quantum system, hydrogen molecule ion (H_2^+), is revisited, once again. Path integral Monte Carlo (PIMC) method is used for evaluation of the stationary state quantum dynamics. PIMC offers a finite temperature approach together with a transparent tool to describe the correlations between the particles involved. We aim at tracing the electron–nuclei coupling effects in the three-body all-quantum (AQ), i.e. non-adiabatic, molecule. This is carried out by comparing the differences in adiabatic Born–Oppenheimer (BO) and AQ simulations, and inspecting the projections from the AQ simulation onto the BO description of the electron-only and nuclear-only subsystems.

The approach turns out to be computationally demanding, but with the chosen pseudopotential for the attractive Coulomb potential and extrapolation to infinite Trotter number the task becomes feasible. By choosing low enough temperature, 300 K, we are able to compare our data to those from zero–Kelvin quantum methods available in literature. Among others we have evaluated spectroscopic constants and molecular deformation, also considering the isotope effects.

With our fully basis set free, trial wave function free and model free approach we are not able to compete in accuracy with the zero–Kelvin benchmark values. However, due to the mixed state density matrix formalism of PIMC we are able to present the most transparent description of the particle–particle correlations.

Total energies from our simulations are more binding in nature compared to the benchmark values, see Table II. This is an expected effect of the pseudopotential in use, see Fig. 2 and FD_{PP} therein. Quantum dynamics of the system is well described and distinct features of coupling are observed for the nuclei: shift of 0.056 a_0 in the equilibrium bond length, increase of 0.040 a_0 in the width of the pair correlation function of the nuclei and non-adiabatic correction of about 0.00097 Ha to dissociation energy. Electronic distribution is less influenced by the coupling than the nuclear one upon the inclusion of non-adiabatic effects, see Figs. 3 and 4.

Projection of the non-adiabatic three-body system with the help of Morse wave functions onto two-body nuclei-only subsystem indicates that Morse potential is not capable of describing non-adiabatic effects correctly, see Fig. 5.

V. ACKNOWLEDGEMENTS

For financial support we thank Graduate School of Tampere University of Technology and the Academy of Finland, and for computational resources the facilities of Finnish IT Center for Science (CSC) and Material Sciences National Grid Infrastructure (M-grid, akaatti).

[1] D. Marx and M. Parrinello, J. Chem. Phys. **104**, 4077 (1996).
[2] T. Lopez-Ciudad, R. Ramìrez, J. Schulte, and M. C. Böhm, J. Chem. Phys. **119**, 4328 (2003).
[3] R. Ramìrez, C. P. Herrero, and E. R. Hernàndez, Phys. Rev. B **73**, 245202(8) (2006).
[4] H.-P. Cheng, R. N. Barnett, and U. Landman, Chem. Phys. Lett. **237**, 161 (1995).
[5] M. Leino, J. Nieminen, and T. T. Rantala, Surface Science **600**, 1860 (2006).
[6] M. Leino, I. Kylänpää, and T. T. Rantala, Surface Science **601**, 1246 (2007).
[7] M. E. Tuckerman, D. Marx, M. L. Klein, and M. Parrinello, Science **275**, 817 (1997).
[8] B. N. Dickinson, J. Chem. Phys. **1**, 317 (1933).
[9] J. N. Silverman, D. M. Bishop, and J. Pipin, Phys. Rev. Lett. **56**, 1358 (1986).
[10] L. Adamowicz and R. J. Bartlett, J. Chem. Phys. **84**,

4988 (1986).
[11] H. W. Jones and B. Etemadi, Phys. Rev. A **47**, 3430 (1993).
[12] J. H. Macek and S. Y. Ovchinnikov, Phys. Rev. A **49**, R4273 (1994).
[13] V. V. Serov, B. B. Joulakian, D. V. Pavlov, I. V. Puzynin, and S. I. Vinitsky, Phys. Rev. A **65**, 062708(7) (2002).
[14] V. I. Korobov, Phys. Rev. A **74**, 052506 (2006).
[15] M. Vincke and D. Baye, J. Phys. B.: At. Mol. Opt. Phys. **18**, 167 (1985).
[16] J. F. Babb and A. Dalgarno, Phys. Rev. Lett. **66**, 880 (1991).
[17] K. T. Tang, J. P. Toennies, and C. L. Yiu, J. Chem. Phys. **94**, 7266 (1991).
[18] U. Kappes and P. Schmelcher, Phys. Rev. A **53**, 3869 (1996).
[19] A. Bouferguene, C. A. Weatherford, and H. W. Jones, Phys. Rev. E **59**, 2412 (1999).
[20] R. E. Moss, Phys. Rev. A **61**, 040501(R) (2000).
[21] C. Amovilli and N. H. March, Int. J. Quantum Chem. **106**, 533 (2006).
[22] A. K. Bhatia and R. J. Drachman, Phys. Rev. A **59**, 205 (1999).
[23] J. M. Taylor, A. Dalgarno, and J. F. Babb, Phys. Rev. A **60**, R2630 (1999).
[24] V. I. Korobov, Phys. Rev. A **63**, 044501(3) (2001).
[25] R. E. Moss and L. Valenzano, Mol. Phys. **64**, 649 (2002).
[26] Y. Ohta, J. Maki, H. Nagao, H. Kono, and Y. Fujimura, Int. J. Quantum Chem. **91**, 105 (2003).
[27] T. Kreibich and E. K. U. Gross, Phys. Rev. Lett. **86**, 2984 (2001).
[28] T. Kreibich, R. van Leeuwen, and E. K. U. Gross, *Multi-component density-functional theory for electrons and nuclei* (2006), URL `http://www.citebase.org/abstract?id=oai:arXiv.org:cond-mat/0609697`.
[29] C. A. Traynor, J. B. Anderson, and B. M. Boghosian, J. Chem. Phys. **94**, 3657 (1991).
[30] D. Bressanini, M. Mella, and G. Morosi, Chem. Phys. Lett. **272**, 370 (1997).
[31] X.-P. Li and J. Q. Broughton, J. Chem. Phys **86**, 5094 (1987).
[32] L. Knoll and D. Marx, Europ. Phys J. D **10**, 353 (2000).
[33] M. P. Surh, K. J. Runge, T. W. Barbee, E. L. Pollock, and C. Mailhiot, Phys. Rev. B **55**, 11330(12) (1997).
[34] M. C. Gordillo, Phys. Rev. B **60**, 6790 (1999).
[35] M. C. Gordillo and D. M. Ceperley, Phys. Rev. B **65**, 174527 (2002).
[36] M. Boninsegni, Phys. Rev. B **70**, 125405 (2004).
[37] J. E. Cuervo and P.-N. Roy, J. Chem. Phys. **125**, 124314 (2006).
[38] F. F. Abraham and J. Q. Broughton, Phys. Rev. Lett. **59**, 64 (1987).
[39] D. M. Ceperley, Rev. Mod. Phys **67**, 279 (1995).
[40] M. Pierce and E. Manousakis, Phys. Rev. Lett. **81**, 156 (1998).
[41] M. Pierce and E. Manousakis, Phys. Rev. B **59**, 3802 (1999).
[42] Y. Kwon and K. B. Whaley, Phys. Rev. Lett. **83**, 4108(4) (1999).
[43] H. Kleinert, *Path Integrals in Quantum Mechanics, Statistics, Polymer Physics, and Financial Markets* (World Scientific Publishing Co. Pte. Ltd, Singapore, 2004), 3rd Edition.
[44] E. L. Pollock and D. M. Ceperley, Phys. Rev. B **36**, 8343 (1987).
[45] R. P. Feynman, *Statistical Mechanics* (Perseus Books, 1998).
[46] D. M. Ceperley, Rev. Mod. Phys. **67**, 279 (1995).
[47] N. Metropolis, A. W. Rosenbluth, M. N. Rosenbluth, A. H. Teller, and E. Teller, J. Chem. Phys. **21**, 1087 (1953).
[48] C. Chakravarty, M. C. Gordillo, and D. M. Ceperley, J. Chem. Phys. **109**, 2123 (1998).
[49] M. F. Herman, E. J. Bruskin, and B. J. Berne, J. Chem. Phys. **76**, 5150 (1982).
[50] J. M. Thijssen, *Computational Physics* (Cambridge, 2000).
[51] S. D. Ivanov, A. P. Lyubartsev, and A. Laaksonen, Phys. Rev. E **67**, 066710 (2003).
[52] A. Dal Corso, A. Pasquarello, A. Baldereschi, and R. Car, Phys. Rev. B **53**, 1180 (1996).
[53] I. Kylänpää, Master's thesis, Tampere University of Technology (2006).
[54] S. A. Alexander and R. L. Coldwell, Chem. Phys. Lett. **413**, 253 (2005).
[55] P. M. Morse, Phys. Rev. **34**, 57 (1929).
[56] J. Lounila and T. T. Rantala, Phys. Rev. A **44**, 6641 (1991).
[57] D. ter Haar, Phys. Rev. **70**, 222 (1946).
[58] J. Kobus, L. Laaksonen, and D. Sundholm, *A Numerical Hartree-Fock Program for Diatomic Molecules* (2005), URL `http://scarecrow.1g.fi/num2d.html`.